Nutrients, Productivity, and Redox Conditions during Greenhouse Extinctions in the Panthalassic Ocean

Shane D. Schoepfer

A dissertation
submitted in partial fulfillment of the
requirements for the degree of

Doctor of Philosophy

University of Washington
2014

Reading Committee:

Peter Ward, Chair

Bruce Nelson

Eric Steig

Program Authorized to Offer Degree:
Earth and Space Sciences

University of Washington

Abstract

Nutrients, Productivity, and Redox Conditions during Greenhouse Extinctions in the Panthalassic Ocean

Shane D. Schoepfer

Chair of the Supervisory Committee:
Professor Peter D. Ward
Biology and Earth and Space Sciences

This study aims to better understand the series of events leading up to and following the Permian-Triassic mass extinction as it took place in the Panthalassic Ocean basin, with a particular focus on the oceanographic factors controlling nutrient cycles, redox conditions, and the ecology of the planktonic community. The first two chapters focus on the Opal Creek section, in Alberta, Canada, which records deposition in a slope setting at subtropical latitudes on the northwestern margin of Pangaea. The first chapter of this study uses organic carbon and nitrogen isotopes, as well as the abundant but homogenous conodont community, to infer the presence of a nutrient rich coastal upwelling system along the continental margin, with highly enriched nitrogen isotopes interpreted as reflecting denitrification in a well-developed water column oxygen minimum zone. Subsequent analysis using trace element proxies for redox and productivity, as well as declining nitrogen isotope values, suggest a substantial weakening of coastal upwelling in the earliest Triassic coinciding with the extinction of the benthic sponge fauna and an increase in the sedimentation rate.

Marine primary productivity is among the most important variables influencing water column redox conditions and benthic community structure, however it is extremely difficult to estimate from ancient marine rocks. The final chapter of this study aims to develop quantitative tools for estimating paleoproductivity, based on parameters that can be measured or calculated for most marine sedimentary systems. This study uses a compilation of 93 Cenozoic (primarily Quaternary) marine cores for which the sedimentary bulk accumulation rate could be calculated. Accumulation rates of organic carbon, phosphorus and biogenic barium are compared to estimates of primary and export productivity in the modern ocean derived from carbon-14 uptake and satellite measurements of chlorophyll. The resulting equations relating proxy accumulation to productivity can be applied to a wide variety of ancient marine systems, allowing for more quantitative reconstructions of paleoproductvity and comparison to other geochemical proxies for nutrient availability or environmental stress.

Table of Contents:

Introduction:

The Permian-Triassic Extinction and the Greenhouse Paradigm

In recent years, the paleobiological community has seen a revolution in its understanding of Phanerozoic mass extinctions. The root causes of several of these catastrophic events are no longer regarded as astronomical but, rather, have been located deep within the Earth and its oceans. Voluminous eruptions of flood basalts and the associated greenhouse gases appear to have caused rapid warming of the atmosphere, sluggish ocean circulation, marine transgression, seawater anoxia, and rapid fluctuations in the availability of nutrients (Kidder and Worsley 2010). The archetypical example of this greenhouse model of mass extinction is the end-Permian event, the most catastrophic period of extinctions ever experienced by life on Earth (Erwin et al. 2002).

The end-Permian extinction has now been firmly linked to the eruption of the Siberian Traps large igneous province (Reichow et al. 2009), which is hypothesized to have triggered a cascade of environmental stresses. Increased atmospheric CO_2, potentially supplemented by additional carbon from pre-existing coal deposits (Retallack and Jahren 2008, Svensen et al. 2009) and degassing methane hydrates (Krull et al. 2000, Benton and Twitchett 2003), led to rapid global warming, which peaked in the Early Triassic (Sun et al. 2012; Romano et al., 2013). The resulting decrease in latitudinal temperature gradients may have led a general weakening of oceanic overturning circulation (Kiehl and Shields 2005), intensified water-column stratification (Song et al. 2013), ocean acidification (Beauchamp and Grasby 2012), and expanded anoxia in oxygen-minimum zones (Algeo et al. 2011). All of these effects, as well as hypercapnia

(poisoning by excess CO_2; Knoll et al. 1996, 2007) and euxinia (production of H_2S in anoxic environments; Kump et al. 2005, Grice et al. 2005) have been proposed as the ultimate kill mechanism for the Permian-Triassic boundary mass extinction.

Knoll et al. (2007) correctly point out that these hypotheses are neither mutually exclusive nor associated by chance, but part of series of related stresses stemming from high pCO_2. All rely on a weakening of ocean circulation and increase in stratification. However, the extensive ocean stagnation thought to stem from high atmospheric CO_2 has proven difficult to model, with a large increase in nutrient availability necessary to generate widespread anoxia and euxinia even against a backdrop of stagnation (Hotinski 2001, Winguth and Maier-Reimer 2005, Meyer et al. 2008). An increase in nutrients would fuel marine primary productivity, and lead to anoxia through increased biological oxygen demand, as sinking organic matter decomposed, potentially fueling euxinic conditions in water column oxygen minimum zones (Algeo et al. 2010)

Mass extinctions represent a deviation from normal patterns of biodiversity, and it is crucial to understand the backdrop against which they occurred, i.e., the chemistry and biology of the warm, sluggishly circulating, and potentially strongly stratified world ocean as it existed under greenhouse conditions. Such conditions preceded some Phanerozoic mass extinctions and persisted after them, even as biodiversity began to return to pre-crisis levels. In this regard, these greenhouse worlds represent environments for which we have no real modern analogue. Because the global ocean was no more a single ecosystem during these greenhouse intervals than it is today, a geographically broad-based approach is needed in order to characterize the spatially complex changes associated with these crises. Focusing on environments that are especially sensitive to

environmental change can allow us to clarify, ground-truth, and refine our models, yielding a more complete understanding of the cascade of events that led from the eruption of the Siberian Traps to the most severe extinction of the Phanerozoic.

N cycling and the end-Permian Greenhouse

The role of inorganic nutrients in regulating marine productivity as the ocean switches between icehouse and greenhouse modalities over geologic time has been addressed theoretically, but field-based empirical studies have focused on the modern, where nutrient concentrations and productivity can be measured directly. The availability, residence time, and spatial distribution of nitrogen and phosphorus are difficult to assess directly in paleomarine systems; however, the nitrogen isotope composition of sedimentary organic matter, which generally reflects that of seawater nitrate (Altabet and Francois 1994), provides a tool for evaluating the relative importance of various nitrogen cycle processes.

Nitrogen isotope ($\delta^{15}N$) values close to the atmospheric value of 0 ‰ have been observed during numerous greenhouse episodes and events during Earth history, including the late Devonian (Levman and von Bitter 2002), the Permian-Triassic boundary (Luo et al. 2011), the Triassic-Jurassic boundary (Sephton et al. 2002, Quan et al. 2008), and Cretaceous ocean anoxic events (Kashiyama et al. 2008). A recently published Phanerozoic compilation (Algeo et al., 2014) reflects a shift in the modality of the nitrogen cycle related to the icehouse and greenhouse climate stages over Phanerozoic time. Low values close to the composition of atmospheric nitrogen have dominated during greenhouse periods, and are attributed to an expanded role of non-fractionating

sedimentary denitrification on the flooded shelves of a more stratified, suboxic ocean (Algeo et al., 2014).

Denitrification is hypothesized to have expanded generally during greenhouse intervals, as a result of sluggish ocean circulation and hence, increased suboxia and anoxia (Kidder and Worsley, 2010). The effects of this enhanced denitrification on global N cycling are less clear. The residence time of fixed N in the modern ocean is geologically extremely short (~3000 years, Gruber 2004) and would be expected to be even shorter under conditions of enhanced denitrification. For the total pool of fixed N to remain in steady state, enhanced denitrification would need to be balanced through enhanced N fixation by diazotrophic cyanobacteria, or else the pool of available nitrate would be rapidly depleted. While isotopic studies of greenhouse intervals suggest enhanced N fixation from the atmosphere (Algeo et al. 2014), it is not known whether N availability ever became sufficiently low to limit primary productivity on a global scale.

Although low global productivity has been attributed to N limitation during warm intervals (Falkowski, 1997; Saltzmann, 2005), this hypothesis runs counter to the prevailing view of nutrient limitation derived from study of the modern ocean. Tyrell (1999) argued that while dissolved N may limit phytoplankton growth proximally, given sufficient N limitation diazotrophic cyanobacteria will predominate ecologically and compensate by fixing nitrogen from the atmosphere until seawater nitrate is returned to the Redfieldian balance with phosphorus (i.e., a 16:1 molar ratio), the ultimate limiting nutrient on geologic timescales. N fixation may be homeostatically coupled to denitrification in the modern, oxygenated ocean (Deutsch et al., 2007, DeVries et al., 2013), thus making P the ultimate limiting nutrient, as proposed by Tyrell (1999). This

view, however, is based on modern rates of denitrification and, perhaps more importantly, it assumes that diazotrophs have been able to fix nitrogen at current rates through geologic time. It is not clear whether diazotrophs would be able to "keep pace" with phosphorus inputs in a greenhouse regime, due to the energetic burdens of diazotrophy (Tyrell, 1999), a shorter residence time of fixed N in the ocean, and the sequestration in sulfide minerals of the metal cofactors needed for N fixation, under euxinic conditions (Kidder and Worsley, 2010, Takahashi et al. 2014).

Northeastern Panthalassa and the Geography of Extinction

A decrease in nutrient availability is likely to be particularly pronounced in upwelling regions, where a majority of nutrients are delivered through vertical advection of deep water to the surface. That such regions typically support an oxygen-minimum zone (OMZ), where denitrification imparts a strong isotopic signal to the local nitrogen supply, making them recognizable in the rock record (Algeo et al. 2008). Coastal upwelling regions are an unusual oceanographic system in that their essential characteristics, high primary productivity and an expanded OMZ, must be dynamically maintained by continuous upwelling of nutrient-rich deep water. This makes them a uniquely sensitive environment in which to study changes in ocean circulation in the geologic past; an environment where small changes in the intensity of marine overturning circulation can be magnified into observable geochemical signals.

The Northeastern Panthalassic Ocean, a region that fronted on the northwestern margin of the Pangaean supercontinent during the Permo-Triassic, was identified on the basis of sedimentological indicators as a coastal upwelling zone by Ziegler (1998).

Recent modeling results have generally agreed in identifying this coast as a region of exceptionally high marine productivity (Winguth and Maier-Reimer 2005). Models have also inferred a substantially expanded oxygen minimum zone (Hotinski 2001, Winguth and Winguth 2012a, 2012b), with Winguth and Winguth (2012a) finding thermocline water depths off of western Pangaea to be the only Permian water mass in which the oxygen supply could be completely depleted by increased CO_2 alone, without adding additional nutrients. This upwelling zone also appears to be quite sensitive to climatic conditions, with its intensity varying on both Milankovitch and seasonal time scales (Winguth and Winguth 2012b).

The Opal Creek section, in southern Alberta (see Chapters I, II), exists in a continuum of late-Permian sedimentary records extending through northern Alberta and British Columbia and into the Sverdrup Basin of the Canadian Arctic (Beauchamp and Baud 2002, Wignall and Newton 2003, Algeo et al. 2012). These sections share a lithology composed primarily of spiculitic cherts in the late Permian (Algeo et al. 2012), pyritic horizons (Grasby and Beauchamp 2009) and enriched nitrogen isotope values (Algeo et al. 2012, Knies et al. 2013). Where biostratigraphic data are available, this region appears to have experienced an extinction of the endemic benthic sponge fauna coinciding with the end of the *Mesogondolella sheni* conodont zone, which would place the extinction approximately 100 kyr prior to the main extinction horizon observed at the type section in China (Chapter I, Algeo et al. 2012), and roughly coincident with the onset of carbon cycle disturbances there (Shen et al. 2011, Burgess et al. 2014). This early extinction, which has yet to be fully explored, may be another indication of the unique sensitivity of this region to latest Permian changes.

Relationship of N cycling to Productivity

Isotopic tools can be useful in understanding disturbances to global nutrient cycling, but these data are most interesting when interpreted in light of changes in marine productivity. Independent estimates or productivity, when compared with N isotopic records, are perhaps the best way to address the question of whether diazotrophs are able to keep the marine fixed nitrogen supply in balance with available phosphorus under the increased denitrification regime of a greenhouse ocean. To fully address this question, productivity proxy records would need to be compared side by side with nitrogen isotope records over a range of spatial and temporal scales, during both greenhouse and icehouse intervals. While nitrogen isotopes studies are becoming more common, to the point where a Phanerozoic compilation can be assembled (Algeo et al. 2014), comparable reliable records of paleoproductivity are lacking.

Productivity is a fundamentally important aspect of marine ecosystems that is extremely difficult to estimate accurately, due to the large number of processes that affect geochemical proxies between their assimilation into biomass and long-term storage in the rock record. Carbon isotope excursions surrounding mass extinction boundaries have been interpreted as a reflection of changes in productivity (Ward et al. 2001), but these records are subject to enough influences to complicate interpretation. Most other approaches to measuring productivity rely on the accumulation of geochemical components directly associated with biomass, including organic carbon itself (Tyson et al. 2001, 2005), phosphorus (Schenau et al. 2005), and a variety of trace elements (Brumsack 2006, Tribovillard et al. 2006). Barite, which forms in supersaturated microenvironments during the decomposition of organic matter (Paytan and Griffith

2007), has also been widely interpreted as a proxy for export production (Dymond et al. 1992, Francois et al. 1995, Eagle et al. 2003)

Productivity in paleoenvironments is often estimated in relative terms (Riquier et al. 2006, Algeo et al. 2010), an approach recommended by Tribovillard et al. (2006). Looking for broad agreement between productivity proxies with different modes of diagenesis under reducing conditions is another approach calculated to minimize preservational effects. However, these approaches do not lend themselves well to converting proxy data into estimates of actual productivity, i.e., the mass flux of carbon from the atmosphere into the ocean.

"Calibrating" proxies for productivity is fundamentally difficult and can only be attempted for modern oceanic environments, in which productivity can be measured independently of the proxies that one is attempting to calibrate. Chapter III is an attempt to better understand three of the major proxies for productivity using (1) data compiled from sediment cores from a range of environments in the modern ocean and (2) regionally averaged estimates of productivity from two fully independent sources. The goal is to relate actual in-situ productivity measurements to the accumulation rates of sedimentary productivity proxies, while correcting for the effects of two major influences that we can reasonably estimate in almost all marine sedimentary settings, i.e., redox conditions and sediment accumulation rates. By doing so, it is hoped we can begin to establish tools to more robustly estimate productivity in a wide range of ancient marine environments. This tool kit will yield numerical estimates of carbon flux, which can be related to nutrient cycling, as discussed above, as well as to the many other changes in the ocean over Phanerozoic time that future workers may wish to investigate.

References:

Algeo, T., Rowe, H., Hower, J.C., Schwark, L., Herrmann, A., Heckel, P., 2008. Changes in ocean denitrification during Late Carboniferous glacial-interglacial cycles. Nature Geoscience 1, 709-714; doi:10.1038/ngeo307.

Algeo, T.J., Kuwahara, K., Sano, H., Bates, S., Lyons, T., Elswick, E., Hinnov, L., Ellwood, B., Moser, J., Maynard, J.B., 2010. Spatial variation in sediment fluxes, redox conditions, and productivity in the Permian-Triassic Panthalassic Ocean, Palaeogeography, doi: 10.1016/j.palaeo.2010.07.007

Algeo, T.J., Kuwahara, K., Sano, H., Bates, S., Lyons, T., Elswick, E., Hinnov, L., Ellwood, B.B., Moser, J., and Maynard, J.B., 2011. Spatial variation in sediment fluxes, redox conditions, and productivity in the Permian-Triassic Panthalassic Ocean. Palaeogeography Palaeoclimatology Palaeoecology, v. 308, p. 65-83.

Algeo, T., Henderson, C.M., Ellwood, B., Rowe, H., Elswick, E., Bates, S., Lyons, T., Hower, J.C., Smith, C., Maynard, J.B., Hays, L.E., Summons, R.E., Fulton, J., and Freeman, K.H., 2012. Evidence for a diachronous Late Permian marine crisis from the Canadian Arctic region. Geological Society of America Bulletin, v. 124 (9/10), p. 1424-1448.

Algeo, T. J., Meyers, P. A., Robinson, R. S., Rowe, H., and Jiang, G. Q. 2014. Icehouse–greenhouse variations in marine denitrification. Biogeosciences, v. 11(4), p. 1273-1295.

Altabet, M.A. and Francois, R., 1994, Sedimentary nitrogen ratio as a recorder for surface ocean nitrate utilization: Global Geochemical Cycles, v. 8, p. 103-116.

Beauchamp, B., Baud, A., 2002. Growth and demise of Permian biogenic chert along northwest Pangea: evidence for end-Permian collapse of thermohaline circulation. Palaeogeography, Palaeoclimatology, Palaeoecology 184, 37-63.

Beauchamp, B., and Grasby, S. E. 2012. Permian lysocline shoaling and ocean acidification along NW Pangea led to carbonate eradication and chert expansion. Palaeogeography, Palaeoclimatology, Palaeoecology, v. 350, p. 73-90.

Benton, M.J. and Twitchett, R.J., 2003. How to kill (almost) all life: the end-Permian extinction event. TRENDS in Ecology and Evolution Vol.18 No.7 July 2003

Brumsack, H.J., 2006. The trace metal content of recent organic carbon-rich sediments: Implications for Cretaceous black shale formation. Palaeogeography Palaeoclimatology Palaeoecology, v. 232(2), p. 344-361.

Burgess, S. D., Bowring, S., and Shen, S. Z. 2014. High-precision timeline for Earth's most severe extinction. Proceedings of the National Academy of Sciences, v. 111(9), p. 3316-3321.

Deutsch, C., Sarmiento, J. L., Sigman, D. M., Gruber, N., and Dunne, J. P. 2007. Spatial coupling of nitrogen inputs and losses in the ocean. Nature,v. 445(7124), p.163-167.

DeVries, T., Deutsch, C., Rafter, P. A., and Primeau, F. 2013. Marine denitrification rates determined from a global 3-D inverse model. Biogeosciences, v. 10(4).

Dymond, J., Suess, E., Lyle, M., 1992. Barium in deep-sea sediment: a geochemical proxy for paleoproductivity. Paleoceanography, v. **7**(2), p. 163-181.

Eagle, M., Paytan, A., Arrigo, K.R., van Dijken, G., Murray, R.W., 2003. A comparison between excess barium and barite as indicators of carbon export. Paleoceanography, v. 18(1), 1021, 13 pp.

Erwin, D.H., Bowring, S.A., Jin, Y.G. 2002. End-Permian mass extinctions: a review. Boulder Geological Society of America Special Paper 356, 363–384.

Falkowski, P.G., 1997. Evolution of the nitrogen cycle and its influence on the biological sequestration of CO_2 in the ocean. Nature, v. 387, p. 272-275.

François, R., Honjo, S., Manganini, S.J., Ravizza, G.E., 1995. Biogenic barium fluxes to the deep sea: implications for paleoproductivity reconstruction. Global Biogeochemical Cycles, v. 9(2), p. 289-303.

Grasby, S.E., Beauchamp, B., 2009. Latest Permian to Early Triassic basin-to-shelf anoxia in the Sverdrup Basin, Arctic Canada. Chemical Geology 264, 232-246.

Grice, K., Cao, C., Love, G.D., Bottcher, M.E., Twitchett, R.J., Grosjean, E., Summons, R.E., Turgeon, S.C., Dunning, W., Jin, Y., 2005. Photic zone euxinia during the Permian–Triassic superanoxic event. Science 307, 706–709.

Gruber, N. 2004. The dynamics of the marine nitrogen cycle and atmospheric CO2. In ‘‘Carbon Climate interactions’’ (Oguz, T., and Follows, M., eds.). Kluwer, Dordrecht. pp. 97–148.

Hotinski, R.M., Bice, K.L., Kump, L.R., Najjar, R.G., Arthur, M.A., 2001. Ocean stagnation and end-Permian anoxia. Geology 29, 7-10.

Kashiyama Y., Ogawa, N.O., Kuroda, J., Shiro M., Nomoto S., Tada R., Kitazato H., Ohkouchi N., 2008. Diazotrophic cyanobacteria as the major photoautotrophs during mid-Cretaceous oceanic anoxic events: Nitrogen and carbon isotopic evidence from sedimentary porphyrin. Organic Geochemistry 39, 532–549

Kidder, D.L. and Worsley, T.R. 2010. Phanerozoic large igneous provinces (LIPs), HEATT (haline euxinic acidic thermal transgression) episodes, and mass extinctions. Palaeogeography, Palaeoclimatology, Palaeoecology v. 295, p. 162–191

Kiehl, J.T., and Shields, C.A., 2005. Climate simulation of the latest Permian: implications for mass extinction. Geology 33, 757–760.

Knies, J., Grasby, S. E., Beauchamp, B., Schubert, C. J. 2013. Water mass denitrification during the latest Permian extinction in the Sverdrup Basin, Arctic Canada. Geology, v. 41(2), p. 167-170.

Knoll, A. H., Bambach, R. K., Canfield, D. E., Grotzinger, J. P. 1996. Comparative Earth History and Late Permian Mass Extinction. Science, v. 273(5274), p. 452-457.

Knoll, A. H., Bambach, R. K., Payne, J. L., Pruss, S., Fischer, W. W. 2007. Paleophysiology and end-Permian mass extinction. Earth and Planetary Science Letters, v. 256(3), p. 295-313.

Krull, E.S., Retallack, G.J., Campbell, H.J., Lyon, G.L.. 2000. $\delta^{13}C_{org}$ chemostratigraphy of the Permian-Triassic boundary in the Maitai Group, New Zealand: Evidence for high-latitudinal methane release. New Zealand Journal of Geology and Geophysics v. 43, p. 21-32.

Kump, L.R., Pavlov, A., Arthur, M.A., 2005. Massive release of hydrogen sulfide to the surface ocean and atmosphere during interval of oceanic anoxia. Geology 33, 397–400.

Levman, B. G., and Bitter, P. H. V. 2002. The Frasnian-Famennian (mid-Late Devonian) boundary in the type section of the Long Rapids Formation, James Bay Lowlands, northern Ontario, Canada. Canadian Journal of Earth Sciences, v. 39(12), p. 1795-1818.

Luo, G., Wang, Y., Algeo, T. J., Kump, L. R., Bai, X., Yang, H., Yao L., and Xie, S. 2011. Enhanced nitrogen fixation in the immediate aftermath of the latest Permian marine mass extinction. Geology, v. 39(7), p, 647-650.

Meyer, K. M., Kump, L. R., & Ridgwell, A. 2008. Biogeochemical controls on photic-zone euxinia during the end-Permian mass extinction. Geology, v. 36(9), p. 747-750.

Paytan, A., Griffith, E.M., 2007. Marine barite: recorder of variations in ocean export productivity. Deep-Sea Research II, v. 54, p. 687-705.

Quan, T. M., van de Schootbrugge, B., Field, M. P., Rosenthal, Y., & Falkowski, P. G. 2008. Nitrogen isotope and trace metal analyses from the Mingolsheim core (Germany): Evidence for redox variations across the Triassic-Jurassic boundary. Global Biogeochemical Cycles, v. 22(2).

Reichow, M.K., Pringle, M.S., Al'Mukhamedov, A.I., Allen, M.B., Andreichev, V.L., Buslov, M.M., Davies, C.E., Fedoseev, G.S., Fitton, J.G., Inger, S., Medvedev, A.Y., Mitchell, C., Puchkov, V.N., Safanova, I.Y., Scott, R.A., Saunders, A.D., 2009. The timing and extent of the eruption of the Siberian Traps large igneous province: Implications for the end-Permian environmental crisis. Earth and Planetary Science Letters 277, 9-20.

Retallack, G.J., Jahren, A.H., 2008. Methane release from igneous intrusion of coal during Late Permian extinction events. Journal of Geology 116, 1-20.

Riquier, L., Tribovillard, N., Averbuch, O., Devleeschouwer, X., & Riboulleau, A. 2006. The Late Frasnian Kellwasser horizons of the Harz Mountains (Germany): two oxygen-deficient periods resulting from different mechanisms.Chemical Geology, v. 233(1), p. 137-155.

Romano, C., Goudemand, N., Vennemann, T. W., Ware, D., Schneebeli-Hermann, E., Hochuli, P. A., Brühwiler, T., Brinkmann, W. & Bucher, H. 2013. Climatic and biotic upheavals following the end-Permian mass extinction. Nature Geoscience, v. 6(1), p. 57-60.

Saltzman, M.R. 2005. Phosphorus, nitrogen, and the redox evolution of the Paleozoic oceans. Geology, v. 33(7), p. 573-576.

Schenau, S.J., Reichart, G.J., De Lange, G.J., 2005. Phosphorus burial as a function of paleoproductivity and redox conditions in Arabian Sea sediments. Geochimica et Cosmochimica Acta, v. 69(4), p. 919-931.

Sephton, M.A., Amor, K., Franchi, I.A., Wignall, P.B., Newton, R. and Zonneveld, J.P. 2002. Carbon and nitrogen isotope disturbances and an end-Norian (Late Triassic) extinction event. Geology, v. 30, p. 1119-1122.

Shen, S.Z., Crowley, J.L., Wang, Y., Bowring, S.A., Erwin, D.H., Sadler, P.M., Cao, C.Q., Rothman, D.H., Henderson, C.M., Ramezani, J., Zhang, H., Shen, Y., Wang, X.D., Wang, W., Mu, L., Li, W.Z., Tang, Y.G., Liu, X.L., Liu, L.J., Zeng, Y., Jiang, Y.F., Jin, Y.-G. 2011. Calibrating the end-Permian mass extinction. Science v. 334, p. 1367-1372.

Song, H., Tong, J., Algeo, T. J., Horacek, M., Qiu, H., Song, H., & Chen, Z. Q. 2013. Large vertical $\delta^{13}C_{DIC}$ gradients in Early Triassic seas of the South China craton: Implications for oceanographic changes related to Siberian Traps volcanism. Global and Planetary Change, v.105, p. 7-20.

Sun, Y., Joachimski, M. M., Wignall, P. B., Yan, C., Chen, Y., Jiang, H., Wang, L., Lai, X. 2012. Lethally hot temperatures during the Early Triassic greenhouse.Science, v. 338(6105), p. 366-370.

Svensen, H., Planke, S., Polozov, A. G., Schmidbauer, N., Corfu, F., Podladchikov, Y. Y., & Jamtveit, B. 2009. Siberian gas venting and the end-Permian environmental crisis. Earth and Planetary Science Letters, v. 277(3), p. 490-500.

Takahashi, S., Yamasaki, S. I., Ogawa, Y., Kimura, K., Kaiho, K., Yoshida, T., & Tsuchiya, N. 2014. Bioessential element-depleted ocean following the euxinic maximum of the end-Permian mass extinction. Earth and Planetary Science Letters, v. 393, p. 94-104.

Tribovillard N, Algeo TJ, Lyons T, Riboulleau A. 2006. Trace metals as paleoredox and paleoproductivity proxies: An update. Chemical Geology v. 232, p. 12–32

Tyrrell, T., 1999. The relative influences of nitrogen and phosphorus on oceanic primary production. Nature, v. 400, p. 525-531.

Tyson, R.V., 2001. Sedimentation rate, dilution, preservation, and total organic carbon: some results of a modeling study. Organic Geochemistry, v. 32, p. 333-339.

Tyson, R.V., 2005. The "productivity versus preservation" controversy; cause, flaws, and resolution, in Harris, N.B. (Ed.), Deposition of Organic-Carbon-Rich Sediments: Models, Mechanisms, and Consequences: Society for Sedimentary Geology (SEPM-SSG) Special Publication 82, pp. 17-33.

Ward, P.D., Haggart, J.W., Carter, E.S., Wilbur, D., Tipper, H.W., and Evans, T. 2001. Sudden productivity collapse associated with the Triassic-Jurassic boundary mass extinction. Science, v. 292, p. 1148–1151.

Wignall, P.B. and Newton, R. 2003. Contrasting deep-water records from the Upper Permian and Lower Triassic of South Tibet and British Columbia: evidence for a diachronous mass extinction. Palaios, 18, 153–167.

Winguth, A.M.E., Maier-Reimer, E., 2005. Causes of marine productivity and oxygen changes associated with the Permian-Triassic boundary: A reevalution with ocean general circulation models. Marine Geology 217, 283-304.

Winguth, A., and C. Winguth, 2012a. Precession-driven monsoon variability at the Permian-Triassic Boundary – Implications for anoxia and mass extinctions. Global and Planetary Change, v. 105, p. 160-170.

Winguth, C., and A.M.E. Winguth, 2012b. Simulating Permian-Triassic oceanic anoxia distribution: Implications for species extinction and recovery. Geology, 40, p. 127-130.

Ziegler A.M., Gibbs M.T., Hulver M.L., 1998. A mini-atlas of oceanic water masses in the Permian period. Proceedings of the Royal Society of Victoria 110 (1/2), 323–343.

Chapter I: Cessation of a Productive Coastal Upwelling System in the Panthalassic Ocean at the Permian-Triassic Boundary

Published in Palaeogeography, Palaeoclimatology, Palaeoecology v. 313, 2012

Contributing Authors: Shane D. Schoepfer[1], Charles M. Henderson[2], Geoff H. Garrison[1], Peter D. Ward[1]

Author Affiliations:

[1] Department of Earth and Space Sciences, University of Washington, Seattle, WA 98195, U.S.A.

[2] Department of Geoscience, University of Calgary, Calgary, AB, Canada

Abstract

While the end-Permian extinction in the marine realm is well known from the Tethys Ocean, it remains little studied in the vast Panthalassic Ocean. Opal Creek, Alberta, Canada is a biostratigraphically continuous Permian-Triassic Boundary (PTB) section that is interpreted to have been deposited in a deep outer shelf setting along the Panthalassic western margin of Pangaea. Significant organic carbon and nitrogen isotope excursions record the extinction of the dominant Late Permian benthic organisms (siliceous sponges). Geochemical comparison with underlying Guadalupian age rocks and analysis of the conodont fauna suggest that the latest Permian at Opal Creek records the shutdown of a productive cold-water upwelling ecosystem with a mid-water column oxygen minimum followed by the transition to a warm and less vigorously circulating system with a bottom-water oxygen minimum. The transition from a low-diversity, cold-water conodont fauna in the Middle Permian to a more diverse latest Permian fauna containing equatorial species coincides with a transition from elevated $\delta^{15}N$ values characteristic of coastal zones with denitrification in a mid-water oxygen minimum to more normal marine values. A spike in the $\delta^{13}C$ of organic carbon following a latest Permian marine transgression along western Pangaea is here attributed to transient increased productivity in the photic zone preceding the main extinction, likely related to the synergistic effects of warming, increased nutrient runoff, and residual upwelling. This is followed by an equilibration to lower $\delta^{13}C_{org}$ values characteristic of a lower productivity regime in the Early Triassic.

1. Introduction

The Panthalassic Ocean, covering some 70% of the globe, was the largest surficial feature of the Permian and Triassic world, and had the potential to exercise fundamental control of global biogeochemistry. Unfortunately, the sparsity of preserved sedimentary records has made Panthalassic ecology difficult to study. Here we examine outer shelf marine sediments from the eastern Panthalassic Ocean to determine the ecosystem's response to environmental perturbations associated with the Permian-Triassic extinction, the greatest biodiversity crisis of the Phanerozoic, , which fundamentally and irrevocably altered marine ecosystems for the entirety of the subsequent Phanerozoic (Raup and Sepkoski, 1982).

Many potential extinction mechanisms have been proposed for the Permian-Triassic mass extinction, ranging from extraterrestrial impact (Becker et al., 2001) to rapid warming of climate (Kidder and Worsley, 2004; Kump et al., 2005). However, the mechanism of extinction remains poorly understood, possibly in part because the majority of the available data is drawn from a limited region of the Permian world surrounding the Tethys Ocean (e.g. Baud et al., 1989; Jin et al., 2000; Brookfield et al., 2003.), with the exception of the mid-Panthalassic oceanic sediments exposed in Japan (Isozaki, 1994, 1997; Algeo et al., 2010a, 2010b).

Among the Late Permian through Early Triassic environmental disruptions that may have been causally related to the extinction are changes in crustal weathering patterns (Kidder and Worsley, 2003), changes in paleosols in non-marine sections (Retallack et al., 2003), aridification, vegetation loss, and fluvial drainage alteration (Ward et al., 2000), greenhouse conditions due to massive volcanic eruptions, possible

methane clathrate releases (Benton and Twitchett, 2003) and warming of the global ocean due to increased atmospheric CO_2 (Winguth et al., 2002). Warm temperatures are determined by warm climate flora at polar latitudes (Taylor et al., 2000), as well as the global demise of high latitude, cool-water, siliceous sponges (Henderson 1997; Beauchamp and Baud, 2002), and a breakdown of temperature-based conodont provincialism (Mei and Henderson, 2001). There is also growing evidence that between the Middle Permian and Early Jurassic the oxygen content of Earth's atmosphere may have varied markedly with important biological consequences (Wignall and Hallam, 1993; Wignall and Twitchett, 1996; Berner and Kothavala, 2001; Berner, 2002; Retallack et al., 2003; Huey and Ward, 2005).

Dramatic changes in inorganic and organic $\delta^{13}C$ records characterize Permian/Triassic Boundary (PTB) geochemical records in the available rock record (Retallack et al., 2003; Payne et al., 2004; Ward et al., 2005), with a negative excursion characterizing the latest Permian in Tethyan sections (Korte and Kozur, 2010; Luo et al., 2011). Negative shifts have been explained by addition of ^{13}C-depleted CO_2 to the global atmosphere-ocean reservoir by catastrophic methane release and oxidation (Retallack et al., 2003), exposure and oxidation of buried organic matter (Berner, 2002), anoxic ocean overturn (Knoll et al., 1996), and CO_2 release during massive volcanism (Erwin, 2002; White, 2002). Positive shifts in the organic $\delta^{13}C$ of marine sediments, which have been observed in other Panthalassic deep water sections (Isozaki 2009) have proven more difficult to explain, potentially reflecting both changes in the productivity and composition of marine planktonic communities (O'Leary, 1981, 1988), and variation in the degree to which various organic components (such as proteins) are preferentially

degraded in a stratified ocean and pervasively anoxic one (Isozaki 2009). As productivity and associated biological oxygen demand may have fueled Permian marine anoxia, it is important to understand the interplay between Panthalassic biology and oxygen availability.

Here we present the results of a carbon and nitrogen isotope study from a section in Southwest Alberta---Opal Creek. Sediments that comprise these strata were deposited in an outer shelf setting in the Panthalassic Ocean, on the downwarped western margin of the North American plate (Henderson, 1989, Richards, 1989) at approximately 30° North paleolatitude. This site has a complete conodont zonation from the uppermost Permian across the PTB in an area far removed from the Paleotethys. The site is the southernmost of a series of Upper Permian-Lower Triassic sections running north into the Arctic. This environmental record from off the northwest shores of Pangaea provides augmentation to the numerous Tethyan and mid-Panthalassic studies and improves our understanding of environmental changes across the world's largest ocean basin. This site contains a well-preserved boundary interval deposited in a deep-water facies, with sufficient biostratigraphic control to allow global correlation (Henderson et al., 1994; Henderson 1997).

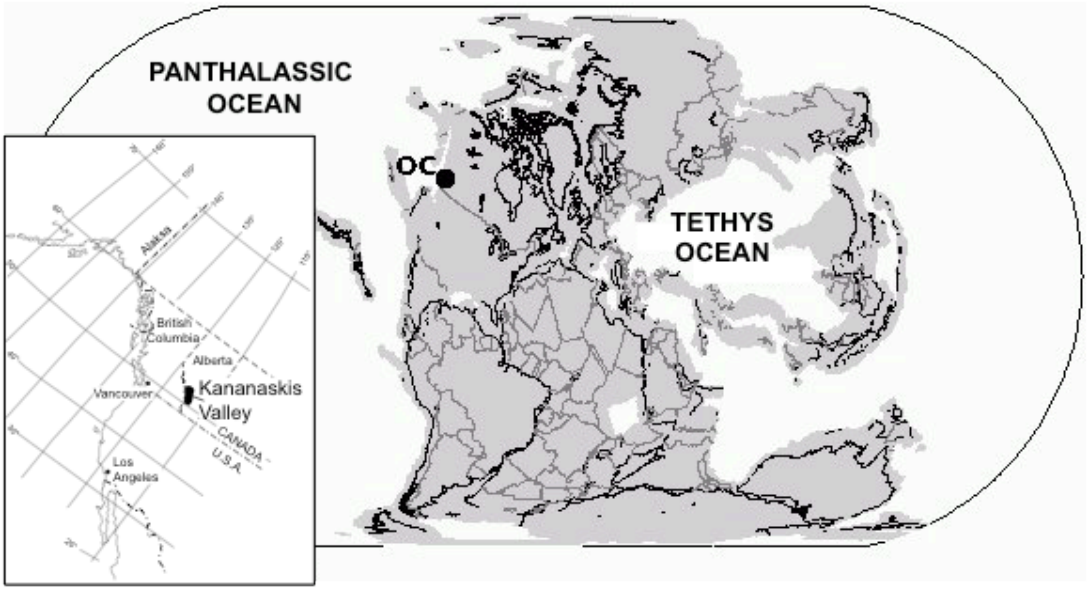

Figure 1: Paleomap showing the position of the continents and oceans in the latest Permian. OC = location of Opal Creek section. Map software from PaleoDB, copyright Alroy 2010. Inset displays the modern location of the Kananaskis Valley in Alberta.

1.1 Geologic Setting and Biostratigraphy:

The Opal Creek Permian-Triassic boundary section is located in southwest Alberta along the southern bank of Opal Creek in Kananaskis Valley in the foothills of the Canadian Rockies (Figure 1). The Ranger Canyon and Fantasque formations, consisting of spiculitic chert grading into carbonate and silica cemented immature sandstone and phosphatic siltstones, (Figure 3) range from southeastern British Columbia to the southern Mackenzie Fold Belt in northern Canada (Henderson, 1989). These units were deposited on deep water outer shelf or slope as determined by the predominance of sponge spicules, the abundance of phosphatic material, and the absence of shallow water sedimentary structures (Henderson, 1997). At Opal Creek the Ranger Canyon Formation

is only 235 cm thick and includes the conodonts *Mesogondolella bitteri* and at the top *M. rosenkrantzi*; indicating a Capitanian age (Mei and Henderson, 2001). The presence of *M. rosenkrantzi* may indicate an early Wuchiapingian or latest Capitanian age given the overlap with *M. bitteri* (Mei and Henderson, 2001). Middle and Late Permian species of *Mesogondolella* are typical of cool-water environments as inferred by their strong boreal provincialism (Mei and Henderson, 2001) at that time. The most common fossils in the Ranger Canyon Formation chert are large monaxon siliceous sponges spicules (up to 4 cm long), possibly of the class Demospongea. Elsewhere, the presence of these "silica factories" has been used to infer nutrient-rich, cold marine waters with active oceanic circulation (Beauchamp and Baud, 2002).

Unconformably overlying the Ranger Canyon Formation is the Phroso Siltstone Member of the Sulphur Mountain Formation, equivalent to the Grayling Formation in northeastern British Columbia (Wignall and Newton, 2003), which is composed of silty shale with minor dolomite, as well as abundant pyrite, concentrated in a cm-think bed located 10.5 cm above the unconformity. Like the Ranger Canyon, the lower Sulphur Mountain Formation also has abundant siliceous monaxon sponge spicules to 2 cm in length. These disappear abruptly at 0.4 meters above the base, which coincides with the sudden influx of new Late Permian conodont species belonging to the genus *Clarkina,* likely representing the main end-Permian extinction. Above this boundary, the Sulphur Mountain Formation is composed of black to dark grey, pyritic, thin-bedded shale and siltstone. There is a dearth of benthic biota or bioturbation, suggesting suboxic to anoxic bottom waters during deposition (Figure 2) (Gibson, 1969, 1974; Gibson and Barclay, 1989; Henderson, 1997).

The temporal extent of the regional unconformity can be approximated using conodont biostratigraphy from carbonate lenses within the Ranger Canyon Formation and from slightly calcareous silty shale of the Sulphur Mountain Formation. The oldest rocks of the Sulphur Mountain Formation include *Mesogondolella sheni* and presumed reworked specimens of *M. bitteri* and *M. rosenkrantzi*. *M. sheni* appears to be a good index for the cool-water Changhsingian (Mei and Henderson, 2001) and is widely distributed from Selong, Tibet (Mei, 1996) to the Sverdrup Basin in the Canadian Arctic (Beauchamp et al., 2009). The presence of *M. sheni* from the basal transgressive systems tract (TST) of the Sulphur Mountain Formation indicates a Changhsingian age, but the exact relationships between these specimens and the type material from Selong, Tibet (Mei, 1996; Shen et al., 2006) still need to be established. The duration of the unconformity separating the Ranger Canyon and Sulphur Mountain formations includes all or most of the Wuchiapingian and part or most of the Changhsingian and is therefore on the order of 5 to 7 million years (Shen et al., 2010).

Four conodont biozones comprise the studied portion of the Sulphur Mountain Formation at Opal Creek, including in ascending order: 1) *M. sheni*, 2) *C. hauschkei – C. meishanensis*, 3) *Hindeodus parvus – C. taylorae*, and 4) *C. taylorae – C. cf. carinata* Zones (Figure 3), with the local first occurence of *H. parvus* in association with the first occurence of C. taylorae at 150 cm above the unconformity indicating the biostratigraphic Permian-Triassic Boundary.

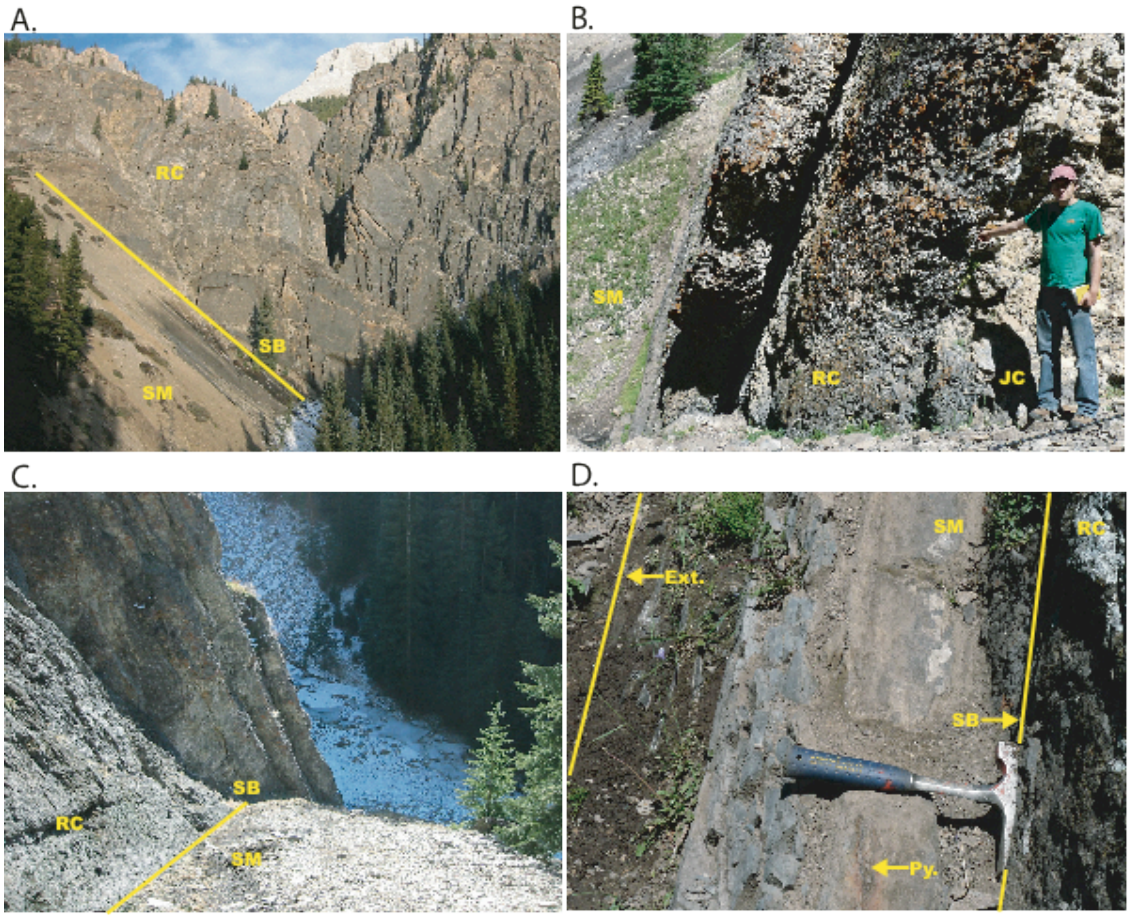

Figure 2: Photographs of outcrop at Opal Creek. A: Facing outcrop from trail. Beds dip nearly vertically, cliff forming unit is the Ranger Canyon Formation, with the face representing the unconformable upper contact. The Sulfur Mountain siltstones form most of the slope in the foreground. B: Cross sectional view of Ranger Canyon formation, author pointing to lower contact with underlying Johnston Canyon dolostones. Ranger Canyon unit is approximately 2 m. thick. C: View along cliff face showing contact between resistant, silicified Ranger Canyon material and fissile Sulphur Mountain siltsones. D: Close up of latest Permian deposits following the unconformity at Opal Creek. Hammer for scale.

JC = Johnston Canyon Formation, RC = Ranger Canyon Formation, SM = Sulphur Mountain Formation, SB = Unconformable sequence boundary, Py. = Pyrite bed, Ext. = main extinction horizon.

2. Materials and Methods:

Samples 0.5 kg – 3 kg in mass were collected at meter scale throughout the section for conodont biostratigraphy. Additionally, samples 3-10 g in mass were collected at meter to sub-centimeter scale in the lowermost strata surrounding the PTB, for isotopic analysis Sedimentary organic $\delta^{13}C_{org}$ and $\delta^{15}N$ were analyzed via elemental analyzer–continuous-flow isotope ratio mass spectrometry (EA-CFIRMS) at the ISOLAB stable isotope laboratory at the University of Washington. Samples were chosen to avoid cracks and visible surface alteration and weathering and sonicated in methanol and deionized water. Samples were then powdered and acidified with an excess of 10% HCl and kept at 40°C for at least 12 hours to remove inorganic carbonate material. Samples were then triple rinsed with ultra pure (>18 MΩ) deionized water and oven dried at 40°C. Analyses were made with a Costech ECS 4010 Elemental Analyzer coupled to a ThermoFinnigan MAT253 mass spectrometer via a ThermoFinnigan CONFLO III gas interface.

Carbon and oxygen isotopes ($\delta^{13}C_{carb}$ and $\delta^{18}O_{carb}$) of the carbonate fraction of the cherts and siltstones were measured by IRMS on a Micromass Isoprime dual inlet mass spectrometer. Samples were introduced via a Micromass carbonate autosampler system. Samples were held in evacuated 5 ml. vacutainers with proprietary CO_2-impermeable seals and acidified with 103% (dehydrated) phosphoric acid at 90°C for 10 minutes; the evolved CO_2 was cryogenically stripped of water vapor prior to being introduced to the mass spectrometer.

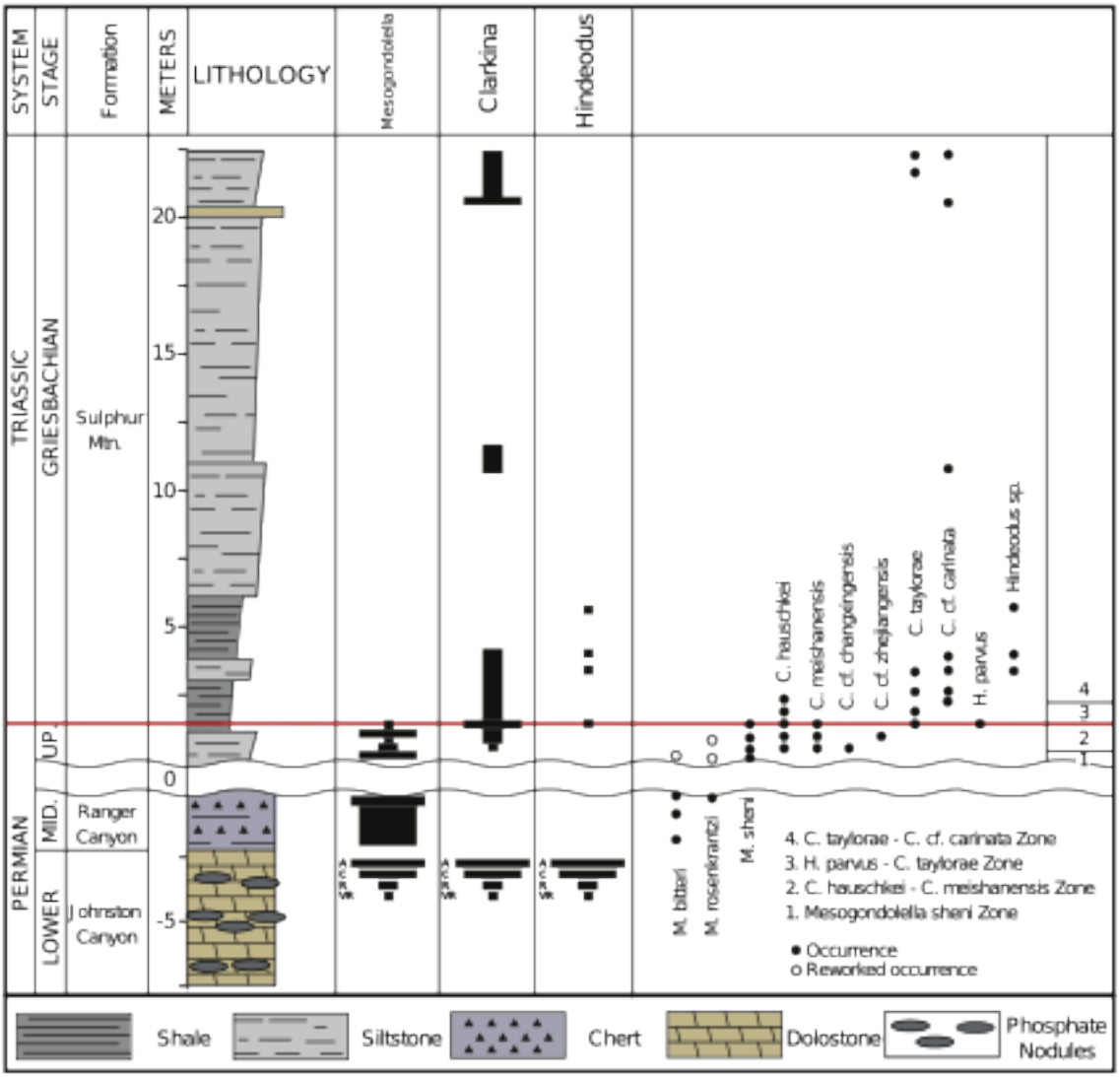

Figure 3: Stratigraphic column of the Opal Creek section, showing conodont occurences and zonation, as well as the abundances of three conodont genera. A = Abundant (>20/kg), C = common (10-20/kg), R = Rare (5-10/kg), VR = Very Rare (1-5/kg). Only P1 conodont elements were counted, samples were each approximately 2-3 kg of rock.

All stable isotope ratios are reported in standard delta (δ) notation indicating the per mil (‰) difference from a standard with an accepted value such that:

$$\delta = (R_{sample}/R_{std.}\text{-}1)\cdot 1000$$

where R equals $^{15}N/^{14}N$ for nitrogen and $^{13}C/^{12}C$ for carbon. The standard for nitrogen is air; the standard for carbon and oxygen is Vienna PeeDee Belemnite (VPDB).

The standard deviation (σ) of sample replicates was 0.15‰ for $\delta^{13}C_{org}$ (n = 36), 0.26‰ for $\delta^{15}N$ (n = 57), 0.10‰ for $\delta^{13}C_{carb}$ (n = 50), and 0.25‰ for $\delta^{18}O_{carb}$ (n = 50). Analytical precision based on routine analyses of internal laboratory reference materials was 0.15‰ for $\delta^{13}C_{org}$, 0.10‰ for $d^{15}N$, and 0.32‰ for $\delta^{13}C_{carb}$ and $\delta^{18}O_{carb}$. Many samples contain low levels of nitrogen, to avoid error, we here report only samples with an integrated peak area of >12 mV at mass 28.

Samples generally contain high Total Organic Carbon, ranging from 0.52 to 3.37 percent and generally increasing upward throughout the section (Figure 5), and thus organic carbon isotopes are unlikely to reflect contamination by hydrocarbon fluids. The Conodont Alteration Index (CAI) for conodont elements at Opal Creek is 2.5, suggesting low to moderate thermal alteration of the sediments.

Chemical composition of the samples was measured by the ALS Chemex company of Vancouver, BC, using Inductively Coupled Plasma Atomic Emission Spectroscopy (ICP-AES). A 0.25 g sample was digested in hydrochloric, nitric, perchloric and hydrofluoric acids. The residue was suspended in dilute HCl and analyzed for element composition by ICP-AES, with sub-ppm lower detection limits for most elements. In order to determine the nature of carbonate minerals in the section, eight thin sections were prepared and examined with a petrographic microscope.

3. Results

3.1 Carbonates

The $\delta^{18}O$ of the carbonate fraction was measured at 147 points in the Middle Permian Ranger Canyon Formation and across the PTB in the first 22 meters of the Sulphur Mountain Formation. These display a wide range of variation, with $\delta^{18}O$ from -8.34‰ to -2.68‰ .The $\delta^{13}C$ of inorganic carbonate was measured at 155 points, and ranges from -9.22‰ to -1.20‰. Thin-section petrography of Opal Creek sediments revealed carbonates present as microcrystalline cements, dolomite rhombs, and reworked calcite grains. As multiple generations of carbonate are present, and isotope values indicate almost certain diagenetic alteration, carbonate isotopes are not assumed to reflect depositional conditions and will not be considered further. However, the lack of correlation between organic and inorganic carbon isotopes ($R^2 = 0.031$, Figure 4) suggests that the organic carbon signal is not a function of diagenetic alteration.

3.2 Organic Carbon

The $\delta^{13}C$ of organic carbon was measured at 189 points throughout the section (Figure 5). Organic carbon isotopes showed a stable equilibrium at -29.23 ± 0.62‰ (n=13) throughout the Ranger Canyon Formation. The Sulphur Mountain sediments immediately overlying the unconformity have similar values. However, there is a dramatic spike to values as high as -25.7 ‰ in the section's most pyritic interval at 10.5 cm After the excursion, organic carbon isotopes settle to a steady equilibrium with a mean $\delta^{13}C$ of -31.21 ± 0.48 ‰ (n=169).

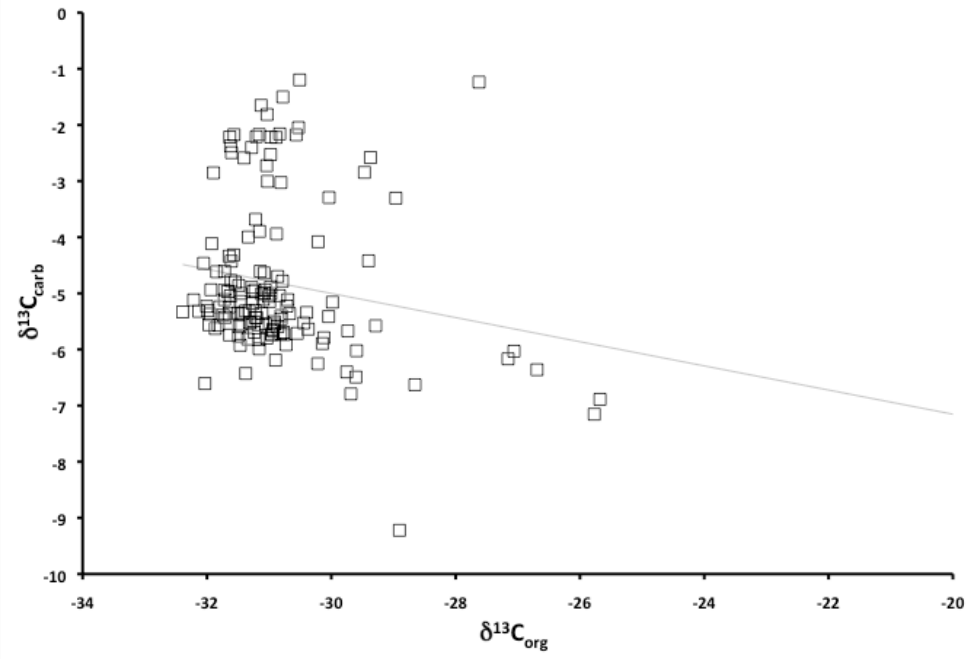

Figure 4: Crossplot of Organic and Inorganic carbon isotopes with best-fit regression. R^2 = .031. Lack of correlation suggests organic carbon isotopes have not been affected by diagenesis.

3.3 Nitrogen

Nitrogen isotopes were measured at 57 points across the PTB and in the underlying strata (Figure 5). Nitrogen isotope values in the Ranger Canyon Formation are generally quite high, with a mean value of 8.28 ± 0.92 ‰, (n=9). Nitrogen values peak in the lowermost Sulphur Mountain, reaching values as high as 10.14 ‰ in the 10.5 cm above the unconformity. The most pyritic interval of the section, at 10.5 cm, corresponds to a rapid drop off in $\delta^{15}N$ to values averaging 2.92 ± 0.41 ‰ for the laminated siltstones (n = 42), a more typical value for marine sedimentary organic matter.

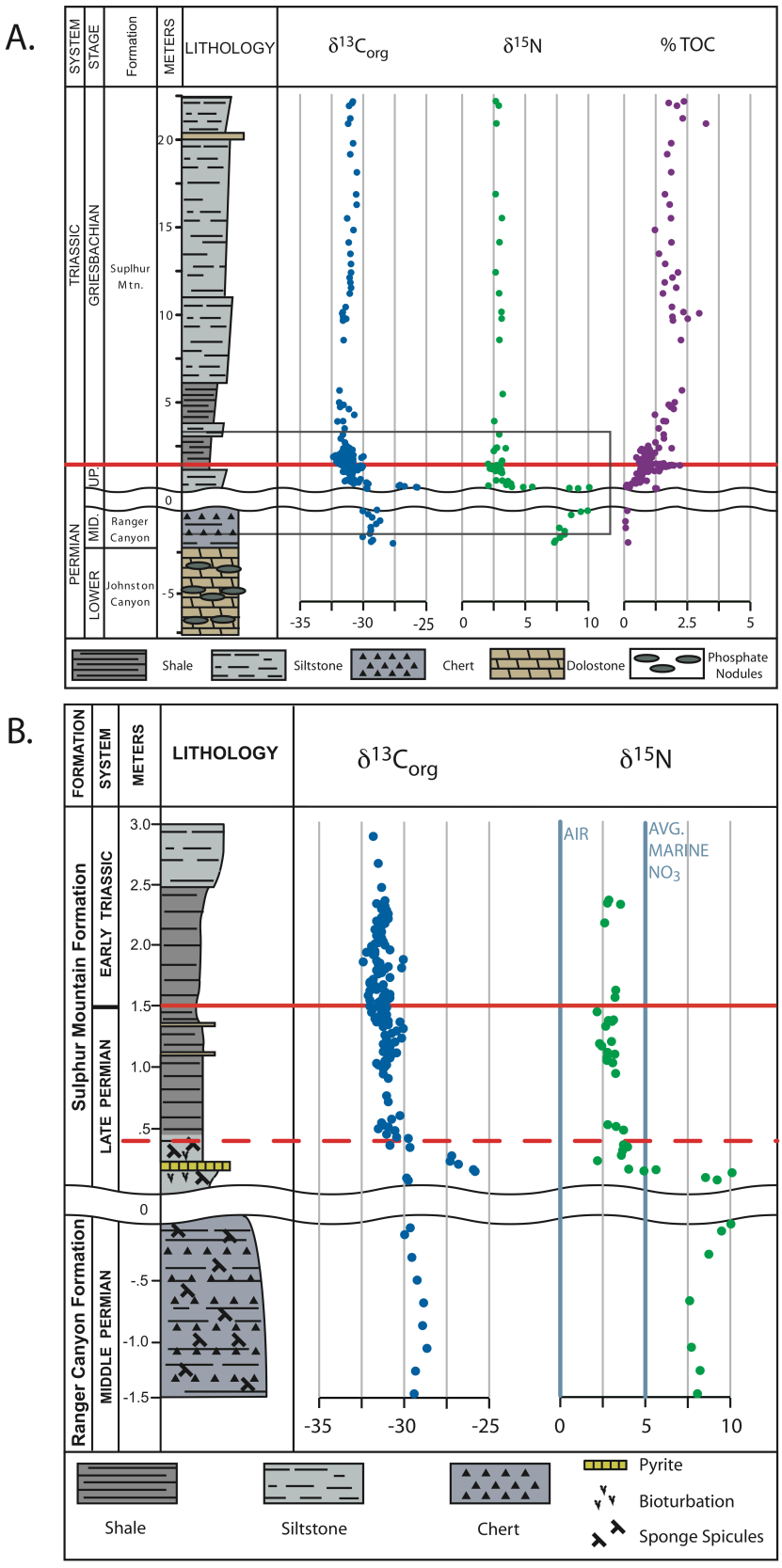

Figure 5: A: Stratigraphic column of the Opal Creek section showing organic carbon isotopes (VPDB) and nitrogen isotopes (AIR), as well as % Total Organic Carbon (TOC). Highlighted area is expanded in B: Expanded stratigraphic column of shaded area around Permian Triassic Boundary. Dashed red line indicates main extinction horizon, solid red line indicates biostratigraphic PTB. Vertical lines on Nitrogen graph show the isotopic values of atmospheric N_2 (AIR) and an average value of modern marine nitrate (NO_3^-).

3.4 Aluminum Content

The presence of reworked conodonts around the unconformity indicates that some mixing of sediments has occurred. In order to assess the degree to which reworking or biological mixing of sediments can explain the resemblance of nitrogen isotopes in the lowermost Sulphur Mountain Formation to the middle Permian Ranger Canyon Formation, we measured the aluminum content of samples at 25 points throughout the section. Aluminum varies markedly between the Ranger Canyon Formation and Sulphur Mountain Formation lithologies, and is relatively unaffected by biochemical processes in the ocean (Tribovillard et al., 2006), which makes it useful as a measure of the degree to which material has been physically mixed across the contact. Exclusive of the points immediately above and below the unconformity, the Ranger Canyon Formation has an average aluminum content of 0.53% (s = 0.25%), whereas the Sulphur Mountain Formation has a much higher average of 7.08% (s = 0.86%). The samples immediately surrounding the unconformity had intermediate values, with a simple mixing model suggesting an approximately 13% contribution of Sulphur Mountain material to the uppermost measured Ranger Canyon sample, 4 cm below the unconformity, and a 22% contribution of Ranger Canyon material to the lowermost measured Sulphur Mountain sample, 10.5 cm above the unconformity.

Assuming similar nitrogen content, this is sufficient to explain the high nitrogen value measured in the pyrite bed at 10.5 cm However, it is inconsistent with the *maximum* $\delta^{15}N$ values being measured just above the unconformity, as well as the lack of an apparent Sulphur Mountain Formation contribution to the uppermost Ranger Canyon Formation . Furthermore, the discrete peak in organic carbon isotopes at 10.5 cm as well

as the presence of an uninterrupted centimeter thick pyrite bed suggests that mixing was not the primary control of the geochemistry of this interval.

4. Discussion

Here we interpret the disappearance of siliceous sponge spicules, 40 cm above the beginning of the Sulphur Mountain Formation transgressive sequence, as representing the principal Permian-Triassic marine extinction event. The disappearance of chert units at higher latitudes along the latest Permian Panthalassic margin of Pangaea has been previously described by Beauchamp and Baud (2002) who suggest that silica sponges thrived in cold bottom water, which would contain higher levels of dissolved oxygen and suppress competition from carbonate producers. Our nitrogen and organic carbon isotope data support the hypothesis that a shutdown of cold-water upwelling and the corresponding high organic productivity occurred along the western margin of Pangaea in the latest Permian, leading to the demise of the sponges. Such a breakdown of longstanding circulation patterns and the consequent decrease in deepwater oxygen concentrations may be attributable to warming of the latest Permian oceans and consequently the cessation of thermally-driven ocean circulation and warming of the deep ocean (Kiehl and Shields, 2005).

Because the $\delta^{15}N$ of Opal Creek organic material reflects that of organisms that generally fractionate nitrogen during uptake, depleting it by 2-3 ‰, the available nitrate pool in the original Middle Permian water column overlying Ranger Canyon sediments may have had a $\delta^{15}N$ of 10-11 ‰. This enrichment likely reflects the presence of a mid-water column anoxic zone, where denitrification was taking place (Algeo et al., 2008). This anaerobic process, whereby nitrate is reduced to N_2 gas, imparts a large fractionation

effect (ε=-20 ‰, Brandes and Devol 2002) and strongly enriches the remaining nitrate pool. Such mid-water anoxic zones are known from many modern regions of the ocean, such as the Peru Margin and Arabian Sea, where upwelling nutrients fuel rapid export of organic matter from the photic zone (Brandes and Devol 2002). Such regions often have sedimentary $\delta^{15}N$ values in the 7-10 ‰ ranges (Algeo et al. 2008)

As a result of these processes, the intensity of the coastal upwelling system can be inferred from the $\delta^{15}N$ of organic matter in the underlying sediments. The persistence of strong upwelling into the latest Permian can be seen in the enriched nitrogen isotope values of the lowermost Phroso Siltstone, from samples above the unconformity surface. We propose that the subsequent return to a sedimentary $\delta^{15}N$ of 2-3, corresponding to a marine nitrate value of 4-6, represents the final collapse of the mid-water denitrification zone and the productive cold-water upwelling system that had persisted along the western margin of Pangaea since the Artinskian (Beauchamp and Baud, 2002). This would correspond to a transition to lower productivity conditions, and an increased reliance on nitrogen fixed directly from the atmosphere ($\delta^{15}N = 0$). Under such conditions of slowing circulation, the water column likely transitioned from having a mid-water oxygen minimum to a bottom-water oxygen minimum, which would contribute to the general increase in organic carbon content (through increased preservation) and conspicuous lack of bioturbation in the earliest Triassic.

While positive organic carbon isotope excursions may be attributed to the rapid burial of light organic carbon biomass following a mass die-off, the major $\delta^{13}C_{org}$ excursion at Opal Creek precedes the main extinction event at 40 cm. Changes in the total carbon pool, such as an addition of carbon to the atmosphere through volcanism or

methane degassing is expected to decrease $\delta^{13}C$ (Korte et al., 2010; Luo et al., 2011).

The pre-extinction positive spike in $\delta^{13}C_{org}$ at Opal Creek may represent a decrease in photosynthetic fractionation, with the excursion preceding the extinction possibly indicating a pulse of high productivity, in which organisms were competing to uptake dissolved carbon (a situation described as carboxylation-limitation, (O'Leary, 1988). Such decreases in photosynthetic fractionation have been interpreted as cyanobacteria using the β-carboxylation pathway (Kashiyama et al., 2008), and cyanobacteria may have become predominant in an increasingly nitrogen limited environment (Luo et al. 2011). Alternatively, this may represent the increasing contribution of anoxygenic photosynthsizers, which show a smaller carbon fractionation effect than oxygenic photosynthesizers (O'Leary, 1981) and may be associated with the expansion of photic zone euxinia in the latest Permian world as indicated by the presence of a pyrite interval (Grice et al., 2005; Grasby and Beauchamp, 2009). However, neither explanation is consistent with a collapse of marine productivity prior to the main extinction event. Following this interpretation, the return to a lower equilibrium $\delta^{13}C_{org}$ in the Sulphur Mountain Formation likely represents a lower productivity regime in an increasingly nutrient limited environment,though the addition of light volcanic or methanogenic carbon to the dissolved carbon pool may have also played a role.

It is noteworthy that the carbon isotope transition corresponds to the beginning of significant ecological diversity in the conodont fauna, with several species of the genus *Clarkina* appearing in significant numbers alongside *Mesogondolella*. The Ranger Canyon ecosystem was dominated by high abundances of a single species, *Mesogondolella bitteri*, which is replaced by abundant *M. sheni* in the lowermost Sulphur

Mountain. High-abundance, low-diversity ecosystems in the fossil record have been interpreted to represent eutrophic environments (Brasier, 1995), which favor organisms that can rapidly exploit the available resources, and all of these conodonts displayed strong cold-water provincialism. The transition to a more diverse conodont fauna, including the previously equatorial genus *Clarkina*, corresponds temporally to the drop in sedimentary $\delta^{15}N$, providing further support for the collapse of a eutrophic coastal upwelling environment (Figure 3), with the loss of cold upwelling surface water removing a temperature barrier to migration (Mei and Henderson, 2001).

Complete and essentially coterminous peaks in $\delta^{13}C_{org}$ and $\delta^{15}N$ suggest that the decrease in productivity associated with the termination of upwelling was not a monotonic trend. This interval may represent a transient period of increased algal productivity at Opal Creek, relative to the subsequent Sulphur Mountain Formation. This increase may have been due to the synergistic effects of the residual deepwater upwelling, with its high nutrient content, which may have been further aggravated by additional nutrient runoff from the Pangaean continent (Wignall and Newton, 2003; Ward et al., 2000; Algeo, 2010b) and the sudden warming of the Permian sea surface. When warming advanced to the point of stopping the upwelling system, productivity returned to lower levels. Such a spike in sinking organic flux would have created extreme biological oxygen demand and may have driven high levels of biological sulfate reduction, contributing to end-Permian euxinia (Grice et al., 2005; Kump et al., 2005; Meyer and Kump, 2008; Grasby and Beauchamp, 2009), with photosynthetic sulfur bacteria possibly surviving in the photic zone (Hays et al., 2007).

Such an expansion of anoxic waters into the shallow photic zone, whether driven

by increased productivity or not, may also have contributed to a positive organic carbon isotope excursion by creating more homogenous redox conditions throughout the water column. By weakening vertical redox gradients, the preferential degradation of certain organic components (mainly proteins) in oxic waters and its associated isotope fractionation would have been reduced. This has been observed by Isozaki (2009) in several deep water Panthalassic sections accreted onto Japan. As the opposite (a negative $\delta^{13}C_{org}$ excursion) was seen in shallow-water atoll carbonates, the positive excursion at Opal Creek would support the conclusion that the section was deposited below the chemocline, even prior to the PTB crisis interval.

It is unclear if the termination of upwelling represented the return to "normal" marine conditions or to the stratified ocean hypothesized for the Permian-Triassic boundary (Wignall and Newton, 2003; Isozaki, 1994). Stratification of the entire Panthallassic Ocean has proven difficult to sustain in models (Hotinski et al., 2001), and such an extreme condition would be likely to leave evidence in the stable isotope data. Trace metals from Panthalassic sections spanning the PTB have indicated suboxic rather than fully euxinic bottom waters (Algeo et al., 2010a).

5. Conclusions

Despite the Panthalassic Ocean's potentially dominant role in Permian biogeochemical cycling, there has been little direct evidence for biogeochemical changes leading up to the end-Permian extinction. While a slowing down or rearrangement of ocean circulation in the latest Permian has been previously proposed, here we present isotopic evidence for the cessation of coastal upwelling along western Pangaea.

Latest Permian deposits at Opal Creek display distinctive enrichments in ^{15}N and $^{13}C_{org}$, suggesting a period of elevated productivity and anoxia before the final termination of the western Panthallassic upwelling zone, the loss of benthic siliceous sponges, and the Permian/Triassic extinction. This productivity spike may have been due to the synergistic effects of nutrient upwelling and rapid warming and may have contributed to photic zone euxinia by increasing biological oxygen demand.

6. Acknowledgments

The authors would like to acknowledge the generous support provided by The United States National Science Foundation (NSF) and NASA Astrobiology Institute (NAI) University of Washington node as well as the Natural Sciences and Engineering Research Council (NSERC) of Canada, and the University of Washington Earth and Space Sciences Department. Our special thanks as well to the staff of the University of Washington IsoLab facility for their extensive help with our isotopic analyses.

References:

Algeo, T., Rowe, H., Hower, J.C., Schwark, L., Herrmann, A., Heckel, P., 2008. Changes in ocean denitrification during Late Carboniferous glacial-interglacial cycles. Nature Geoscience 1, 709-714; doi:10.1038/ngeo307.

Algeo, T.J., Hinnov, L., Moser, J., Maynard, J.B., Elswick, E., Kuwahara, K., Sano, H., 2010a.

Changes in productivity and redox conditions in the Panthalassic Ocean during the latest Permian. Geology 38, 187-190; doi:10.1130/G30483.1.

Algeo, T.J., Kuwahara, K., Sano, H., Bates, S., Lyons, T., Elswick, E., Hinnov, L., Ellwood, B., Moser, J., Maynard, J.B., 2010b. Spatial variation in sediment fluxes, redox conditions, and productivity in the Permian-Triassic Panthalassic Ocean, Palaeogeography, doi: 10.1016/j.palaeo.2010.07.007

Baud, A., Magaritz, M., Holser, W.T., 1989. Permian–Triassic of the Tethys: carbon isotope studies. Geologische Rundschau 78, 649–677.

Beauchamp, B., and Baud, A., 2002. Growth and demise of Permian biogenic chert along northwest Pangea: evidence for end-Permian collapse of thermohaline circulation. Palaeogeography, Palaeoclimatology, Palaeoecology, 184, 37-63.

Beauchamp, B., Henderson, C.M., Grasby, S.E., Gates, L.T., Beatty, T.W., Utting, J., and James, N.P. 2009. Late Permian sedimentation in the Sverdrup Basin, Canadian Arctic: the Lindström and Black Stripe Formations. Bulletin of Canadian Petroleum Geology, 57, 167-191.

Becker, L., Poreda, R.J., Hunt, A.G., Bunch, T.E., Rampino, M. 2001. Impact event at the Permian–Triassic boundary: evidence from extraterrestrial noble gases in fullerenes. Science 291, 1530–1533.

Benton, M.J. and Twitchett, R.J., 2003. How to kill (almost) all life: the end-Permian extinction event. TRENDS in Ecology and Evolution Vol.18 No.7 July 2003

Berner, R.A., and Kothavala, Z., 2001. GEOCARB III: a revised model of atmospheric CO2 over Phanerozoic time. American Journal of Science. 301, 182–204.

Berner, R.A., 2002. Examination of hypotheses for the Permo–Triassic boundary extinction by carbon cycle modeling. Proceedings of National Academic Science of the United States of America 99, 4172–4177.

Brandes, J.A. and Devol, A.H. 2002. A global marine-fixed nitrogen isotopic budget: Implications for Holocene nitrogen cycling.Global Biogeochemical Cycles 16, 1120

Brasier, M.D., 1995. Fossil indicators of nutrient levels, 1. Eutrophication and climate change. Geological Society of London Special Publications 83, pp. 113–132.

Brookfield, M.E., Twitchett, R.J., and Goodings, C., 2003. Palaeoenvironments of the Permian Triassic transition sections in Kashmir, India: Palaeogeography, Palaeoclimatology, Palaeoecology, 198, 353-371.

Erwin, D.H., Bowring, S.A., Jin, Y.G. 2002. End-Permian mass extinctions: a review. Boulder Geological Society of America Special Paper 356, 363–384.

Gibson, D.W., 1969. Triassic stratigraphy of the Bow River-Crowsnest Pass region, Rocky Mountains of Alberta and British Columbia. Geological Survey of Canada, Paper 68, 29, 48.

Gibson, D.W., 1974. Triassic rocks of the Southern Canadian Rocky Mountains.

Geological Survey of Canada, Bulletin 230, 65.

Gibson, D.W. and Barclay, J.E., 1989. Middle Absaroka Sequence, The Triassic Stable Craton. In Ricketts, B. (ed.) Basin Analysis - The Western Canada Sedimentary Basin, Canadian Society of Petroleum Geologists Special Publication, pp. 219-231.

Grasby, S.E., Beauchamp, B., 2009. Latest Permian to Early Triassic basin-to-shelf anoxia in the Sverdrup Basin, Arctic Canada. Chemical Geology 264, 232–246.

Grice, K., Cao, C., Love, G.D., Bottcher, M.E., Twitchett, R.J., Grosjean, E., Summons, R.E., Turgeon, S.C., Dunning, W., Jin, Y., 2005. Photic zone euxinia during the Permian–Triassic superanoxic event. Science 307, 706–709.

Hays, L.E., Beatty, T., Henderson, C.M., Love, G.D., Summons, R.E., 2007. Evidence for photic zone euxinia through the end-Permian mass extinction in the Panthalassic Ocean (Peace River Basin, Western Canada). Paleoworld 16, 39-50.

Henderson, C.M., 1989. Absaroka Sequence - The Lower Absaroka Sequence: Upper Carboniferous and Permian (Chapter 10). In Ricketts, B. (ed.) Basin Analysis - The Western Canada Sedimentary Basin, Canadian Society of Petroleum Geologists Special Publication, pp. 203-217.

Henderson, C.M., Richards, B.C., and Barclay, J.E., 1994. Permian. In Mossop, G.D. (ed.) Geological Atlas of the Western Canada Sedimentary Basin Joint publication of the Canadian Society of Petroleum Geologists and the Alberta Research Council, pp. 251-258.

Henderson, C.M., 1997. Uppermost Permian conodonts and the Permian-Triassic boundary in the Western Canada Sedimentary Basin. Bulletin of Canadian Petroleum Geology, 45, 693-707.

Hotinski, R.M., Bice, K.L., Kump, L.R., Najjar, R.G., and Arthur, M.A., 2001. Ocean stagnation and end-Permian anoxia. Geology 29, 7-10

Huey, R.B. and Ward, P.D., 2005. Hypoxia, global warming, and terrestrial Late Permian extinctions. Science 308, 398–401.

Isozaki, Y., 1994. Superanoxia across the Permo–Triassic boundary: record in accreted deep-sea pelagic chert in Japan. In: Embry, A.F., Beauchamp, B., Glass, D.J. (Eds.), Pangea: Global Environments and Resources. Canadian Society of Petroleum Geologists, Memoir, vol. 17, pp. 805–812.

Isozaki, Y., 1997. Permo–Triassic boundary superanoxia and stratified superocean: records from lost deep-sea. Science 276, 235–238.

Isozaki, Y., 2009. Integrated ‘‘plume winter” scenario for the double-phased extinction during the Paleozoic–Mesozoic transition: The G-LB and P-TB events from a Panthalassan perspective. Journal of East Asian Earth Sciences 36, 459–480.

Jin, Y.G., Wang, Y., Wang, W., Shang, Q.H., Cao, C.Q., and Erwin, D.H., 2000. Pattern of marine mass extinction near the Permian Triassic boundary in South China. Science, 289, 432-436.

Kashiyama Y., Ogawa, N.O., Kuroda, J., Shiro M., Nomoto S., Tada R., Kitazato H., Ohkouchi N., 2008. Diazotrophic cyanobacteria as the major photoautotrophs during mid-Cretaceous oceanic anoxic events: Nitrogen and carbon isotopic evidence from sedimentary porphyrin. Organic Geochemistry 39, 532–549

Kidder, D.L., and Worsley, T.R., 2003. Late Permian warming, the rapid latest Permian transgression, and the Permo-Triassic extinction, 2003 GSA Annual Meeting: Seattle, WA.

Kidder, D.L., and Worsley, T.R., 2004. Causes and consequences of extreme Permo–Triassic warming to globally equable climate and relation to the Permo–Triassic extinction and recovery. Palaeogeography, Palaeoclimatology, Palaeoecology 203, 207–237.

Kiehl, J.T., and Shields, C.A., 2005. Climate simulation of the latest Permian: implications for mass extinction. Geology 33, 757–760.

Kim, S.T. and O'Neil, J. R.. 1997. Equilibrium and nonequilibrium oxygen isotope effects in synthetic carbonates. Geochimica et Cosmochimica Acta 61, 3461–3475.

Kump, L.R., Pavlov, A., Arthur, M.A., 2005. Massive release of hydrogen sulfide to the surface ocean and atmosphere during interval of oceanic anoxia. Geology 33, 397–400.

Korte, C., and Kozur, H.W., 2010. Carbon-isotope stratigraphy across the Permian–Triassic boundary: A review. Journal of Asian Earth Sciences 39, 215-235

Korte, C., Pande, P., Kalia, P., Kozur, H.W., Joachimski, M., Oberhänsli. H., 2010. Massive volcanism at the Permian–Triassic boundary and its impact on the isotopic composition of the ocean and atmosphere. Journal of Asian Earth Sciences 37, 293–311.

Kozur, H.W., 2005. Pelagic uppermost Permian and Permian-Triassic boundary conodonts of Iran. Part II: investigated sections and evaluation of the conodont faunas. Hallesches Jahrbuch Fur Geowissenschaften, Reihe B: Geologie, Palaontologie, Mineralogie, 19, 49-86.

Luo, G., Wang, Y., Yang, H., Algeo, T.J., Kump L.R., Huang, J., Xie, S., 2011. Stepwise and large-magnitude negative shift in δ13Ccarb preceded the main marine

mass extinction of the Permian–Triassic crisis interval. Palaeogeography, Palaeoclimatology, Palaeoecology 299, 70–82

Mei, S., 1996. Restudy of conodonts from the Permian-Triassic boundary beds at Selong and Meishan and the natural Permian-Triassic boundary. In: Wang, H. and Wang, X. (eds.). Memorial Volume of Prof. Sun Yunzhu: Palaeontology and Stratigraphy. Centennial China University of Geosciences Press, Wuhan, pp. 141–148.

Mei, S., and Henderson, C.M. 2001. Evolution of Permian conodont provincialism and its significance in global correlation and paleoclimatic implication. Palaeogeography, Palaeoclimatology, Palaeoecology, 170, 237-260.

Meyer K.M., and Kump L.R., 2008. Oceanic euxinia in Earth history: Causes and consequences. Annual Review of Earth and Planetary Sciences 36, 251–288.

O'Leary, M.H., 1981. Carbon isotope fractionation in plants. Phytochemistry 20, 553–567.

O'Leary, M. H., 1988. Carbon isotopes in photosynthesis. Bioscience 38, 328–336.

Payne, J.L., Lehrmann, D.J., Wei, J., Orchard, M.J., Schrag, D.P., and Knoll, A.H., 2004. Large Perturbations of the Carbon Cycle During Recovery from the End-Permian Extinction. Science, 305, 506-509.

Raup, D.M. and Sepokoski, J.J., 1982. Mass extinction in the marine fossil record. Science 215, 1501–1503.

Retallack, G.J., Smith, R.M.H., Ward, P.D., 2003. Vertebrate extinction across the Permian–Triassic boundary in Karoo Basin, South Africa. Geological Society of America Bulletin 115, 1133–1152.

Richards, B.C., 1989. Upper Kaskaskia Sequence: Uppermost Devonian and Lower Carboniferous. In Ricketts, B. (ed.) Basin Analysis - The Western Canada Sedimentary Basin, Canadian Society of Petroleum Geologists Special Publication, pp. 165-201.

Shen, S.Z., Henderson, C.M., Bowring, S.A., Cao, C.Q., Wang, Y., Wang, W., Zhang, H., Zhang, Y.C., and Mu, L., 2010. High-resolution Lopingian (Late Permian) timescale of South China. Geological Journal, 45, 122-134.

Shen, S., Cao, C., Henderson, C.M., Wang, X., Shi, G.R., Wang, Y. and Wang, W., 2006. End-Permian mass extinction pattern in the northern peri-Gondwanan region. Palaeoworld, 15, p. 3–30.

Taylor, E.T., Taylor, T.N., and Cúeno, R., 2000. Permian and Triassic high latitude paleoclimates: evidence from fossil biotas, in Huber, B., Macleod, K., and S., W., (eds.) Warm Climates in Earth History: Cambridge, Cambridge University Press, pp. 321-350.

Tribovillard N, Algeo TJ, Lyons T, Riboulleau A. 2006. Trace metals as paleoredox and paleoproductivity proxies: An update. Chemical Geology 232, 12–32

Ward, P.D., Montgomery, D.R., Smith, R., 2000. Altered river morphology in South Africa related to the Permian–Triassic extinction. Science 289, 1740–1743.

Ward, P.D., Botha, J., Buick, R., De Kock, M.O., Erwin, D.H., Garrison, G., Kirschvink, J., Smith, R., 2005. Abrupt and Gradual Extinction Among Late Permian Land Vertebrates in the Karoo Basin, South Africa. www.sciencexpress.org / 20 January 2005 / Page 1/ 10.1126/science.1107068

White, R.V., 2002. Earth's biggest 'whodunnit': unravelling the clues in the case of the

end-Permian mass extinction: Philosophical Transactions of the Royal Society of London, Series B, 360, 2963-2985.

Wignall, P.B., Hallam, A., 1992. Anoxia as a cause of the Permian/Triassic mass extinction: facies evidence from northern Italy and the western United States. Palaeogeography, Palaeoclimatology, Palaeoecology 93, 21–46.

Wignall, P.B. and Hallam, A., 1993. Griesbachian (Earliest Triassic) palaeoenvironmental changes in the Salt Range, Pakistan and southeast China and their bearing on the Permo-Triassic mass extinction. Palaeogeography, Palaeoclimatology, Palaeoecology. 102, 215-237.

Wignall, P.B., Twitchett, R.J., 1996. Oceanic anoxia and the end Permian mass extinction. Science 272, 1155–1158.

Wignall, P.B. and Newton, R. 2003. Contrasting deep-water records from the Upper Permian and Lower Triassic of South Tibet and British Columbia: evidence for a diachronous mass extinction. Palaios, 18, 153–167.

Winguth, A.M.E., Heinze, C., Kutzbach, J. E., Maier-Reimer, E., Mikolajewicz, U., Rowley, D., Rees, A., and Ziegler, A. M., 2002. Simulated warm polar currents during the middle Permian, Paleoceanography, 17(4), 1057, doi:10.1029/2001PA000646..

Chapter II: Termination of a continent-margin upwelling system at the Permian-Triassic boundary (Opal Creek, Alberta, Canada*)*

Published in Global and Planetary Change, v. 105, 2013

Contributing Authors: Shane D. Schoepfer[1], Charles M. Henderson[2], Geoffrey H. Garrison[1], Julien Foriel[3], Peter D. Ward[1], David Selby[4], James C. Hower[5], Thomas J. Algeo[6], Yanan Shen[7]

Author Affiliations:

[1] Department of Earth and Space Sciences, University of Washington, Seattle, WA 98195, U.S.A.

[2] Department of Geoscience, University of Calgary, Calgary, AB, Canada

[3] Department of Earth and Planetary Science, Washington University, St. Louis, MO 63130, U.S.A.

[4] Department of Earth Sciences, Durham University, Durham, DH1 3LE, U.K.

[5] Center for Applied Energy Research and Department of Earth & Environmental Sciences, University of Kentucky, Lexington, KY 40506, U.S.A.

[6] Department of Geology, University of Cincinnati, Cincinnati, OH 45221 U.S.A.

[7] Chinese Academy of Sciences Key Laboratory of Crust-Mantle Materials and Environments, School of Earth and Space Sciences, University of Science and Technology of China, Hefei 230026, China

Abstract

Models of mass extinctions caused by greenhouse warming depend on the ability of warming to affect the oxygenation of the ocean, either through slowing circulation or changes in biological productivity and the organic carbon budget. Opal Creek, Alberta, Canada is a biostratigraphically continuous Permian-Triassic Boundary (PTB) section deposited in deep water on an outer shelf setting in the vast and understudied Panthalassic Ocean, along the western margin of Pangaea. The latest-Permian extinction is here represented as the disappearance of the previously dominant benthic fauna (siliceous sponges). On the basis of nitrogen and reduced sulfur isotopes as well as productivity-sensitive trace elements, the Middle Permian at Opal Creek is interpreted as a highly productive coastal upwelling zone where vigorous denitrification and sulfate reduction occurred in a mid-water oxygen minimum. Similar conditions appear to have continued into the latest Permian until the onset of a euxinic episode represented by a discrete pyrite bed and several trace element indicators of high productivity. This euxinic pulse is followed by the extinction of benthic fauna and a shift in nitrogen and sulfur isotopes to more normal marine values, suggesting the cessation of coastal upwelling and the consequent weakening of the mid-water oxygen minimum. The Lower Triassic appears to be a dysoxic, relatively unproductive environment with a bottom water oxygen minimum. Rhenium-Osmium isotope systematics show a minimum of radiogenic Os near the main extinction event, which may be due to volcanic input, and increasingly radiogenic values approaching the PTB, possibly due to increased continental erosion. The Opal Creek system demonstrates that, while the biogeochemical crisis in the latest Permian was capable of impacting the coastal upwelling modality of ocean circulation, a transient

increase in productivity likely drove the system toward euxinia and, ultimately, extinction.

1. Introduction

The latest Permian mass extinction (LPME), at ~252 Ma, was the greatest biodiversity crisis of the Phanerozoic (Erwin et al., 2002), fundamentally and permanently altering terrestrial and marine ecosystems (Benton et al., 2004; Bottjer et al., 2008). The trigger for this crisis is thought to have been eruption of the Siberian Traps flood basalts (Wignall, 2007; Reichow et al., 2009), which led to strong global warming as a consequence of emissions of CO_2 and possibly methane (Payne and Kump, 2007; Retallack and Jahren, 2008). Climatic warming or related effects led to perturbations of terrestrial environments, including changes in weathering patterns, aridification, vegetation loss, and fluvial drainage alteration (Retallack, 1999; Looy et al., 1999, 2001; Ward et al., 2000). In the marine realm, warming is thought to have been an important factor in reduced deepwater ventilation, a buildup of hydrogen sulfide, hypercapnia, seawater acidification, and depletion of certain nutrients such as nitrate (Knoll et al., 1996; Kump et al., 2005; Fraiser and Bottjer, 2007; Luo et al., 2011). The development of global greenhouse conditions at this time is paleontologically evident in the appearance of warm-climate floras at polar latitudes (Taylor et al., 2000); the demise of high-latitude, cool-water siliceous sponge communities (Henderson, 1997; Beauchamp and Baud, 2002); and a breakdown of temperature-based conodont provincialism (Mei and Henderson, 2001).

Direct evaluation of changes in Permian-Triassic ocean circulation patterns has proven difficult, owing to the relative paucity of preserved Permian-Triassic boundary

(PTB) sections from the Panthalassic Ocean, which covered some 70% of the globe at the time of the extinction (Fig. 1) and hence is central to investigations of global change related to the LPME. Extant Panthalassic sections are limited to a few areas and depositional facies, including deep-sea cherts (Isozaki, 1994, 1997; Algeo et al., 2010, 2011b; Sano et al., 2010) and shallow atoll carbonates from Japan (Musashi et al., 2001), volcanic-arc slope sediments in New Zealand (Krull et al., 2000), and a series of deep-shelf or upper slope siliciclastic successions in western North America (Beauchamp and Baud, 2002; Wignall and Newton, 2003; Hays et al., 2007, Beatty et al., 2008). Anoxic facies have been documented at widespread PTB sections, leading some workers to infer that such redox changes were global in extent, and due to strongly reduced overturning circulation ("ocean stagnation") (Isozaki, 1994, 1997; Wignall and Twitchett, 1996, 2002). Paleoceanographic modeling studies have demonstrated that, while strong climatic warming could slow the meridional overturning circulation significantly, it would generally not be sufficient to generate the persistent, highly reducing conditions necessary to drive surface euxinia without a substantial increase in nutrient availability (Hotinski et al., 2001; Meyer et al., 2008). Modeling of paleoceanographic conditions at the PTB generally supports the hypothesis that overturning circulation persists despite extreme greenhouse conditions (Kiehl and Shields, 2005; Winguth and Maier-Reimer, 2005).

Recently, attention has focused on the role of increased nutrient inventories in ocean-surface waters, and consequent increases in marine primary productivity, in driving PTB oceans toward anoxia (Algeo et al., 2011a). This hypothesis has received support from studies demonstrating a substantial expansion of the mid-ocean oxygen-

minimum zone in periequatorial regions (Algeo et al., 2010, 2011b) as well as a steepening of shallow-to-deep carbon isotopic gradients in epicratonic seas (Meyer et al., 2011; Song et al., in review).

In this study, we examine changes along the eastern margin of the subtropical Panthalassic Ocean between the Early Permian and Early Triassic. Our primary goal is to test models of anoxia development in the Panthalassic ocean by collecting field geochemical evidence for changes in circulation and organic productivity rates during the PTB transition interval. The site for this study is the Opal Creek section in southwestern Alberta, which represents an outer-shelf or upper slope setting on the western margin of the North American plate at a paleolatitude of ~30°N (Henderson, 1989, Richards, 1989).

As shown by both field data and paleoceanographic modelling, this region was characterized by strong upwelling during much of the Permian (Ziegler et al., 1998, Beauchamp and Baud, 2002, Winguth and Maier-Reimer, 2005), a mode of circulation potentially sensitive to global climate changes. A shift in ocean circulation patterns is suggested by major changes in boreal marine biotas during the Late Permian (Henderson and Baud, 1997; Beauchamp and Baud, 2002; Gates et al., 2004; Beauchamp et al., 2009), culminating in a regional extinction of sponges in the late Changhsingian (Algeo et al., 2012), as well as a shift from the enriched nitrogen isotope values characteristic of coastal upwelling zones to values characteristic of more nitrogen-limited environments (Schoepfer et al., 2012). Here, we present sulfur isotope and trace-element concentration data in order to (1) document changes in redox conditions, productivity, and euxinia within the upwelling system of the eastern subtropical Panthalassic Ocean during Early Permian to Early Triassic, and (2) evaluate the relationship of changes in this region

during the PTB transition to broader changes in the global environment based on detailed biostratigraphic correlations (Henderson et al., 1994; Henderson, 1997).

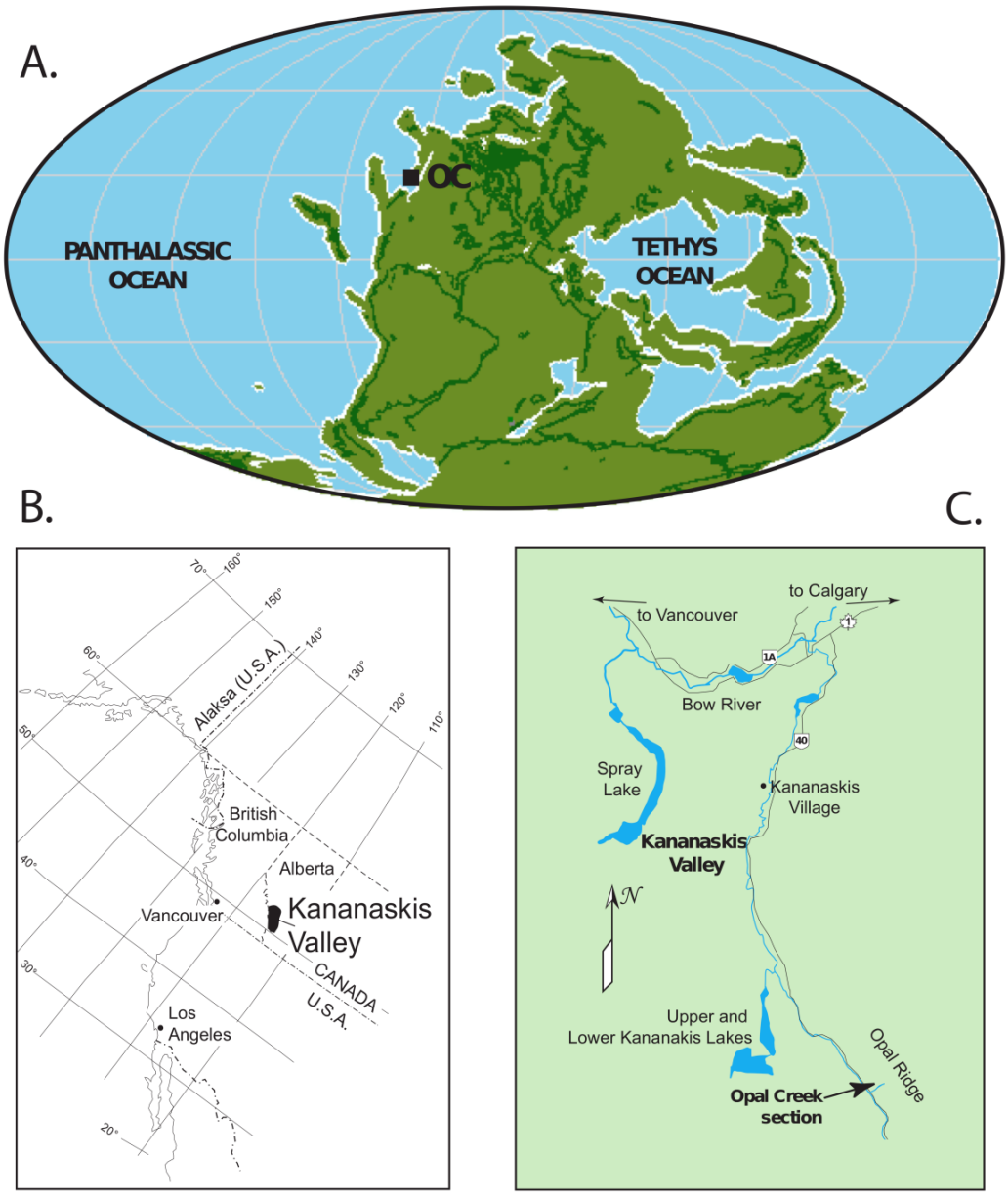

Figure 1: (A) Late Permian paleogeography, showing the major ocean basins and location of the Opal Creek section. Map generated by PaleoDB.org, Alroy 2010. (B) Map of Canada showing the location of the Kananaskis Valley in southwestern Alberta. (C) Map showing the location of the Opal Creek section in the Kananaskis Valley.

2. Geologic setting and biostratigraphy

The Opal Creek section is located in the Kananaskis Valley, in the foothills of the Canadian Rockies west of Calgary (Fig. 1). It comprises ~25 meters of Lower Permian through Lower Triassic strata assigned to the Johnston Canyon, Ranger Canyon, and Sulphur Mountain formations. Beds dip nearly vertically, with cherts and silicified siltstones forming prominent cliffs while more fissile siltstones are exposed in hill slopes (Fig. 2). The thermal maturity of the section is moderate, as shown by a conodont color alteration index (CAI) of ~2.5 (Schoepfer et al., 2012), equivalent to a maximum burial temperature of ~150°C (Tissot and Welte, 1984; Hunt, 1996). Similar maturity levels have been inferred for other PTB sections in the Canadian Western Sedimentary Basin on the basis of vitrinite reflectance (Radke et al., 1982), CAI (Utting et al., 2005), and biomarker studies (Hays et al., 2007).

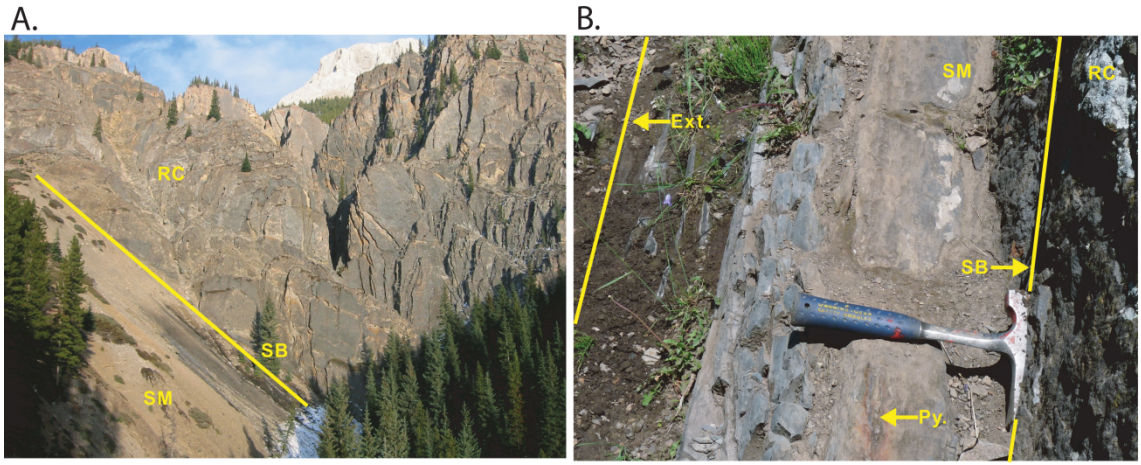

Figure 2: (A) Photograph of Opal Creek outcrop from approach. Note cliff-forming, silicified Ranger Canyon and less resistant Sulphur Mountain silts exposed in hillside. The cliff face corresponds to the unconformity. (B) Close up of Permian-Triassic boundary. Pyrite bed weathers to reddish in outcrop. RC = Ranger Canyon Formation, SM = Sulphur Mountain Formation, SB = unconformable Sequence Boundary, Py. = Pyrite layer, Ext. = main extinction horizon.

The Early Permian is represented by the Johnson Canyon Formation (Fig. 3), which is composed of silty dolostone containing abundant nodular phosphate layers. This unit exhibits lithologic cyclicity, likely as a consequence of glacio-eustatic fluctuations during the Early Permian, when ice is believed to have existed at the poles (Haq and Schutter, 2008).

The Middle Permian is represented by the Ranger Canyon Formation (RCF, Figs. 3-4), which (together with its stratigraphic equivalent, the Fantasque Formation) extends from southeastern British Columbia northward to the southern Mackenzie Fold Belt in the Yukon (Henderson, 1989). The Ranger Canyon, which is just 2.35 m thick at Opal Creek, consists of completely bioturbated, recrystallized spiculitic chert to cherty immature siltstone containing microcrystalline carbonate cements and some reworked chert and carbonate grains. The predominance of sponge spicules, abundance of phosphatic material including abundant conodonts, and absence of shallow-water sedimentary structures (Henderson, 1997) suggest an outer shelf or slope environment at a few hundred meters water depth, below storm wave base and probably oligophotic. The most common fossils are large monaxon siliceous sponges spicules (up to 6 cm long), possibly of the class Demospongea. Also abundant are conodonts of the genus *Mesogondolella,* which in the Middle and Late Permian are indicative of cool-water environments, as inferred from their boreal provincialism (Mei and Henderson, 2001). The main species are *M. bitteri* and, toward the top of the formation, *M. rosenkrantzi*, indicating a Capitanian age or, where *M. rosenkrantzi* is found without *M. bitteri*, an early Wuchiapingian age (Henderson and Mei, 2007).

The upper contact of the RCF is defined by a major regional unconformity, coinciding with the Guadalupian-Lopingian lowstand (Haq and Schutter, 2008). On the basis of the conodont biostratigraphy, the duration of this unconformity has been estimated at 5-7 million years. The Late Permian and Early Triassic are represented by the Phroso Siltstone Member of the Sulphur Mountain Formation (SMF; Figs. 3-4), which is equivalent to the Grayling Formation in northeastern British Columbia (Wignall and Newton, 2003). The basal ~10 m of this unit represent a transgressive systems tract (TST) characterized by an upward fining succession. Sediment consists of angular, immature silt to fine sand and contains dolomite rhombs as well as reworked chert, micas, and microcrystalline carbonate. Pyrite is also present, concentrated around organic fragments and, especially, in a cm-thick bed that is ~10.5 cm above the basal unconformity. The lowermost beds of this unit are bioturbated and contain abundant siliceous monaxon sponge spicules up to 2 cm in length, but these features disappear abruptly ~40 cm above the basal unconformity. At the same level, the conodont fauna dominated by *Mesogondolella* is abruptly replaced by a new fauna dominated by the genus *Clarkina,* a transition that probably marks the latest Permian mass extinction event (see below). Above this level, the SMF is composed of black to dark grey, pyritic, thin-bedded shale and siltstone. Benthic biota and bioturbation are lost, suggesting suboxic to anoxic bottom waters during deposition (Fig. 2) (Gibson, 1969, 1974; Gibson and Barclay, 1989; Henderson, 1997).

Four conodont biozones are present in the Sulphur Mountain Formation (Figs. 3-4), in ascending order:

1) *Mesogondolella sheni* Zone—Specimens of *M. sheni* from the basal TST of this formation indicate a Changhsingian age, but the exact relationship between these specimens and the type material from Selong, Tibet (Mei, 1996; Shen et al., 2006) remains uncertain. Specimens of *M. rosenkrantzi* and *M. bitteri* are considered to have been reworked from the underlying Ranger Canyon Formation during the transgression. The extent of reworking is difficult to address since all specimens are fragmented in these deformed shale units. At Ursula Creek in northeastern British Columbia, the uppermost Fantasque Formation contains both *M. sheni* and *M. rosenkrantzi*, indicating a Changhsingian age (Henderson, 1997; Wignall and Newton, 2003). We suggest a Late Changhsingian age for this assemblage at Opal Creek given that indisputably latest Changhsingian species are recovered only 40 cm higher in the section.

2) *Clarkina hauschkei–Clarkina meishanensis* Zone—This zone is defined by the association of *C. hauschkei*, *C. meishanensis*, *C. cf. changxingensis*, and *C. cf. zhejiangensis*. A comparable assemblage was recovered from the basal Blind Fiord Formation in the Canadian Arctic (Algeo et al., 2012). *C. hauschkei* is similar to specimens described as *C. hauschkei borealis* by Kozur (2005) from a zone immediately below the end-Permian microbialite facies at Abadeh, Iran. *C. meishanensis sensu stricto* is restricted to Beds 25 to 28 at Meishan (Jiang et al., 2007), but a similar species *C. zhangi* originally described as a subspecies of *C. meishanensis* (Mei et al., 1998) ranges from Bed 23 to 24e at Meishan. These two species may be synonymous and therefore range from Late Permian (Bed 23) to Lower Triassic (Bed 28). Kozur (2005) indicated that *C. meishanensis* migrated into Iran during the late Changhsingian, correlative with the Bed 23-24e interval at Meishan. At Opal Creek, the base of this zone is marked by a

sharp reduction in *Mesogondolella* (which survives to the PTB) and the appearance of the genus *Clarkina*. The latter genus is typical of the equatorial warm-water province during the Late Permian (Mei and Henderson, 2001), and its appearance in the Canadian Western Sedimentary Basin is thus indicative of a breakdown of a temperature barrier to migration (Henderson and Mei, 2007). The faunal turnover at Opal Creek either is equivalent in age to, or slightly precedes, the main extinction horizon (Bed 25) at Meishan, China (Jin et al., 2000).

3) *Hindeodus parvus–Clarkina taylorae* Zone—*H. parvus* is the key marker for the base of the Triassic at the GSSP in Meishan, China (Yin et al., 1996, 2001); its occurrence elsewhere does not define the PTB, but according to chronostratigraphic principles indicates only proximity to it within the *H. parvus* Zone (Henderson, 2006). At Meishan and elsewhere, the lowermost Triassic is typically characterized by a short-term acme of *Hindeodus* (Chen et al., 2009; Jiang et al., 2007; Zhang et al., 2007). Although this genus is rare at Opal Creek, some small, poorly preserved specimens were found in the lower ~6 m of the SMF. The local first occurrence of *H. parvus* is ~1.5 m above the base of the SMF, where it is found in association with *C. taylorae.* The latter taxon has not been recovered with certainty below the PTB (Orchard et al., 1994), so the co-occurrence of these two species is probably a good marker for the stratigraphic position of the PTB at Opal Creek.

4) *Clarkina taylorae–Clarkina cf. carinata* Zone—*C. carinata* (= *Neogondolella* of some authors) is the most commonly identified Lower Triassic conodont species (Clark, 1959; Orchard and Krystyn, 1998; Sweet, 1970). The co-occurrence of *C. taylorae* and *C. cf. carinata* indicates a Griesbachian (Lower Induan) age.

3. Materials and methods

3.1. Field protocol

A total of 55 samples were collected over a 30-m-thick stratigraphic interval ranging from the Lower Permian Johnston Canyon Formation through the Lower Triassic Sulphur Mountain Formation for analysis of S isotopic compositions, S speciation, and trace-metal concentrations, with collection concentrated in the basal Sulphur Mountain Formation, around the extinction and PTB. An additional 14 samples were collected over a 1.4-m-thick stratigraphic interval at the base of the Sulphur Mountain Formation for analysis of Re-Os abundances and Os isotopic compositions. Samples were collected at 10 cm spacing from 20 cm above the Ranger Canyon/Sulphur Mountain unconformity to a level 1.6 m above the unconformity.

A separate set of 99 samples was collected at 40 cm intervals from the basal 44 m of the SMF, and processed for TOC, % total S, and $\delta^{34}S_{pyrite}$ at the University of Cincinnati. These data are presented in Figure 5.

3.2. Sulfur isotopes and concentrations

The ratio of sulfur stable isotopes ($^{34}S/^{32}S$) was measured by elemental analyzer continuous-flow isotope-ratio mass spectrometry (EA-CF-IRMS), at the University of Washington's IsoLab facility, using a Eurovector EA and Thermo Finnigan Conflo III and MAT253 isotope-ratio mass spectrometer.

All stable isotope ratios for samples are reported in standard delta (δ) notation indicating the per mille (‰) difference from a standard:

$$\delta = (R_{sample}/R_{std.}-1)\cdot 1000$$

where R equals $^{34}S/^{32}S$ of the standard or sample. The standard used for sulfur isotopes is Vienna Canyon Diablo Troilite (VCDT). The accuracy of ^{34}S measurements ($1\sigma = 0.2‰$, n = 20) was estimated through analysis of NIST NBS127 and NZ1 reference materials. Analytical precision (1σ) was determined based on replicates of an internal laboratory standard (Sigma Aldrich $BaSO_4$) during each run and was ≤0.2‰ (n = 5 to 10). The average precision (1σ) for sample duplicates was larger (0.6‰, n = 2-3), probably owing to sample heterogeneity.

Sulfur concentrations were also calculated for each sample by calibrating the total S signal for a range of masses of the internal standard during each isotopic analysis. In order to identify the relative contributions of different sulfur species (sulfates including carbonate associated sulfates, sulfides, organic sulfur, and barite) to total sulfur, different sample fractions were obtained by chemical processing. Sulfates were removed from sample aliquots by an acidification step, i.e., washing with an HCl solution (2N hydrochloric acid, 36-72 hours at 60°C), leaving only sulfide and organic S in the residue. An aliquot of the residue was then bleached, i.e., treated with a 5.5% NaClO solution (12-24h, 60°C) to remove organic sulfur, leaving only the sulfide component, although some of the sulfide fraction may have been removed by this oxidation step. An aliquot of this second residue was then treated with a nitric acid wash (6N HNO_3, 24-48h, 60°C) in order to oxidize sulfides and isolate a possible barite component.

Carbon and sulfur elemental concentrations of the University of Cincinnati sample set were determined using an Eltra 2000 C-S analyzer, and results calibrated using USGS and internal laboratory standards. Analytical precision was better than ±2.5% for carbon and ±5% for sulfur. An aliquot of each sample was digested in HCl at 50°C for 12 hours, washed and filtered, and reanalyzed for C and S in order to determine concentrations of total organic carbon (TOC) and non-acid volatile sulfur (NAVS).

3.3. Re-Os isotopes

The Re-Os analytical protocol followed that described in detail by Selby and Creaser (2003) and Selby et al. (2007) and was carried out in the TOTAL Laboratory for Source Geochronology and Geochemistry at Durham University. Re was recovered by anion chromatography and further purified using single anion bead chromatography. The Re and Os isolates were analyzed for their isotopic compositions by negative thermal ionization mass spectrometry. The data presented here were analyzed in two separate batch analyses. Total procedural blanks for each batch were very similar, yielding [Re] = 15.1 and 17.2 pg/g, [Os] = 150 and 193 fg/g, and $^{187}Os/^{188}Os$ of 0.21 and 0.19 for the first and second batches, respectively. In-house standard solutions of Re and Os were also run and were identical to the long-term running average reported by Rooney et al. (2010) and references therein.

3.4. Trace element concentrations

The chemical composition of the samples was measured by the ALS Chemex company of Vancouver, BC (Method ME-MS61). About 0.25 g of each sample was

digested in perchloric, nitric, hydrofluoric and hydrochloric acids. The residue was suspended in dilute hydrochloric acid and analyzed by inductively coupled plasma-atomic emission spectrometry (ICP-AES). Samples containing high concentrations of bismuth, mercury, molybdenum, silver, or tungsten were diluted accordingly, then analyzed by inductively coupled plasma-mass spectrometry (ICP-MS). Results were corrected for spectral interelemental interferences. Detection limits were 0.01% by mass for most major elements and <1 ppm for most trace elements.

To control for variations in sedimentation rate and terrigenous input, elemental data were normalized to aluminum (Al), which was used as a tracer for the aluminosilicate fraction of the sediment. For ease of comparison, elemental concentrations are reported as enrichment factors (EFs), which were calculated as:

$$EF_x = (\text{wt. \% X/wt. \% Al})_{\text{sample}} / (\text{wt. \% X/wt. \% Al})_{\text{AUCC}}$$

where X is the element in question and AUCC is Average Upper Continental Crust, as determined by McLennan (2001).

3.5. Petrographic analysis

Petrographic study of a subset of samples was undertaken at the University of Cincinnati and University of Kentucky. Standard petrographic thin sections were examined at 20-400X magnification under reflected light using a Leitz Laborlux 12-Pol optical microscope. Measurements were calibrated with a Zeiss micrometer. Polished sample chips were photographed under oil-immersion lenses at varying magnifications.

4. Results

4.1. Previous isotope results

Organic carbon and nitrogen isotope datasets were generated for the Ranger Canyon and Sulphur Mountain formations at the University of Washington's IsoLab facility. Both records showed significant excursions in the lowermost SMF, with a positive peak in $\delta^{13}C_{org}$ and a negative shift in $\delta^{15}N$. These data were previously published by Schoepfer et al. (2012) with a full description of methods and supplementary data table; the data are shown here in Figures 3-4 for easy comparison with sulfur and trace element results.

4.2. Sulfur speciation

Average S concentrations of bulk samples (2.7±1.1%, n = 18) and acidified samples (2.7±1.2%, n = 48) (omitting sample OC24, the pyrite bed) are nearly identical. In addition, the difference between $\delta^{34}S$ for bulk and acidified extracts of the same samples is small (0.8±1.0‰, n = 18). These observations suggest a negligible contribution of sulfates to the total sulfur signal. All fully chemically processed (i.e., nitric-acid-treated) samples showed sulfur levels below detection limits or too low (< 0.03 wt%) to be significant, so little if any barite is present. The bleaching step lowered sulfur levels significantly in all but one sample (OC24, the pyrite bed), often to below detection limits. With such low S levels, $\delta^{34}S$ analysis for bleached samples is much less precise, yet bleached $\delta^{34}S$ values are within +/- 5‰ of the acidified-only $\delta^{34}S$ values, a much narrower spread than for the whole data set (> 30‰). The relatively good agreement suggests the bleaching process was removing the majority of a homogenous,

labile sulfur pool that may be dominated by marcasite. This suggests the acidified fraction represents an isotopically homogenous reduced sulfur pool ($S_{reduced}$, Fig. 3-4), incorporating both sulfides and organic S.

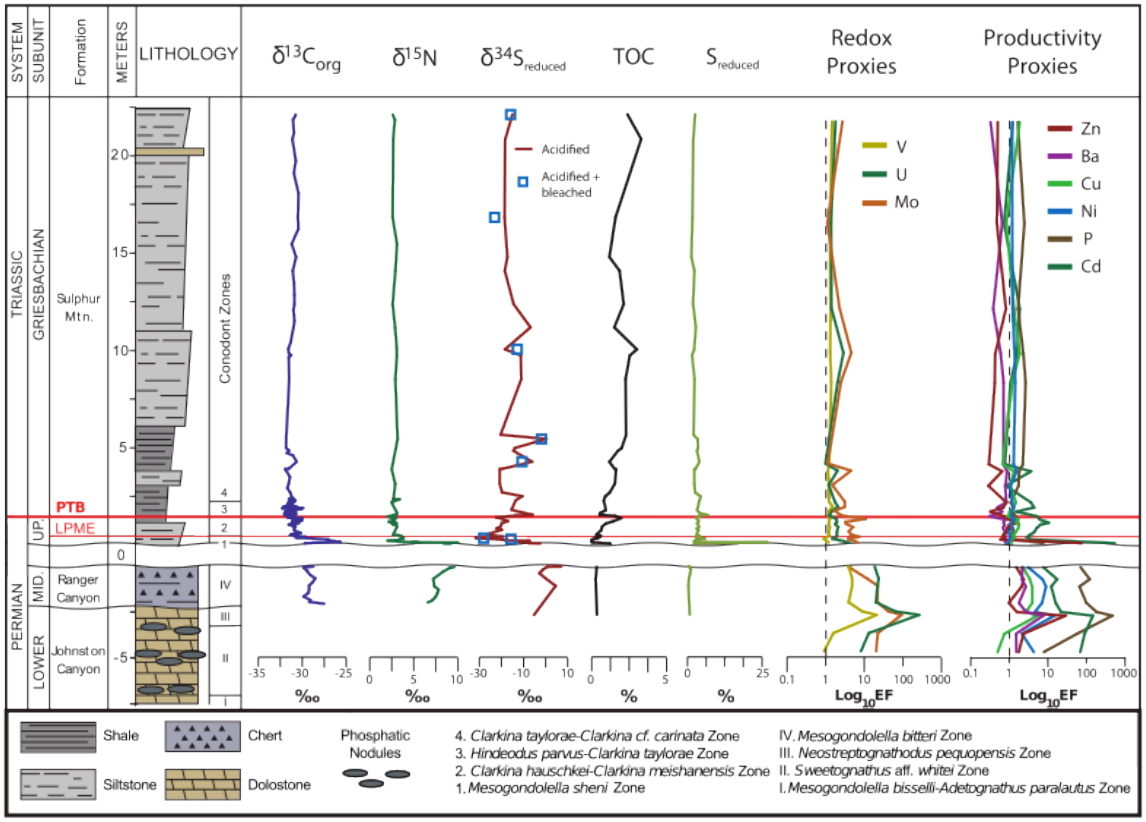

Figure 3: Stratigraphic column with lithostratigraphy as well as isotopic and trace element records for the Opal Creek section. Heavy red line corresponds to the biostratigraphic PTB, the thin red line corresponds to the main marine extinction event. The number of samples analyzed for each proxy is as follows: $\delta^{13}C_{org}$, n = 191, $\delta^{15}N$, n = 58, $\delta^{34}S$, n = 56 acidified (n = 7 acidified+bleached), %S, n = 55, TOC, n = 185, All trace element proxies, n = 29.

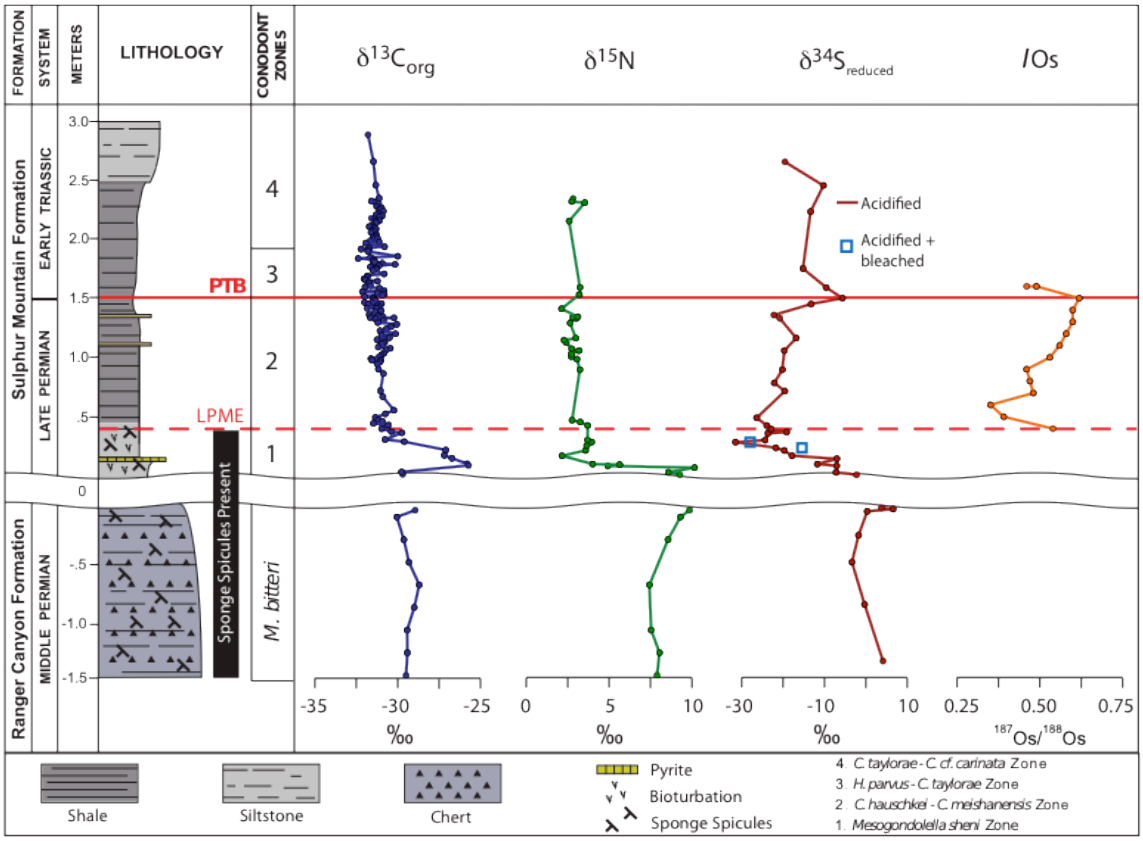

Figure 4: Expanded stratigraphic column for 4.5-m-thick interval of the Opal Creek section bracketing the unconformity and PTB, with isotope measurements and calculated initial osmium isotope ratios (*I*Os, see Re-Os Analysis in Results section). Solid red line indicates the biostratigraphic PTB, the dashed red line indicates the main extinction event. *M. bitteri* zone overlaps with *M. rosenkrantzi* in uppermost 5-10 cm of Ranger Canyon Formation. The number of measurements shown for each proxy is as follows: $\delta^{13}C_{org}$, n = 149, $\delta^{15}N$, n = 41, $\delta^{34}S$, n = 36 acidified (n = 2 acidified+bleached), *I*Os, n = 14.

4.3. Sulfur concentration and isotopic profiles

Sulfur isotopes vary markedly throughout the section, and several phases can be distinguished (Figs. 3-4). In the Lower and Middle Permian, sediments are generally sulfur poor (< 0.9 wt. %) and isotopically heavy, with $\delta^{34}S$ ranging from -5.4 to 7.2 ‰ (mean = 1.2 ‰, σ = 4.0), with the peak value 2.4 cm below the unconformity.

Heavy isotope values persist above the unconformity in the Late Permian lowermost SMF, despite much higher total sulfur content. A continuous and rapid decline in $\delta^{34}S$ can be observed between 1.5 and 29 cm (Fig. 4). This trend passes through the S wt. % maximum in the pyrite bed at ~10 cm, which has an S content of 26.4% by weight. Bleached extract for this sample yields S > 15wt% (IRMS signal saturated), and the S/Fe ratio is 1.13, nearly identical to the S/Fe ratios in pyrite (1.14), which along with field observation confirms that S in this layer is mostly in the form of pyrite. The declining isotope trend terminates in the section's $\delta^{34}S$ minimum at 29 cm ($\delta^{34}S$ = –32.0).

Above this minimum, sulfur concentrations and isotopes reach an equilibrium that they maintain for the remainder of the section. Sulfur weight % is generally at a few percent (mean = 2.3 %, σ = 1.0 %, Fig. 5) and $\delta^{34}S$ has a mean of -17.0‰ with a standard deviation of 6.0 ‰, though there is a gradual and poorly defined trend toward less negative values. There are also several minor positive excursions in $\delta^{34}S$. A small positive excursion in $\delta^{34}S$ (to –6 ‰) around 150 cm (sample OC145) is accompanied by a significant S concentration peak (6.3%).

		cm	Al	TOC	Mo	U	V	Ni	Cu	Zn	P	Ba	Cd	Mo	U	V	Ni	Cu	Zn	P	Ba	Cd	Mo/TOC
			%	%	*ppm*	*ppm*	*ppm*	*ppm*	*ppm*	*ppm*	*ppm*	*ppm*	*ppb*	*EF*	*EF*	*EF*	*EF*	*EF*	*EF*	*EF*	*EF*	*EF*	*x10⁴*
Triassic	Sulphur Mountain	2215	7.6	2.4	3.8	4.7	146	48	42.8	32	1060	160	110.0	2.7	1.8	1.5	1.2	1.8	0.5	1.6	0.3	1.2	1.6
		1684	7.0	1.6	1.4	3.3	118	44	17.6	28	1470	300	60.0	1.1	1.4	1.3	1.2	0.8	0.5	2.4	0.6	0.7	0.9
		1237	7.6	2.1	3.2	3.7	134	50	30.5	53	1090	190	170.0	2.3	1.4	1.3	1.2	1.3	0.8	1.6	0.4	1.8	1.5
		1003.5	6.9	3.0	6.0	6.9	118	50	38.7	25	1360	270	130.0	4.7	2.9	1.3	1.3	1.8	0.4	2.3	0.6	1.6	2.0
		850.5	7.1	2.3	3.3	5.0	129	54	25.7	25	1600	330	90.0	2.5	2.0	1.4	1.4	1.2	0.4	2.6	0.7	1.0	1.5
		423.5	8.9	1.2	1.8	3.0	143	62	17.8	22	1710	410	80.0	1.1	1.0	1.2	1.3	0.6	0.3	2.2	0.7	0.7	1.5
		386	6.6	1.7	5.6	4.6	98	54	26.4	36	1000	380	290.0	4.6	2.0	1.1	1.5	1.3	0.6	1.8	0.8	3.6	3.4
		310.5	8.3	1.6	2.3	3.4	132	48	26.4	20	1230	430	80.0	1.5	1.2	1.2	1.0	1.0	0.3	1.7	0.8	0.8	1.4
		223.5	6.2	0.9	3.6	3.7	99	39	27.8	44	570	340	270.0	3.1	1.7	1.2	1.1	1.4	0.8	1.1	0.8	3.6	4.2
		196.5	7.9	1.0	4.6	5.7	156	54	30.9	47	840	250	420.0	3.1	2.1	1.5	1.3	1.3	0.7	1.2	0.5	4.4	4.4
		175.5	8.5	1.0	2.7	4.3	136	52	25.9	23	830	360	150.0	1.7	1.5	1.2	1.1	1.0	0.3	1.1	0.6	1.5	2.7
		150.5	7.6	0.6	3.7	3.2	116	45	20.8	48	940	150	490.0	2.6	1.2	1.1	1.1	0.9	0.7	1.4	0.3	5.3	6.1
Permian		133.5	7.0	2.0	14.6	4.5	117	50	35.8	57	640	360	520.0	11.2	1.9	1.3	1.3	1.7	0.9	1.1	0.8	6.1	7.4
		116.75	5.8	1.4	3.5	3.9	91	35	26.5	84	600	270	750.0	3.2	1.9	1.2	1.1	1.5	1.6	1.2	0.7	10.7	2.4
		106.25	6.5	1.0	4.1	3.9	104	38	35.1	60	540	320	500.0	3.4	1.7	1.2	1.1	1.7	1.1	1.0	0.7	6.3	4.1
		90.15	6.0	0.8	5.8	4.4	100	37	31.5	45	630	270	380.0	5.2	2.1	1.2	1.1	1.7	0.8	1.2	0.7	5.2	7.7
		67	6.1	0.7	4.5	4.1	97	31	26.5	45	660	310	320.0	4.0	1.9	1.2	0.9	1.4	0.8	1.3	0.7	4.3	6.7
		52.5	6.7	0.6	5.7	4.5	108	36	26.2	39	600	330	270.0	4.5	1.9	1.2	1.0	1.3	0.7	1.0	0.7	3.3	9.6
		40	7.0	0.5	10.0	4.6	102	40	29.7	43	660	360	240.0	7.6	1.9	1.1	1.0	1.4	0.7	1.1	0.7	2.8	20.9
		29	6.6	0.3	4.8	3.4	77	35	21.5	33	740	320	300.0	3.8	1.5	0.9	1.0	1.0	0.6	1.3	0.7	3.7	16.4
		10.5	5.6	0.1	7.2	8.0	88	27	19.6	3850	3720	300	39900.0	6.8	4.1	1.2	0.9	1.1	77.4	7.6	0.8	581.4	75.5
	R.C.	-4	1.4	0.4	1.0	8.7	71	24	9.9	19	8450	210	130.0	3.7	17.8	3.8	3.1	2.3	1.5	69.3	2.2	7.6	2.7
		-70	0.8	0.3	1.6	6.0	48	30	8.1	16	7870	110	160.0	11.4	22.7	4.7	7.3	3.4	2.4	118.9	2.1	17.3	5.6
		-110	0.3	0.3	1.1	2.0	17	13	3.3	5	1520	50	40.0	21.4	21.3	4.7	8.9	3.9	2.1	64.7	2.7	12.2	3.6
		-200	0.6	0.4	2.2	3.8	29	22	7.0	5	4840	70	110.0	21.1	19.1	3.8	7.1	3.9	1.0	97.5	1.8	15.8	5.8
	J.C.	-250	0.6	0.3	4.8	13.4	72	16	5.4	9	10000*	120	170.0	39.9	60.1	8.5	4.6	2.7	1.6	179.5	2.7	21.8	15.0
		-270	0.3	0.4	4.1	21.8	67	20	4.2	63	10000*	130	440.0	88.3	250.4	20.1	14.6	5.4	28.5	459.4	7.6	144.4	10.8
		-370	0.7	0.5	2.8	3.0	14	8	1.6	14	3300	70	730.0	21.7	12.7	1.5	2.1	0.8	2.3	55.7	1.5	88.1	5.5
		-470	0.8	0.7	2.8	2.1	9	18	1.2	12	520	80	630.0	19.5	7.9	0.9	4.3	0.5	1.8	7.9	1.5	68.0	4.1
		AUCC†	8.0	-	1.5	2.8	107	44	25.0	71	700	550	98	1.0	1.0	1.0	1.0	1.0	1.0	1.0	1.0	1.0	-

* indicates that the concentration exceeded the maximum detectable limit

Table 0: Concentrations and enrichment factors of some major and trace elements

†AUCC = Average Upper Continental Crust (McLennan 2001)

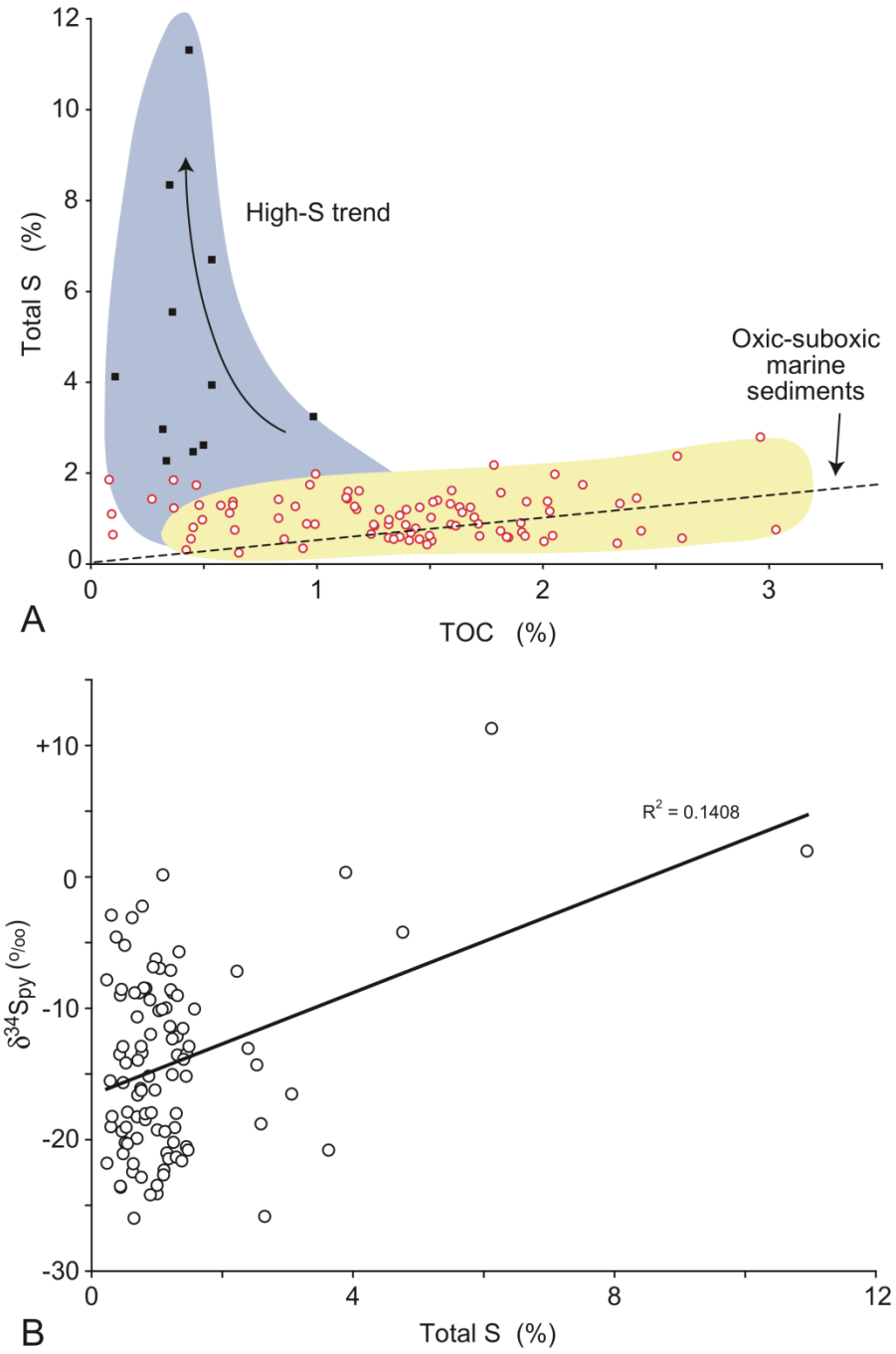

Figure 6: (A) TOC versus total S. The majority of samples fall along the oxic-suboxic trend of Berner and Raiswell (1983). A subset of samples (n ~12) plots distinctly above the oxic-suboxic trend; they represent the basal 4 m of the SMF plus a few pyritic layers higher in the section. (B) Total S versus pyrite $\delta^{34}S$. Note that high-S samples are low in TOC and enriched in ^{34}S. Samples shown in this figure are a separate set processed at the U. of Cincinnati.

4.4. Petrographic data

Petrographic study revealed characteristic relationships between pyrite, organic matter, and calcite within the study samples. The basal beds (pre-LPME) of the SMF are characterized by high concentrations of sulfides in the form of massive pyrite (Fig. 6A) and large (5-50 μm), partially interlocking crystals of marcasite (Fig. 6B). These sulfides show no relationship to primary sediment fabric; their quantity and form suggest that they may be of hydrothermal original. The beds immediately above the LPME are characterized by abundant pyrite framboids, although these framboids tend to be larger (5-10 μm; Fig. 6C) than those formed in a euxinic water column (<5 μm; Wilkin et al., 1996; Wignall and Newton, 1998). Many of the framboids show evidence of later diagenetic overgrowths (Fig. 6C-D), and blocky authigenic pyrite crystals are common (Fig. 6D-E). Higher in the section, most pyrite occurs as clusters of framboidal or blocky crystals grown either within or on the surface of large (50-500 μm) organic particles (e.g., Fig. 6G-H, L-N, P). Individual framboids in these samples are often 10-40 μm in diameter (Fig. 6H, L, O) and hence distinctly larger than syngenetic framboids (Wilkin et al., 1996). This form of pyrite is commonly associated with large, blocky calcite crystals that have grown diagenetically within the sediment (e.g., Fig. 6G-J). Blocky to massive authigenic pyrite is sometimes found in the middle of large carbonate-cemented areas without any obvious association with organic matter (e.g., Fig. 6F, K).

Several generations of carbonate are present in the sediments, including cements, with isotopic measurements indicating a diagenetic origin (Schoepfer et al., 2012). This is consistent with an increase in porewater alkalinity due to biological sulfate reduction and

the inference that most of the pyrite in the section formed in the sediments after deposition.

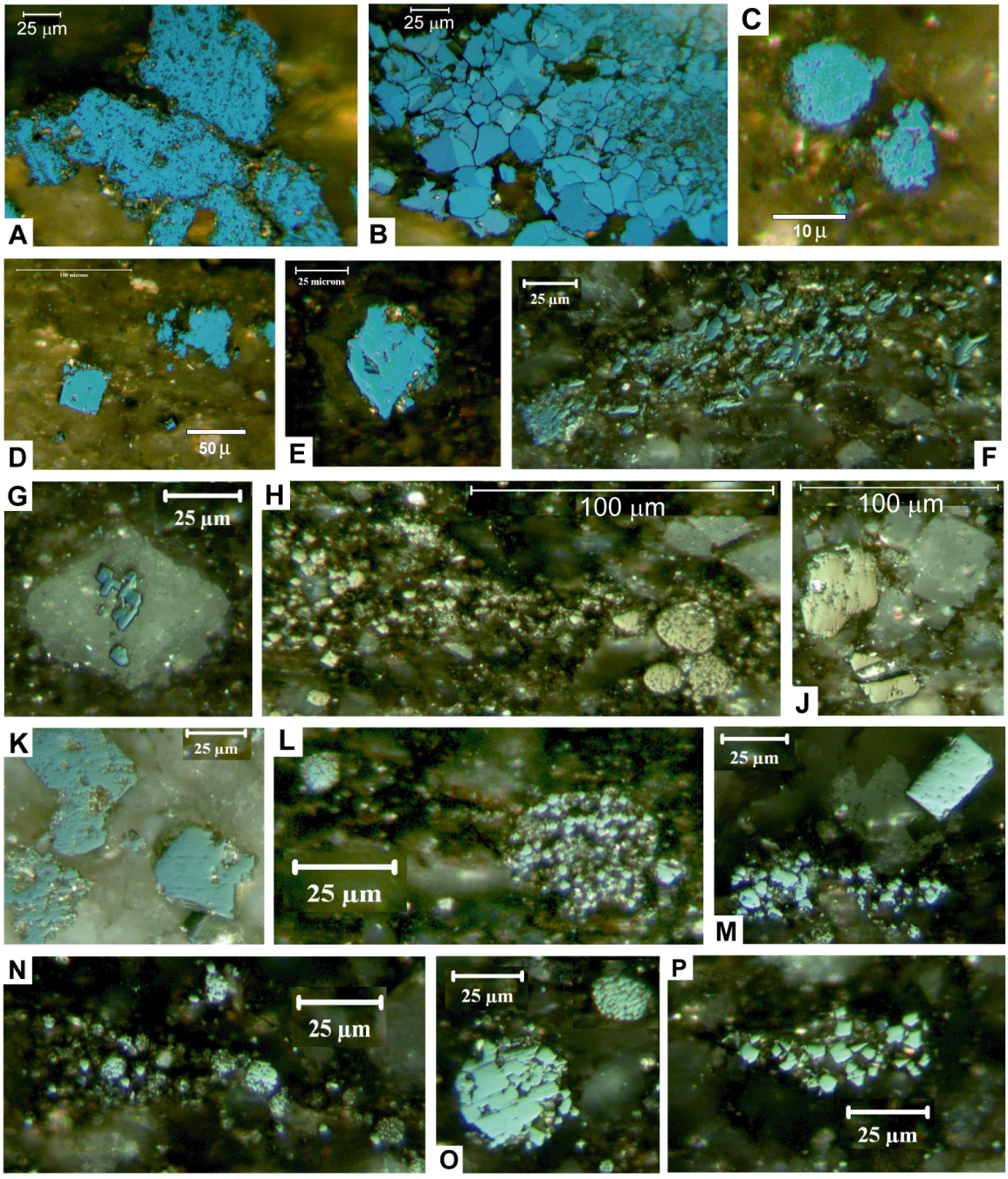

See next page for Figure Caption

Figure 6: Reflected light petrographic photomicrographs of SMF: (A) Massive pyrite in calcareous silicate matrix. (B) Massive marcasite in silicate matrix. (C) Medium-sized (8-12 µm) pyrite framboids with partial diagenetic overgrowths. (D) Coarse euhedral and irregular diagenetic pyrite masses. (E) Large (35 µm) pyrite framboid with diagenetic overgrowths. (F) Fine (3-10 µm) diagenetic pyrite crystals in a large organic particle. (G) Fine diagenetic pyrite within a diagenetic calcite crystal. (H) Variably sized (4-20 µm) pyrite framboids along an organic-rich lamina. (J) Coarse diagenetic pyrite associated with diagenetic carbonate crystals. (K) Coarse diagenetic pyrite within a carbonate nodule. (L) Variably sized (10-40 µm) pyrite framboids along an organic-rich lamina. (M) Organic particle with diagenetic pyrite overgrowths (lower left) and blocky diagenetic pyrite (upper right). (N) Fine (4-12 µm) pyrite framboids along an organic-rich lamina. (O) Coarse (20-40 µm) pyrite framboids with diagenetic overgrowths on larger framboid. (P) Fine (3-8 µm) diagenetic pyrite crystals in an organic particle.

4.5. Re-Os analysis

The Re-Os data are presented in Table 2. Samples collected from 20 and 30 cm above the Ranger Canyon/Sulphur Mountain unconformity are siltstone and did not contain measurable Re and Os. Between 30 and 40 cm above the unconformity the siltstone grades into black shale. The samples collected from this interval and to 1.6 m above the unconformity are enriched in both Re and Os (~4 to 11 ppb; 78 to 157 ppt, respectively, Table 2). The $^{187}Re/^{188}Os$ range between ~240 and 400, with the $^{187}Os/^{188}Os$ being moderately radiogenic (~1.5 to 2.2). The initial $^{187}Os/^{188}Os$ (IOs) is calculated based on the GTS 2008 age for the Permian-Triassic boundary, 252.2 Ma (Ogg et al., 2008; Shen S.Z. et al., 2011) and the ^{187}Re decay constant of Smoliar et al. (1996). The calculated IOs values are shown in Figure 4. Beginning 0.4 m above the unconformity (the LPME), the IOs values become less radiogenic from 0.54 to 0.35. From the less

radiogenic *I*Os at 0.6 m above the unconformity to 1.5m (Permian-Triassic boundary) the *I*Os values become steadily more radiogenic. At 1.6m the *I*Os trends to a less radiogenic value (~0.49).

cm	Re (ppb)	±	Os (ppt)	±	$^{187}Re/^{188}Os$	±	$^{187}Os/^{188}Os$	±	rho	*IOs*†
40	6.01	0.02	93.3	0.8	394.5	4.6	2.1993	0.03	0.764	0.54
50	8.86	0.03	156.5	1.2	331.9	3.3	1.7877	0.022	0.695	0.39
60	6.64	0.02	100.7	0.9	395.7	4.5	2.0164	0.027	0.753	0.35
70	5.02	0.02	90.5	0.8	328	3.8	1.8624	0.026	0.758	0.48
80	6.35	0.02	102.8	0.9	371.8	4.1	2.0355	0.027	0.743	0.47
90	5.04	0.02	78.7	0.7	387.2	5	2.0863	0.031	0.789	0.46
100	6.05	0.02	129.7	1	269.5	2.8	1.662	0.021	0.713	0.53
110	5.19	0.03	98.3	0.6	312.4	2.3	1.8707	0.013	0.482	0.56
120	4.77	0.03	101.9	0.6	273	2.1	1.7331	0.013	0.46	0.58
130	6.15	0.03	112.7	0.6	326.3	2.2	1.9701	0.011	0.398	0.6
140	3.95	0.01	77.6	0.5	301.8	2	1.8687	0.014	0.672	0.6
150	5.84	0.04	110.3	0.7	315.6	2.6	1.9491	0.015	0.441	0.62
160	4.9	0.02	97.1	0.8	293.7	3.3	1.7236	0.023	0.742	0.49

Table 1: Re and Os concentrations and isotopes. *I*Os uncertainties were less than or equal to .004.

†Initial osmium compositions (*I*Os) calculated for an age of 252.2 Ma.

4.6. Trace-element redox proxies

Certain trace elements tend to be authigenically enriched in sediments under reducing conditions, including uranium (U), vanadium (V), and molybdenum (Mo) (Algeo and Maynard, 2004; Tribovillard et al., 2006). The calculated Enrichment Factors of these elements show similar patterns (Fig. 3), suggesting that they responded to a common redox control. All three elements are highly enriched in the Johnston Canyon and Ranger Canyon Formations, with Mo and U have EFs averaging >10x their concentrations in AUCC. These values are probably indicative of sulfidic bottom water conditions throughout the deposition of these units. All three elements show steep declines in the overlying SMF, although varying somewhat in detail. V exhibits near-

average values (EF ~1) throughout the SMF. Mo and U remain modestly enriched (EF <10) in the SMF, with somewhat greater enrichment in the basal 3 meters than higher in the formation. Relatively large EFs are associated with the pyrite bed at ~10 cm, where Mo has an EF of 6.8 and U has an EF of 4.1.

As euxinic water conditions will often increase the particle reactivity of redox sensitive metals, which often form organo-metallic compounds (Tribovillard et al., 2006), trace element concentrations were also normalized to TOC to control for the effects of particle flux. While the actual ratios varied greatly between elements, all were generally enriched in metals relative to TOC below the unconformity, but showed strong peaks in the lowermost Sulphur Mountain Formation coincident with the pyrite bed, and remained enriched throughout the latest Permian generally.

4.7. Trace-element productivity proxies

Several trace elements sensitive to changes in organic carbon export showed significant fluctuations throughout the section. Cu, Ni, Cd, Zn, Ba, and P all show a nutrient-like distribution in seawater and are mainly transferred to sediments through sinking carbon flux. Of these, Cu, Cd, Ni, and Zn can be precipitated as sulfide minerals under euxinic or sufficiently reducing conditions, and are likely to be preserved in sediments, whereas barium is generally precipitated as barite, a sulfate, and may be released back into the water column in a regime of sulfate reduction (Dehairs et al., 1980; Averyt and Paytan, 2004). Phosphorous is mainly stored in sediments in organic matter or phosphate minerals. Under reducing conditions, phosphate may be remineralized and re-enter the water column (Meyer and Kump, 2008).

EFs were calculated for Ba, P, Cu, Ni, Cd and Zn. These elements all showed significant enrichments above AUCC in the Johnston and Ranger Canyon Formations, with P in particular being enriched above AUCC by at least a factor of 7.9 and by 2 orders of magnitude in some samples. (Two samples collected 250 and 270 cm above the unconformity saturated the ICP-AES Phosphorous peak. The maximum detectable concentration, 10^4 ppm, was used.) Directly above the unconformity, P remains highly enriched with an EF of 7.6 while Zn is also extremely enriched, with an EF of 77.4, likely due to precipitation as a sulfide in the pyrite bed. Cadmium, which also forms sulfide minerals, is also orders of magnitude more enriched in this layer than the rest of the section (EF=581.4). The other elements (Ba, Cu, Ni) drop off immediately above the unconformity to values similar to AUCC, with Ba and Cu generally below an EF of 1, whereas Ni remains just above. After the pyrite bed, Zn drops off to just below average EFs similar to Cu, Ni and Ba, while P remains slightly more enriched with EFs ranging from 1 to 2.6 through the remainder of the section. EFs are shown in logarithmic scale in Figure 3.

5. Discussion

5.1. Effects of sediment mixing on geochemical signals

Reworked conodonts above the unconformity indicate that some reworking of subaerially exposed Middle Permian cherts or biological mixing of sediments has occurred. This has the potential to exercise a controlling effect on geochemical signals, especially as the resemblance of the Late Permian lowermost Sulphur Mountain to the Middle Permian Ranger Canyon in many parameters (i.e. $\delta^{15}N$, $\delta^{34}S$, several trace

elements) is central to interpretation of the outcrop.

While the lowermost Sulphur Mountain shows elevated EFs in several trace elements similar to or lower than the Ranger Canyon, this is after aluminum normalization, which obscures the often higher absolute concentrations of many elements in the more aluminosilicate rich Sulphur Mountain siltstones. For example, the uppermost Ranger Canyon has a measured Zn content of 19 ppm, whereas the lowermost Sulphur Mountain has 3.85 ppt. In light of this orders-of-magnitude variation, it would be difficult for reworking or upward mixing of Ranger Canyon material to exercise any major control on the trace element content above the unconformity. The presence of discrete peaks in geochemical signals above the unconformity--for example, the presence of a ~1 cm thick pyrite bed, the positive organic carbon isotope excursion reported in Schoepfer et al. (2012), and Cd content, which spikes to 39.9 ppm at ~10 cm above the unconformity despite an average of 0.3 ppm in the Ranger Canyon Formation--suggest that mixing over decimeter scales is not a controlling factor on the inorganic geochemistry of this interval.

The major isotopic shifts observed in the basal Sulphur Mountain, however, occur over smaller spatial scales, and without an independent tracer, control by mixing cannot be completely ruled out. If mixing is predominantly responsible for the heavy $\delta^{15}N$ and $\delta^{34}S$ values seen in the basal Sulphur Mountain, then the environmental changes implied by these isotopic shifts may have occurred at any time during the missing 5-7 My Lopingian interval, and may have occurred more gradually than the preserved isotope signals would suggest. However, it is worth noting that Luo et al. (2011) observed abrupt nitrogen isotope shifts of similar magnitude immediately preceding the main LPME at several Tethyan sections in South China.

5.2. Benthic redox conditions

Sulfur isotopic compositions provide information about the processes of sulfide formation and, hence, paleomarine redox conditions. Syngenetic framboidal pyrite, which forms in the water column and thus from an unlimited sulfate reservoir, commonly exhibits a large negative fractionation relative to source sulfate (Goldhaber and Kaplan, 1974; Canfield and Thamdrup, 1994). In contrast, authigenic pyrite formed in the sediment exhibits heavier $\delta^{34}S$ values; if all porewater sulfate is consumed within a closed diagenetic system, the resulting sulfide will have an average $\delta^{34}S$ value equal to that of the source sulfate. The degree of shift toward heavier $\delta^{34}S$ values depends on the timing of bacterial sulfate reduction (BSR); early BSR in a relatively open system will produce more ^{34}S-depleted sulfide than late BSR in a relatively closed system (Goldhaber and Kaplan, 1974; Chambers and Trudinger, 1979).

Modern seawater sulfate has a $\delta^{34}S$ of +20‰, yielding sulfide $\delta^{34}S$ values of about -30 to -40‰ in anoxic marine systems (Lyons, 1997; Wilkin and Arthur, 2001; Werne et al., 2003). The isotopic composition of seawater sulfate varied between +10‰ and +30‰ during the PTB transition, possibly shifting toward heavier values in the Early Triassic (Strauss, 1999; Newton and Wignall, 2004; Riccardi et al., 2006) although much variation exists within and between sections (Luo et al., 2010; Song et al., in review). Given a BSR fractionation of -30 to -60‰ (Habicht and Canfield, 2001), syngenetic pyrite in PTB sections should yield isotopic compositions between -10 and -40‰ (cf. Nielsen and Shen, 2004; Algeo et al., 2008).

Reduced sulfur $\delta^{34}S$ in the Johnston Canyon and Ranger Canyon formations average 1.0 ± 4.2‰ (n = 8). These relatively heavy values suggest precipitation in a

closed system, consistent with a diagenetic origin for pyrite in this interval. The evidence of quantitative reduction of porewater sulfate in this interval despite the low organic content suggests poor postdepositional preservation may be responsible for the lack of preserved carbon despite other evidence of high productivity (see below).

The Johnston Canyon and Ranger Canyon formations contain high concentrations of V, U, and Mo. Coeval enrichments in Mo, U, and V (Fig. 3) suggest the presence of anoxic water in the Early and Middle Permian. That these enrichments are found in bioturbated sediments supporting an abundant (if homogenous) benthic fauna suggests that bottom water was oxygenated, and trace element enrichments may have resulted from a water column oxygen minimum impinging on the bottom. Coastal upwelling zones often dynamically maintain an oxygen minimum zone (OMZ) in the mid-water column through the decomposition of sinking organic material. When the sinking flux of carbon exceeds the supply of oxygen, other electron acceptors are often used in decomposition, including nitrate and sulfate, with upwelling zones being among the primary zones of denitrification in the modern ocean (Seitzinger et al., 2006).

Nitrogen isotopes (Schoepfer et al., 2012) from Opal Creek suggest the Middle Permian upwelling system supported a mid-water oxygen minimum where denitrification and sulfate reduction were occurring. Denitrification has a substantial fractionation effect, and when it does not occur quantitatively, enriches the residual marine nitrate pool. $\delta^{15}N$ in the Ranger Canyon is consistently high, spiking to values above 9 ‰, values typically seen in modern environments where denitrification occurs in a strong water column oxygen minimum (Algeo et al., 2008).

The lower ~4 m of the SMF contains the largest concentrations of small framboids, and these beds exhibit some of the most ^{34}S-depleted values—a pattern consistent with pyrite mainly of syngenetic origin. $\delta^{34}S_{reduced}$ in the SMF averages -16.5 ± 6.8‰ (n = 47), which is distinctly higher than the isotope compositions expected for syngenetic framboidal pyrite. These compositions are consistent with pyrite formation in the diagenetic environment under quasi-open conditions, or with diagenetic overgrowths on syngenetic pyrite under somewhat more closed conditions.

TOC-S relationships are consistent with predominantly suboxic conditions during deposition of the SMF. Most samples fall along the oxic-suboxic ("normal marine") trend of Berner and Raiswell (1983; Fig. 5). A relative handful of samples, mostly in the lower ~4 m of the SMF, exhibit S concentrations considerably above those expected for oxic-suboxic facies; other evidence supports this interval having been deposited under primarily euxinic conditions (see below). Three horizons higher in the SMF (at 4.7, 12.8, and 20.4 m) also exhibit significant S enrichment above the oxic-suboxic trendline (Fig. 5). Unlike samples from the base of the formation, however, these samples are associated with markedly heavier $\delta^{34}S$ values—an indication that the pyrite concentrations in these samples formed in the sediment and not in the water column, which is supported by petrographic data. The extinction of bioturbating benthic communities may have contributed to these intervals of near-quantitative sulfate reduction in the sediments (Shen Y., et al., 2011).

Secondary pyrite overgrowths are common in many framboidal layers, and framboid sizes are larger than those associated with syngenetic formation, especially above the basal 4 m of the SMF (Fig. 5). The observation that most framboids grew in

clusters within or on the surface of large organic particles, rather than as isolated crystal aggregates, indicates a strong association of BSR with such organic substrates. The distribution of calcite within the samples, mostly as blocky diagenetic crystals adjacent to organic particles, or as "halos" enclosing these particles, is an indication that BSR within the sediment produced local increases in alkalinity that stimulated secondary carbonate precipitation (Berner, 1984).

Trace element proxies support these redox interpretations for the SMF. Mo, U, and V remain slightly enriched throughout the SMF, suggesting low oxygen conditions persisted, which along with the dearth of benthic biota, lack of bioturbation, and increased organic preservation indicate that the system transitioned to a bottom water oxygen minimum. Mo, which forms highly particle reactive oxythiomolybdates under euxinic conditions (Tribovillard et al., 2006), is particularly enriched in the lowermost 4 meters of the SMF, suggesting free sulfide in the water column during this interval.

Except for the basal ~50 cm of this formation, $\delta^{15}N$ is low and stable (Schoepfer et al., 2012; Figs. 3-4), providing no evidence of water-column denitrification as might be expected if suboxic conditions were due to high sinking fluxes of organic matter (e.g., Jenkyns et al., 2001; Algeo et al., 2008). Although the SMF consists predominantly of black shale (Munsell color), TOC values are only moderate (0.2-3.0%) yet locally higher than expected for oxic-suboxic facies (Algeo and Maynard, 2004). One explanation for this pattern may be a marked reduction in bioturbation intensity during the Early Triassic, as a consequence of the loss of most benthic infauna during the LPME (Twitchett and Wignall, 1996) and transition from a mid-water to bottom water oxygen minimum. Reduced bioturbation would severely constrain ventilation of the sediment and allow

greater quantities of organic matter to be preserved for a given flux of organic matter to the sediment-water interface. Thus, multiple lines of evidence confirm that the basal ~4 m of the SMF coincided with a euxinic event, and that the remainder of the formation was deposited under oxic to suboxic conditions.

5.3. Marine circulation and productivity

The consistent enrichments in Ba, Cu, Ni, Zn, P, and Cd in the Johnson Canyon and Ranger Canyon formations are here interpreted as representing a highly productive, eutrophic marine system, despite the generally low organic carbon content of these units, which may results from poor preservation in well-ventilated bottom water. The presence of phosphate nodules in the Johnson Canyon and minor phosphatic material in the Ranger Canyon is consistent with a high-productivity environment, and the dominant fauna of the Ranger Canyon, rock-forming abundances of filter-feeding sponges, suggests a vigorous export of organic detritus from the photic zone.

High-abundance but low-diversity conodont assemblages have been suggested to indicate eutrophic conditions (Brasier, 1995), because fast-breeding species capable of rapidly exploiting the available resources tend to dominate the environment. The conodont assemblage of the Ranger Canyon Formation is dominated by high abundances of the genus *Mesogondolella*, which had a circumboreal distribution in the Middle Permian and is therefore also indicative of cold-water conditions (Henderson, 1997; Mei and Henderson, 2001).

The biota of the Johnston Canyon and Ranger Canyon formations is consistent with a high-nutrient, cold-water environment. Replacement of this prolific carbonate

factory by a siliceous sponge-dominated biota occurred between the Artinskian (late Early Permian) and Guadalupian (late Middle Permian) as a consequence of climatic cooling and an increase in nutrient levels (Beauchamp and Henderson, 1994; Reid et al., 2007; Bensing et al., 2008). The high concentration of sponge-derived chert in Upper Permian beds has been interpreted as evidence of vigorous thermohaline circulation and nutrient upwelling in the Panthalassic Ocean, and its absence in Lower Triassic beds as evidence of sluggish circulation and nutrient-poor surface waters (Beauchamp, 1994; Beauchamp and Desrochers, 1997; Beauchamp and Baud, 2002). Hyalosponge facies, indicative of cold, deepwater conditions, are widespread along the western margin of Pangaea during the Early to Middle Permian, and have been used to infer the presence of coastal upwelling down to subtropical latitudes, as well as cold northern polar currents driven by sea ice in contact with the ocean (Beauchamp and Baud, 2002). Upwelling at subtropical latitudes along western Pangaea is also inferred by Ziegler et al. (1998) from sedimentological evidence, and has been modeled under a range of atmospheric conditions by Winguth and Maier-Reimer (2005).

The locality was erosive throughout most of the Lopinigian lowstand, but when sedimentation resumed in the Changhsingian the depositional environment resembled that of the Ranger Canyon in many ways. Silica sponges were still the abundant, predominant benthic fauna, although sponge spicules were increasingly diluted with siliciclastic sediments. Nitrogen and sulfur isotopes remain highly enriched, suggesting that an anoxic zone, fed by sinking organic matter and ultimately by upwelling nutrients, persisted into the latest Permian. Sediments remain bioturbated in this interval, indicating that the sea floor was relatively well oxygenated, with the oxygen minimum occurring in

the water column.

~10 cm above the unconformity is a continuous bed containing >26% sulfur by weight, mostly in the form of pyrite, suggestive of highly euxinic water conditions, which is supported by orders-of-magnitude enrichments in the S/TOC and Mo/TOC ratios. This ~1 cm thick pyrite bed corresponds with a discrete, ~ 8 ‰ spike in organic carbon isotopes that has been interpreted as transient increase in productivity (Schoepfer et al., 2012) which may have driven the system toward euxinia, Enrichments in P, Zn, and Cd are also suggestive of enhanced productivity in this interval: while Zn and Cd are expected to complex in the sulfide sediments, P should be unaffected by euxinia and record productivity, whereas minor depletions in Ba relative to AUCC may reflect the difficulty of preserving barite ($BaSO_4$) under conditions of euxinia.

The trace element enrichments suggest that this euxinic interval may have been fueled by transient increased productivity. Numerous workers have suggested a substantial increase in continental weathering and erosion in the latest Permian (Ward et al., 2000; Sephton et al., 2005; Algeo and Twitchett, 2010; Algeo et al., 2011a). This would have carried an increased complement of terrigenous nutrients, such as phosphate and iron, and may have pushed organic productivity above its already-high levels, driving the system toward euxinia.

This hypothesis receives some support from the *I*Os data (Fig. 4). The primary feature of this data set is a shift from relatively non-radiogenic values (0.35-0.40) around the LPME boundary toward more radiogenic values (~0.45 to 0.62) between 60 and 150 cm above the unconformity. This suggests that the primary control of the Os composition in seawater during this interval (Os_{SW}) is the influx of radiogenic detritus from the

cratonic continental crust (Cohen et al., 1999; Peucker-Ehrenbrink and Ravizza, 2000), into the ocean, beginning roughly with the onset of the euxinic pulse. Non-radiogenic Os values seen prior to this shift may be related to the input of Os associated with the eruption of the Siberian Traps, which would be expected to possess mantle-like Os isotope signatures (~0.13-0.15; Horan et al., 1995). Values for Os_{SW} during the late Permian Arctic black shale of the Mid-Norwegian shelf yield *I*Os values of ~0.6 (Georgiev et al., 2011), which is similar to the *I*Os value of the extinction interval (~0.55) at Opal Creek, suggesting these continental weathering effects may have been widespread in the global ocean. However, in stark contrast to the Arctic black shales the $^{187}Re/^{188}Os$ values of the Opal Creek P-T section are typical of most marine organic-rich sedimentary rocks (269-394; Table 2) and therefore indicate that the conditions that permitted elevated $^{187}Re/^{188}Os$ values (~2000 to 6000) in the Arctic is regional rather than global as suggested by Georgiev et al. (2011).

The end of this intensely euxinic interval corresponds with a drop off in the previously enriched isotopes of nitrogen and sulfur. Nitrogen isotopes fall toward low values of approximately 2-3 ‰, lower than average modern marine nitrate and likely reflecting the influence of nitrogen fixation from the atmosphere in a nutrient limited environment. These low nitrogen values persist with remarkable uniformity throughout the remainder of the SMF, reflecting a new nutrient cycling regime in which water denitrification, fueled by respiration of sinking organic matter, no longer occurred on a significant scale. These changes probably reflect the collapse of vigorous coastal upwelling and the concomitant high organic productivity that fueled anaerobic respiration in the water column.

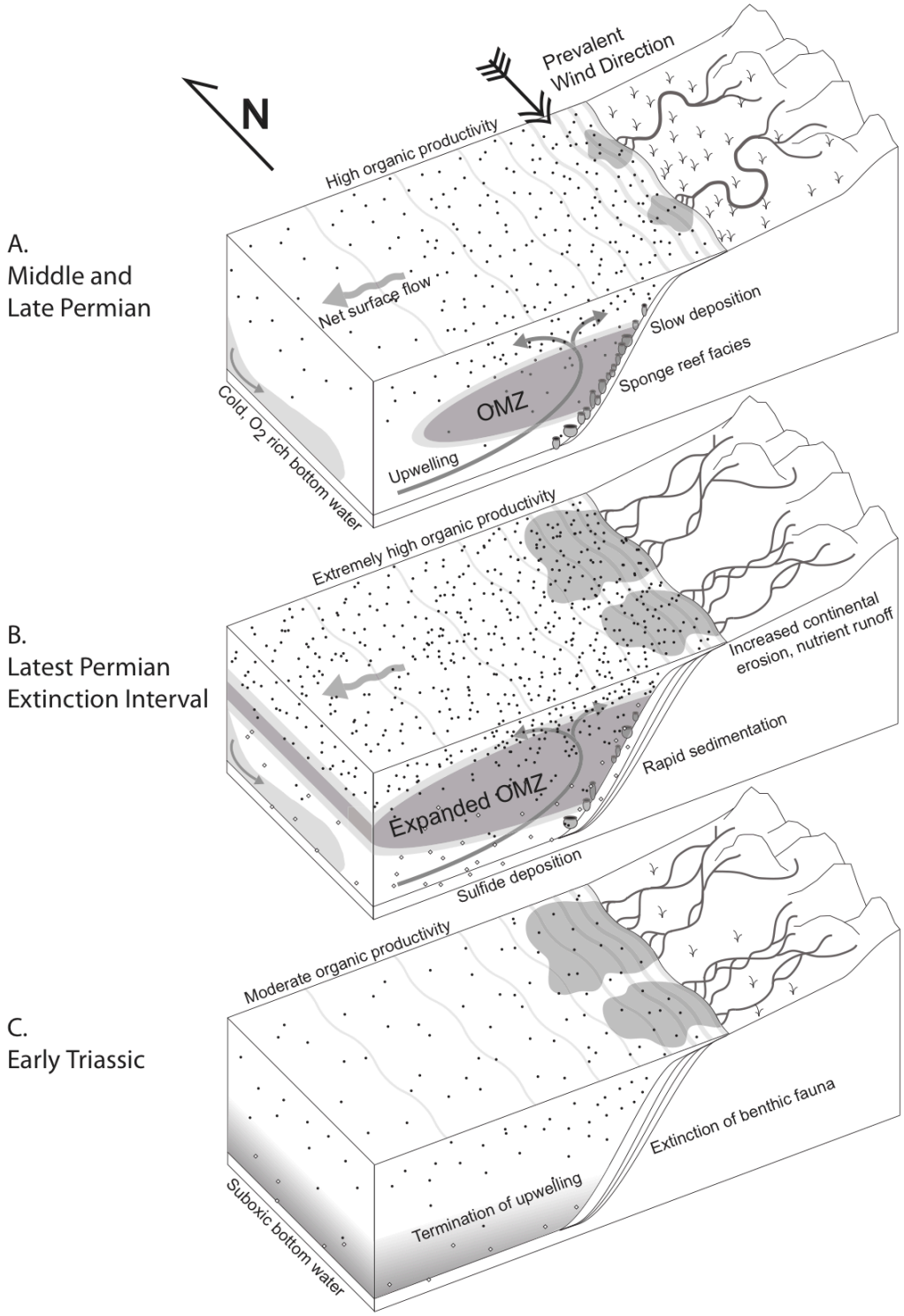

Figure 7: Integrated model of environmental conditions on the subtropical eastern Panthalassic margin (A) During the Early and Middle Permian (B) During the main latest Permian extinction interval (C) During the earliest Triassic

This is supported by the collapse of all productivity-sensitive trace elements to values very near AUCC throughout the remainder of the section (excepting P and Cd, which remain slightly enriched), and by the disappearance of silica-producing sponges 30 cm above the pyrite bed, in what we interpret as corresponding to the main Permian-Triassic marine extinction. Productivity in the subsequent SMF likely reflected typical values for oligotrophic marine settings, rather than those of continental margin upwelling systems, and may have been limited by nitrogen availability, with diazotrophic prokaryotes likely playing an important role. The cessation of upwelling may have been the result of warming following the eruption of the Siberian traps, with a consequent flattening of global thermal gradients and slowing of ocean and atmospheric circulation, with both euxinia and increasing nutrient limitation playing a role in bringing about benthic extinctions in this ecosystem.

5.4. Integrated model

Here we present evidence that a coastal upwelling system, a major mode of Panthalassic ocean circulation that had persisted for tens of millions of years, abruptly terminated preceding the Permian-Triassic boundary, shifting to a relatively unproductive, nutrient limited system with suboxic to dysoxic bottom water. However, this transition was preceded by an interval of intense euxinia, corresponding to the pyrite bed and preceding the main pulse of marine extinction. This likely resulted from a transient intensification of marine productity, which may have been caused by a combination of warming climate with residual upwelling of nutrient rich waters, before the circulation slowed dramatically (Fig. 7). Higher temperatures could allow for faster

algal growth and nutrient cycling, and ultimately faster and more explosive productivity. Alternatively, this pulse of high productivity may have been a global ocean scale event. The end-Permian has been linked to a change in fluvial morphology patterns, and a die off of vegetation combined with a warmer and more acidic hydrosphere following the eruption of the Siberian traps may have led to faster continental weathering and increased nutrient input into the oceans. The immaturity of siliciclastic sediments in the lowermost Sulphur Mountain Formation suggests rapid weathering was occurring. Thin pyrite beds have been found in latest Permian marine sediments along western Pangaea up into the Canadian Arctic (Grasby and Beauchamp, 2009). Increased nutrient inputs may have led to one or several pulses of high productivity in latest Permian coastal oceans, driving environments to extinction-causing levels of anoxia and euxinia despite the long-term trend toward slower circulation and nutrient cycling into the Triassic.

6. Conclusions

The Permian at Opal Creek records an active cold-water coastal upwelling zone that supported high productivity and a mid-water oxygen minimum zone where anaerobic respiration occurred. This system persisted for tens of millions of years only to abruptly terminate preceding the latest-Permian extinction. Despite the Panthalassic Ocean's potentially dominant role in Permian biogeochemical cycling, there have been few ways to test the impact of the latest-Permian crisis on circulation and ventilation. Here we present isotopic and trace element evidence for the cessation of coastal upwelling, a modality of oceanic circulation that leaves distinctive isotopic signatures. Despite the apparent slowdown of circulation at the end Permian, a major, discrete euxinic episode

preceded the extinction, and corresponds to a number of geochemical indicators of high productivity. A transient pulse of increased carbon export may have been necessary to drive coastal oceans toward the euxinia necessary for mass extinction.

7. Acknowledgments

The authors would like to acknowledge the generous support provided by The United States National Science Foundation (NSF) and NASA Astrobiology Institute (NAI) University of Washington node as well as the Natural Sciences and Engineering Research Council (NSERC) of Canada, and the University of Washington Earth and Space Sciences Department. Our gratitude goes out to the staff of the University of Washington IsoLab facility for their extensive help with our isotopic analyses. TJA thanks the National Science Foundation for support (EAR-0618003, EAR-0745574, and EAR-1053449). YS would like to thank the National Natural Science Foundation of China for their support (41025011).

References:

Algeo, T.J., Maynard, J.B., 2004. Trace element behavior and redox facies in core shales of Upper Pennsylvanian Kansas-type cyclothems. Chemical Geology 206, 289-318.

Algeo, T.J., Twitchett, R.J., 2010. Anomalous Early Triassic sediment fluxes due to elevated weathering rates and their biological consequences. Geology 38, 1023-1026.

Algeo, T.J., Wilkinson, B.H., Lohmann, K.C, 1992. Meteoric-burial diagenesis of Pennsylvanian carbonate: water/rock interactions and basin geothermics. Journal of Sedimentary Petrology 62, 652-670.

Algeo, T.J., Shen, Y., Zhang, T., Lyons, T., Bates, S., Rowe, H., Nguyen, T.K.T., 2008. Association of ^{34}S-depleted pyrite layers with negative carbonate δ^{13}C excursions at the Permian-Triassic boundary: Evidence for upwelling of sulfidic deep-ocean water masses. Geochemistry Geophysics Geosystems 9, Q04025, 10 pp.

Algeo, T., Rowe, H., Hower, J.C., Schwark, L., Herrmann, A., Heckel, P., 2008. Changes in ocean denitrification during Late Carboniferous glacial-interglacial cycles. Nature Geoscience 1, 709-714; doi:10.1038/ngeo307.

Algeo, T.J., Hinnov, L., Moser, J., Maynard, J.B., Elswick, E., Kuwahara, K., Sano, H., 2010. Changes in productivity and redox conditions in the Panthalassic Ocean during the latest Permian. Geology 38, 187-190; doi:10.1130/G30483.1.

Algeo, T.J., Chen, Z.Q., Fraiser, M.L., Twitchett, R.J., 2011a. Terrestrial-marine teleconnections in the collapse and rebuilding of Early Triassic marine ecosystems. Palaeogeography, Palaeoclimatology, Palaeoecology 308, 1-11.

Algeo, T.J., Kuwahara, K., Sano, H., Bates, S., Lyons, T., Elswick, E., Hinnov, L., Ellwood, B., Moser, J., Maynard, J.B., 2011b. Spatial variation in sediment fluxes, redox conditions, and productivity in the Permian-Triassic Panthalassic Ocean, Palaeogeography, Palaeoclimatology, Palaeoecology 308, 65-83 doi: 10.1016/j.palaeo.2010.07.007

Algeo, T., Henderson, C., Ellwood, B., Rowe, H., Elswick, E., Bates, S., Lyons, T., Hower, J.C., Smith, C., Maynard, J.B., Hays, L., Summons, R., Fulton, J., Freeman, K., 2012. Evidence for a diachronous Late Permian marine crisis from the Canadian Arctic region. Geological Society of America Bulletin, in press.

Averyt, K.B., Paytan, A., 2004. A comparison of multiple proxies for export production in the equatorial Pacific. Paleoceanography 19, PA4003, 14 pp.

Baublys, K. A., Golding, S. D., Young, E. and Kamber, B. S. (2004), Simultaneous determination of $\delta^{33}S_{V\text{-}CDT}$ and $\delta^{34}S_{V\text{-}CDT}$ using masses 48, 49 and 50 on a continuous flow isotope ratio mass spectrometer. Rapid Communications in Mass Spectrometry, 18: 2765–2769

Baud, A., Magaritz, M., Holser, W.T., 1989. Permian–Triassic of the Tethys: carbon isotope studies. Geologische Rundschau 78, 649–677

Beatty, T.W., Zonneveld, J.P, Henderson, C.M., 2008. Anomalously diverse Early Triassic ichnofossil assemblages in northwest Pangea: A case for a shallow-marine habitable zone. Geology 36, 771-774.

Beauchamp, B., 1994. Permian climatic cooling in the Canadian Arctic, in Klein, G.D., ed., Pangea: Paleoclimate, Tectonics and Sedimentation during Accretion, Zenith and Break-up of a Super-Continent. Geological Society of America Special Paper 288, pp. 229-246.

Beauchamp, B., Baud, A., 2002. Growth and demise of Permian biogenic chert along northwest Pangea: evidence for end-Permian collapse of thermohaline circulation. Palaeogeography, Palaeoclimatology, Palaeoecology 184, 37-63.

Beauchamp, B., Desrochers, A., 1997. Permian warm- to very cold carbonates and cherts in northwest Pangea. In: James, N.P., Clarke, J. (eds.), Cool Water Carbonates. Society of Economic Geologists and Paleontologists Special Publication 56, pp. 327-347.

Beauchamp, B., Henderson, C.M., 1994. The Lower Permian (Artinskian) Raanes, Great Bear Cape, and Trappers Cove formations, Sverdrup Basin, Canadian Arctic: Stratigraphy and conodont zonation. Bulletin of Canadian Petroleum Geology 42, 565-600.

Beauchamp, B., Henderson, C.M., Grasby, S.E., Gates, L.T., Beatty, T.W., Utting, J., James, N.P. 2009. Late Permian sedimentation in the Sverdrup Basin, Canadian Arctic: the Lindström and Black Stripe Formations. Bulletin of Canadian Petroleum Geology 57, 167-191.

Becker, L., Poreda, R.J., Hunt, A.G., Bunch, T.E., Rampino, M. 2001. Impact event at the Permian-Triassic boundary: evidence from extraterrestrial noble gases in fullerenes. Science 291, 1530-1533.

Bensing, J.P., James, N.P., Beauchamp, B., 2008. Carbonate deposition during a time of mid-latitude ocean cooling: Early Permian "subtropical" sedimentation in the Sverdrup Basin, Arctic Canada. Journal of Sedimentary Research 78, 2-15.

Benton, M.J., Tverdokhlebov, V.P, Surkov, M.V., 2004. Ecosystem remodeling among vertebrates at the Permian-Triassic boundary in Russia. Nature 432, 97-100.

Benton, M.J., Twitchett, R.J., 2003. How to kill (almost) all life: the end-Permian extinction event. Trends in Ecology and Evolution, 18 No.7 July 2003.

Berner, R.A., 1984. Sedimentary pyrite formation: an update. Geochimica et Cosmochimica Acta 48, 605-615.

Berner, R.A., 2002. Examination of hypotheses for the Permo-Triassic boundary extinction by carbon cycle modeling. Proceedings of the National Academy of Sciences (U.S.A.) 99, 4172-4177.

Berner, R.A., Kothavala, Z., 2001. GEOCARB III: a revised model of atmospheric CO_2 over Phanerozoic time. American Journal of Science 301, 182-204.

Berner, R.A., Raiswell, R., 1983. Burial of organic carbon and pyrite sulfur in sediments over Phanerozoic time: a new theory. Geochimica et Cosmochimica Acta 47, 855-862.

Bottjer, D.J., Clapham, M.E., Frasier, M.L., Powers, C.M., 2008. Understanding mechanisms for the end-Permian mass extinction and the protracted Early Triassic aftermath and recovery. GSA Today 18, 4-10.

Brasier, M.D., 1995. Fossil indicators of nutrient levels, 1. Eutrophication and climate change. Geological Society of London Special Publications 83, pp. 113-132.

Brookfield, M.E., Twitchett, R.J., Goodings, C., 2003. Palaeoenvironments of the Permian Triassic transition sections in Kashmir, India. Palaeogeography, Palaeoclimatology, Palaeoecology 198, 353-371.

Canfield, D.E., Thamdrup, B., 1994. The production of ^{34}S-depleted sulfide during bacterial disproportionation of elemental sulfur. Science 266, 1973-1975

Chambers, L.A., Trudinger, P.A., 1979. Microbiological fractionation of stable sulfur isotopes: A review and critique. Geomicrobiological Journal 1, 249-293.

Chen, J., Beatty, T.W., Henderson, C.M., Rowe, H., 2009. Conodont biostratigraphy across the Permian-Triassic boundary at the Dawen section, Great Bank of Guizhou, Guizhou Province, South China: Implications for the Late Permian extinction and correlation with Meishan. Journal of Asian Earth Sciences 36, 442-458.

Clark, D.L., 1959. Conodonts from the Triassic of Nevada and Utah. Journal of Paleontology 33, 305-312.

Cohen, A. S., Coe, A. L., Bartlett, J. M., Hawkesworth, C. J., 1999: Precise Re-Os ages of organic-rich mudrocks and the Os isotope composition of Jurassic seawater. Earth and Planetary Science Letters 167, 159-173.

Dehairs, F., Chesselet, R., Jedwab, J., 1980. Discrete suspended particles of barite and the barium cycle in the open ocean. Earth and Planetary Science Letters 49, 528-550.

Erwin, D.H., Bowring, S.A., Jin, Y.-G., 2002. End-Permian mass-extinctions: A review. In: Koeberl, C., MacLeod, K.G. (Eds.), Catastrophic Events and Mass Extinctions: Impacts and Beyond. Geological Society of America Special Paper 356, pp. 353-383.

Fraiser, M.L., Bottjer, D.J., 2007. Elevated atmospheric CO_2 and the delayed biotic recovery from the end-Permian mass extinction. Palaeogeography, Palaeoclimatology, Palaeoecology 252, 164-175.

Fry, B., Silva, S. R., Kendall, C., Anderson, R. K. 2002, Oxygen isotope corrections for online $\delta^{34}S$ analysis. Rapid Communications in Mass Spectrometry, 16: 854–858

Gates, L.M., James, N.P., Beauchamp, B., 2004. A glass ramp: Shallow-water Permian spiculitic chert sedimentation, Sverdrup Basin, Arctic Canada. Sedimentary Geology 168, 125-147.

Georgiev, S., Stein, H.J., Hannah, J.L., Bingen, B., Weiss, H.M., Piasecki, S. 2011. Hot acidic Late Permian seas stifle life in record time. Earth and Planetary Science Letters 310, 389-400.

Gibson, D.W., 1969. Triassic stratigraphy of the Bow River-Crowsnest Pass region, Rocky Mountains of Alberta and British Columbia. Geological Survey of Canada, Paper 68, 29, 48.

Gibson, D.W., 1974. Triassic rocks of the Southern Canadian Rocky Mountains. Geological Survey of Canada, Bulletin 230, 65.

Gibson, D.W., Barclay, J.E., 1989. Middle Absaroka Sequence, The Triassic Stable Craton. In: Ricketts, B. (ed.) Basin Analysis --The Western Canada Sedimentary Basin, Canadian Society of Petroleum Geologists Special Publication, pp. 219-231.

Goldhaber, M.B., Kaplan I.R., 1974. The sulfur cycle. In: Goldberg, E.D. (ed.), The Sea, vol. 5. Wiley, pp. 569-655.

Grasby, S.E., Beauchamp, B., 2009. Latest Permian to Early Triassic basin-to-shelf anoxia in the Sverdrup Basin, Arctic Canada. Chemical Geology 264, 232-246.

Grice, K., Cao, C., Love, G.D., Bottcher, M.E., Twitchett, R.J., Grosjean, E., Summons, R.E., Turgeon, S.C., Dunning, W., Jin, Y., 2005. Photic zone euxinia during the Permian-Triassic superanoxic event. Science 307, 706-709.

Habicht, K.S., Canfield, D.E., 2001. Isotope fractionation by sulfate-reducing natural populations and the isotopic composition of sulfide in marine sediments. Geology 29, 555-558.

Haq, B.U., Schutter, S.R., 2008. A chronology of Paleozoic sea-level changes. Science 322, 64–68.

Hays, L.E., Beatty, T., Henderson, C.M., Love, G.D., Summons, R.E., 2007. Evidence for photic zone euxinia through the end-Permian mass extinction in the Panthalassic Ocean (Peace River Basin, Western Canada). Palaeoworld 16, 39-50.

Henderson, C.M., 1989. Absaroka Sequence - The Lower Absaroka Sequence: Upper Carboniferous and Permian (Chapter 10). In: Ricketts, B. (ed.) Basin Analysis - The Western Canada Sedimentary Basin, Canadian Society of Petroleum Geologists Special Publication, pp. 203-217.

Henderson, C.M., 1997. Uppermost Permian conodonts and the Permian-Triassic boundary in the Western Canada Sedimentary Basin. Bulletin of Canadian Petroleum Geology 45, 693-707.

Henderson, C.M., 2006. Beware of your FO and be aware of the FAD. Permophiles 47, 8-9.

Henderson, C.M., Baud, A., 1997. Correlation of the Permian-Triassic boundary in Arctic Canada and comparison with Meishan, China, in Proceedings of the 30th International Geological Congress, v. 11, VSP Scientific Publishers, pp. 143-152.

Henderson, C.M., Mei, S., 2007. Geographical clines in Permian and Lower Triassic gondolellids and its role in taxonomy. Palaeoworld 16, 190-201.

Henderson, C.M., Richards, B.C., Barclay, J.E., 1994. Permian. In: Mossop, G.D. (ed.) Geological Atlas of the Western Canada Sedimentary Basin Joint publication of the Canadian Society of Petroleum Geologists and the Alberta Research Council, pp. 251-258.

Horan, M.F., Walker, R.J., Fedorenko, V.A., Czamanske, G.K. 1995. Osmium and neodymium isotopic constraints on the temporal and spatial evolution of Siberian flood basalt sources. Geochimica et Cosmochimica Acta 59, 5159–5168

Hotinski, R.M., Bice, K.L., Kump, L.R., Najjar, R.G., Arthur, M.A., 2001. Ocean stagnation and end-Permian anoxia. Geology 29, 7-10.

Huey, R.B., Ward, P.D., 2005. Hypoxia, global warming, and terrestrial Late Permian extinctions. Science 308, 398-401.

Hunt, J.M., 1996. Petroleum Geochemistry and Geology, 2nd ed., W.H. Freeman, New York, 743 pp.

Isozaki, Y., 1994. Superanoxia across the Permo–Triassic boundary: record in accreted deep-sea pelagic chert in Japan. In: Embry, A.F., Beauchamp, B., Glass, D.J. (eds.), Pangea: Global Environments and Resources. Canadian Society of Petroleum Geologists, Memoir, vol. 17, pp. 805–812.

Isozaki, Y., 1997. Permo-Triassic boundary superanoxia and stratified superocean: records from lost deep-sea. Science 276, 235-238.

Isozaki, Y., Kawahata, H., Ota, A., 2007. A unique carbon isotope record across the Guadalupian-Lopingian (Middle-Upper Permian) boundary in mid-oceanic paleo-atoll carbonates: The high-productivity "Kamura event" and its collapse in Panthalassa. Global and Planetary Change 55, 21-38.

Jenkyns, H.C., Gröcke, D.R., Hesselbo, S.P., 2001. Nitrogen isotope evidence for water mass denitrification during the early Toarcian (Jurassic) oceanic anoxic event. Paleoceanography 16, 593-603.

Jiang, H., Lai, X., Luo, G., Aldridge, R., Zhang, K., Wignall, P., 2007. Restudy of conodont zonation and evolution across the P/T boundary at Meishan section, Changxing, Zhejiang, China. Global and Planetary Change 55, 39-55.

Jin, Y.G., Wang, Y., Wang, W., Shang, Q.H., Cao, C.Q., Erwin, D.H., 2000. Pattern of marine mass extinction near the Permian Triassic boundary in South China. Science 289, 432-436.

Kashiyama Y., Ogawa, N.O., Kuroda, J., Shiro M., Nomoto S., Tada R., Kitazato H., Ohkouchi N., 2008. Diazotrophic cyanobacteria as the major photoautotrophs during mid-Cretaceous oceanic anoxic events: Nitrogen and carbon isotopic evidence from sedimentary porphyrin. Organic Geochemistry 39, 532-549.

Kidder, D.L., Worsley, T.R., 2003. Late Permian warming, the rapid latest Permian transgression, and the Permo-Triassic extinction, 2003 GSA Annual Meeting: Seattle, WA.

Kidder, D.L., Worsley, T.R., 2004. Causes and consequences of extreme Permo-Triassic warming to globally equable climate and relation to the Permo-Triassic extinction and recovery. Palaeogeography, Palaeoclimatology, Palaeoecology 203, 207-237.

Kiehl, J.T., Shields, C.A., 2005. Climate simulation of the latest Permian: implications for mass extinction. Geology 33, 757-760.

Kim, S.T., O'Neil, J. R.. 1997. Equilibrium and nonequilibrium oxygen isotope effects in synthetic carbonates. Geochimica et Cosmochimica Acta 61, 3461-3475.

Knoll, A.H., Bambach, R.K., Canfield, D.E., Grotzinger, J.P., 1996. Comparative Earth history and Late Permian mass extinction. Science 273, 452-457.

Korte, C., Kozur, H.W., 2010. Carbon-isotope stratigraphy across the Permian-Triassic boundary: A review. Journal of Asian Earth Sciences, doi:10.1016/j.jseaes.2010.01.005

Korte, C., Pande, P., Kalia, P., Kozur, H.W., Joachimski, M., Oberhänsli. H., 2010. Massive volcanism at the Permian–Triassic boundary and its impact on the isotopic composition of the ocean and atmosphere. Journal of Asian Earth Sciences 37, 293-311.

Kozur, H.W., 2005. Pelagic uppermost Permian and Permian-Triassic boundary conodonts of Iran. Part II: investigated sections and evaluation of the conodont faunas. Hallesches Jahrbuch Fur Geowissenschaften, Reihe B: Geologie, Palaontologie, Mineralogie, 19, 49-86.

Krull, E.S., Retallack, G.J., Campbell, H.J., Lyon, G.L.., 2000. $\delta^{13}C_{org}$ chemostratigraphy of the Permian-Triassic boundary in the Maitai Group, New Zealand: Evidence for high-latitudinal methane release. New Zealand Journal of Geology and Geophysics 43, 21-32.

Kump, L.R., Pavlov, A., Arthur, M.A., 2005. Massive release of hydrogen sulfide to the surface ocean and atmosphere during interval of oceanic anoxia. Geology 33, 397-400.

Looy, C.V., Twitchett, R.J., Dilcher, D.L., van Konijnenburg-van Cittert, J.H.A., Visscher, H., 2001. Life in the end-Permian dead zone. Proceedings of the National Academy of Sciences (U.S.A.) 98, 7879-7883.

Luo, G., Kump, L.R., Wang, Y., Tong, J., Arthur, M.A., Yang, H., Huang, J., Yin, H., Xie, S., 2010. Isotopic evidence for an anomalously low oceanic sulfate concentration following end-Permian mass extinction. Earth and Planetary Science Letters 300, 101-111.

Luo, G., Wang, Y., Kump, L.R., Bai, X., Algeo, T.J., Yang, H., Xie, S., 2011. Enhanced nitrogen fixation in the immediate aftermath of the latest Permian marine mass extinction. Geology, v. 39, p. 647-650.

Lyons, T.W., 1997. Sulfur isotopic trends and pathways of iron sulfide formation in upper Holocene sediments of the anoxic Black Sea. Geochimica et Cosmochimica Acta 61, 3367-3382.

McLennan, S.M., 2001. Relationships between the trace element composition of sedimentary rocks and upper continental crust. Geochemistry Geophysics Geosystems, 2, GC000109, 24 pp.

Mei, S., 1996. Restudy of conodonts from the Permian-Triassic boundary beds at Selong and Meishan and the natural Permian-Triassic boundary. In: Wang, H. and Wang, X. (eds.). Memorial Volume of Prof. Sun Yunzhu: Palaeontology and Stratigraphy. Centennial China University of Geosciences Press, Wuhan, pp. 141-148.

Mei, S., Henderson, C.M. 2001. Evolution of Permian conodont provincialism and its significance in global correlation and paleoclimatic implication. Palaeogeography, Palaeoclimatology, Palaeoecology 170, 237-260.

Mei, S.L., Zhang, K.X., Wardlaw, B.R., 1998. A refined succession of Changhsingian and Griesbachian neogondolellid conodonts from the Meishan section, candidate of the global stratotype section and point of the Permian-Triassic boundary. Palaeogeography, Palaeoclimatology, Palaeoecology 143, 213-226.

Meyer, K.M., Kump, L.R., 2008. Oceanic euxinia in Earth history: Causes and consequences. Annual Review of Earth and Planetary Sciences 36, 251-288.

Meyer, K.M., Ridgwell, A., and Kump, L.R., 2008. Biogeochemical controls on photic zone euxinia during the end-Permian mass extinction. Geology 36(9), 747-750.

Meyer, K.M., Yu, M., Jost, A.B., Kelley, B.M., Payne, J.L., 2011. $\delta^{13}C$ evidence that high primary productivity delayed recovery from end-Permian mass extinction. Earth and Planetary Science Letters 302, 378-384.

Musashi, M., Isozaki, Y., Koike, T., Kreulen, R., 2001. Stable carbon isotope signature in mid-Panthalassa shallow-water carbonates across the Permo-Triassic boundary: evidence for ^{13}C-depleted superocean. Earth and Planetary Science Letters 191, 9-20.

Newton, R.J., Pevitt, E.L., Wignall, P.B., Bottrell, S.H., 2004. Large shifts in the isotopic composition of seawater sulphate across the Permo-Triassic boundary in northern Italy. Earth and Planetary Science Letters 218, 331-345.

Nielsen, J.K., Shen, Y., 2004. Evidence for sulfidic deep water during the Late Permian in the East Greenland Basin. Geology 32, 1037-1040.

Ogg, J. G., Ogg, G., Gradstein, F.M. 2008. The Concise Geologic Time Scale, Cambridge University Press

O'Leary, M.H., 1981. Carbon isotope fractionation in plants. Phytochemistry 20, 553-567.

O'Leary, M. H., 1988. Carbon isotopes in photosynthesis. Bioscience 38, 328-336.

Orchard, M.J., Krystyn, L., 1998. Conodonts of the lowermost Triassic of Spiti, and new zonation based on Neogondolella successions. Revista Italiana di Paleontologia Stratigraphia 104 (3), 341-368.

Orchard, M.J., Nassichuk, W.W., Rui, L., 1994. Conodonts from the Lower Griesbachian Otoceras latilobatum bed of Selong, Tibet and the position of the P-T boundary. Canadian Society of Petroleum Geologists. Proceedings of Pangea Conference Memoir, vol. 17, pp. 823-843.

Payne, J.L., Kump, L.R., 2007. Evidence for recurrent Early Triassic massive volcanism from quantitative interpretation of carbon isotope fluctuations. Earth and Planetary Science Letters 256, 264-277.

Payne, J.L., Lehrmann, D.J., Wei, J., Orchard, M.J., Schrag, D.P., Knoll, A.H., 2004. Large perturbations of the carbon cycle during recovery from the end-Permian extinction. Science 305, 506-509.

Peucker-Ehrenbrink, B., Ravizza, G., 2000. The marine osmium isotope record. Terra Nova 12, 205-219.

Radke, M., Welte, D.H., Willsch, H., 1982. Geochemical study on a well in the Western Canada Basin: relation of the aromatic distribution pattern to maturity of organic matter. Geochimica et Cosmochimica Acta 46, 1-10.

Raup, D.M., Sepokoski, J.J., 1982. Mass extinction in the marine fossil record. Science 215, 1501-1503.

Reichow, M.K., Pringle, M.S., Al'Mukhamedov, A.I., Allen, M.B., Andreichev, V.L., Buslov, M.M., Davies, C.E., Fedoseev, G.S., Fitton, J.G., Inger, S., Medvedev, A.Y., Mitchell, C., Puchkov, V.N., Safanova, I.Y., Scott, R.A., Saunders, A.D., 2009. The timing and extent of the eruption of the Siberian Traps large igneous province: Implications for the end-Permian environmental crisis. Earth and Planetary Science Letters 277, 9-20.

Reid, C.M., James, N.P., Beauchamp, B., Kyser, T.K., 2007. Faunal turnover and changing oceanography: late Palaeozoic warm-to-cool water carbonates, Sverdrup Basin, Canadian Arctic Archipelago. Palaeogeography, Palaeoclimatology, Palaeoecology 249, 128-159.

Retallack, G.J., 1999. Postapocalyptic greenhouse paleoclimate revealed by earliest Triassic paleosols in the Sydney Basin, Australia. Geol. Soc. Am. Bull. 111, 52-70.

Retallack, G.J., Jahren, A.H., 2008. Methane release from igneous intrusion of coal during Late Permian extinction events. Journal of Geology 116, 1-20.

Retallack, G.J., Smith, R.M.H., Ward, P.D., 2003. Vertebrate extinction across the Permian–Triassic boundary in Karoo Basin, South Africa. Geological Society of America Bulletin 115, 1133-1152.

Riccardi, A.L., Arthur, M.A., Kump, L.R., 2006. Sulfur isotopic evidence for chemocline upward excursions during the end-Permian mass extinction. Geochimica et Cosmochimica Acta 70, 5740-5752.

Richards, B.C., 1989. Upper Kaskaskia Sequence: Uppermost Devonian and Lower Carboniferous. In: Ricketts, B. (ed.) Basin Analysis - The Western Canada Sedimentary Basin, Canadian Society of Petroleum Geologists Special Publication, pp. 165-201.

Rooney, A.D., Selby, D., Houzay, J-P., Renne, P.R., 2010. Re-Os geochronology of Mesoproterozoic sediments from the Taoudeni basin, Mauritania: Implications for basin-wide correlations, supercontinent reconstruction and Re-Os systematics of organic-rich sediments. Earth and Planetary Science Letters 289, 486-496.

Sano, H., Kuwahara, K., Yao, A., Agematsu, S., 2010. Panthalassic seamount-associated Permian-Triassic boundary siliceous rocks, Mino terrane, central Japan. Paleontological Research 14, 293-314.

Schoepfer, S.D., Henderson, C.M., Garrison, G.H., Ward, P.D. 2012 Cessation of a productive coastal upwelling system in the Panthalassic Ocean at the Permian–Triassic Boundary, Palaeogeography, Palaeoclimatology, Palaeoecology 313–314, 181-188

Seitzinger, S., Harrison, J.A., Böhlke, J.K., Bouwman, A.F., Lowrance, R., Peterson, B., Tobias, C., Van Drecht, G., 2006. Denitrification across landscapes and waterscapes: a synthesis. Ecological Applications 16, 2064–2090.

Selby, D.A., Creaser, R.A., 2003. Re-Os geochronology of organic rich sediments: an evaluation of organic matter analysis methods. Chemical Geology 200, 225-240.

Selby, D. 2007. Direct rhenium-osmium age of the oxfordian-kimmeridgian boundary, Staffin Bay, Isle of Skye, UK and the Late Jurassic geologic timescale. Norwegian Journal of Geology, 87, 291-299.

Sephton, M.A., Looy, C.V., Brinkhuis, H., Wignall, P.B., de Leeuw, J.W., Visscher, H. 2005 Catastrophic soil erosion during the end-Permian biotic crisis. Geology 33, 941-944

Shen, S., Cao, C., Henderson, C.M., Wang, X., Shi, G.R., Wang, Y. and Wang, W., 2006. End-Permian mass extinction pattern in the northern peri-Gondwanan region. Palaeoworld 15, 3-30.

Shen, S.Z., Crowley, J.L., Wang, Y., Bowring, S.A., Erwin, D.H., Sadler, P.M., Cao, C.Q., Rothman, D.H., Henderson, C.M., Ramezani, J., Zhang, H., Shen, Y., Wang, X.D., Wang, W., Mu, L., Li, W.Z., Tang, Y.G., Liu, X.L., Liu, L.J., Zeng, Y., Jiang, Y.F., Jin, Y.-G. 2011. Calibrating the end-Permian mass extinction. Science 334, 1367-1372.

Shen, S.Z., Henderson, C.M., Bowring, S.A., Cao, C.Q., Wang, Y., Wang, W., Zhang, H., Zhang, Y.C., Mu, L., 2010. High-resolution Lopingian (Late Permian) timescale of South China. Geological Journal 45, 122-134.

Shen, Y., Farquhar, J., Zhang, H., Masterson, A., Zhang, T., Wing, B.A., 2011. Multiple S-isotopic evidence for episodic shoaling of anoxic water during Late Permian mass extinction. Nature Communications 2:210, doi: 10.1038/ncomms1217

Smoliar, M. I., Walker, J.R., Morgan, J.W. 1996. Re-Os isotope constraints on the age of Group IIA, IIIA, IVA, and IVB iron meteorites. Science 271, 1099-1102.

Song, H.Y., Tong, J.N., Algeo, T.J., Qiu, H.O., Song, H.J., Tian, L., Chen, Z.Q., in review. Large shallow-to-deep $\delta^{13}C$ gradients in Early Triassic seas of the South China craton: Evidence for elevated primary productivity and its role in sustaining oceanic anoxia and delaying marine ecosystem recovery following the end-Permian mass extinction. Global and Planetary Change, submitted October 2011.

Song, H.Y., Tong, J.N., Algeo, T.J., Song, H.J., in review. Coupling of the marine carbon and sulfur cycles during the Early Triassic. Nature Geoscience, submitted November 2011.

Strauss, H., 1999. Geological evolution from isotope proxy signals—sulfur. Chemical Geology 161, 89-101.

Sweet, W.C., 1970. Uppermost Permian and Lower Triassic conodonts of the Salt Range and Trans-Indus Ranges — West Pakistan. In: Kummel, B., Teichert, C. (eds.), Stratigraphic Boundary Problems: Permian and Triassic of West Pakistan. University of Kansas, Special Publications, vol. 4, pp. 207-275.

Taylor, E.T., Taylor, T.N., Cúeno, R., 2000. Permian and Triassic high latitude paleoclimates: evidence from fossil biotas. In: Huber, B., Macleod, K. (eds.) Warm Climates in Earth History: Cambridge, Cambridge University Press, pp. 321-350.

Tissot, B.P., Welte, D.H., 1984. Petroleum Formation and Occurrence, 2nd ed., Springer, Berlin, 699 pp.

Tribovillard, N., Algeo, T.J., Lyons, T., Riboulleau, A., 2006. Trace metals as paleoredox and paleoproductivity proxies: An update. Chemical Geology 232, 12-32.

Twitchett, R.J., Wignall, P.B., 1996. Trace fossils and the aftermath of the Permo-Triassic mass extinction: evidence from northern Italy. Palaeogeography, Palaeoclimatology, Palaeoecology 124, 137-151.

Utting, J., Zonneveld, J.P., MacNaughton, R.B., Fallas, K.M., 2005. Palynostratigraphy, lithostratigraphy and thermal maturity of the Lower Triassic Toad and Grayling, and Montney formations of western Canada, and comparisons with coeval rocks of the Sverdrup Basin, Nunavut. Bulletin of Canadian Petroleum Geology 63, 5-24.

Ward, P.D., Montgomery, D.R., Smith, R., 2000. Altered river morphology in South Africa related to the Permian-Triassic extinction. Science 289, 1740-1743.

Ward, P.D., Botha, J., Buick, R., De Kock, M.O., Erwin, D.H., Garrison, G., Kirschvink, J., Smith, R., 2005. Abrupt and Gradual Extinction Among Late Permian Land Vertebrates in the Karoo Basin, South Africa. Science 307, 709-714.

Werne, J.P., Lyons, T.W., Hollander, D.J., Formolo, M.J., Sinninghe Damsté, J.S., 2003. Reduced sulfur in euxinic sediments of the Cariaco Basin: sulfur isotope constraints on organic sulfur formation. Chemical Geology 195, 159-179.

White, R.V., 2002. Earth's biggest 'whodunnit': unravelling the clues in the case of the end-Permian mass extinction: Philosophical Transactions of the Royal Society of London, Series B, 360, 2963-2985.

Wignall, P.B., 2007. The End-Permian mass extinction—how bad did it get? Geobiology 5, 303-309.

Wignall, P.B., Hallam, A., 1992. Anoxia as a cause of the Permian/Triassic mass extinction: facies evidence from northern Italy and the western United States. Palaeogeography, Palaeoclimatology, Palaeoecology 93, 21-46.

Wignall, P.B., Hallam, A., 1993. Griesbachian (Earliest Triassic) palaeoenvironmental changes in the Salt Range, Pakistan and southeast China and their bearing on the Permo-Triassic mass extinction. Palaeogeography, Palaeoclimatology, Palaeoecology 102, 215-237.

Wignall, P.B., Newton, R., 1998. Pyrite framboid diameter as a measure of oxygen deficiency in ancient mudrocks. American Journal of Science 298, 537-552.

Wignall, P.B., Newton, R. 2003. Contrasting deep-water records from the Upper Permian and Lower Triassic of South Tibet and British Columbia: evidence for a diachronous mass extinction. Palaios 18, 153-167.

Wignall, P.B., Twitchett, R.J., 1996. Oceanic anoxia and the end Permian mass extinction. Science 272, 1155-1158.

Wignall, P.B., Twitchett, R.J., 2002. Extent, duration, and nature of the Permian-Triassic superanoxic event. In: Koeberl, C., MacLeod, K.G. (eds.), Catastrophic Events and Mass Extinctions: Impacts and Beyond. Geological Society of America Special Paper 356, pp. 395-413.

Wilkin, R.T., Arthur, M.A., 2001. Variations in pyrite texture, sulfur isotope composition, and iron systematics in the Black Sea: Evidence for late Pleistocene to Holocene excursions of the O2-H2S redox transition. Geochimica et Cosmochimica Acta 65, 1399-1416.

Wilkin, R.T., Barnes, H.L., Brantley, S.L., 1996. The size distribution of framboidal pyrite in modern sediments: an indicator of redox conditions. Geochimica et Cosmochimica Acta 60, 3897-3912.

Winguth, A.M.E., Heinze, C., Kutzbach, J. E., Maier-Reimer, E., Mikolajewicz, U., Rowley, D., Rees, A., and Ziegler, A. M., 2002. Simulated warm polar currents during the middle Permian, Paleoceanography 17(4), 1057, doi:10.1029/2001PA000646.

Winguth, A.M.E., Maier-Reimer, E., 2005. Causes of marine productivity and oxygen changes associated with the Permian-Triassic boundary: A reevalution with ocean general circulation models. Marine Geology 217, 283-304.

Yin, H.F., Sweet, W.C., Glenister, B.F., Kotlyar, G., Kozur, H., Newell, N.D., Sheng, J.Z., Yang, Z.Y., Zakharov, Y.D., 1996. Recommendation of the Meishan section as Global Stratotype Section and Point for basal boundary of Triassic system. Newsletter on Stratigraphy 34, 81-108.

Yin, H.F., Zhang, K.X., Tong, J.N., Yang, Z.Y., Wu, S.B., 2001. The Global Stratotype Section and Point (GSSP) of the Permian–Triassic boundary. Episodes 24, 102-114.

Zhang, K., Tong, J., Shi, G.R., Lai, X., Yu, J., He, W., Peng, Y., Jin, Y., 2007. Early Triassic conodont-palynological biostratigraphy of the Meishan D section in Changxing, Zhejiang Province, South China. Palaeogeography, Palaeoclimatology, Palaeoecology 252, 4-23.

Ziegler A.M., Gibbs M.T., Hulver M.L., 1998. A mini-atlas of oceanic water masses in the Permian period. Proceedings of the Royal Society of Victoria 110 (1/2), 323–343.

Chapter III: Total organic carbon, organic phosphorus, and biogenic barium fluxes as proxies for paleomarine productivity

Accepted for publication at Earth Science Reviews, May 2014

Contributing Authors: Shane D. Schoepfer[1], Jun Shen[2,3], Hengye Wei[3,4], Richard V. Tyson[5], Ellery Ingall[6], and Thomas J. Algeo[2,3]

Author Affiliations:

[1] Department of Earth and Space Sciences, University of Washington, Seattle, WA 98195, U.S.A.

[2] State Key Laboratory of Geological Processes and Mineral Resources, China University of Geosciences, Wuhan, Hubei, 430074, P.R. China

[3] Department of Geology, University of Cincinnati, Cincinnati, Ohio 45221-0013, U.S.A.

[4] Department of Earth Science, East China Institute of Technology, Nanchang, Jiangxi, 330013, P.R. China

[5] GETECH, Kitson House, Elmete Hall, Elmete Lane, Leeds LS8 2LJ, United Kingdom

[6] School of Earth and Atmospheric Sciences, Georgia Institute of Technology, Atlanta, Georgia 30332, U.S.A.

Abstract:

Although marine productivity is a key parameter in the global carbon cycle, reliable estimation of productivity in ancient marine systems has proven difficult. In this study, we evaluate the accumulation rates of three commonly used proxies for productivity from a set of primarily Quaternary sediment cores at 94 marine sites, compiled from 37 published sources. For each core, mass accumulation rates were calculated for total organic carbon (TOC), organic phosphorus (P_{org}), and biogenic barium (Ba_{bio}). Calculated mass accumulation rates were compared to two independent estimates of modern regional primary productivity and export productivity, as well as to two potential controlling variables, bulk accumulation rate (BAR) and redox environment. BAR was found to exercise a strong control on the preservation of organic carbon. The linear regression equations relating preservation factor to BAR can be transformed to yield equations for primary and export production as a function of TOC and BAR, two variables that can be readily measured or estimated in paleomarine systems. Paleoproductivity can also be estimated from empirical relationships between elemental proxy fluxes and modern productivity rates. Although these equations do not attempt to correct for preservation, organic carbon and phosphorus (but not barium) accumulations rates were found to exhibit a systematic relationship to primary and export production. All of the paleoproductivity equations developed here have a large associated uncertainty and, so, must be regarded as yielding order-of-magnitude estimates.

Relationships between proxy fluxes and BAR provide insights regarding the dominant influences on each elemental proxy. Increasing BAR exerts (1) a strong preservational effect on organic carbon that is substantially larger in oxic facies than in

suboxic/anoxic facies, (2) a weak clastic-dilution effect that is observable for organic phosphorus (but not for organic carbon or biogenic barium, owing to other dominant influences on these proxies), and (3) a large negative effect on biogenic barium that is probably due to reduced uptake of barium at the sediment-water interface. These effects became evident through analysis of our globally integrated dataset; analysis of individual marine sedimentary units most commonly reveals autocorrelations between elemental proxy fluxes and BAR as a result of the latter being a factor in the calculation of the former. We conclude that organic carbon and phosphorus fluxes have considerable potential as widely useful paleoproductivity proxies, but that the applicability of biogenic barium fluxes may be limited to specific oceanic settings.

1. Introduction

Organic productivity is a fundamental parameter of all marine ecosystems, playing a pivotal role in ecological dynamics, environmental redox conditions, and the cycling of carbon, nitrogen, phosphorus, and other nutrient elements. In the modern open ocean, the main primary producers are single-celled phytoplankton in the surface mixed layer (Levinton, 2008). Some phytoplankton, e.g., calcareous coccolithophores and siliceous diatoms, produce mineralized tests whose fluxes to the sediment can be used as productivity proxies (e.g., Kinkel et al., 2000; Rageneau et al., 2000). Although biogenic sediments are common in the Paleozoic and early Mesozoic pelagic ocean, mainly as radiolarites (e.g., Hori, 1992; Algeo et al., 2010), mineralized phytoplankton did not become common until the Triassic, and phytoplankton tests did not become a dominant component of marine sediments until the Cretaceous (Martin, 1995; Ridgwell, 2005).

Even in the modern ocean, many marine algae lack mineralized tests (Tomas, 1997) and contribute only amorphous organic matter (AOM) to the sediment (Taylor et al., 1998). In regions dominated by non-mineralized algae, productivity has been estimated on the basis of geochemical proxies such as total organic carbon (TOC), organic phosphorus (P_{org}), and biogenic barium (Ba_{bio}) (Tribovillard et al., 2006; Calvert and Pedersen, 2007).

The utility of TOC, P_{org}, and Ba_{bio} as paleomarine productivity proxies depends on a dominantly marine source of organic matter and favorable conditions for preservation in the sediment. Carbon and phosphorus have the advantages of being major components of marine algal biomass and having few other sources in open-ocean settings. The only other significant source of either component to marine sediments is terrestrial organic matter, which is prevalent mainly in coastal areas (Hedges and Parker, 1976; Showers and Angle, 1986). Preservation factors (PF) for organic carbon (i.e., the fraction of primary production preserved in the sediment) can be as high as 30% in reducing facies but are commonly far lower ($\leq$1%) in oxic facies (Canfield, 1994; Tyson, 2005). On the other hand, burial efficiencies (BE; i.e., the fraction of the organic carbon sinking flux preserved in the sediment) are typically in the range of 10-50% (Canfield, 1994; Tyson, 2005) and, thus, can be more reliably estimated for paleomarine systems (Algeo et al., 2013). P_{org} is preferentially recycled back into the water column under reducing conditions (Van Cappellen and Ingall, 1994) but can be effectively retained within the sediment under oxic to suboxic conditions (Föllmi, 1996; Algeo and Ingall, 2007). The utility of Ba_{bio} as a productivity proxy is ascribed to the close relationship between the production of authigenic barite and the decay of organic matter in contact with seawater, which is the source of Ba_{bio} (Paytan and Griffith, 2007). An advantage of

this proxy is that the mineral barite is relatively resistant to dissolution under oxic to suboxic conditions, providing a means of estimating export production in non-reducing paleomarine systems. Because of the incomplete preservation of all of these components in marine sediments, estimates based on measured concentrations represent minimum values of both primary productivity (i.e., the flux of carbon fixed from the atmosphere into the surface ocean) and export productivity (i.e., the flux of carbon from the surface mixed layer to the thermocline region of the ocean).

In this contribution, we undertake an analysis of TOC, P_{org}, and Ba_{bio} fluxes in modern marine settings with the goal of evaluating their utility as paleoproductivity proxies. To this end, we (1) calculated the fluxes of TOC, P_{org}, and Ba_{bio} in a range of modern marine settings, (2) compared these data with estimates of primary and export productivity for each setting, and (3) evaluated the relative influences of productivity versus preservation (which is closely related to sediment bulk accumulation rates) on the accumulation of TOC, P_{org}, and Ba_{bio}.

In a companion paper in this volume by Shen et al. (2014), the findings of the present study are applied to an analysis of productivity variations during the Permian-Triassic transition, the most severe biodiversity crisis of the Phanerozoic (Erwin et al., 2002). While marine anoxia is widely agreed to have played a major role in the extinction (Isozaki, 1997; Wignall and Newton, 2003), models suggest this could not have occurred without a substantial increase in marine export production (Hotinski et al., 2001; Winguth and Winguth, 2012).

2. Paleoproductivity proxies

2.1. General considerations

A variety of geochemical proxies have been used to reconstruct past changes in biological productivity, including methods based on C and N isotopes, organic biomarkers, and trace metal (Cu, Ni, Cd, Zn) abundances (see reviews in Tribovillard et al., 2006, and Calvert and Pedersen, 2007). Each proxy is affected by a host of environmental factors such as temperature, redox conditions, and ocean circulation, in addition to factors that influence the composition and structure of marine ecosystems (Tribovillard et al., 2006). Since all paleoproductivity proxies are subject to substantial uncertainties and no single proxy is inherently reliable under all conditions, it is generally advisable to make paleoproductivity estimates based on multiple proxies (Averyt and Paytan, 2004). In this study, we focus on TOC, P_{org}, and Ba_{bio}, which are among the most widely used paleoproductivity proxies.

Inferences concerning productivity in paleomarine systems are commonly based on fluxes rather than concentration data (e.g., Algeo et al., 2011, 2013). The amounts of TOC, P_{org}, and Ba_{bio} in a sedimentary succession are not good proxies for productivity because minor-component concentrations are strongly influenced by site-specific sediment accumulation rates, and changes in the flux of diluents (e.g., clay minerals, or biogenic carbonate or silica) can result in variation in component concentrations in the absence of any actual changes in productivity. The most robust method of productivity reconstruction therefore requires the construction of an age-depth model for each study site, and the subsequent conversion of concentration data to flux estimates. Age-depth models can be constructed on the basis of radiogenic isotopic dates (Winckler et al.,

2005), astronomical tuning (Algeo et al., 2011), or, at a coarser temporal resolution, average sedimentation rates for entire geologic stages or substages (Algeo et al., 2013). Although absolute productivity estimates are inherently uncertain owing to the multitude of factors that influence preservation, secular variation in proxy fluxes at a single locale often can provide reliable information about how productivity has changed locally through time.

2.2. Total organic carbon (TOC)

Organic carbon, representing the single largest constituent of organic matter, provides the most direct proxy for productivity (Pedersen and Calvert, 1990; Canfield, 1994; Tyson, 2005; Zonneveld et al., 2010). Primary producers in the photic zone take up CO_2 from the atmosphere to form organic matter via photosynthesis (Fig. 1A). A substantial portion of carbon fixed via photosynthesis (primary productivity) is recycled within the ocean-surface mixed layer (which varies spatially and temporally, but is generally tens to a few hundreds of meters deep), while the remainder sinks into the thermocline and deep ocean as necromass and fecal pellets. The flux of organic carbon leaving the ocean-surface layer (known as 'export production') can be expressed as a fraction of total primary productivity, i.e., the *pe* (particle export) ratio *sensu* Dunne et al. (2005). The *f*-ratio, referring to the proportion of productivity fueled by exogenous nutrient inputs, is used interchangeably with '*pe* ratio' in some studies (e.g., Eagle et al. 2003), as these terms are expected to be equal under steady-state conditions. This parameter varies widely in the modern ocean as a result of varying nutrient availability,

plankton community structure, and ballasting by inorganic sediment components, and, therefore, shows little predictable geographic variation (Dunne et al., 2005).

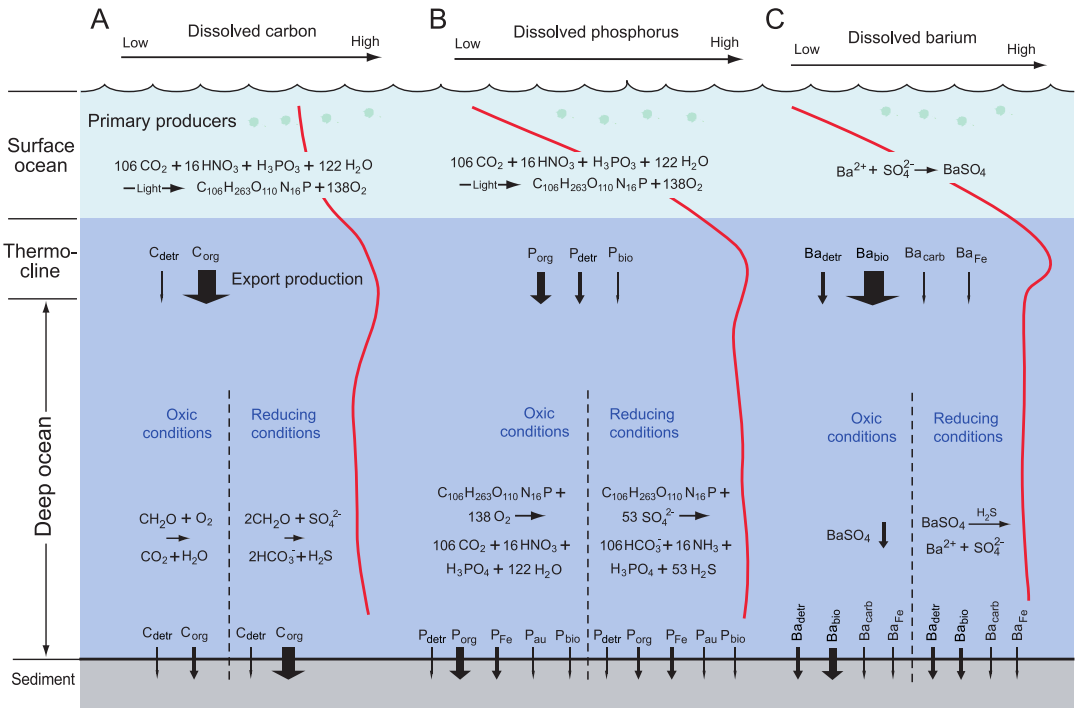

Figure 1: Schematic illustrating fluxes from the surface ocean to the sediment of (A) organic carbon, (B) organic phosphorus, and (C) biogenic Ba. Arrow width shows the relative magnitude of fluxes. C_{detr} = detrital organic carbon, C_{org} = primary marine organic carbon; P_{detr} = detrital P (in silicates and other minerals), P_{org} = organic P, P_{Fe} = Fe-bound P, P_{au} = authigenic P (e.g., francolite), P_{bio} = biogenic P (fish teeth, bones, scales, conodont elements); Ba_{detr} = detrital Ba, Ba_{carb} = Ba in carbonate facies, Ba_{Fe} = Fe-bound Ba (based on Dymond et al., 2002; Filippelli and Delaney, 1996; Paytan and McLaughlin, 2007; Kraal, 2010).

Most of the organic carbon in sediments comes from sinking particles of organic material produced in the surface ocean, together with a component of terrigenous organic carbon in some marginal marine settings (e.g., Goñi et al., 1997; Opsahl and Benner,

1997). In most marine systems, the bulk of the organic material exported from the surface ocean is decomposed by bacterial respiration before reaching the sediment (Deuser, 1971; Opsahl and Benner, 1997). A relatively small fraction of primary production (generally ~0.1% to 10%) survives to be deposited at the sediment-water interface (Müller and Suess, 1979; Canfield, 1994; Hedges and Keil, 1995), and a substantial portion of this organic matter is subsequently lost to anaerobic respiration via (i) denitrification, (ii) manganese, iron, or sulfate reduction, or (iii) methanogenesis after burial in the sediments (e.g., Fig. 1A; Froelich et al., 1979).

Many studies of modern and ancient marine sediments have used total organic carbon (TOC) to reconstruct primary productivity (e.g., Pedersen and Calvert, 1990; Canfield, 1994; Kuypers et al., 2002; Algeo et al., 2013; Felix, 2014). However, the measured TOC content of sediments is a function not only of primary productivity but also: 1) the *pe* ratio, 2) preservation of organic carbon in the water column and during diagenesis, and 3) dilution of organic carbon by lithogenic or biogenic components in the sediment (Canfield, 1994; Tyson, 1995, 2001, 2005). Since organic carbon is typically a minor component of marine sediments and only a small fraction of primary production is preserved, small changes in the PF of organic carbon can have a major effect on the TOC content of the sediment (Tyson, 2005). Aerobic respiration of organic material by bacteria is the most efficient form of carbon remineralization (Fig. 1A), and sediments underlying an oxic water column may have a low TOC content even if surface-water productivity is high (Berner and Raiswell, 1983; Berner, 1984). Organic matter preservation is enhanced by minimizing the exposure of organic material to oxygen through (1) more reducing bottomwater conditions, and (2) more rapid sedimentation.

Both of these conditions result in more rapid passage of organic matter through the zone of aerobic respiration, in which decay is rapid, and into the zone of anaerobic respiration, in which decay is approximately an order of magnitude slower (Simon et al., 1994; Bastviken et al., 2004).

Organic carbon accumulation rates and preservation factors show a strong positive correlation with sedimentation rates in the modern ocean, in which oxic bottom-water conditions predominate (Tyson, 2005). Carbon accumulation rates in suboxic and anoxic regions, which may be a better analogue for many paleomarine systems, show less of a dependence on sedimentation rates, probably because oxygen exposure and preservation rate are less of a control on sediment TOC content under such conditions. The convergence of these trends at ~$10^{3.1}$ g m^{-2} yr^{-1} (Tyson, 2005) suggests that little to no aerobic respiration occurs below the sediment-water interface at bulk accumulation rates higher than this value (Algeo et al., 2013). High sedimentation rates also have the potential to dilute the OC flux to the sediments, and in environments where the predominant phytoplankton groups have mineralized tests, 'autodilution' may occur, where variations in the fluxes of OC and biogenic diluents reflect the same fluctuations in primary productivity. Although enhanced preservation appears to be the predominant effect of high sedimentation rates in the modern ocean, high-TOC sediments deposited in reducing paleomarine systems may reflect periods of slow sediment accumulation (Betts and Holland, 1991; Tyson, 2001, 2005; Algeo and Heckel, 2008).

In addition to water-column redox conditions and sedimentation rates, other factors related to sediment properties and depositional environmental conditions can have a large influence on the preservation of organic matter (Pedersen and Calvert, 1990;

Canfield, 1994). Bioturbation of the sediments by macrofauna or physical mixing processes can increase the exposure of organic material to oxygen during burial. On the other hand, exposure to H_2S in reducing porewater environments can contribute to the formation of sulfidized organic compounds that are relatively more resistant to degradation (Tribovillard et al., 2004; Zonneveld et al., 2010). In some paleomarine systems, organic content also shows a strong relationship to mineral surface area (a metric largely dependent on clay-mineral, especially smectite, content), suggesting that adsorption to clay mineral surfaces may be an important mechanism of organic carbon preservation (Kennedy et al., 2002, 2014; Kennedy and Wagner, 2011). These parameters are not independent and can interact in synergistic ways to promote preservation or decomposition of organic material. For example, clay-rich sediments tend to have low permeability, which is likely to promote a reducing porewater environment and, hence, sulfidization.

The processes discussed above reflect the chemical, physical, and ecological conditions in the surface layer, water column, and sediments during formation and deposition of organic matter. Late diagenetic processes can also affect TOC content through loss of carbon during thermal maturation. Temperature appears to be the single most important factor in the loss of organic matter from sediments during late burial diagenesis (Raiswell and Berner, 1987). Maximum burial temperature can be estimated for paleomarine systems by vitrinite reflectance, conodont alteration index, or a number of other methods, and the original TOC content before thermal maturation potentially can be back-calculated (Daly and Edman, 1987; Skjervoy and Sylta, 1993; Peters et al., 2006; Modica and Lapierre, 2012; Algeo et al., 2013).

In order to generate paleoproductivity estimates from the burial flux of organic carbon (Fig. 1A), one or more transform function(s) are required to account for organic carbon losses within the water column and sediment (e.g., Algeo et al., 2013). Organic carbon losses due to diagenetic processes within the sediment can be estimated with relative confidence, yielding an estimate of the sinking flux of organic carbon (i.e., its rate of delivery to the sediment-water interface). Organic carbon losses within the thermocline and deep layers of the ocean are somewhat less predictable, although relationships to water depth (e.g., Suess, 1980; Sarnthein et al., 1988; Antia et al., 2001) can be used to estimate export production from organic carbon sinking flux. However, burial efficiency, which is dependent on sedimentation rate, appears to account for more variation in sediment TOC than organic carbon sinking flux, which is dependent on water depth (Felix, 2014). On the other hand, the substantial and unpredictable variability of *pe* ratios makes reliable estimation of primary productivity from organic carbon sinking flux impossible in most paleomarine systems (Dunne et al., 2005, Algeo et al., 2013). Fortunately, the export production parameter is of considerable interest in paleomarine studies, as it is directly related to benthic ecology and redox conditions.

2.3. Organic phosphorus (P_{org})

Phosphorus is an essential nutrient for marine phytoplankton growth, being a structural and functional component of all organisms (Redfield, 1958). It is present in seawater in both dissolved and particulate forms (Paytan and McLaughlin, 2007). The dissolved fraction includes inorganic phosphorus (generally in the soluble orthophosphate form) and macromolecular colloidal phosphorus. Particulate P includes organic P within

living and dead plankton as well as bioapatite (e.g., fish teeth and scales, conodont elements), precipitates of authigenic phosphorus minerals, and phosphorus adsorbed to particulates (e.g., iron-bound P) (Filippelli and Delaney, 1996; Schenau et al., 2005; Paytan and McLaughlin, 2007; Kraal, 2010).

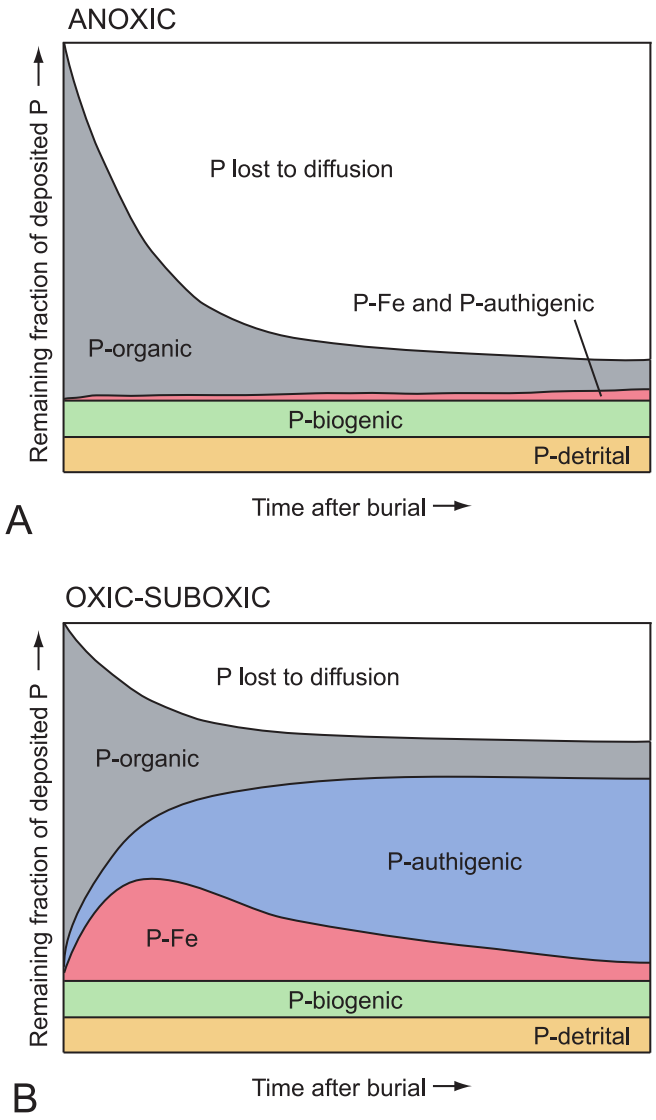

Figure 2: Diagenetic changes in sedimentary P phases with time in (A) anoxic facies and (B) oxic-suboxic facies (adapted from Filippelli and Souch, 1999; Kraal, 2010).

Organic matter is the ultimate source of most P in marine sediments (Fig. 1B; Ingall et al., 1993), whereas detrital P (i.e., in terrigenous silicates and other minerals) generally comprises <20% of total P (Fig. 2; Algeo and Ingall, 2007). As a consequence, total P is commonly used as a proxy for organically derived phosphorus ('P_{org}' in this study) (e.g., Algeo and Ingall, 2007). Bioapatite is usually also a minor component of marine sediment but can represent a substantial portion of the burial flux of phosphorus flux in some highly productive upwelling settings (Schenau et al., 2005; Díaz-Ochoa et al., 2009). In the oxygenated modern ocean, most organic P is remineralized after burial, and a considerable fraction of organic and Fe-bound P is released to sediment porewaters, most of which (>90%) subsequently diffuses back into the overlying water column (Benitez-Nelson, 2000). However, some of the released P is retained in the sediment and ultimately incorporated into authigenic mineral phases such as francolite, a carbonate fluorapatite mineral (Fig. 2; Filippelli and Delaney, 1996; Filippelli and Souch, 1999; Algeo and Ingall, 2007). As a consequence, the depositional flux of P adsorbed to Fe-oxyhydroxides can be comparable to that associated with organic matter in continental shelf deposits (Filippelli, 2001).

Unlike TOC, whose burial efficiency depends primarily on preservation of the original sedimentary component (organic material), the burial efficiency of P is a function of several diagenetic processes affecting the fate of P in sediment porewaters after regeneration (Ingall and Van Cappellen, 1990; Ingall and Jahnke, 1997; Vink et al., 1997). The efficacy of these processes in retaining P within the sediment depends strongly on bottom-water oxygen concentrations, with oxygenated sites promoting phosphorus retention more strongly than anoxic sites (Fig. 1B; Gächter and Müller, 2003;

Ingall et al., 2005). Under oxic conditions, remineralized organic P is retained through a combination of processes, including adsorption onto and complexation with metal oxyhydroxides, as well as biological sequestration in polyphosphates (Filippelli, 2001; Tribovillard et al., 2006; Díaz et al., 2008). These P-trapping mechanisms can result in porewater P concentrations reaching saturation, leading to precipitation of authigenic phosphate minerals that, once formed, are stable in the burial environment (Fig. 2; Kraal, 2010). The dominant mechanism for P retention may be adsorption onto Fe-oxyhydroxides, with redox cycling of the latter within the sediment resulting in multiphase adsorption and release of P (Tribovillard et al., 2006). Under reducing conditions, iron is likely to be in the form of dissolved ions rather than oxyhydroxide particles, and a less active benthic microbiota is less likely to form dissolved ortho- and polyphosphate ions (Díaz et al., 2008). As a result, P released to sediment porewaters under reducing conditions has a greater potential to diffuse back into the overlying water column (Ingall et al., 2005). However, some sulfide-oxidizing bacteria can form apatite and immobilize porewater P under anoxic conditions, which may be important to the formation of phosphorites in upwelling zones (Goldhammer et al., 2010).

Phosphorus accumulation rates have been used as a productivity indicator in both modern (Schenau and De Lange, 2001) and ancient sediments (Compton et al., 1990; Schenau et al., 2005). However, care must be taken to understand potential interactions between productivity and bottomwater redox conditions. High P accumulation rates coincided with periods of high productivity in the Quaternary Arabian Sea despite a concurrent decrease in P burial efficiency (Fig. 3; Schenau et al., 2005). High P accumulation rates also coincided with the onset of organic sedimentation during the

Cenomanian-Turonian oceanic anoxic event (OAE2), suggesting that P accumulation mirrored productivity changes until intense bottom-water anoxia hindered P retention (Mort et al., 2007). As a result of complex interactions between productivity, redox conditions, and burial efficiency, P accumulation rates cannot be assumed to have a linear relationship with primary or export productivity (Tribovillard et al., 2006).

Phosphorites in the sedimentary record typically coincide with high organic carbon content and have been linked to high-productivity regions such as upwelling zones (Föllmi, 1996; Goldhammer et al., 2010). The Permian Phosphoria Formation of the northwestern United States has been linked to a productive coastal upwelling system impinging on a shallow, semi-restricted shelf embayment (Hiatt and Budd, 2003), and the few regions of the modern ocean where phosphorite formation has been observed are closely linked to coastal upwelling (Bremner and Rogers, 1990; Rao and Lamboy, 1995). However, phosphorites also can be produced (or enhanced) through physical sedimentary processes such as winnowing (Föllmi, 1990). Among a large suite of redox and productivity proxies, Brumsack (2006) found that P concentration is one of the few metrics capable of distinguishing effectively between organic-rich sediments formed in productive upwelling zones versus ‘stagnant’ depositional basins such as the Black Sea, with P being consistently more enriched in sediments of the former. Brumsack (2006) concluded that P is one of the most robust and widely applicable productivity proxies.

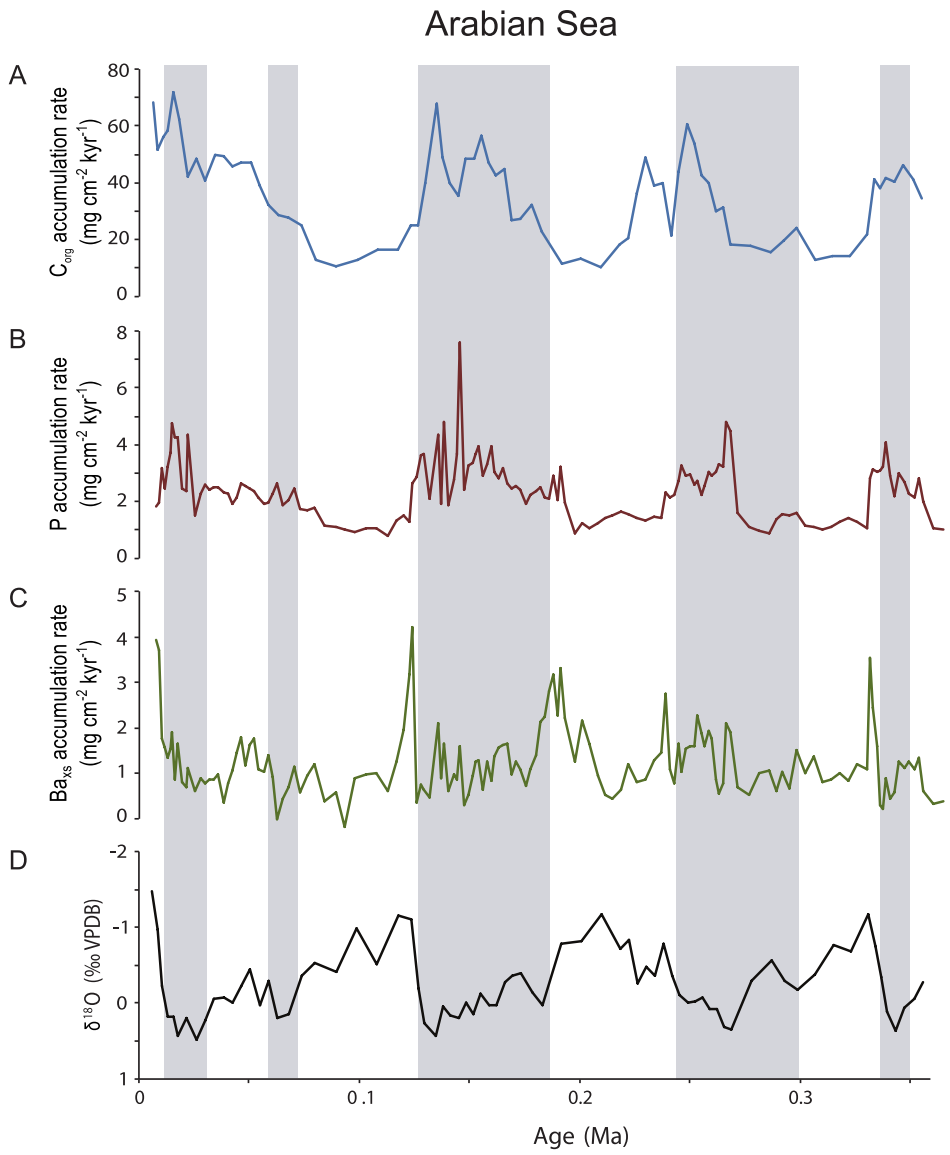

Figure 3: Mass accumulation rates (MARs) for core ODP117-722B from the Owen Ridge, Arabian Sea (16.62° N, 59.80° E, water depth 2022 m). (A) Total organic carbon (TOC), (B) phosphorus (P), (C) excess barium (Ba_{xs}, a proxy for biogenic barium Ba_{bio}), and (D) $d^{18}O$ paleotemperature proxy data. Note glacial/interglacial cycles in productivity proxies; glacial intervals are shaded. Oxygen isotopes were measured in the foraminifer *Globigerinoides sacculifer*. Phosphorus, barium, and aluminum concentration data are from Shimmield and Mowry (1991) and TOC data from Murray and Prell (1991). Ba_{bio} was calculated using a Ba/Al ratio of 0.00475, based on a Ba-versus-Al crossplot. MAR was calculated based on the age model and dry bulk density measurements of Murray and Prell (1991). Data accessed through PANGAEA data portal <http://www.pangaea.de>.

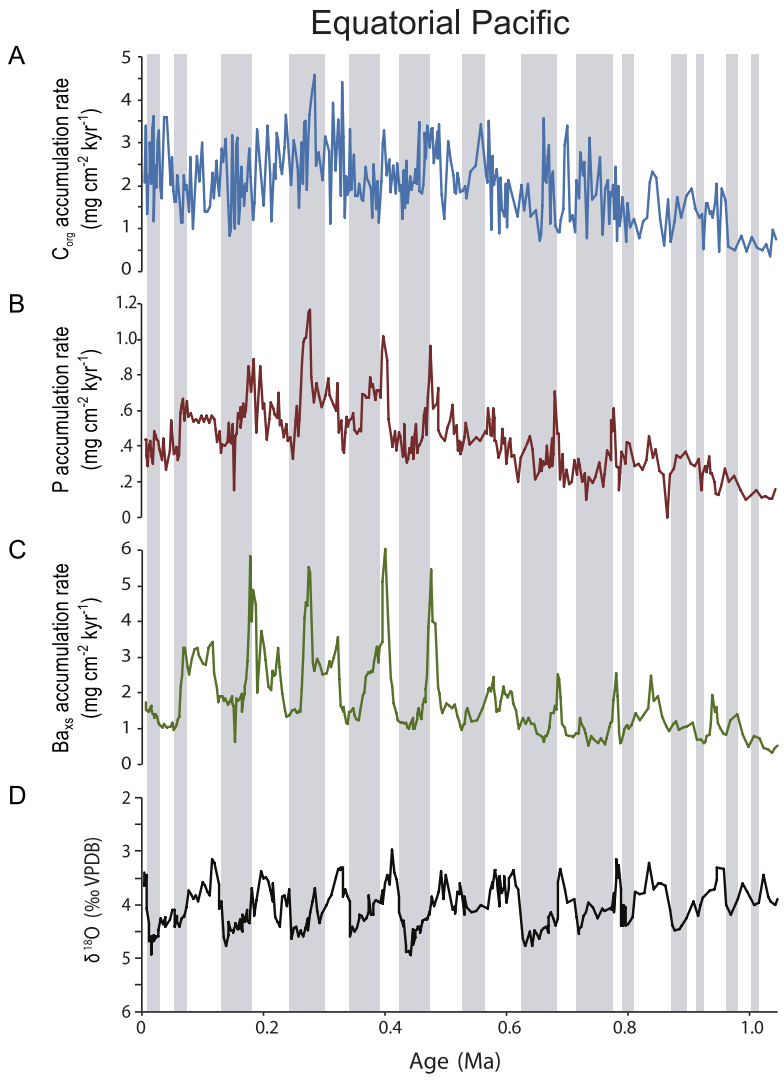

Figure 4: Mass accumulation rates (MARs) for core TT013-PC72 from the tropical eastern Pacific (0.11° N, 139.40° W, water depth 4298 m). (A) Total organic carbon (TOC), (B) phosphorus (P), (C) excess barium (Ba_{xs}, a proxy for biogenic barium Ba_{bio}), and (D) $d^{18}O$ paleotemperature proxy data. Note glacial/interglacial cycles in productivity proxies; glacial intervals are shaded. Oxygen isotopes were measured in the foraminifer *Cibicides wuellerstorfi*. Phosphorus, barium, and aluminum concentration data are from Murray et al. (2000) and TOC data from Murray et al. (2012). Ba_{bio} was calculated using a Ba/Al ratio of 0.0065, based on average shale (PAAS, Taylor and McLennan, 1985). MAR was calculated based on the age model of Murray et al. (2000) with dry bulk density estimated using the equation of Curry and Lohmann (1986). Data accessed through SedDB data portal <http://www.earthchem.org/seddb>.

2.4. Biogenic barium (Ba_{bio})

The chemical behavior and cycling of barium in seawater are now fairly well understood (Ganeshram et al., 2003; Paytan and Griffith, 2007; Van Beek et al., 2007; Griffith and Paytan, 2012). Barium has a relatively short residence time in seawater (~10 kyr; Dickens et al., 2003). Its main source is river runoff, and its primary sink is burial of barite ($BaSO_4$) in marine sediments. A large part of the barite burial flux is delivered to the sediment-water interface by sinking organic matter (Fig. 1C), leading to local Ba enrichment of the sediment. This fraction is referred to as 'biogenic barium' (Ba_{bio}), i.e., Ba associated with the sinking flux of organic matter. Other sinks for seawater Ba include adsorption onto aluminosilicate, carbonate, and ferromanganese oxyhydroxide sedimentary phases (Dymond et al., 1992; Eagle et al., 2003; Gonneea and Paytan, 2006).

The origin of Ba_{bio} has been a matter of some controversy. Some phytoplankton (Bertram and Cowan, 1997; Gonzalez-Muñoz et al., 2012) and zooplankton (Rieder et al., 1982; Bernstein et al., 1992) assimilate Ba intracellularly, which can yield concentrations substantially exceeding that of seawater (Fisher et al., 1991). However, barite precipitation by marine organisms (Gooday and Nott, 1982; Bertram and Cowen, 1997) or replacement of celestite ($SrSO_4$) in acantharians (Bernstein et al., 1992, 1998) are minor sources compared with authigenic precipitation of barite within decaying organic matter (Fig. 1B; Bishop, 1988; Van Beek et al., 2007). The operation of the latter process is demonstrated by formation of barite throughout the oceanic water column rather than in the photic zone alone (Van Beek et al., 2007). Barite formation is commonly associated with the decay of coccolithophore and diatom biomass, two phytoplankton groups that are not known to precipitate barite intracellularly (Ganeshram et al., 2003).

The decay process results in the localized development of microenvironments on organic particle surfaces, where Ba is concentrated via adsorption onto Fe-oxyhydroxides (Sternberg et al., 2005), and where the solubility product of barium (Ba^{+2}) and sulfate (SO_4^{-2}) exceeds the equilibrium constant of barite ($BaSO_4$), causing spontaneous nucleation of barite crystals (Dehairs et al., 1980, 1992; Bishop, 1988). This process is assisted by elevated concentrations of sulfate within sinking organic particles due to oxidation of organic-derived sulfur compounds such as amino acids (Dymond and Collier, 1996) or reoxidation of H_2S produced through bacterial sulfate reduction.

Seawater is moderately undersaturated with respect to barite through most of the global ocean, including most surface waters, although parts of the deep ocean are supersaturated (Monnin et al., 1999). This pattern reflects the export of Ba from the ocean-surface layer in association with sinking organic particles (Fig. 1C). Despite widespread undersaturation of seawater with respect to barite, particulate barite is nearly ubiquitous in the world's oceans. Particulate barite is generally small (mean size ~1 μm) and is found in association with organic aggregates in surface waters and as free particles in deep waters (Bishop, 1988; Dehairs et al., 1990; Bertram and Cowen, 1997). However, formation of particulate barite is relatively more vigorous in the deep ocean, where seawater is closer to saturation with barite, than in the ocean-surface layer and thermocline, where lower saturation levels are found (Fig. 1C). Spatial gradients in Ba concentration are found in the deep ocean as a consequence of export of particulate barite from the North Atlantic to the North Pacific via the global oceanic conveyor belt (Broecker, 1991).

Both Ba_{bio} and barite have been used as a paleoproductivity proxy in oceanographic studies of marine sediments of various ages, including the Recent (Dehairs et al., 1987; Prakash et al., 2002; Weldeab et al., 2003), Quaternary (Paytan et al. 1996; Moreno et al., 2002; Klöcker et al., 2006; Jaccard et al. 2013), Neogene-Paleogene (Latimer and Filippelli, 2002; Anderson and Delaney, 2005; Paytan et al., 2007), Cretaceous (Zachos et al., 1989; Bąk, 2007), and Paleozoic (Jewell, 1994; Kasten et al., 2001). As a paleoproductivity proxy, barite has the advantages of being relatively refractory and having a high burial efficiency under oxic conditions (~30-50% of the Ba sinking flux versus <10% for organic carbon and phosphorus) (Dymond et al., 1992; Paytan and Kastner, 1996; Balakrishnan Nair et al., 2005; Paytan and Griffith, 2007). Even in reducing environments that are not conducive to barite preservation, the high flux of biogenic Ba to the sediment-water interface nonetheless can make it a useful paleoproductivity proxy (Falkner et al., 1993; Thomson et al., 1995; van Sanvoort et al., 1996; Nijenhuis et al., 1999; Martinez-Ruiz et al., 2000; Kasten et al., 2001; Prakash et al., 2002; Martinez et al., 2003; Scopelliti et al., 2004; Bak, 2007).

The fate of particulate barite in the sediment is critical to its potential utility as a paleoproductivity proxy. Barite is relatively insoluble under oxidizing conditions and, hence, tends to be well preserved where bottom waters are oxygenated (Fig. 1C; Paytan and Kastner, 1996; Balakrishnan Nair et al., 2005; Paytan and Griffith, 2007), although barite particles are potentially subject to winnowing or corrosion (Dymond, 1981). However, barite in surficial sediments may dissolve when exposed to anoxic porewaters from which the sulfate has been removed by microbial activity (Van Os et al., 1991; Von Breymann et al., 1992; Torres et al., 1996; McManus et al., 1994, 1998, 1999; Paytan and

Kastner, 1996; Schenau et al., 2001), a process which limits the use of Ba as a paleoproductivity proxy in some modern continental margin settings (Shimmield et al., 1994; Ganeshram et al., 1999). As reducing conditions are widely present at shallow depths within marine sediments, some loss of authigenic Ba during burial may be common (Berelson et al., 1996). Comparison of water-column sediment-trap with sediment data suggests that, on average, ~30% of the particulate Ba flux to the seafloor is preserved in the open Pacific (Dymond et al., 1992). However, this value varies widely (~10-70%) as a function of bulk accumulation rate, with superior barite preservation associated with higher sedimentation rates (Dymond et al., 1992). Once buried, barite particles tend to remain stable owing to the generally saturated condition of sediment porewaters with respect to barite.

One issue of importance for the application of Ba_{bio} as a paleoproductivity proxy is whether seawater has remained saturated (or nearly so) with respect to barite through time. If ancient seawater was ever strongly undersaturated with respect to barite, then authigenic barite would not have accumulated in the sediment under any productivity conditions. Seawater undersaturation with respect to barite could have resulted from large-scale removal of sulfate to the sedimentary reservoir. However, seawater has contained substantial quantities of dissolved sulfate since the Early Proterozoic, when oxidative weathering of sulfides intensified due to rising atmospheric pO_2 (Canfield, 2005). Even if seawater sulfate concentrations fell, as has occurred episodically during the Phanerozoic (Lowenstein et al., 2001; Luo et al., 2011; Wortmann and Paytan, 2012; Song et al., 2014), it is not certain that this would have resulted in undersaturation with respect to barite. Because barite is the dominant sink for Ba in seawater, any decrease in

dissolved sulfate concentrations would have been compensated by a rise in Ba^{2+} concentrations, maintaining an approximately constant solubility product for barite. Therefore, it seems likely that the saturation level of barite in seawater has not varied greatly since possibly ~2 Ga.

2.5. Covariation among TOC, P_{org}, and Ba_{bio}

Because no single proxy is inherently more reliable than others, paleoproductivity assessments should generally be made on the basis of multiple proxies (Averyt and Paytan, 2004). In many modern marine systems, the fluxes of TOC, P_{org}, and Ba_{bio} (or authigenic barite) are coupled (e.g., Figs. 3, 4), suggesting that—under conditions favoring their preservation—all three components may serve as proxies for export productivity (Dymond et al., 1992; François et al., 1995; Dymond and Collier, 1996; Jeandel et al., 2000; Weldeab et al., 2003; Fagel et al., 2004; Balakrishnan Nair et al., 2005; Paytan and Griffith, 2007). Furthermore, these proxies have been shown to exhibit significant secular covariation at glacial-interglacial timescales, e.g., in Late Quaternary marine sediments of the Arabian Sea (Fig. 3; Murray and Prell, 1991; Shimmield and Mowbry, 1991, Shimmield, 1992; Schultz et al., 1998; Rostek et al. 1997) and the eastern tropical Pacific (Fig. 4; Lyle et al., 1992; Gardner et al., 1997; Ganeshram and Pedersen, 1998, Murray et al., 2000, Murray et al., 2012). However, attention must be paid to the possibility that such covariation is linked to changes in the sedimentation rate and provenance of lithogenic components that may influence Ba or Al concentrations (Weldeab et al., 2003).

In the well-ventilated modern ocean, the fluxes of TOC, P_{org}, and Ba_{bio} vary strongly with water depth. These patterns reflect a preservational control on organic carbon and phosphorus associated with depth-dependent decay time and redox conditions. Remineralization rates of organic carbon and phosphorus remain high until reaching the sediment-water interface, especially in well-oxygenated water columns (Pace et al., 1987; Le Moigne et al., 2013). Rates of decay in anoxic water columns are significantly lower (Canfield, 1994; Tyson, 2005). P-bearing organic compounds are relatively more labile than non-P-bearing compounds, as a consequence of which the TOC/P ratios of organic matter can change with increasing water depth and decay (Ingall and Van Cappellan, 1990). In shallow delta and shelf environments, TOC/P ratios are generally close to the canonical Redfield ratio (106:1) owing to rapid sinking and burial of organic matter (Ruttenberg and Goñi, 1997). On the upper continental slope (i.e., within the oxygen-minimum zone, or OMZ), TOC/P ratios increase to a maximum of ~400 owing to preferential remineralization of P-bearing compounds and lack of retention of P in the sediment under suboxic conditions (Ingall and Van Cappellan, 1990; Schenau and De Lange, 2001). In the deep ocean, TOC/P ratios can fall below the Redfield ratio owing to retention of P within the sediment of oxic facies (Fig. 5A; Algeo and Ingall, 2007).

The depth dependence of Ba_{bio} accumulation is a function of the relative saturation of barite in the water column. The deep ocean is closer to saturation with respect to barite than the surface mixed layer and thermocline, so particulate barite is more likely to precipitate within and survive transit through deeper waters (Gingele and Dahmke, 1994; Van Beek et al., 2007). TOC/Ba_{bio} varies systematically with water depth

in the modern ocean, especially below 1500 m (Fig. 5B; Dymond et al., 1992; Schenau et al., 2001; Calvert and Pedersen, 2007). TOC/Ba_{bio} ratios of 100-125 are typical of surface waters of the pelagic ocean but decrease to ≤25 at abyssal depths (Dymond et al., 1992). TOC/Ba_{bio} ratios are somewhat higher in marginal marine environments with high sedimentation rates, although the pattern of decreasing ratios with increasing water depth still prevails (François et al., 1995; Dehairs et al., 2000; Schenau et al., 2001; Fagel et al., 2004). This pattern is a consequence of the simultaneous decay of organic matter and formation of authigenic barite within sinking organic aggregates. For this reason, sediments deposited above the OMZ on shallow continental shelves may exhibit a tight coupling between TOC and Ba_{bio} that reflects the influence of productivity more than preservation (see Section 2.6).

The ratios among TOC, P_{org}, and Ba_{bio} can also vary along lateral transects, from continent margins to the deep ocean (François et al., 1995; Dehairs et al., 2000). As a result, although organic carbon, phosphorus, and biogenic barium often show covariation that is likely related directly to changes in primary productivity, the ratio of TOC to either of the other two proxies can vary substantially, making it difficult to estimate carbon export from P_{org} or Ba_{bio} without additional information that often can only be estimated in paleomarine systems.

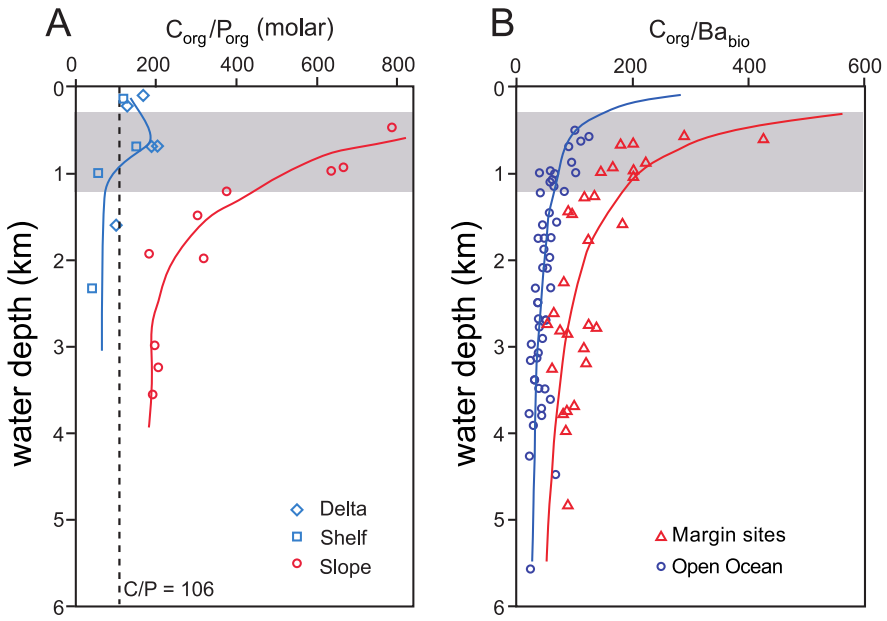

Figure 5: (A) Molar $(C/P)_{org}$ ratios of sedimentary organic matter; note differences between Mississippi Delta and Gulf of Mexico shelf sediments (Ruttenberg and Goñi, 1997) versus Arabian Sea slope sediments (Schenau and De Lange, 2001). A molar $(C/P)_{org}$ of 106:1 is the Redfield ratio for marine phytoplankton (Redfield, 1958). (B) C_{org}/Ba_{bio} ratios of settling particles; note differences between open-ocean (Dymond et al., 1992; François et al., 1995) and shelf-margin sites (François et al., 1995; Dehairs et al., 2000; Fagel et al., 2004).

2.6. Influences on paleoproductivity estimates

Two of the most important controls on organic matter preservation and, hence, on paleomarine productivity estimates are (1) bottomwater redox conditions (Canfield, 1994; Meyers, 1997), and (2) sediment bulk accumulation rates (BAR) (Tyson, 2005; Algeo et al., 2013). Redox conditions generally exert a strong influence on the accumulation of elemental productivity proxies in the sediment. For example, the PF of organic carbon increases rapidly with decreasing dissolved oxygen concentration (Canfield, 1994), whereas those of P_{org} and Ba_{bio} generally decrease under the same conditions (Fig. 6). In

contrast, the refractory nature of barite in oxidizing environments may make it a more effective recorder of productivity than TOC in oxic marine systems with low sedimentation rates. BAR also exerts a strong influence on the accumulation of these elemental proxies, the preservation of which is enhanced at higher sedimentation rates (Tyson, 2005). With increasing BAR, the influence of benthic redox conditions on the accumulation of TOC, P_{org}, and Ba_{bio} becomes much less pronounced as a consequence of rapid burial and reduced oxygen exposure time (Canfield, 1994; Tyson, 2005).

The relative importance of redox versus productivity controls on organic matter accumulation may be distinguishable on the basis of patterns of covariation among TOC, P_{org}, and Ba_{bio}. In the redox-dominant scenario, the accumulation of these components is more strongly influenced by the differing preservation patterns of these proxies, resulting in negative covariation of TOC with P_{org} and Ba_{bio} (Fig. 6A). This scenario applies equally to oxidizing and reducing environments. In reducing environments, a high sinking flux of TOC commonly intensifies reducing conditions through high biological oxygen demand, thus enhancing organic matter preservation and increasing the burial flux of organic carbon. In contrast, reducing conditions tend to diminish the burial fluxes of P_{org} and Ba_{bio} owing to reductive dissolution of Mn-Fe-oxyhydroxide particles, thus releasing adsorbed P, and barite crystals, releasing Ba (Tyson, 2005). On the other hand, oxidizing environments generally facilitate the preservation and retention of P_{org} and Ba_{bio} within the sediment, whereas the burial efficiency of organic carbon is reduced owing to greater aerobic remineralization (Tyson, 2005). In the productivity-dominant scenario, the export of organic matter from the surface ocean is the main factor influencing the fluxes of TOC, P_{org}, and Ba_{bio} to the sediment (Fig. 6B). Although

preservational effects may alter the ratios of these components, their sensitivity to changes in productivity imposes a strong positive correlation among all proxies across the spectrum of redox conditions (Tyson, 2005).

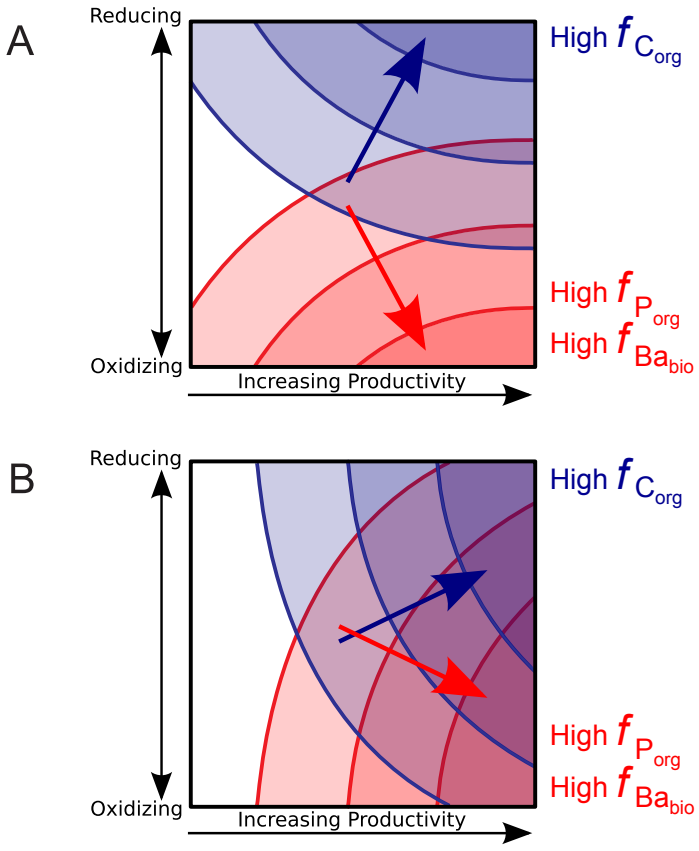

Figure 6: Inferred covariant relationships among fluxes (*f*) of C_{org}, P_{org}, and Ba_{bio} as a function of primary productivity (abscissa) and benthic redox conditions (ordinate). Curved lines represent isofluxes, and arrows indicate direction of increasing fluxes. Theoretically, C_{org} accumulation is favored by high productivity and reducing conditions, and P_{org} and Ba_{bio} accumulation by high productivity and oxidizing conditions. In the redox-dominant scenario (A), redox variation exerts a stronger influence on proxy fluxes than productivity variation (reflected in subhorizontal isoflux contours), resulting in negative covariation between f_{Corg} and f_{Porg} or $f_{Ba\text{-}xs}$. In the productivity-dominant scenario (B), productivity variation exerts the stronger influence (reflected in subvertical isoflux contours), potentially allowing positive covariation among all three productivity proxies (e.g., along either of the trends shown by colored arrows). See text for examples.

Examples of both redox- and productivity-dominant environments can be found in Holocene and older marine systems, even within a single type of environmental setting, e.g., OMZs in productive upwelling regions. The Quaternary eastern tropical Pacific exemplifies a redox-dominant system, in which P_{org} and Ba_{bio} show strong positive covariation ($r^2 = 0.74$) with little relationship of either proxy to organic carbon flux on glacial-interglacial timescales (Fig. 4; Murray et al., 2000, 2012). A second example is the Benguela upwelling system, in which TOC and Ba/Al covary negatively (Robinson et al., 2002; n.b., neither proxy shows a consistent relationship to P). On the other hand, the Quaternary Arabian Sea exemplifies a productivity-dominant system, in which TOC exhibits strong positive covariation with both P_{org} and Ba_{bio} (Fig. 3; Reichart et al., 1997; Balakrishnan Nair et al., 2005) despite possible diagenetic losses of Ba_{bio} (Murray and Prell, 1991; Shimmield and Mowbray, 1991). A second example of a productivity-dominant system is the highly productive Chilean margin upwelling system, in which TOC covaries positively Ba/Al (Muñoz et al., 2012; n.b., P was not measured in this study).

BAR is a second major factor influencing the accumulation of TOC, P_{org}, and Ba_{bio}. Organic carbon accumulation rates show a strong correlation with BAR (Müller and Suess, 1979), although the nature of the relationship differs between fully oxic and fully anoxic environments (Tyson, 2005). In oxic environments, higher BAR minimizes the exposure time of organic matter to aerobic decay in the shallow burial zone, increasing its BE (Hartnett et al., 1998, Iversen and Ploug, 2010). While the labile fraction of organic carbon is degraded efficiently even under anaerobic conditions (Henrichs and Reeburg, 1987; Hulthe et al., 1998; Kristensen and Holmer, 2001;

Bastviken et al., 2004), the residence time of the residual organic matter at the sediment-water interface or in the shallow burial zone appears to be less of a control on preservation where bottom waters are anoxic (Tyson, 2001, 2005); this may be due to intrinsically slower degradation of refractory compounds in the absence of oxygen (Benner et al., 1984; Colburg, 1988; Schink 1988; Ding and Sun, 2005), exclusion of bacteria-grazing protozoa and macrofauna (Lee, 1992), adsorption to mineral surfaces (Hedges and Keil, 1995; Henrichs, 1995) or a dependence of refractory compound degradation on the overall sediment metabolic rate (Canfield, 1994).

Higher BAR also enhances the BE of Ba_{bio}, but for a different reason. When burial is rapid, biogenic barite passes quickly into the zone of reducing porewaters in which it tends to dissolve, but a relatively closed diagenetic system prevents diffusion of Ba^{2+} out of the sediment and facilitates its subsequent reprecipitation as a diagenetic barite phase (Dymond et al., 1992).

In contrast to TOC and Ba_{bio}, organic P does not appear to show a simple linear relationship to BAR. Ingall and Van Cappellen (1990) observed that TOC:P_{org} ratios vary in a complex manner as a function of sedimentation rate, with low and high rates (<2 and >1000 cm kyr^{-1}) associated with TOC:P_{org} of ~100-200 and intermediate rates (~10-250 cm kyr^{-1}) associated with TOC:P_{org} of ~500-800. The underlying control on this pattern is not certain but possibly related to the interplay of sedimentation rates with redox conditions. High TOC:P_{org} ratios are associated with reducing environments (Algeo and Ingall, 2007), which tend to have sedimentation rates between those of highly oxidizing environments in open-ocean settings (low BAR) and those in continent-margin systems (high BAR) (Ingall and Van Cappellen, 1990; Tromp et al., 1995). Although TOC/P_{org}

increases with burial depth, this largely reflects a transfer of P from organic to authigenic phases, resulting in little change in C_{org}/P_{total} ratios (Filippelli, 2001; Algeo and Ingall, 2007).

3. Methods

3.1. Compilation of modern sediment core database

Our primary goal in this study is to evaluate the robustness of the sediment components TOC, P_{org}, and Ba_{bio} as proxies for primary and export productivity in paleomarine systems. To this end, we generated a database containing (1) TOC, P_{org}, Ba_{bio}, and Al concentrations for 5914 individual samples from 94 sedimentary cores, representing a range of oceanic localities and depositional environments (Figure 7), and (2) modern primary productivity estimates for the same 94 sites based on several techniques (see Section 3.4). The cores used in this study are all of Cenozoic (<65 Ma) and mostly of Quaternary (<2.4 Ma) age, allowing for direct comparisons of sediment proxies with modern primary productivity data. The sediment geochemical data were compiled from 37 references that are summarized in Table 1, which were either downloaded from the online PANGAEA database (pangaea.de) or extracted from published sources. To assess the effects of redox conditions on productivity proxies, each site was assigned a redox classification based on its location. Sites below the chemocline of the Black Sea, Cariaco Basin, and Saanich Inlet were classified as anoxic (dissolved $O_2 = 0$ mL L^{-1}), those in upwelling zones of the Arabian Sea and the West African coast were classified as suboxic (dissolved O_2 >0 to 2 mL L^{-1}), and the remaining (mainly open-ocean) sites were classified as oxic (dissolved O_2 >2 mL L^{-1}).

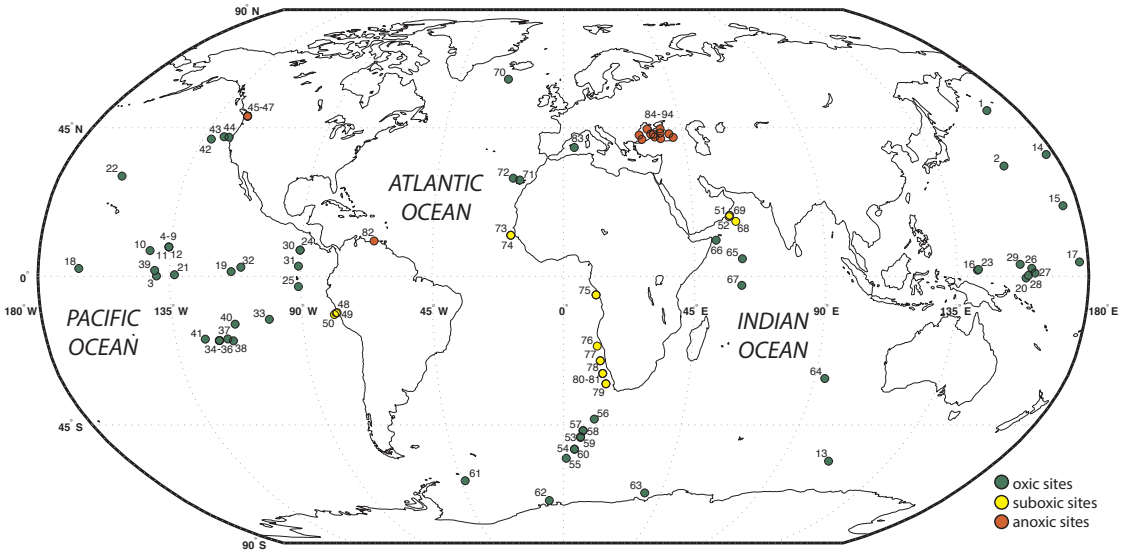

Figure 7: World map showing locations of sites used in this study, and their redox category. Site numbers correspond to those used in Table 1.

3.2. Calculation of organic P and biogenic Ba

We used organic phosphorus (P_{org}) rather than total phosphorus (P or P_{total}) in our flux calculations in order to more accurately assess biogenic P fluxes. We calculated P_{org} from total P by subtracting a detrital phosphorus fraction (P_{detr}) estimated from each sample's Al content as follows:

$$[P_{org}] = [P_{total}] - [Al] \times (P/Al)_{detr} \quad (1)$$

We assumed a detrital P/Al ratio of 0.0087 based on the average P and Al concentrations of upper continental crust (McLennan, 2001). Because detrital P comprised <5% of total P in all of the study units, minor uncertainties regarding the choice of detrital P/Al ratio have little effect on calculated P_{org} fluxes. Indeed, the calculated proportions of detrital P are so small in most open-ocean settings as to be effectively negligible. This calculation assumes that all non-detrital P was ultimately derived from marine phytoplankton

biomass. This inference is generally true of P adsorbed onto Fe-oxyhydroxides or preserved in authigenic phosphate (Kraal, 2010), but it does not take into account P contributions from biogenic fluorapatite, e.g., fish scales and bones (P_{bio} in Fig. 1B), which may be quantitatively important in some samples (Fig. 2).

Biogenic Ba was determined by calculating the amount of barium in excess (Ba_{xs}) of the expected detrital Ba concentration (Ba_{detr}) as follows:

$$[Ba_{xs}] = [Ba_{total}] - [Al] \times (Ba/Al)_{detr} \quad (2)$$

We assumed that Ba_{bio} is equivalent to Ba_{xs}, i.e., that all non-detrital Ba is biogenic in origin, although a small fraction of non-detrital Ba may derive from Ba adsorbed onto carbonates or ferromanganese oxyhydroxides. These adsorbed fractions may be quantitatively more important in sediments from high-productivity zones such as the equatorial Pacific, where Ba in biogenic barite accounts for just ~70 % of Ba_{xs} (Eagle et al., 2003).

Table 1. Summary of sites used in this study. The *n* = column indicates the number of individual samples from each site. Estimates of modern productivity at a given site were based on the oceanic provinces of Longhurst et al. (1995; see Table 2). Table on following page.

	Site	Location	Latitude	Longitude	Water depth (m)	n =	Redox Category	Longhurst et al. (1995) province	Reference
1	ODP Leg 882 (Hole)	Detroit Seamount	50.35	167.58	3244	105	oxic	PSAW	Jaccard et al. (2009)
2	S-2 and AC-2	Shatsky Rise	33.36	159.13	3107	61	oxic	NPSW	Arno & Minagawa (2003)
3	PC72	Abyssal Equatorial Pacific	0.11	-139.40	4298	312	oxic	PEQD	Murray et al. (2000, 2012)
4	199-1218	Abyssal Equatorial Pacific	8.89	-135.67	4827.2	45	oxic	PNEC	Lyle & Lyle (2005)
5	199-1218	Abyssal Equatorial Pacific	8.89	-135.67	4827.2	178	oxic	PNEC	Lyle & Lyle (2005)
6	199-1218	Abyssal Equatorial Pacific	8.89	-135.67	4827.2	42	oxic	PNEC	Lyle & Lyle (2005)
7	199-1218	Abyssal Equatorial Pacific	8.89	-135.67	4827.2	199	oxic	PNEC	Lyle & Lyle (2005)
8	199-1218	Abyssal Equatorial Pacific	8.89	-135.67	4827.2	41	oxic	PNEC	Lyle & Lyle (2005)
9	199-1218	Abyssal Equatorial Pacific	8.89	-135.67	4827.2	61	oxic	PNEC	Lyle & Lyle (2005)
10	199-1219	Abyssal Equatorial Pacific	7.80	-142.02	5063.4	351	oxic	PNEC	Lyle & Lyle (2005)
11	199-1218	Abyssal Equatorial Pacific	8.89	-135.67	4827.2	163	oxic	PNEC	Lyle & Lyle (2005)
12	199-1218	Abyssal Equatorial Pacific	8.89	-135.67	4827.2	76	oxic	PNEC	Lyle & Lyle (2005)
13	28-266	SE Indian Ocean ridge	-56.40	110.11	4167	10	oxic	ANTA	Moody et al. (1988)
14	32-310	Central Pacific seamount	36.87	176.90	3516	12	oxic	NPSE	Moody et al. (1988)
15	62-463	Central Pacific seamount	21.35	174.67	2532	9	oxic	NPTG	Moody et al. (1988)
16	7-62A	Caroline Basin	1.87	141.94	2591	15	oxic	WARM	Moody et al. (1988)
17	7-65	Abyssal Equatorial Pacific	4.35	176.99	6130	12	oxic	WARM	Moody et al. (1988)
18	7-66A	Abyssal Equatorial Pacific	2.38	-166.12	5293	8	oxic	WARM	Moody et al. (1988)
19	85-572	East Pacific Rise	1.44	-113.84	3893	10	oxic	PEQD	Moody et al. (1988)
20	89-586	Ontong-Java Plateau	-0.50	158.50	2207	10	oxic	WARM	Moody et al. (1988)
21	9-77	East Pacific Rise	0.48	-133.23	4291	16	oxic	PEQD	Moody et al. (1988)
22	GPC-3	Abyssal Central Pacific	30.32	-157.67	5705	9	oxic	NPSE	Moody et al. (1988)
23	Core MD97-2140	Caroline Basin	2.07	142.27	2547	237	oxic	WARM	Thevenon et al. (2004)
24	138-844B	East Pacific Rise	7.92	-90.48	3414.5	32	oxic	PNEC	Filippelli & Delaney (1995)
25	138-846	East Pacific Rise	-3.10	-90.82	3296	226	oxic	PEQD	Emeis et al. (1995)
26	Hole 803D	Ontong-Java Plateau	2.43	160.54	3410	20	oxic	WARM	Filippelli & Delaney (1996); Delaney & Filippelli (1994)
27	Hole 804B/C	Ontong-Java Plateau	1.00	161.59	3861	15	oxic	WARM	Filippelli & Delaney (1996); Delaney & Filippelli (1994)
28	Hole 806B	Ontong-Java Plateau	0.32	159.36	2520	9	oxic	WARM	Filippelli & Delaney (1996); Delaney & Filippelli (1994)
29	Hole 807A/C	Ontong-Java Plateau	3.63	156.63	2806	24	oxic	WARM	Filippelli & Delaney (1996); Delaney & Filippelli (1994)
30	Hole 844	East Pacific Rise	7.92	-90.48	3415	35	oxic	PNEC	Filippelli & Delaney (1996); Delaney & Filippelli (1994)
31	Hole 846B	East Pacific Rise	3.10	-90.82	3296	68	oxic	PNEC	Filippelli & Delaney (1996)
32	Hole 851B	East Pacific Rise	2.77	-110.57	3760	68	oxic	PEQD	Filippelli & Delaney (1996)
33	Hole 34-319	Bauer Deep, SE Pacific	-13.02	-101.52	4296	21	oxic	SPSG	Dymond et al. (1977)
34	Aria-2	East Pacific Rise	-19.42	-119.83	3654	6	oxic	SPSG	Leinen & Graybeal (1986)
35	Aria-5	East Pacific Rise	-19.40	-119.88	3680	4	oxic	SPSG	Leinen & Graybeal (1986)
36	Aria-6	East Pacific Rise	-19.39	-119.81	3600	6	oxic	SPSG	Leinen & Graybeal (1986)
37	Aria-8	East Pacific Rise	-18.93	-116.84	3350	7	oxic	SPSG	Leinen & Graybeal (1986)
38	Aria-13	East Pacific Rise	-19.50	-114.96	3435	5	oxic	SPSG	Leinen & Graybeal (1986)
39	Core RC11-210	Abyssal Equatorial Pacific	1.82	-140.05	4420	174	oxic	PEQD	Rea et al. (1991)
40	GS7202-35	East Pacific Rise	-14.47	-113.50	3044	181	oxic	SPSG	Mills et al. (2010)
41	Site 92-598	East Pacific Rise	-19.00	-124.68	3699	50	oxic	SPSG	Ruhlin & Owen (1986)
42	W8709A-1BC	California margin	41.54	-131.96	3680	25	oxic	OCAL	Lyle et al. (1992)
43	W8709A-8PC and 8TC	California margin	42.26	-127.68	3111	70	oxic	OCAL	Lyle et al. (1992)
44	W8709A-13PC and 13TC	California margin	42.12	-125.75	2712	51	oxic	CCAL	Lyle et al. (1992)
45	ODP Leg 169S (Hole 1033B)	Saanich Inlet	48.59	-123.50	238	29	anoxic	n/a	Russell and Morford (2001); Filippelli (2001)
46	ODP Leg 169S (Hole 1034B)	Saanich Inlet	48.63	-123.50	203	37	anoxic	n/a	Filippelli (2001)
47	ODP Leg 169S (Hole 1033E)	Saanich Inlet	48.59	-123.50	238	20	anoxic	n/a	Filippelli (2001)
48	112-679D	Peru margin	-11.06	-78.27	462	3	suboxic	CHIL*	Lückge et al. (1996)
49	112-681B	Peru margin	-10.99	-77.96	162	2	suboxic	CHIL*	Lückge et al. (1996)
50	112-688	Peru margin	-11.54	-78.94	3829.8	3	suboxic	CHIL	Lückge et al. (1996)
51	117-723	Oman margin	18.05	57.61	808	5	suboxic	ARAB	Lückge et al. (1996)
52	117-724	Oman margin	18.46	57.79	600	4	suboxic	ARAB	Lückge et al. (1996)
53	1756-5	Abyssal Southern Ocean	-48.63	6.71	3828	48	oxic	SANT	Nürnberg et al. (1997)
54	1768-8	Antarctic margin	-52.59	4.48	3299	70	oxic	SANT	Nürnberg et al. (1997)
55	1772-8	Abyssal Southern Ocean	-55.46	1.16	4137	33	oxic	ANTA	Nürnberg et al. (1997)
56	2082-1	Abyssal Southern Ocean	-43.22	11.71	4610	71	oxic	SSTC	Nürnberg et al. (1997)
57	1754-1	Mid-Atlantic Ridge	-46.77	7.61	2519	29	oxic	SANT	Frank et al. (2000)
58	1754-2	Mid-Atlantic Ridge	-46.77	7.59	2534	6	oxic	SANT	Frank et al. (2000)
59	1756-5	Mid-Atlantic Ridge	-48.90	6.71	3828	85	oxic	SANT	Frank et al. (2000)
60	1768-8	Mid-Atlantic Ridge	-52.59	4.48	3299	52	oxic	SANT	Frank et al. (2000)
61	1575-1	Antarctic margin	-62.85	-43.34	3461	123	oxic	APLR	Bonn et al. (1998)
62	1648-1	Antarctic margin	-69.74	-6.69	2529	88	oxic	APLR	Bonn et al. (1998)
63	1821-6	Antarctic margin	-67.07	37.48	4027	170	oxic	APLR	Bonn et al. (1998)
64	121-752A	Broken Ridge	-30.89	93.58	1097	46	oxic	ISSG	Owen and Zimmerman (1991)
65	MD 90940	Madingley Rise	5.34	61.41	3875	59	oxic	MONS	Des Combes et al. (1999)
66	MD 962073	Socotra	10.94	52.62	3142	67	oxic	MONS	Des Combes et al. (2005)
67	115-711A	Abyssal NW Indian Ocean	-2.74	61.16	4439	22	oxic	MONS	Bostrom and Backman (1990)
68	ODP Leg 117 (Hole 722B)	Owen Ridge	16.62	59.80	2028	147	suboxic	ARAB	Shimmield and Mowbray (1991)
69	ODP Leg 117 (Hole 724C)	Owen Ridge	18.46	57.79	593	155	suboxic	ARAB	Shimmield and Mowbray (1991)
70	ODP Leg 162 (Site 983)	Reykjanes Ridge	60.40	-23.64	1983.7	65	oxic	ARCT	Hyun et al. (1999)
71	GeoB4301-1	Canary Islands	29.15	-15.50	3614	11	oxic	NASE	Freudenthal et al. (2001)
72	GeoB4242-4	Canary Islands	29.68	-17.89	4292	7	oxic	NASE	Freudenthal et al. (2001)
73	GeoB9526-5	Cape Verde	12.44	-18.06	3231	86	suboxic	NATR	Zarriess and Mackensen (2010)
74	GeoB9527-5	Cape Verde	12.44	-18.22	3671	59	suboxic	NATR	Zarriess and Mackensen (2010)
75	GeoB6518-1	Congo Fan	-5.59	11.22	962	144	suboxic	GUIN	Weijers et al. (2009)
76	Hole 1082	SW African margin	-21.09	11.82	1280.6	20	suboxic	BENG	Giraudeau et al. (2002)
77	Hole 1084	SW African margin	-25.51	13.03	1992.2	18	suboxic	BENG	Giraudeau et al. (2002)
78	Hole 1085	SW African margin	-29.37	13.99	1713.1	20	suboxic	BENG	Giraudeau et al. (2002)
79	Hole 1087	SW African margin	-32.47	15.31	1371.6	20	suboxic	BENG	Giraudeau et al. (2002)
80	175-1085A	SW African margin	-29.37	13.99	1713.2	337	suboxic	BENG	Diester-Haass et al. (2001)
81	ODP Site 1085	SW African margin	-29.37	13.99	1713.1	33	suboxic	BENG	Murray et al. (2002)
82	ODP Let 165 (Hole 1002)	Cariaco Basin	10.71	-65.17	892.9	235	anoxic	GUIA	Yarincik et al. (2000)
83	M40/4_SL87	Balearic Basin	38.99	4.02	1897	130	oxic	MEDI	Weldeab et al. (2003)
84	Core 1430	Black Sea	41.43	29.43	663	5	anoxic	MEDI	Hirst (1974)
85	Core 1432	Black Sea	43.01	34.08	2248	15	anoxic	MEDI	Hirst (1974)
86	Core 1436	Black Sea	43.40	36.60	2158	18	anoxic	MEDI	Hirst (1974)
87	Core 1437	Black Sea	41.69	36.47	973	7	anoxic	MEDI	Hirst (1974)
88	Core 1440	Black Sea	42.20	34.36	207	23	anoxic	MEDI	Hirst (1974)
89	Core 1443	Black Sea	44.59	31.92	1057	24	anoxic	MEDI	Hirst (1974)
90	Core 1452	Black Sea	42.78	28.60	728	20	anoxic	MEDI	Hirst (1974)
91	Core 1462	Black Sea	43.05	33.04	2186	17	anoxic	MEDI	Hirst (1974)
92	Core 1470	Black Sea	42.07	41.27	1068	15	anoxic	MEDI	Hirst (1974)
93	Core 1472	Black Sea	43.15	39.91	1588	16	anoxic	MEDI	Hirst (1974)
94	Core 1484	Black Sea	44.70	36.89	386	12	anoxic	MEDI	Hirst (1974)

Because detrital Ba can represent a large fraction of total Ba (sometimes >50%), the choice of a suitable detrital Ba/Al ratio is important for correct estimation of Ba_{bio}. Although the influence of $(Ba/Al)_{detr}$ on $[Ba_{bio}]$ is relatively minor in the abyssal ocean where sediments are primarily biogenic, calculated values of $[Ba_{bio}]$ are quite sensitive to variation in $(Ba/Al)_{detr}$ in siliciclastic sediments from marginal marine settings (Dymond et al., 1992). Compilations of crustal composition data yield $(Ba/Al)_{detr}$ ratios between 0.005 and 0.010 (e.g., Taylor and McLennan, 1985), which have been used to estimate Ba_{bio} (or Ba_{xs}) in many studies (Dymond et al., 1992; Nürnberg et al., 1997; Bonn et al., 1998; Prakash Babu et al., 2002). However, a substantial fraction of Ba in detrital sediments appears to be lost during weathering and transport in the terrestrial environment, yielding siliciclastic $(Ba/Al)_{detr}$ ratios around 0.002-0.004 upon deposition in marine systems (Rutsch et al., 1995; Reitz et al., 2004). Thus, commonly used $(Ba/Al)_{detr}$ ratios based on average upper crustal compositions may overestimate $(Ba/Al)_{detr}$ and underestimate Ba_{bio} (or Ba_{xs}).

The accuracy of Ba_{bio} estimates can be improved by using formation-specific $(Ba/Al)_{detr}$ ratios. In modern marine systems, this can be done by finding the intercept of an exponential regression line on a Ba/Al vs. water depth crossplot (Klump et al., 2000; Pfeifer et al., 2001) or by detailed modeling of various detrital contributions in the area of interest (Pirrung et al., 2008). As these methods are difficult to apply to paleomarine systems, we used an approach based on estimating $(Ba/Al)_{detr}$ ratios from Al vs. Ba crossplots, in which a high concentration of samples along a line that passes through the origin is assumed to represent the detrital component of Ba (see Shen et al., 2014, for examples). This method yielded $(Ba/Al)_{detr}$ ratios for specific study units ranging from

0.0032 to 0.0046, which are consistent with the siliciclastic Ba/Al ratios reported by Rutsch et al. (1995) and Reitz et al. (2004). This method is conservative, since it assumes that the samples with the lowest Ba/Al ratios contain no biogenic barium. However, one must exercise caution in marine systems in which productivity is high and strongly correlated with detrital input, and a large proportion of barium is in the form of biogenic barite. In such cases, an array of samples exhibiting positive covariation of Ba with Al may not reflect the detrital Ba component. For example, abyssal samples from the modern equatorial Pacific yield a well-defined array with a Ba/Al ratio of ~0.32 (Murray et al., 2000), which is nearly two orders of magnitude higher than the average crustal $(Ba/Al)_{detr}$ ratio of 0.0065 (McLennan, 2001). In this case, the observed strong positive covariation of Ba and Al probably reflects a close coupling between eolian detrital input and primary productivity.

3.3. Calculation of productivity proxy fluxes

The calculation of mass accumulation rates (MAR) for the productivity proxies used in this study (TOC, P_{org}, and Ba_{bio}) is an improvement over the use of raw or Al-normalized elemental concentrations or enrichment factors, which can be strongly influenced by dilution effects (Tribovillard et al., 2006). In the following analysis, we report MARs for TOC, P_{org}, and Ba_{bio} in the same units of flux per unit area (i.e., mg cm^{-2} kyr^{-1}) with which marine productivity is reported in this study. MARs were calculated by multiplying the weight fractions [TOC], $[P_{org}]$, and $[Ba_{bio}]$ by the bulk accumulation rate (BAR) for a given sample:

$$MAR(X) = [X] \times BAR \quad (3)$$

where X is the productivity proxy of interest (TOC, P_{org}, or Ba_{bio}) and BAR is calculated as:

$$BAR = \rho \times LSR \quad (4)$$

where ρ is sediment dry bulk density (in units of g cm^{-3}) and LSR is linear sedimentation rate (in units of cm kyr^{-1}; Algeo et al., 2011, 2013). Henceforth, we will refer to the MARs of organic C, organic P, and biogenic Ba as OCAR, PAR, and BaAR, respectively.

In order to calculate productivity-proxy MARs, it is necessary to measure or estimate values for ρ and LSR for each sample. For the majority of the 94 sites examined here, ρ was reported in the source publication. For the remaining sites, we used an exponential function to estimate ρ as a function of sediment age:

$$\rho = 0.0794 \times \ln(x) + 0.650 \quad (5)$$

where ρ is sediment dry bulk density (in units of g cm^{-3}) and x is the age of the sample (in units of kyr, or thousands of years). The relationship in Equation 5, which yields a standard deviation of 0.08 g cm^{-3} and $r^2 = 0.90$, was derived from several dry bulk density datasets (Amo and Minagawa, 2003; Gallego-Torres et al., 2007; Freudenthal et al., 2001; Lyle et al., 1992; Murray and Prell, 1991). We found that bulk density showed a better relationship to sediment age than to burial depth.

Calculation of linear sedimentation rates requires an age-depth model for each sediment core that is typically based on a series of biostratigraphically or radiometrically dated tie points, between each pair of which sedimentation rates are assumed to be linear. The accuracy of this procedure is limited by the number of age tie points and the age uncertainty attached to each. In general, the effect of assuming linear sedimentation rates

between tie points is to even out short-term variability in sediment accumulation. With increasing burial depth, compaction causes a reduction in LSRs, but a corresponding increase in the dry bulk density of the sediment compensates for this effect and yields an unchanged mass accumulation rate, assuming no loss or gain of material in the sediment.

An age-depth model for each of the 94 study units was constructed from age and depth information provided in the original published source, from which a LSR was determined for each sample. For many of the study units, highly detailed age-depth models could be constructed, e.g., owing to the availability of oxygen-isotope correlations linked to the standard marine isotope stage (MIS) stratigraphy, for which calibrated astrochronologies are now available (Lisecki and Raymo, 2005). In addition, deep-ocean successions tend to be relatively more complete and to contain fewer temporal gaps than shallow-marine and continental successions (Sadler, 1981), introducing fewer uncertainties into the age-depth models for such units.

3.4. Modern oceanic primary productivity and export productivity estimates

We compared our calculated values of OCAR, PAR, and BaAR with site-specific estimates of modern marine productivity for the 94 study sites. In order to assign a productivity value to each site, we used estimates derived from three sources: (1) satellite measurements of chlorophyll 'a' concentrations for 57 oceanic provinces (Longhurst et al., 1995), (2) 122 field measurements of primary productivity based on several methods, as compiled by Dunne et al. (2005), and (3) >3000 field measurements of productivity based on the ^{14}C uptake method, from an Oregon State University database (www.science.oregonstate.edu/ocean.productivity/). These datasets will be referred to

subsequently as L95, D05, and OS, respectively. Longhurst et al. (1995) and Longhurst (2010) undertook a detailed analysis of spatial variation in chlorophyll 'a' concentrations in the modern ocean, from which they identified 57 irregularly shaped oceanic provinces with internally consistent productivity ranges. Since productivity measurements from the three sources above were rarely available for the exact location of each study core in our database, we employed the ocean-province framework of L95 to assign site-specific estimates of primary productivity and export productivity (Table 2; note that our 94 study sites are located in just 25 of the 57 oceanic provinces of L95). In order to accurately locate the study sites relative to the L95 oceanic provinces, we made use of Google Earth and a shapefile depicting the province boundaries that is available from <www.ecomarres.com>. Because none of the sources above contained productivity estimates for Saanich Inlet, we made use of estimates from Timothy and Soon (2001) based on the ^{14}C uptake method and included them in the OS compilation.

In this study, 'primary productivity' is defined as the rate of fixation of atmospheric or dissolved inorganic carbon as organic matter in the photic zone of the ocean, and 'export productivity' as the rate at which sinking marine organic matter is transferred to the oceanic thermocline (below ~200 m water depth). While phytoplankton biomass is not comprised entirely of carbon, productivity is typically expressed as the mass flux of organic carbon per unit area in order to facilitate comparisons across environments with different primary producers. The productivity estimates in this study are all reported in units of mg C cm^{-2} kyr^{-1}.

Province code	Province name	*pe*-ratio	Dunne et al. 2005 (D05)					Oregon State (OS)				Longhurst et al. 1995 (L95)	
			primary production (mg C cm^{-2} kyr^{-1})		export production (mg C cm^{-2} kyr^{-1})		n =	primary production (mg C cm^{-2} kyr^{-1})		export production (mg C cm^{-2} kyr^{-1})	n =	primary production (mg C cm^{-2} kyr^{-1})	export production (mg C cm^{-2} kyr^{-1})
			mean	std. deviation	mean	std. deviation		mean	std. deviation				
ANTA	Antarctic	38.45%	47,718	30,108	17,984	13,810	11	3,278	1,638	1,260	11	16,500	6,344
APLR	Austral Polar	45.12%	22,419	13,645	11,177	7,858	7	–	–	–	–	39,800	17,959
ARAB	Northwest Arabian Upwelling	20.48%	39,420	13,709	7,644	4,705	8	42,800	23,926	8,765	22	45,400	9,298
ARCT	Atlantic Arctic	71.15%	22,564	–	16,055	–	1	19,581	18,618	13,933	3	48,400	34,438
BENG	Benguela Current Coastal	–	–	–	–	–	–	–	–	–	–	32,300	–
CCAL	California Upwelling Coastal	31.68%	25,515	10,779	7,266	3,254	4	37,942	68,261	12,019	937	38,800	12,291
CHIL	Chile-Peru Current Coastal	32.09%	86,783	4,463	27,672	5,526	2	67,064	51,273	21,522	123	26,900	8,633
GUIA	Guiana Current Coastal	–	–	–	–	–	–	–	–	–	–	69,900	–
GUIN	Guinea Current Coastal	–	–	–	–	–	–	54,473		–	1	49,500	–
ISSG	Indian Ocean South Subtropical Gyre	–	–	–	–	–	–	–	–	–	–	7,100	–
MEDI	Mediterranean and Black Seas	–	–	–	–	–	–	19,702	15,107	–	97	21,600	–
MONS	Indian Ocean Monsoon Gyres	15.19%	23,230	10,271	4,107	4,172	2	2,756	9,536	419	41	10,500	1,595
NASE	North Atlantic Subtropical Gyre East	8.94%	26,609	8,033	2,472	1,333	2	–	–	–	–	12,200	1,091
NATR	North Atlantic Tropical Gyre	–	–	–	–	–	–	22,401	20,814	–	16	10,600	–
NPSE	North Pacific Subtropical Gyre East	–	–	–	–	–	–	–	–	–	–	11,100	–
NPSW	North Pacific Subtropical Gyre West	–	–	–	–	–	–	1,428	2,475	–	23	10,900	–
NPTG	North Pacific Tropical Gyre	7.84%	–	–	–	–	–	14,023	7,195	1,100	50	5,900	463
OCAL*	Offshore California Current	31.68%	25,515	10,779	7,266	3,254	4	37,942	68,261	12,019	937	11,700	3,706
PEQD	Pacific Equatorial Divergence	18.06%	57,975	72,838	13,344	22,477	12	21,880	16,414	3,951	131	11,300	2,040
PNEC	North Pacific Equatorial Countercurrent	14.89%	15,790	1,783	2,289	675	3	10,542	5,526	1,569	87	10,700	1,593
PSAW	Pacific Subarctic Gyre West	–	–	–	–	–	–	–	–	–	–	26,400	–
SANT	Subantarctic	–	–	–	–	–	–	8,490	4,273	–	15	12,000	–
SPSG	South Pacific Subtropical Gyre	9.01%	16,796	11,053	1,652	1,214	5	9,297	8,036	837	30	8,700	784
SSTC	South Subtropical Convergence	–	–	–	–	–	–	–	–	–	–	13,600	–
WARM	Western Pacific Warm Pool	13.59%	30,828	6,406	4,282	1,773	2	9,551	7,159	1,298	40	8,200	1,114

Table 2. Productivity and export production values compiled within the regional framework defined by Longhurst et al. (1995). Particle export ratios were calculated from the mean productivity and export data in the D05 dataset, where primary and export production were separate measurements. Export production for the L95 and OS datasets is an estimate made by multiplying this *pe*-ratio by the mean primary productivity in each province. Since L95 productivity estimates are satellite based and time integrated, they have no standard deviation. *Software available through <http://www.lifewatch.be/> was used to group lat-long coordinates into Longhurst et al. (1995) provinces. Since this program does not distinguish the OCAL and CCAL provinces, these two were combined in the D05 and OS datasets. A separate productivity value was used for OCAL in the L95 dataset.

Net primary production (NPP) is defined as the rate at which primary producers (phytoplankton in marine systems) assimilate carbon into their bodies for purposes of long-term growth, rather than carbon fixation that is used to support respiration. This is in contrast to gross primary production (GPP), which includes all carbon fixation by primary producers, including carbon that is quickly respired to support metabolic processes. The ^{14}C uptake method, which was used in the *in situ* OS productivity estimates and in calibrating the L95 satellite-based estimates, has been the subject of some discussion about whether measurements more closely approximate NPP or GPP. Unlike measurements of O_2 in incubations, where oxygen can be both produced and consumed, ^{14}C uptake measurements are always positive, indicating that they fall somewhere between NPP and GPP (see Marra, 2009). Since many phytoplankton reassimilate respired carbon but not respired oxygen (Marra, 2008), ^{14}C uptake has been contrasted with estimates of GPP derived from oxygen production in order to determine NPP as a fraction of GPP (Hashimoto et al., 2005). Thus, it appears that ^{14}C uptake measurements closely approximate net primary production (NPP) in most natural systems when incubated over a full diurnal (24-hour) cycle (Fahey and Knapp, 2007; Marra, 2009). Since the productivity estimates used in this study are either directly (OS) or indirectly (L95) derived from ^{14}C uptake, they most closely approximate net primary production (NPP).

The export ratio, i.e., the fraction of photosynthetically fixed carbon that is exported from the surface mixed layer, can vary over a wide range (from 4% to 72% according to Dunne et al., 2005). Due to this extreme variability, sedimentary proxies such as OCAR, PAR, and BaAR can be expected to exhibit a stronger relationship to

export productivity than to primary productivity. We estimated modern export productivity fluxes for our 94 study sites from the D05 dataset, which contains paired measurements of primary and export productivity, allowing the export ratio to be determined for each site in that study. We converted these data to the L95 ocean-province framework in order to minimize the effects of seasonal and small-scale spatial variability and to maintain consistency with our primary productivity estimates (Table 2). We then calculated an average export productivity flux and export ratio for each L95 province (note that no export productivity data were available in D05 for 12 of the 25 oceanic provinces considered in this study).

In comparing modern productivity estimates with productivity-proxy MARs in the sediment record, it is important to keep in mind differences in spatial and temporal scales between these datasets. Our estimates of modern productivity fluxes are based on averages for large oceanic areas (i.e., the 57 oceanic provinces of L95), within each of which some spatial variation exists, whereas each of the 94 study cores records productivity at a single, specific site. All modern productivity measurements are instantaneous values in a geologic sense, even when integrated over a series of years as for the L95 dataset. In contrast, marine sediments record a time-averaged signal in which a single centimeter can integrate hundreds to thousands of years of productivity variation, and substantial smoothing of the productivity signal can result from post-depositional bioturbation of the sediment (e.g., Wheatcroft, 1990). Another consideration is that all of the reported modern productivity measurements were made within the past half-century and, thus, potentially record anthropogenic influences on nutrient cycles and marine ecosystems (Galloway et al., 2004; Behrenfeld et al., 2006). On the other hand, some of

the sedimentary productivity flux estimates represent conditions during Quaternary glacial stages or prior to the onset of Northern Hemisphere glaciation at ~2.5 Ma, i.e., times when ocean circulation intensity was somewhat different than at present (Raymo et al., 1992). As a result, modern productivity estimates are not necessarily representative of productivity conditions in a given oceanic region thousands or millions of years ago. Such changes over time are likely to account for much of the divergence between the modern *in-situ* and ancient sediment-based productivity estimates of this study.

3.5. Calculation of preservation factors (PF)

Preservation factors (PF) represent the fraction of either primary or export productivity that is ultimately buried (and thus preserved) in the sedimentary record (Trask, 1953; Bralower and Thierstein, 1987). Its complement, 1– PF, represents the cumulative loss of a given component due to remineralization in the water column and/or the sediment. The relationship of PF to productivity is given by Equation 6 for organic C and Equation 7 for organic P:

$$PF_Z = OCAR / PROD_Z \quad (6)$$

$$PF_Z = PAR \times (C/P)_{org} / PROD_Z \quad (7)$$

where $PROD_Z$ is either primary productivity ($PROD_{prim}$) or export productivity ($PROD_{exp}$), as quantified for a specific study site from the L95, D05, or OS dataset. Because export productivity is always a fraction of primary productivity, a fixed amount of a given component in the sediment will yield a larger PF for the former (exp) relative to the latter (prim).

Based on calculated primary and export productivity fluxes (Section 3.4), we determined preservation factors (PF) for all study samples for which TOC data were available. For a few samples from Saanich Inlet, PF_{prim} exceeded 100%, and these values were converted to 100% for display purposes. This result is not necessarily impossible as short-term organic carbon accumulation rates (as recorded in the sediment record) easily might exceed the average long-term primary productivity rate for a given site.

4. Results

4.1. Robustness of modern productivity estimates

We evaluated the degree of agreement between the two principal methods of modern productivity estimation (i.e., chlorophyll 'a' and ^{14}C uptake) for oceanic provinces having productivity estimates based on both methods. The two datasets based on ^{14}C uptake measurements in part (D05) or in full (OS) showed some agreement, with an r^2 of 0.37 (n = 11). The OS ^{14}C-based and L95 satellite-based estimates, which were both based on a much larger number of measurements than the D05 dataset, showed the strongest agreement, with an r^2 of 0.39 (n = 17). However, there was virtually no relationship between the L95 and D05 datasets (r^2 <0.01, n = 13), largely because the D05 dataset detected much greater productivity than the L95 dataset in coastal upwelling zones, the equatorial Pacific, and the Southern Ocean. Since high productivity drives a great deal of the scientific interest in these systems, it is possible that the *in situ* point measurements used in the D05 dataset reflect a spatial or temporal selection bias, while the L95 dataset integrates larger areas over longer (multi-annual) timescales, thus yielding lower average productivity estimates.

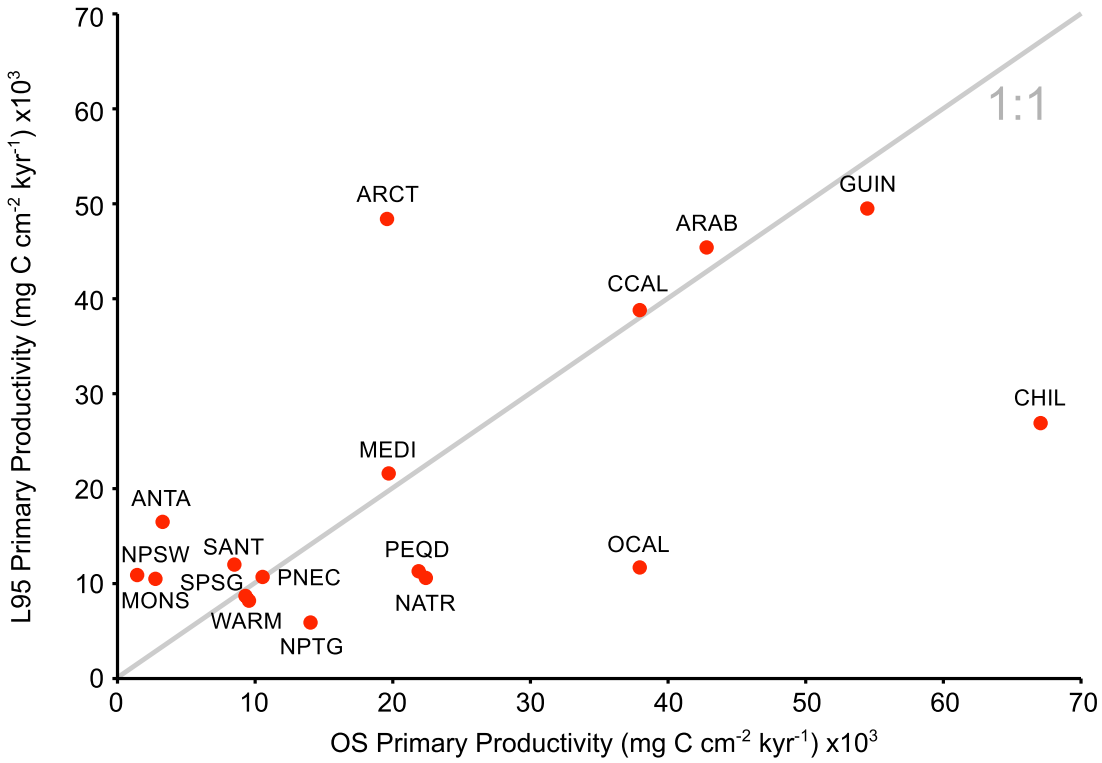

Figure 8: Comparison of estimates of productivity from the Longhurst et al., 1995 (L95) dataset based on satellite chlorophyll measurements, and the Oregon State (OS) dataset based on *in situ* measurements using the ^{14}C uptake method integrated over the depth of the photic zone and averaged by L95 oceanic province. Points are labeled with code indicating which province is represented. For province codes and standard deviations associated with OS regional averages, see Table 2.

Whereas all datasets exhibit a similar range of productivity values (approximately 10,000 to 60,000 mg C cm^{-2} kyr^{-1}), the OS dataset includes a much larger number of individual samples (n = 3170) than the D05 dataset, making it more likely to average out seasonal, climatic, and spatial variability within each oceanic province. Although the oceanic provinces of L95 are based on internally uniform productivity values, it is worth noting that the ^{14}C-uptake sample points taken to represent a given region sometimes cover only a small fraction of a province's total area and, hence, of its internal variation

in productivity. Based on these considerations and the superior agreement between them (Fig. 8), we adopted the L95 and OS productivity datasets as our primary sources of estimates of modern primary productivity, reserving the smaller D05 dataset for estimates of export productivity.

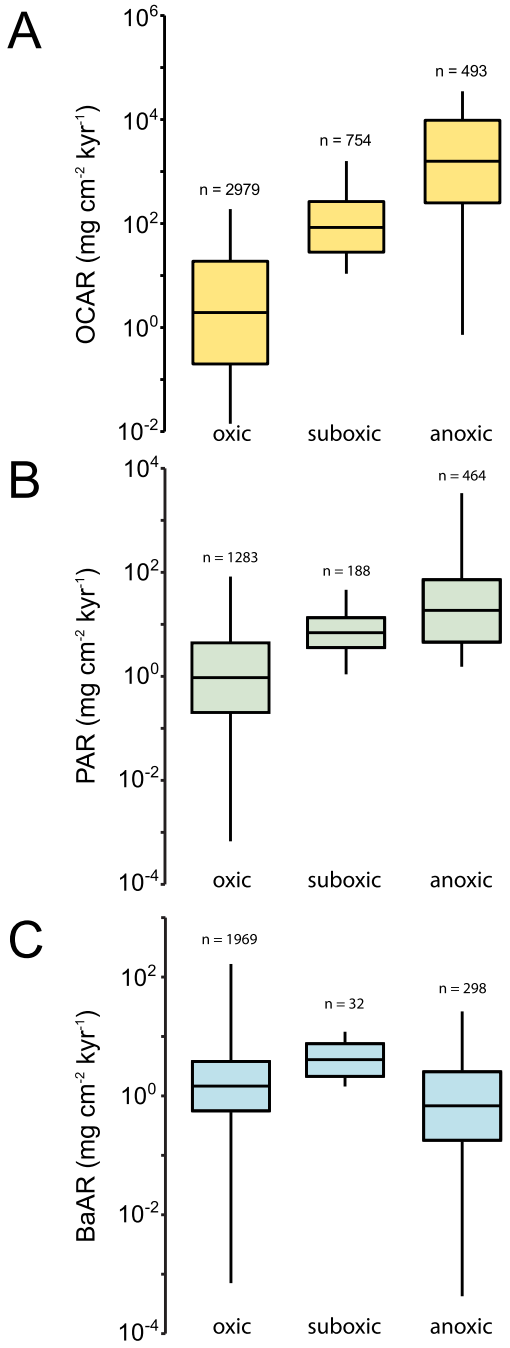

Figure 9: (A) Organic carbon accumulation rate (OCAR), (B) phosphorus accumulation rate (PAR), and (C) biogenic barium accumulation rate (BaAR) by redox facies. Boxes represent means and standard deviation ranges, whereas the whiskers show the full range of values for each redox category.

4.2. Organic carbon accumulation rates (OCAR)

Redox conditions strongly influence the preservation of organic carbon for both the L95 and OS productivity datasets. Both mean and maximum OCAR increase with decreasing dissolved oxygen levels (Fig. 9A). Mean OCAR values increase by a factor of ~30X (1.5 log units) between oxic and suboxic facies, and by another factor of ~30X between suboxic and anoxic facies, implying a major role for water-column redox conditions in organic carbon preservation. OCAR generally represents a minute fraction of primary production in oxic and suboxic facies, in which PF_{prim} averages ~0.1% and ~0.6%, respectively (Table 3). The L95 and OS datasets diverge significantly for anoxic facies, in which PF_{prim} averages ~0.9% (max. 6.3%) in the L95 dataset but 18% (max. 100%, see below) in the OS dataset. This difference is largely due to the inclusion of Saanich Inlet, an anoxic fjord located on Vancouver Island, in the OS dataset, for which calculated PF_{prim} exceeded 100% for a number of samples. Excluding Saanich Inlet, the average PF_{prim} for the OS dataset is reduced to 1.1% (max. 6.9%), which is in good agreement with the L95 dataset. For both the L95 and OS datasets, the differences between redox facies were significant at the $p(a) < 0.01$ level using a two-tailed Student's t-test. Although export ratios for anoxic facies in our database were not available in D05, mean PF_{exp} was higher in the suboxic than in the oxic facies (Table 3). For both the L95 and OS export production estimates, the difference between oxic and suboxic settings was statistically significant at the $p(a) < 0.05$ level using a two-tailed Student's t-test.

	Oxic		Suboxic		Anoxic		
	L95	OS	L95	OS	L95	OS	
Preservation Factor							
Primary Production							
mean	0.07%	0.12%	0.56%	0.64%	0.94%	18.17%	(1.10%)
s.d.	0.14%	0.46%	0.67%	0.53%	0.89%	27.30%	(1.24%)
min	<0.00%	<0.00%	0.03%	0.06%	<0.00%	<0.00%	
max	1.57%	5.97%	5.91%	2.37%	6.33%	100.00%	(6.94%)
n =	2979	2580	754	306	407	258	(172)
Export Production							
mean	0.38%	0.69%	4.13%	2.96%	–	–	
s.d.	0.86%	3.14%	4.38%	2.91%	–	–	
min	<0.00%	<0.00%	0.46%	0.19%	–	–	
max	10.32%	39.32%	18.42%	9.70%	–	–	
n =	2788	2389	17	17	0	0	

Table 3: Preservation factor (PF) calculated as a proportion of primary production and as a proportion export production, for the L95 and OS productivity estimates, and for each of the three redox categories used in this study.

OCAR shows a strong correlation to BAR ($r^2 = 0.86$), with a regression slope (m) of 1.72 for the full dataset (Fig. 10). When considered by redox facies, a steeper slope ($m = 1.76$) was obtained for oxic sites relative to suboxic/anoxic sites ($m = 1.11$). This pattern is broadly consistent with that observed in Holocene data by Tyson (2005), although the regression slopes we calculated from >5000 data points are steeper, indicating a stronger influence of BAR on organic carbon preservation than previously recognized (see Section 2.2). The linear equation in log-log space for our full dataset (Fig. 10) is:

$$\mathrm{Log}_{10}(\mathrm{OCAR}) = 1.72 \times \mathrm{Log}_{10}(\mathrm{BAR}) + 0.09 \quad (8)$$

where OCAR is in units of mg cm^{-2} kyr^{-1} and BAR is in units of g cm^{-2} kyr^{-1}. This is equivalent to the following exponential equation in linear space:

$$\mathrm{OCAR} = 10^{0.09} \times \mathrm{BAR}^{1.72} \quad (9)$$

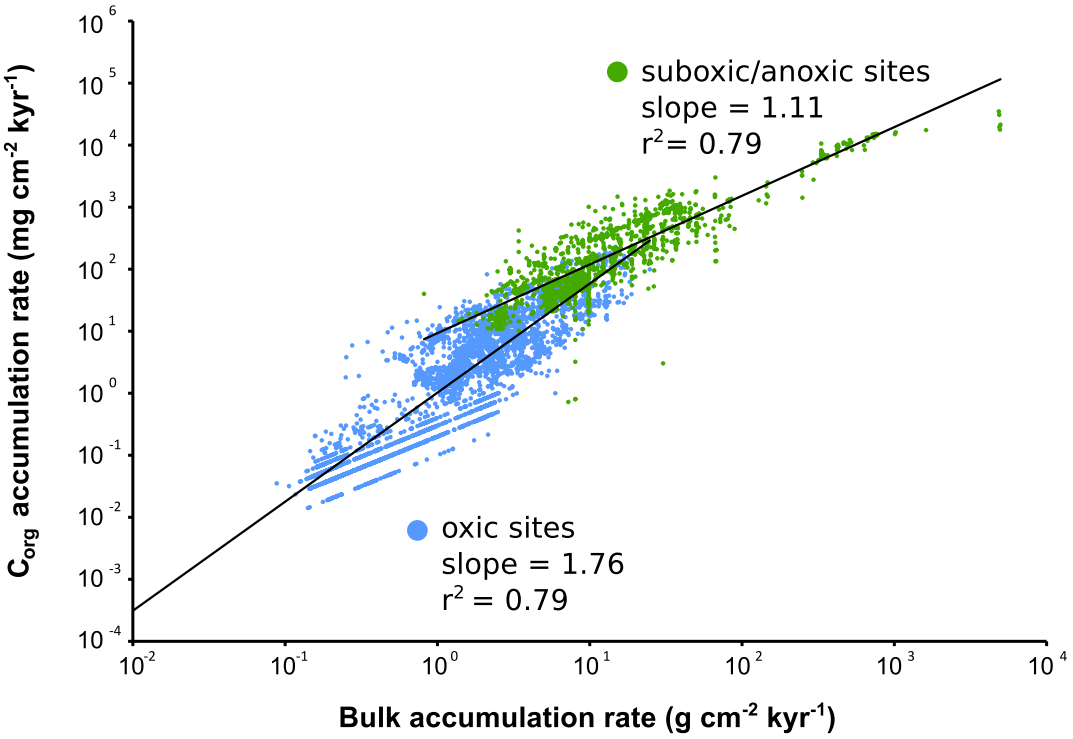

Figure 10: Bulk accumulation rate (BAR) versus organic carbon accumulation rate (OCAR) by redox facies, shown on a log-log scale. The suboxic/anoxic facies exhibits a lower regression slope *m* (1.11) than the oxic facies (1.76); *m* for the combined dataset is 1.72 (r^2 = 0.86; *n* = 4226).

Since OCAR is equal to TOC × BAR × 1000, with the factor of 1000× accounting for the conversion of g to mg, the equation can be simplified by eliminating the BAR × 1000 term from both sides. This operation cancels the units of mass flux and yields a dimensionless term (TOC) as a function of BAR, and rendering the equation in terms of a real relationship between two fully independent variables:

$$TOC = 10^{-3.09} \times BAR^{0.72} \quad (10)$$

Evaluated as a function of redox facies, different regression relationships between OCAR and BAR are exhibited by suboxic/anoxic versus oxic sites (Fig. 10):

$$\mathrm{Log_{10}(OCAR)} = 1.11 \times \mathrm{Log_{10}(BAR)} + 0.97 \quad \text{(suboxic/anoxic)} \tag{11}$$

$$\mathrm{Log_{10}(OCAR)} = 1.76 \times \mathrm{Log_{10}(BAR)} + 0.01 \quad \text{(oxic)} \tag{12}$$

These relationships can be transformed in the same manner as for the full dataset (i.e., via Equations 9 and 10) to yield expressions relating two independent variables (i.e., TOC and BAR) for each redox facies.

When one considers OCAR as a fraction of primary or export production (i.e., as given by the preservation factor, or PF), strong correlations are observed with BAR (in agreement with the findings of Felix, 2014). This relationship is stronger when PF is calculated as a percentage of primary production (Fig. 11A) rather than of export production (Fig. 11B). PF_{prim} covaries positively with BAR in both productivity datasets ($r^2 = 0.87$ for OS; $r^2 = 0.77$ for L95), with PF_{exp} showing a similar but somewhat weaker relationship ($r^2 = 0.78$ for OS; $r^2 = 0.56$ for L95). Since preservation factors are calculated from three fully independent variables (i.e., TOC, BAR, and productivity), this relationship allows primary productivity to be isolated as a function of TOC and BAR, two parameters that can be measured or estimated in most paleomarine systems (see Section 3.3).

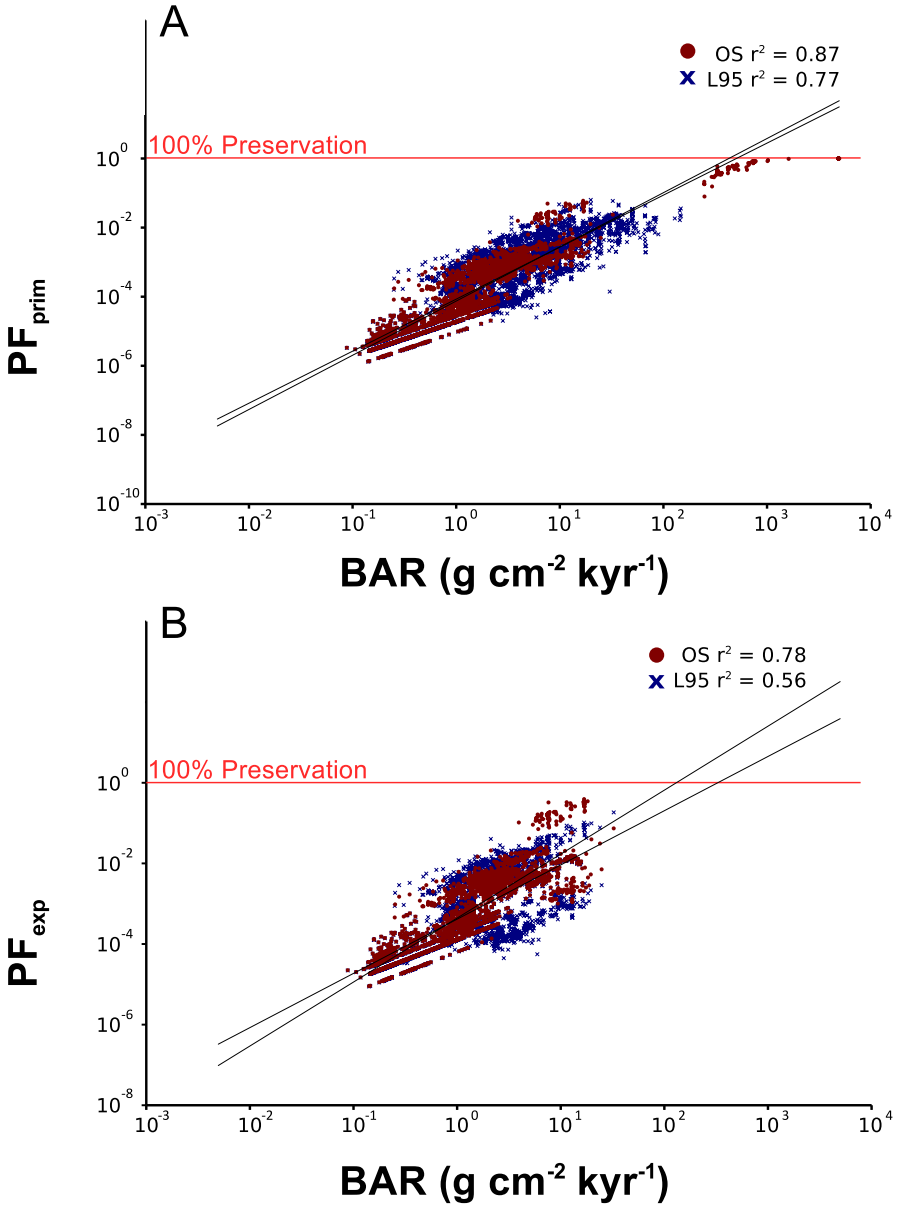

Figure 11: Bulk accumulation rate (BAR) versus organic carbon preservation factor (PF) for (A) primary production and (B) export production, for the L95 and OS datasets. L95: *n* = 4140 for primary production, *n* = 2805 for export production. OS: *n* = 3144 for primary production, *n* = 2406 for export production.

	Regression Equation	r^2
OCAR		
Primary Production		
L95	$Log_{10}(OCAR) = 2.53 \times Log_{10}(Prod.) - 9.92$	0.33
OS	$Log_{10}(OCAR) = 2.07 \times Log_{10}(Prod.) - 7.19$	0.26
Export Production		
L95	$Log_{10}(OCAR) = 1.07 \times Log_{10}(Exp.) - 3.42$	0.20
OS	$Log_{10}(OCAR) = 1.73 \times Log_{10}(Exp.) - 5.70$	0.30
PAR		
Primary Production		
L95	$Log_{10}(PAR) = 1.39 \times Log_{10}(Prod.) - 5.59$	0.30
OS	$Log_{10}(PAR) = 0.36 \times Log_{10}(Prod.) - 1.33$	0.03
Export Production		
L95	$Log_{10}(PAR) = 0.69 \times Log_{10}(Exp.) - 2.25$	0.19
OS	$Log_{10}(PAR) = 0.32 \times Log_{10}(Exp.) - 1.00$	0.05
BaAR		
Primary Production		
L95	$Log_{10}(BaAR) = -0.25 \times Log_{10}(Prod.) + 1.19$	0.03
OS	$Log_{10}(BaAR) = -0.23 \times Log_{10}(Prod.) + 1.14$	0.04
Export Production		
L95	$Log_{10}(BaAR) = -0.09 \times Log_{10}(Exp.) + 0.44$	0.02
OS	$Log_{10}(BaAR) = -0.09 \times Log_{10}(Exp.) + 0.42$	0.01

Table 4: Equations and correlation coefficients for linear regression equations in log-log space relating mass fluxes of organic carbon, phosphorus, and excess barium to primary and export production as estimated in the L95 and OS datasets.

OCAR shows positive covariation with estimates of primary productivity, with r^2 values of 0.26 (L95) and 0.33 (OS) (Table 4, Fig. 12A). Comparable correlations (r^2 = 0.30, L95; r^2 = 0.20, OS) are seen between OCAR and estimates of export production (Table 4, Fig. 12B). While weaker than the correlations observed between BAR and OCAR, these correlations are between fully independent parameters and likely indicate a real relationship between productivity and organic carbon accumulation, albeit modified by preservational factors.

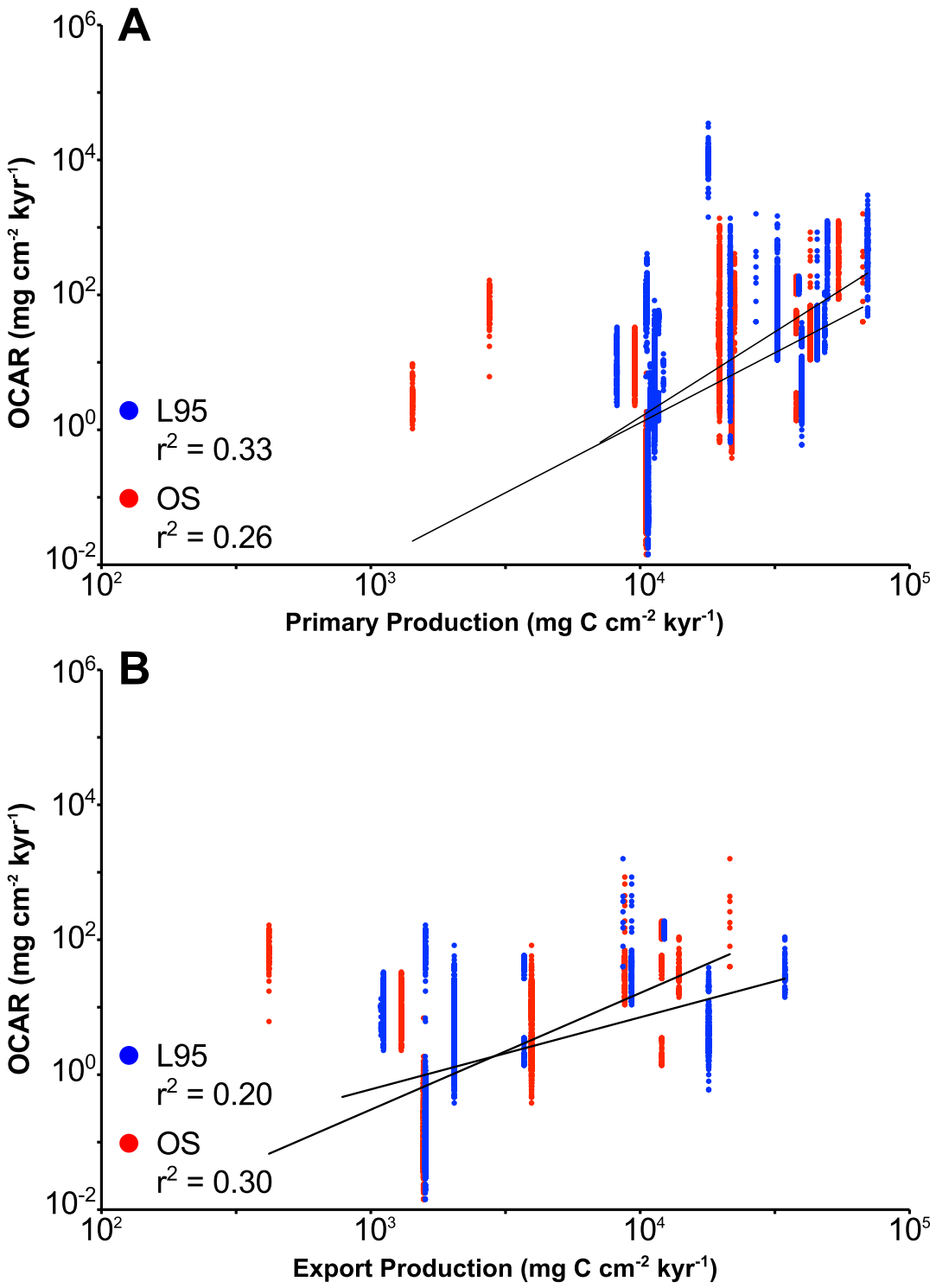

Figure 12: Primary production (A) and export production (B) versus organic carbon accumulation rate (OCAR) for the L95 and OS datasets. *n* = 4226.

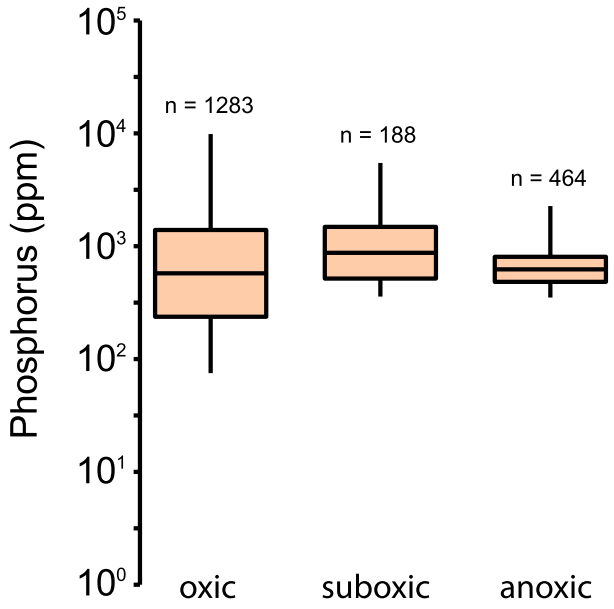

Figure 13: Phosphorus concentrations by redox facies. Boxes represent means and standard deviation ranges, whereas the whiskers show the full range of values for each redox category.

4.4. Organic phosphorus accumulation rates (PAR)

Redox conditions influence sedimentary phosphorus accumulation. Mean PAR increases under more reducing conditions, with average values more than a factor of 10× higher in anoxic facies than in oxic facies (Fig. 9B). Average P_{org} concentrations peak in suboxic systems (1035 ppm), although the differences in mean concentrations between redox facies are not significant (Fig. 13). While there is considerable overlap between redox facies at lower P_{org} concentrations, maximum observed values decrease under more reducing conditions. Thus, oxic facies occasionally yield P_{org} concentrations to >5500 ppm, whereas P_{org} concentrations in anoxic facies are uniformly <2500 ppm (Fig. 13). These patterns reflect the partial retention of remineralized organic phosphorus in oxidized sediments containing Fe-oxyhydroxides (Filippelli and Delaney, 1996; Delaney, 1998; Algeo and Ingall, 2007).

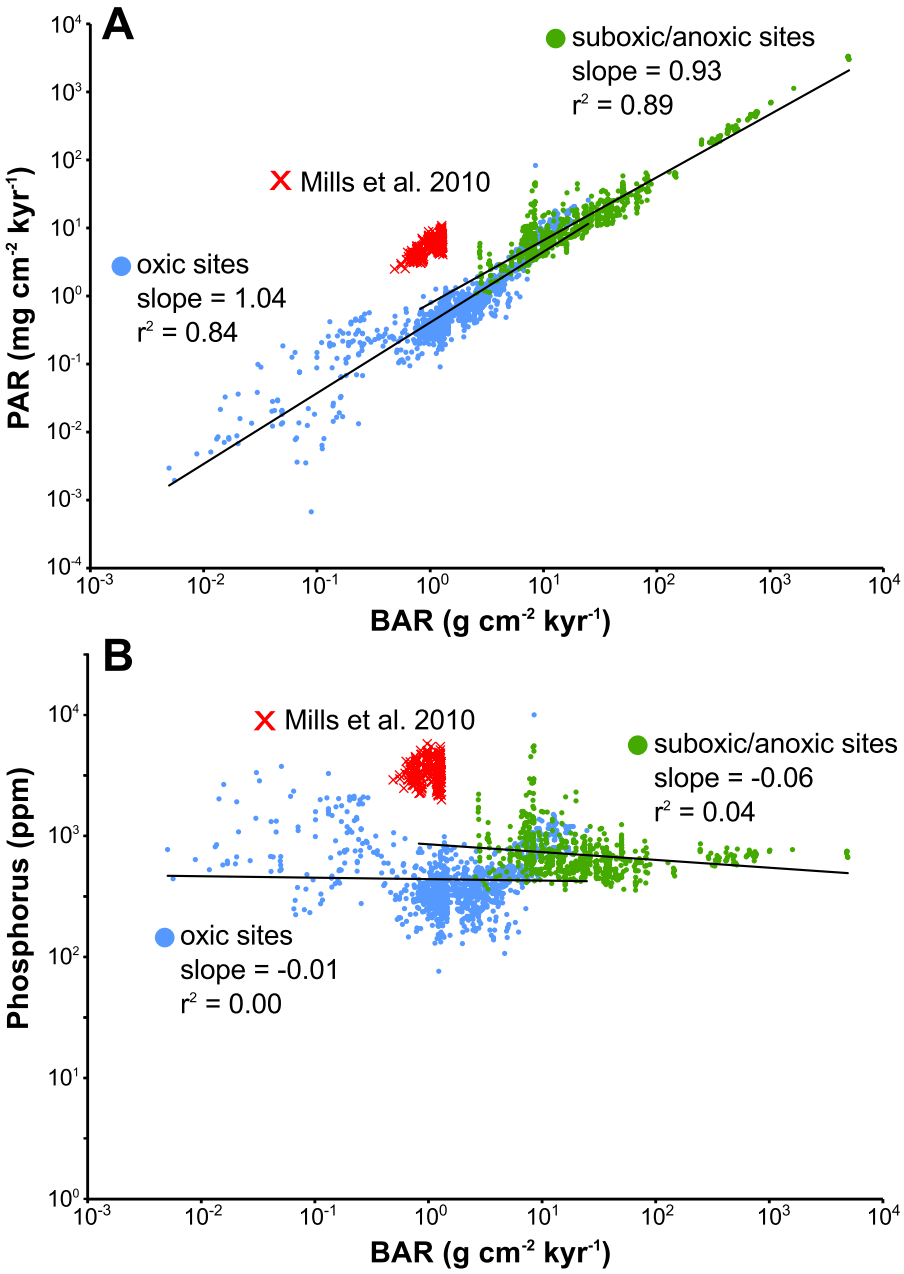

Figure 14: (A) Bulk accumulation rate (BAR) versus organic phosphorus accumulation rate (PAR), shown on a log-log scale. Slopes are approximately 1.0 for both oxic (*m* = 1.04) and suboxic/anoxic (*m* = 0.93) units. Data from Mills et al. (2010) appear to be outliers and are therefore shown separately. *m* for the combined dataset, not including Mills et al., 2010, is 1.07 (r^2 = 0.92; *n* = 1935). (B) Bulk accumulation rate (BAR) versus organic phosphorus concentration, shown on a log-log scale. Slope is essentially flat (*m* = 0.07 for the full dataset, r^2 = 0.05)

PAR shows positive covariation with BAR, yielding a regression slope (m) of 1.07 (r^2 = 0.92) for the full dataset (Fig. 14A). Both oxic and suboxic/anoxic sites exhibit strong positive relationships with BAR, with m of 1.04 (r^2 = 0.84) and 0.93 (r^2 = 0.89), respectively. These calculations exclude the data from Mills et al. (2010), which are from an oceanic hydrothermal plume region and represent obvious outliers in our dataset. When P_{org} concentrations are plotted against BAR, there is little relationship between the variables (r^2 = 0.05), with the former defining a roughly horizontal trend centered on $P_{org} = 10^{2.75}$ (~560) ppm (Fig. 14B).

PAR also shows positive covariation with both primary and export production (Fig. 15). PAR correlates more strongly with the L95 satellite-based primary productivity measurements (r^2 = 0.30) than with the ^{14}C-based OS dataset (r^2 = 0.03), largely due to lower productivity estimates for the Southern and Indian oceans in the latter source (Fig. 15A). However, PAR does not show any systematic increase above productivity values of ~20×10^3 (or ~$10^{4.3}$) mg C cm^{-2} kyr^{-1}. In contrast, PAR increases nearly monotonically with organic carbon export, although the relationship is weaker (Fig. 15B). Correlations with the L95 productivity estimates are stronger (r^2 = 0.19) than those with the OS dataset (r^2 = 0.05).

4.5. Biogenic barium accumulation rates (BaAR)

BaAR exhibits an unusual relationship to redox facies. Although the suboxic facies exhibits the highest mean BaAR (~4 mg cm^{-2} kyr^{-1}), the highest peak values (>30 mg cm^{-2} kyr^{-1}) are found in the oxic facies (Fig. 9C). However, the range of BaARs for the oxic, suboxic, and anoxic facies are not significantly different.

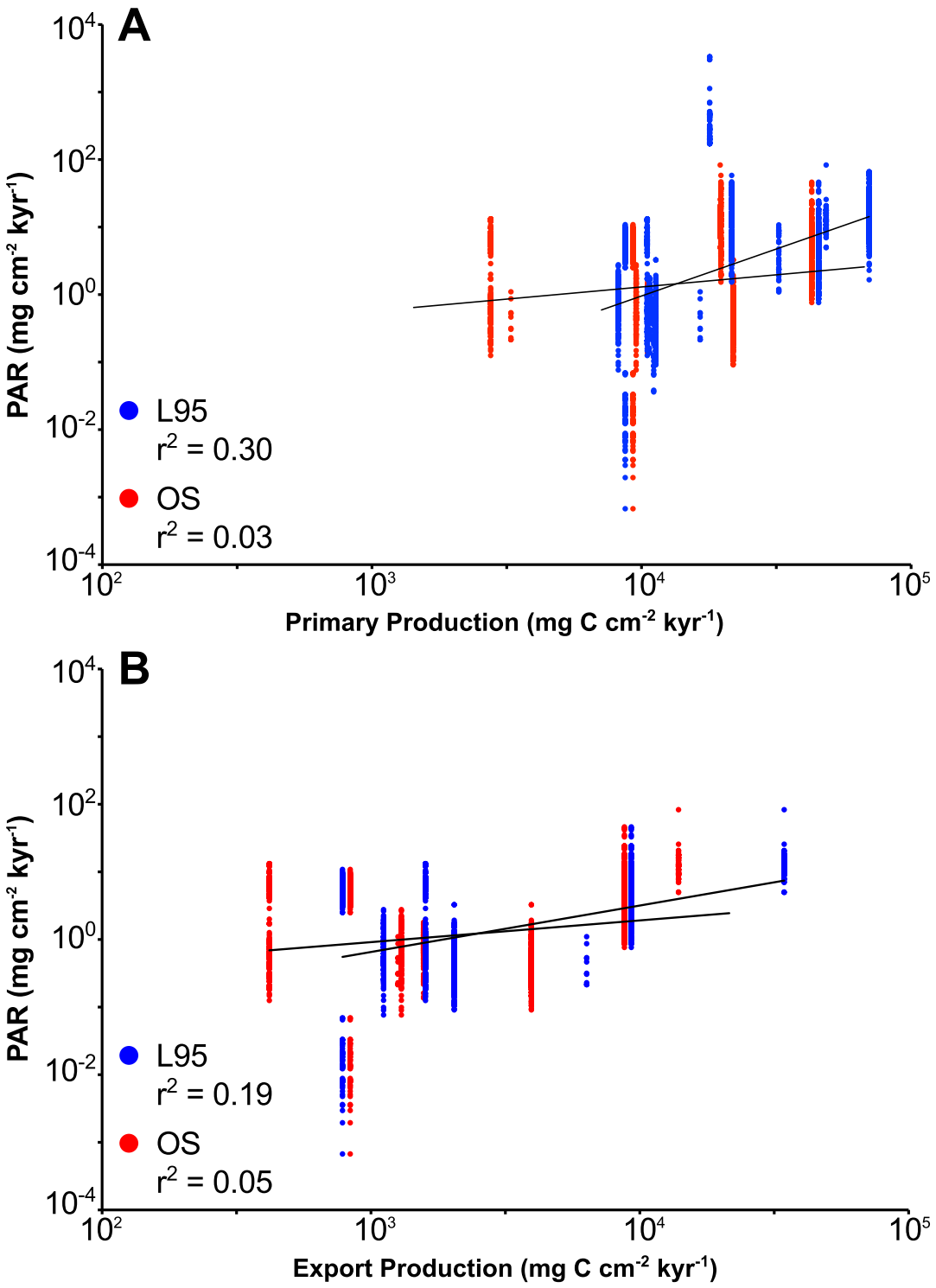

Figure 15: (A) Primary production and (B) export production versus phosphorus accumulation rate (PAR) for the L95 and OS datasets. *n* = 1935.

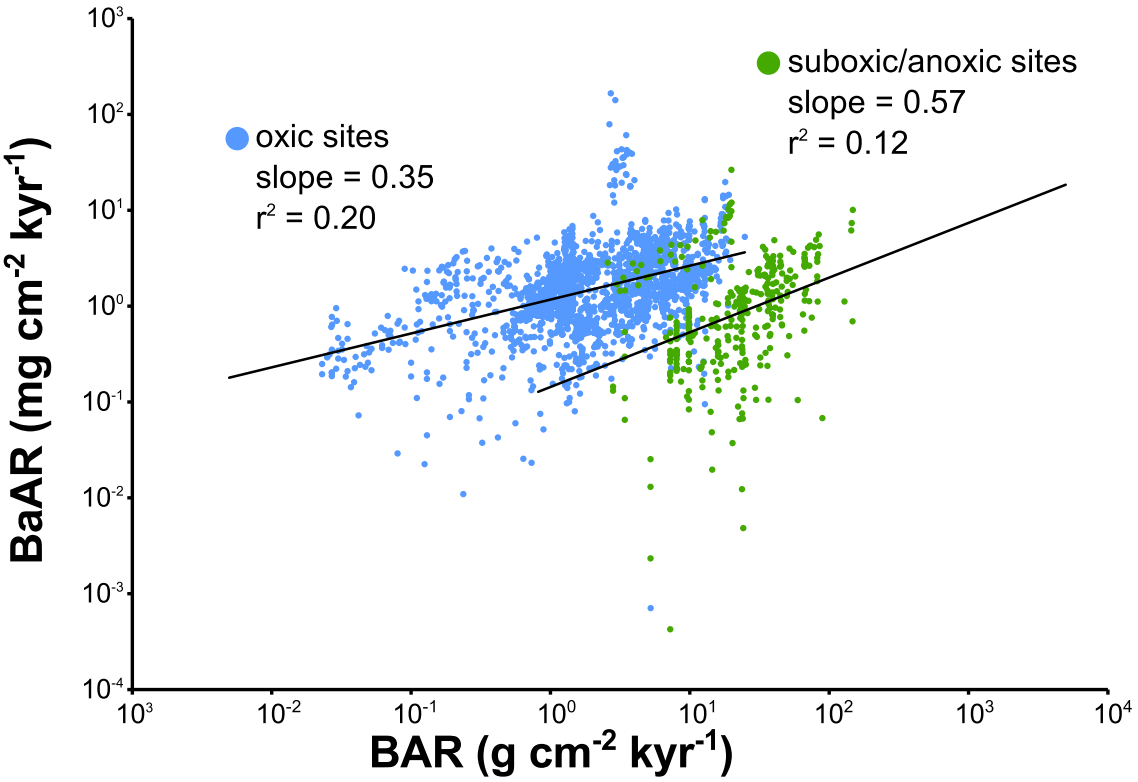

Figure 16: Bulk accumulation rate (BAR) versus organic carbon accumulation rate (BaAR) by redox facies, shown on a log-log scale. The suboxic/anoxic facies exhibits a steeper regression slope *m* (0.57) than the oxic facies (0.35), while the downward shift in intercept suggests a redox effect on preservation. The slope *m* for the combined dataset is 0.16 (r^2 = 0.05; *n* = 2299).

BaAR is not strongly influenced by BAR. For the full dataset, the relationship between BAR and Ba_{bio} accumulation is statistically insignificant (m = 0.16; r^2 = 0.05; Fig. 16). Individual redox facies exhibit somewhat stronger relationships, with oxic facies yielding m of 0.35 (r^2 = 0.20) and suboxic/anoxic facies yielding m of 0.57 (r^2 = 0.12). Although the slopes of the BaAR-BAR relationships for these redox facies are not too different, a distinct offset of the data distributions is evident: for a given BAR, oxic facies yield significantly higher BaAR values than suboxic/anoxic facies (Fig. 16). This pattern

is likely to be related to redox controls on biogenic barite accumulation, specifically, more efficient preservation of barite under oxidizing conditions (see Section 2.4).

BaAR shows little relationship to either primary or export productivity, yielding r^2 <0.05 for both the L95 and OS datasets (Fig. 17). Applying the Dymond et al. (1992) correction for sedimentation rate-enhanced preservation (see Section 5.4) to our BaAR estimates improved the correlation with primary and export production (although r^2 values remained <0.15), largely by increasing the estimated BaAR at low BARs and steepening the negative slope of the BAR-BaAR regression line. These results suggest that the Dymond et al. (1992) equation may overcorrect for low sedimentation rates. Both BaAR and productivity estimates vary over more than two orders of magnitude, so the lack of any relationship appears to bring into question the utility of biogenic Ba as a general productivity proxy. Eagle et al. (2003) found regional differences in the relationship between BaAR and primary productivity, although they reported a strong global correlation with export productivity. Understanding the reason for the different relationships of BaAR to export productivity will require additional investigation.

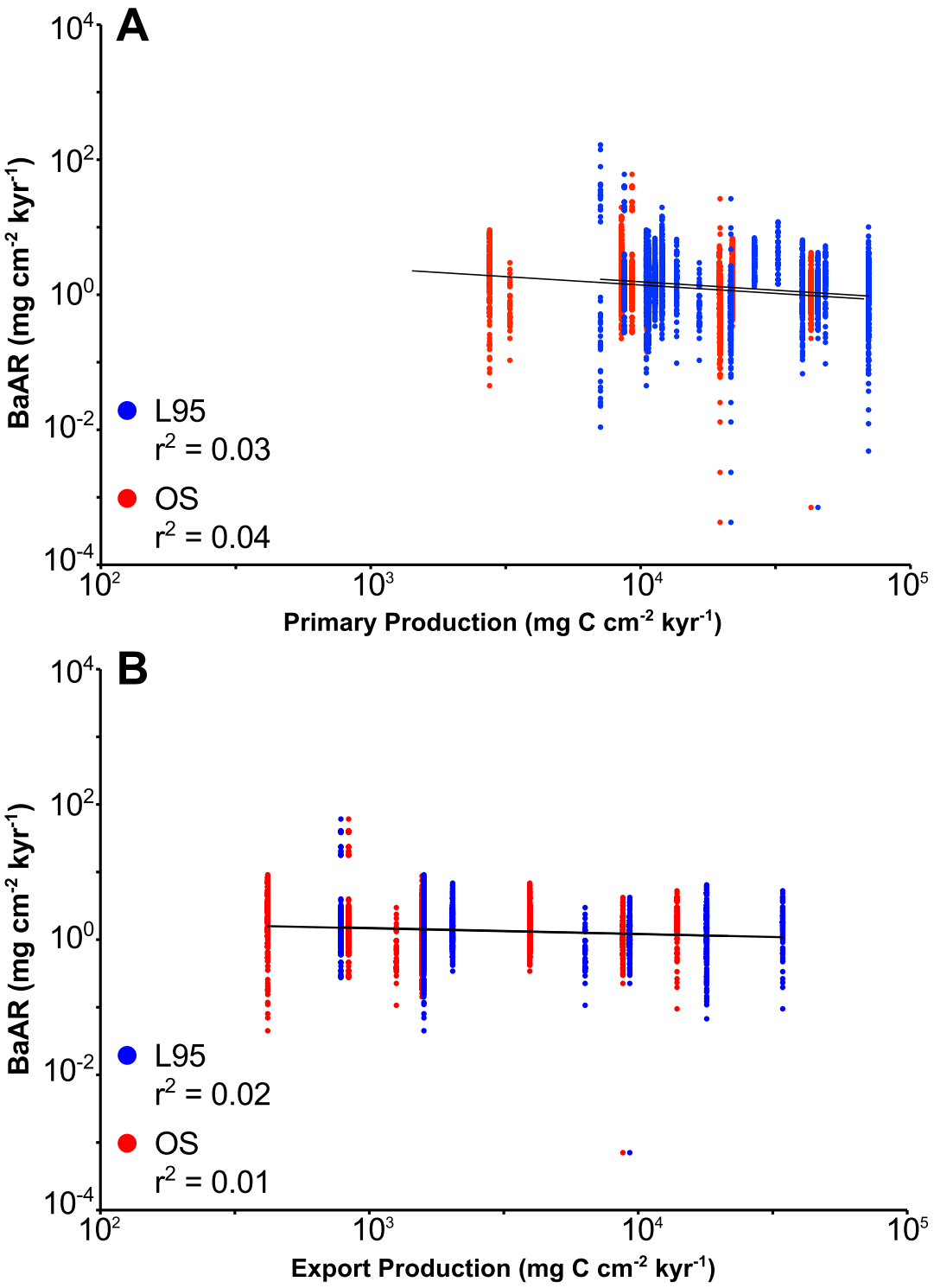

Figure 17: Primary production (A) and export production (B) versus biogenic barium accumulation rate (BaAR) for the L95 and OS datasets. *n* = 2299 for all panels.

5. Discussion

5.1. Relationship of productivity proxy MAR to BAR

In studies in which sediment fluxes have been calculated, productivity estimates generally track BAR closely (e.g., Sternberg et al., 2007; Murray et al., 2012). This may be a real correlation in environments in which sediments are mostly biogenic and sedimentation rate is a function of biological productivity, as in the equatorial Pacific (Murray et al., 2000, 2012). In such cases, BAR itself, as well as the accumulation rate of each of the biogenic components, is likely to be a valid proxy for marine productivity. Such conditions are common in the open pelagic ocean, where the biogenic sediment fraction is derived mainly from primary producers (e.g., diatoms and coccolithophores, Murray et al., 2012) or low-level planktonic consumers (e.g., radiolarians, Hori, 1992; Algeo et al., 2010). However, they are less common in shelf or platform environments, where the biogenic sediment fraction contains a large portion of material derived from benthic macrofauna, and where sediments contain a large lithogenic component, there is no *a priori* reason why productivity should be positively correlated with BAR. One caveat is that studies making use of productivity estimates based on Al- or Ti-normalized proxy concentrations rather than proxy MARs may generate a spurious negative correlation with BAR (e.g., Shimmield and Mowbray, 1991).

The influence of various factors on productivity-proxy fluxes, including enhanced organic matter preservation, siliciclastic dilution, and variable biogenic organic:mineral ratios, can be evaluated from MAR/BAR slopes (m). These patterns are illustrated using OCAR as an example (Fig. 18), but similar relationships could be inferred for PAR and, possibly, BaAR (although the latter proxy is subject to additional influences as a result of

its authigenic origin; see below). In a hypothetical depositional system accumulating only biogenic sediment with a fixed organic:mineral ratio (i.e., a constant weight percent of TOC) and in which there is no effect of BAR on organic carbon preservation, OCAR increases in direct proportion to BAR with *m* equal to 1.0 (or 1:1, representing slopes in log-log space; Fig. 18A). This is a pure expression of the autocorrelation effect, in which OCAR exactly tracks BAR as a result of the latter being a factor in the calculation of the former (see Equation 3). In this hypothetical system, inputs of detrital siliciclastic material dilute the biogenic component of the sediment, lowering *m* to <1.0 (Fig. 18A). Lower values of *m* develop because the addition of non-biogenic diluents causes BAR to increase more rapidly than OCAR, which increases in direct proportion to the biogenic flux. Such a diluent effect should be most evident in continental shelf and epicratonic marine settings, where detrital siliciclastic fluxes are comparatively large. In this scenario, varying the organic:mineral ratio of the biogenic flux (i.e., the weight percent of TOC in the sediment) would raise or lower the regression line, changing the y-intercept without changing *m* (Fig. 18B). The foregoing scenarios assume no effect of BAR on the preservation of organic carbon, even though it is generally accepted that higher BARs enhance organic matter preservation. In depositional systems dominated by biogenic inputs, the enhanced-preservation effect will cause *m* to increase to >1.0 (Fig. 18C). Subtracting the OCAR/BAR autocorrelation slope of 1.0 from the observed *m* thus yields the magnitude of the enhanced-preservation effect. However, the positive effect of enhanced organic preservation on *m* may be offset by the negative effect of detrital dilution in sedimentary systems with large non-biogenic inputs, thus lowering *m* relative to its value in the absence of detrital dilution (Fig. 18C).

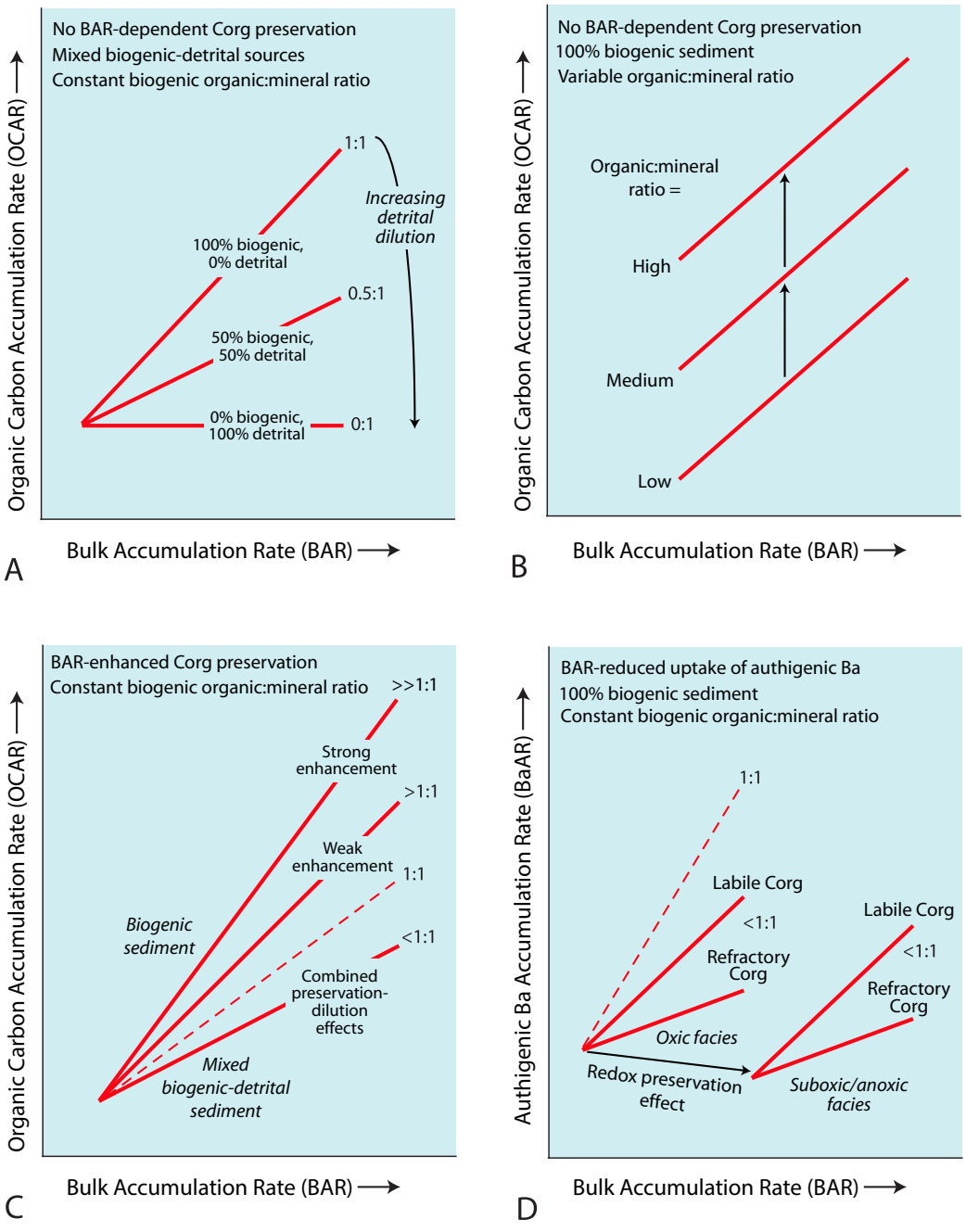

Figure 18: Caption on following page

Conceptual models of variation in OCAR (A-C) and BaAR (D) as a function of bulk accumulation rate (BAR) and various effects. (A) 'Detrital dilution effect': increasing dilution lowers the slope of the regression line (*m*) from 1:1 toward zero. (B) 'Organic:mineral ratio effect': increasing the organic:mineral ratio of biogenic material shifts the regression line upward without changing *m*. (C) 'Enhanced preservation effect': *m* becomes >1:1 when higher BARs cause enhanced preservation of organic carbon in purely biogenic sediments. This effect can potentially be partially offset or negated by the detrital dilution effect, yielding *m* <1:1 in mixed biogenic-detrital sediments. of organic matter yields *m* >1:1. (D) BaAR, the accumulation rate of authigenic Ba, is hypothesized to depend on multiple factors. The dashed 1:1 line represents Ba uptake in direct proportion to OCAR in a 100% biogenic sediment. Observed *m* are significantly lower (0.35 for oxic facies, and 0.57 for suboxic/anoxic facies; Fig. 16) due to two controls: (1) reduced uptake of authigenic Ba at the sediment-water interface in high-BAR systems, and (2) reduced uptake of Ba per unit organic carbon for refractory relative to labile organic matter. Finally, Ba is subject to a redox preservation effect, characterized by a small reduction in BaAR for suboxic/anoxic facies relative to oxic facies as a result of reductive dissolution of barite in the former.

Observed values of *m* for OCAR/BAR regressions exhibit a strong redox dependence. Tyson (2005) determined *m* of 0.84 for suboxic/anoxic facies and 1.38 for oxic facies of Holocene age. Our dataset shows the same pattern of lower *m* for suboxic/anoxic facies (1.11) relative to oxic facies (1.76; Fig. 10), but with higher absolute values of *m* than those reported by Tyson (2005). Lower values of *m* in suboxic/anoxic facies are due to the reduced importance of rapid burial for organic carbon preservation when the overlying water column is depleted of oxygen (Canfield, 1994). As discussed above, the difference in *m* between an observed sample regression and an autocorrelation line (*m* = 1.0) is an indication of the strength of the enhanced-

preservation effect, and the difference in *m* between oxic and suboxic/anoxic samples is an indication of the relationship between BAR and the enhanced-preservation effect. Subtracting the autocorrelation *m* of 1.0 yields an enhanced-preservation effect of 0.76 for oxic facies and 0.11 for suboxic/anoxic facies in our dataset, and 0.38 for oxic facies and -0.16 for suboxic/anoxic facies in the Tyson (2005) dataset. Our dataset thus shows the enhanced-preservation effect for oxic sediments to be twice as large as for the Tyson (2005) dataset, implying a much stronger influence of BAR on the preservation of sedimentary organic matter than recognized heretofore. Further, our dataset documents a small positive effect of BAR on organic matter preservation in suboxic/anoxic sediments, versus a negative effect for the Tyson (2005) dataset. Even under anoxic conditions, increases in BAR are likely to enhance the preservation of organic matter to a small degree, which is consistent with the results of our analysis. The difference in m between oxic and suboxic/anoxic facies reflects the strength of the influence of redox conditions on organic matter preservation. This difference is 0.65 (i.e., 1.76 – 1.11) for our dataset and 0.54 (i.e., 1.38 – 0.84) for the Tyson (2005) dataset. These slopes are quite similar, both indicating that variation in BAR has a much larger influence on organic carbon preservation in oxic facies than in suboxic/anoxic facies.

The point of convergence of the oxic and suboxic/anoxic trends on a BAR-OCAR crossplot has been interpreted as representing the accumulation rate above which aerobic oxidation of organic matter in the sediment becomes insignificant (Algeo et al., 2013). In our dataset, this convergence occurs at a BAR of ~30 (= $10^{1.5}$) g cm^{-2} kyr^{-1} (Fig. 10), which is substantially lower than the convergence point of ~125 (= $10^{2.1}$) g cm^{-2} kyr^{-1} shown in figure 5 of Tyson (2005, n.b., the x-axis scale in that figure should be g m^{-2} yr^{-1},

not g m^{-2} kyr^{-1} as shown). In part, the difference in convergence points is due to the larger dataset used in the present study, which may be better able to distinguish the effects of BAR on organic carbon accumulation. However, it is also a reflection of the larger *m* (1.11) for suboxic/anoxic sites in our dataset. In our dataset, the relationships between BAR and OCAR for oxic versus suboxic/anoxic facies (Fig. 10) appear less as two converging trends than as a continuum, where the regression slopes flatten slightly at higher BARs but remains above 1.0, indicating that rapid burial and, hence, post-depositional decomposition and loss of carbon, continue to exert an influence on carbon preservation. Since suboxic and anoxic environments are generally located in restricted or marginal-marine settings, they tend to have high BARs (Fig. 10). Thus, this flattening of the BAR-OCAR relationship may indicate that rapid burial exercises less, but still some, influence on preservation in low-oxygen settings. It is also possible that the flatter regression slope at high BARs may reflect increasing siliciclastic dilution (Fig. 18A), as substantial detrital sediment input is necessary to achieve the highest BARs.

While the OCAR-BAR regression slopes for our bulk dataset as well as its oxic and suboxic/anoxic facies are >1.0, individual study units generally yield *m* close to 1.0, with a mean of 1.07 and a median of 0.99 (Fig. 19; $n = 34$). This pattern implies the dominant influence of autocorrelation between OCAR and BAR for individual study units (cf. Fig. 18A), which is a characteristic feature of sedimentary units in which BAR is more variable than TOC. An additional factor favoring regression slopes of ~1.0 may be the compensatory effects of BAR-enhanced preservation (increasing *m*) and siliciclastic dilution (decreasing *m*; Fig. 18C). The probable influence of siliciclastic dilution on *m* (Fig. 18A) is particularly evident for individual study units with high BARs

(i.e., >100 g cm^{-2} kyr^{-1}), which generally consist predominantly of lithogenic sediments and which yield *m* of 0.5 to 0.8 (Fig. 19).

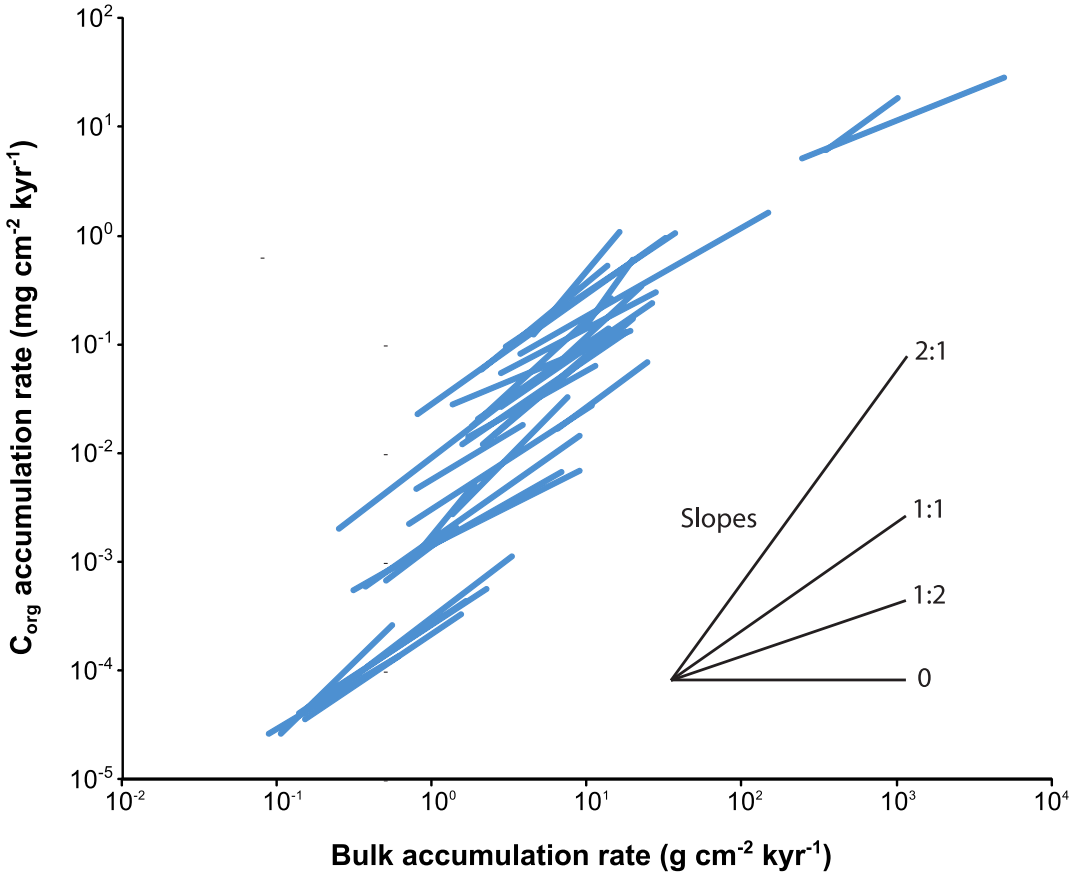

Figure 19: Bulk accumulation rate (BAR) versus the organic carbon accumulation rate (OCAR). Each line shown is the best fit regression lines for an individual site in the dataset. Note that, although the regression slopes (*m*) of individual units are ~1.0, *m* for the bulk dataset is 1.72.

PAR exhibits a simple relationship to BAR with well-defined *m* of 1.04 for oxic facies and 0.93 for suboxic/anoxic facies (Fig. 14A). These slopes are both close to the value of 1.0 characteristic of autocorrelations (see above), indicating that BAR is the

dominant control on PAR. The strong influence of BAR on PAR is expected given that the former is a factor in the calculation of the latter (Equation 3), and that BAR varies over six orders of magnitude versus two for P_{org} concentrations (Fig. 14B). The relative invariance of P_{org} concentrations over a wide range of sediment accumulation rates suggests the operation of a negative feedback mechanism affecting organic P retention in sediments (Ingall et al., 1993; Murphy et al., 2000; see Section 5.4). PAR/BAR slopes of ~1.0 also imply that phosphorus accumulation is not enhanced at higher sedimentation rates, which is unlike the strongly enhanced preservation of organic carbon (see above). The slightly lower *m* of suboxic/anoxic facies (0.93) relative to oxic facies (1.04) is consistent with the effects of clastic dilution at higher BARs (Fig. 18A).

BaAR, the accumulation rate of authigenic Ba, exhibits a more complex set of controls. Three observations must be accounted for: (1) BaAR/BAR regressions exhibit unusually low *m* (<<0.1), (2) a redox effect is evident, with oxic facies having a lower *m* (0.35) than suboxic/anoxic facies (0.57), as well as a higher BaAR for a given BAR and (3) a BAR effect is evident, with both redox catergories showing separate trends of increasing BaAR with increasing BAR (Fig. 16). Controls on the *m* of BaAR/BAR regressions can be inferred within the framework previously developed for OCAR/BAR (Fig. 18A-C) but modified to allow for the authigenic (rather than biogenic) origin of Ba.

If Ba accumulates in direct proportion to OCAR (productivity control), then it should exhibit an *m* of 1:1 in a 100% biogenic sediment lacking preservation effects (Fig. 18D). The low *m* (<<1.0) exhibited by BaAR/BAR cannot be due to detrital dilution (Fig. 18A; see Section 5.1), because such an influence would have operated equally on the OCAR/BAR and PAR/BAR relationships, which is largely not observed (Figs. 10, 14;

note that a very small clastic dilution effect was inferred above for PAR/BAR). While Dymond et al. (1992) demonstrated that overall authigenic barite preservation is enhanced at higher BARs, it is possible that thegaitve preservational effects contribute to an overall BAR/BaAR relationship with a smaller preservational effect ($m<<0.1$) than that seen for organic matter.

The lability of the organic matter and, hence, its rate of decay may affect rates of sulfate reduction, which may impact barite preservation rate (Fig. 18D). A sediment containing more refractory organic matter will have a lower reductant demand than a sediment containing more labile organic matter (Westrich and Berner, 1984; Hulthe et al. 1998). Rapid burial, which minimizes the exposure time of organic material to oxygen, could ensure that a larger pool of labile organic material survives to be buried in the zone of sulfate reduction, where it may facilitate reductive barite dissolution. This mechanism may operate during early diagenesis even where sediments underlie an oxic water column, as anaerobic respiration is responsible for the majority of carbon oxidation even in oxic continental shelf sediments (Canfield, 1994). Reductive dissolution, and less complete organic matter degradation, in the water column are potentially responsible for generally lower preservation in suboxic/anoxic environments (Fig. 18D; see Section 4.5).

5.2. Estimation of paleoproductivity and estimate errors

Paleoproductivity estimates for any ancient marine sedimentary unit potentially can be derived from productivity-proxy flux data. To limit the influence of autocorrelations (e.g., between proxy MARs and BAR; see Section 5.1), we developed paleoproductivity algorithms based on proxy PFs and BAR. Although these latter

variables are not fully independent, the potential for autocorrelations is reduced because PFs depend only indirectly on BAR (see Equations 3 and 6-7). Best-fit linear regressions for organic carbon PF as a function of primary production (prim) versus BAR were nearly identical for the L95 and OS productivity datasets (Fig. 11). A generic form of this relationship, with coefficients intermediate between those calculated for the L95 and OS datasets, is:

$$\mathrm{Log}_{10}(\mathrm{PF}_{\mathrm{prim}}) = 1.54 \times \mathrm{Log}_{10}(\mathrm{BAR}) - 4.10 \quad (13)$$

which is equivalent to the exponential equation:

$$\mathrm{PF}_{\mathrm{prim}} = 10^{-4.10} \times \mathrm{BAR}^{1.54} \quad (14)$$

where BAR is in units of g cm^{-2} kyr^{-1} and PF is a dimensionless variable between 0 and 1. A similar generic equation can be derived for the organic carbon PF as a function of export production (exp), although the poor initial correlation of these variables and the weaker agreement between the L95 and OS productivity datasets means that it should be used with caution:

$$\mathrm{PF}_{\mathrm{exp}} = 10^{-3.37} \times \mathrm{BAR}^{1.47} \quad (15)$$

Combining Equations 3 and 6 yields the following expressions for $\mathrm{PF}_{\mathrm{prim}}$ and $\mathrm{PF}_{\mathrm{exp}}$:

$$\mathrm{PF}_{\mathrm{prim}} = (\mathrm{TOC} \times \mathrm{BAR}) / \mathrm{PROD}_{\mathrm{prim}} \quad (16)$$

$$\mathrm{PF}_{\mathrm{exp}} = (\mathrm{TOC} \times \mathrm{BAR}) / \mathrm{PROD}_{\mathrm{exp}} \quad (17)$$

Inserting the exponents from Equations 14 and 15 and rearranging to solve for productivity yields the following equations:

$$\mathrm{PROD}_{\mathrm{prim}} = 1000 \times (10^{4.10} \times \mathrm{TOC}) / \mathrm{BAR}^{0.54} \quad (18)$$

$$PROD_{exp} = 1000 \times (10^{3.37} \times TOC) / BAR^{0.47} \quad (19)$$

where BAR is in units of g cm^{-2} kyr^{-1}, TOC is a dimensionless weight ratio between 0 and 1, and the factor of 1000 serves to express $PROD_Z$ in our standard units of mg cm^{-2} kyr^{-1}. The significance of Equations 18 and 19 is that they allow estimation of primary and export productivity as a function of two completely independent variables (TOC and BAR) that are readily determinable in many paleomarine systems.

The presence of BAR in the denominator of these equations may be counter-intuitive, as high BAR was previously shown to correlate with high OCAR (Fig. 10). However, the relationship of BAR to TOC and productivity can be understood in the context of its relationship to PF in Equations 13 and 14. Specifically, the y-intercept in Equation 13 ($10^{-4.10}$) represents the average proportion of primary productivity that will be preserved when BAR is zero (i.e., less than one part in twelve thousand). The inverse of this value, seen as the coefficient in the numerator of Equation 18, represents the maximum productivity rate that can be inferred based on a given TOC concentration before accounting for preservational effects. The BAR term in the denominator represents these preservational effects. As BAR increases, the organic carbon PF increases even more rapidly (at a log-log rate of 1.54; Equation 14) so that calculated primary productivity rates for a given TOC concentration must decline (Equation 18). The same considerations apply to export productivity, as given in Equations 15 and 19.

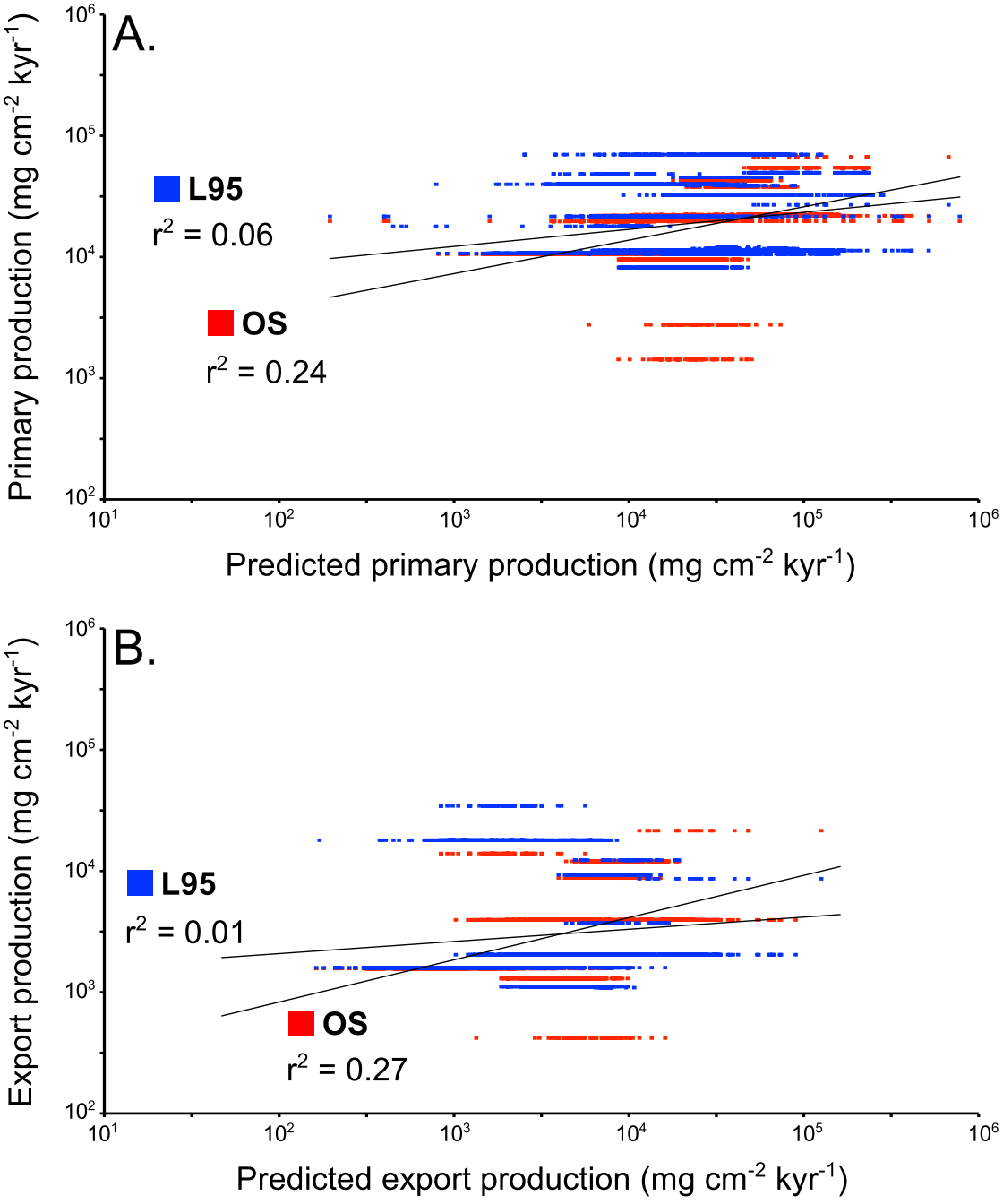

Figure 20: (A) Primary production as predicted from TOC and BAR by Equation 18, versus primary production from the L95 and OS datasets. (B) Export production as predicted from TOC and BAR by Equation 19, versus export production from the L95 and OS datasets. *n* = 4226 for each data series.

To assess the utility of Equations 18 and 19 in reconstructing paleoproductivity, we estimated primary and export productivity rates for all samples in our database for which TOC data were available and then compared them with actual productivity rate measurements from the L95 and OS datasets. Correlation coefficients between the estimated and measured productivity rates are generally low although somewhat better for the OS than for the L95 productivity dataset: $r^2 = 0.24$ (OS) and 0.06 (L95) for primary productivity, and $r^2 = 0.27$ (OS) and 0.01 (L95) for export productivity (Fig. 20). Differences in estimated (est) and measured (meas) productivity rates were quantified as a relative error:

$$\text{Error} = (\text{PROD}_{\text{Z-est}} - \text{PROD}_{\text{Z-meas}}) / \text{PROD}_{\text{Z-meas}} \times 100\% \quad (20)$$

where Z represents either primary (prim) or export (exp) productivity, and 'measured' refers to the L95 and OS productivity estimates. Relative errors were calculated as absolute values in order to indicate the deviation of the productivity estimate from the expected value in either direction. The relative errors thus calculated are commonly large although relatively similar for the OS and L95 productivity datasets. Absolute mean error for primary productivity estimates was 152% (OS) and 158% (L95), and that for export productivity estimates was 143% (OS) and 178% (L95). Median errors were considerably lower: 58% (OS) and 68% (L95) for primary productivity estimates, and 53% (OS) and 76% (L95) for export productivity estimates. The smaller median values indicate that error distributions are highly skewed, i.e., with many small errors and fewer large errors (Fig. 21). This pattern is attributable in part to the upper limit of 100% on calculated errors when $\text{PROD}_{\text{Z-est}} < \text{PROD}_{\text{Z-meas}}$.

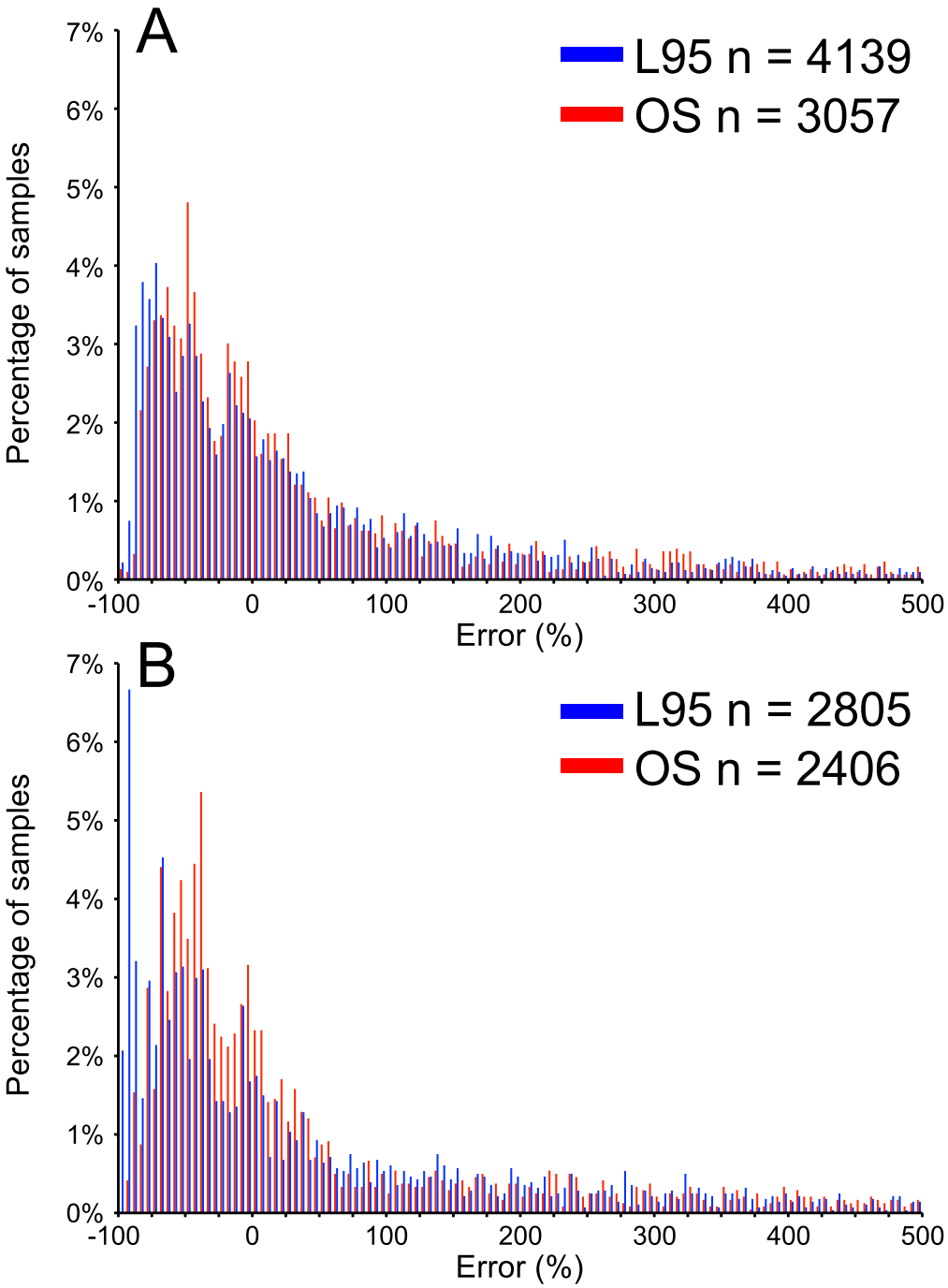

Figure 21: Distribution of error values calculated with Equation 20 for (A) primary production estimates from Equation 18 versus actual primary production from the L95 and OS datasets, and (B) export production estimates from Equation 20 versus actual export production from the L95 and OS datasets. Errors >500% not shown, but both panels show >90% of all error values. Error values binned in increments of 5%

Overall, >70% of productivity estimates for individual samples had an absolute relative error of <100% (Fig. 21). Given the large number of factors that can cause productivity estimates based on sedimentary proxies to deviate from modern *in situ* productivity rates (see Section 3.4), this is a fairly robust result. Because the productivity estimates in our dataset range over more than two orders of magnitude, even a 100% error is an acceptable level of uncertainty for productivity estimates in paleomarine systems. The value of our approach to paleoproductivity estimation is enhanced by the fact that it is based on two independent and easily determined sedimentological parameters (i.e., TOC and BAR). Examples of the application of this method of paleoproductivity analysis will be given in companion papers in the present volume by Shen et al. (2014) and Wei et al. (2014).

5.3. Paleoproductivity estimates based on OCAR

Among the elemental proxy mass fluxes considered in this study, the strongest positive relationship with both primary and export production is shown by OCAR (Fig. 12). It is surprising that OCAR should show a stronger relationship with primary than with export production, since it is carbon exported from the surface ocean that is ultimately preserved in the sediment. The marginally stronger relationship with primary production may reflect the effects of high productivity on redox conditions or the association of high productivity with elevated sedimentation rates. The regressions relating OCAR to primary and export production (Table 4) can be rearranged to predicted primary (prim) and export (exp) production as a function of OCAR, using coefficients intermediate between those determined for the L95 and OS datasets:

$$PROD_{prim} = (10^{8.55} \times OCAR)^{0.43} \quad (21)$$

$$PROD_{exp} = (10^{4.56} \times OCAR)^{0.71} \quad (22)$$

where $PROD_Z$ and OCAR are in units of mg cm^{-2} kyr^{-1}. If OCAR is replaced by TOC and BAR (per Equation 3), Equations 21 and 22 can be recast to estimate paleoproductivity based on the same parameters as used in Equations 18 and 19. However, this reformulation yields a positive relationship between $PROD_Z$ and BAR that is quite different from the inverse relationships seen in Equations 18 and 19. Unlike those equations, Equations 21 and 22 are empirical derivations of paleoproductivity rates that do not account explicitly for the preservational effects of BAR.

Paleoproductivity estimates based on Equations 21 and 22 exhibit weak to modest correlations to modern productivity rates and are subject to potentially large errors. Estimates of primary productivity (Equation 21) yield an r^2 of 0.44 with L95 productivity and an r^2 of 0.06 with OS productivity. Average and median absolute errors, as calculated per Equation 20, were 64% and 59%, respectively, when calculated against L95 productivity, and 119% and 68%, respectively, when calculated against OS productivity. Estimates of export productivity (Equation 22) yield an r^2 of 0.05 with L95 productivity and an r^2 of 0.32 with OS productivity. Average and median absolute errors, as calculated per Equation 20, were 245% and 83%, respectively, when calculated against L95 productivity, and 371% and 83%, respectively, when calculated against OS productivity.

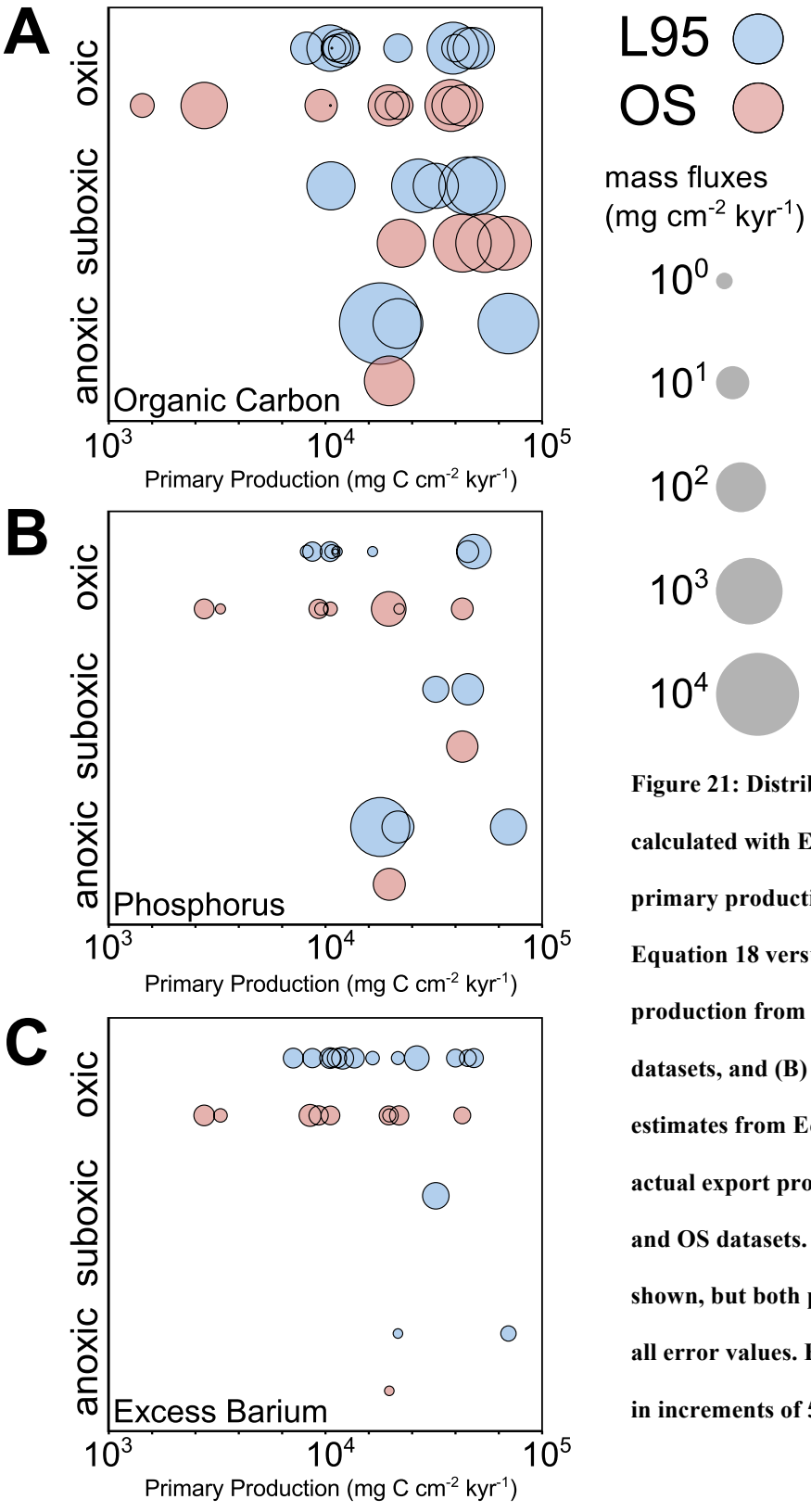

Figure 21: Distribution of error values calculated with Equation 20 for (A) primary production estimates from Equation 18 versus actual primary production from the L95 and OS datasets, and (B) export production estimates from Equation 20 versus actual export production from the L95 and OS datasets. Errors >500% not shown, but both panels show >90% of all error values. Error values binned in increments of 5%.

The relative importance of productivity rates and redox conditions on productivity-proxy fluxes was considered conceptually in Figure 6, and the proxy flux dataset generated in this study provides an opportunity to assess these relationships quantitatively. Although redox facies is clearly an important control on OCAR (Fig. 9A), it is worth noting that BAR and redox conditions are not fully independent variables in our dataset, and it is uncertain to what extent this is reflected in enhanced preservation at high BARs. In fact, OCAR appears to show the influence of both redox and productivity controls, with the highest organic carbon fluxes associated with high-productivity anoxic settings (i.e., lower right of Fig. 22A). Because elevated surface-water productivity can trigger benthic anoxia through the biological oxygen demand imposed by sinking organic matter, these relationships might be interpreted as evidence of the generally dominant influence of productivity on organic matter accumulation in marine sediments. However, a feedback involving the recycling of organic P in marine sediments back into the water column helps to sustain high surface-water productivity in anoxic marine systems (Ingall et al., 1993; Murphy et al., 2000). Thus, the relationships documented here (Fig. 22A) suggest that elevated productivity rates are commonly important in establishing marine anoxia and high OCAR, but that the interplay of productivity and redox conditions is integral to sustaining such conditions (cf. Pedersen and Calvert, 1990; Tyson, 2005).

5.4. Paleoproductivity estimates based on PAR

The most notable feature of the phosphorus dataset is the relative consistency in P concentrations over a wide range of redox conditions (Fig. 13) and BARs (Fig. 14). Although PAR shows only a weak relationship to primary productivity, particularly at

lower productivity rates (Fig. 15A), it becomes nearly invariant at primary productivity rates >20,000 mg cm^{-2} kyr^{-1}, a point that corresponds to the transition between primarily oxic and primarily suboxic/anoxic facies. Its relationship with export production is more monotonic but weaker. It is possible to estimate primary and export production based on PAR using the equations in Table 4 (with coefficients intermediate between those calculated for the L95 and OS datasets):

$$PROD_{prim} = (10^{3.46} \times PAR)^{1.14} \quad (23)$$

$$PROD_{exp} = (10^{1.63} \times PAR)^{1.98} \quad (24)$$

where productivity and PAR are in units of mg cm^{-2} kyr^{-1}. Correlations were weaker and errors higher for these equations than for those derived from OCAR, but they were of the same order of magnitude. As with OCAR, correlations with the L95 productivity estimates (r^2 = 0.27 for primary production, 0.08 for export production) were stronger than those with the OS estimates (r^2 = 0.00 for primary production, 0.05 for export production). For the L95 dataset, mean and median absolute errors of primary production estimates are 229% and 81%, respectively, and the errors of export production estimates are 763% and 88%, respectively. For the OS dataset, mean and median absolute errors for primary production estimates are 2996% and 85%, respectively, and the errors for export production estimates are 1860% and 93%, respectively. For the latter dataset, the large differences between the mean and median errors reflect inclusion of anomalously high PAR values for Saanich Inlet; when these data are excluded, the mean and median absolute errors for primary productivity fall to 314% and 84%, respectively.

P_{org} appears accumulate most rapidly in highly productive, suboxic-to-anoxic settings (Fig. 22B), although the lack of anoxic sites having low productivity rates may

influence this interpretation. Because organic carbon and phosphorus have different modes of preservation as a function of redox variation (see Section 2.6), the similarity of the patterns for OCAR and PAR (Fig. 22A, B) is significant, suggesting the potentially dominant influence of productivity on the accumulation of organic matter in marine sediments (cf. Section 5.2). The narrowing range of P_{org} concentrations observed in increasingly anoxic environments, an effect that is seen more clearly in maximum than in mean values (Fig. 14), suggests that anoxic conditions fundamentally limit P_{org} retention in sediments. This limitation operates through an efficient negative feedback involving the diffusion of remineralized organic P back into the water column under increasingly more reducing conditions (Ingall et al., 1993; Murphy et al., 2000; see Section 4.3).

5.5. Paleoproductivity estimates based on BaAR

BaAR does not seem to show any clear relationship with productivity on a global scale. The weak (and negative) correlations between estimates of productivity and BaAR (Fig. 17) do not inspire confidence in the use of Ba_{bio} as a widely applicable productivity proxy. Although Eagle et al. (2003) found that biogenic barium varied nearly linearly with export production after use of an appropriate local *pe*-ratio*,* this analysis was limited to marine systems with an estimated export production of $<10^4$ mg C cm^{-2} kyr^{-1}. A positive relationship can be discerned between export production and BaAR in the OS dataset over this same productivity range (Fig. 17B), but it breaks down at higher levels of productivity. We include the following equations for estimating paleoproductivity from BaAR for the sake of completeness (i.e., as analogs to Equations 21-22 for OCAR

and Equations 23-24 for PAR), but we emphasize that they have questionable value for estimating productivity in paleomarine depositional systems:

$$PROD_{prim} = (10^{-1.17} \times BaAR)^{-4.17} \quad (25)$$

$$PROD_{exp} = (10^{-0.43} \times BaAR)^{-11.11} \quad (26)$$

where BaAR and production are in units of mg cm^{-2} kyr^{-1}. The correlation coefficients are <0.01 for all estimates of primary and export productivity versus measured productivity values, and average errors are orders of magnitude larger than for productivity estimates based on OCAR or PAR.

The barite productivity proxy was developed largely in the open ocean (Dymond et al., 1992; François et al., 1995; Paytan et al., 1996; Paytan and Kastner, 1996; Eagle et al., 2003, Paytan et al., 2007), in environments dominated by pelagic biogenic sediments (Murray et al., 2000; Prakash Babu et al., 2002), and its applicability may be limited to such systems. Further work will be needed to determine if biogenic barium has value for estimating paleoproductivity in equivalent ancient open-ocean facies, such as radiolarites (e.g., Algeo et al., 2010, 2011).

6. Conclusions

Our analysis of three widely used elemental productivity proxies (TOC, P_{org}, and Ba_{bio}) provides insights regarding controls on their accumulation, their robustness as paleoproductivity proxies, and the range of depositional environments in which they may usefully be applied. Organic carbon accumulation rates were determined to have a strong relationship to BAR, with a large slope *m* (1.72) indicating strongly enhanced preservation of organic carbon at higher sediment accumulation rates. Organic carbon

preservation factors (PF) exhibit a linear relationship with BAR, indicating that the effects of rapid sediment accumulation on preservation can be corrected for, and that paleoproductivity can be estimated from TOC and BAR. The resulting equations can yield order-of-magnitude estimates of primary and export production in paleomarine systems. Phosphorus accumulation rates are strongly correlated to BAR with an *m* of ~1.0, implying a high degree of autocorrelation and, thus, control of P accumulation by BAR. This is consistent with the observed limited variation of sedimentary P concentrations, which is likely due to the operation of homeostatic feedbacks related to porewater redox conditions. At a global scale, the productivity-dominant model appears to account better for observed patterns of organic carbon and phosphorus accumulation rates than the redox-dominant model. Biogenic barium exhibits a weak relationship to BAR, probably because of reduced uptake of Ba at the sediment-water interface with increasing sedimentation rates. Biogenic barium fluxes show no systematic relationship to productivity in modern marine depositional systems generally, although previous studies have identified positive covariation with productivity in specific environments, such as the equatorial Pacific. We conclude that organic carbon and phosphorus fluxes have considerable potential as widely useful paleoproductivity proxies, but that the applicability of biogenic barium fluxes may be limited to specific oceanic settings.

7. Acknowledgments

We thank Peter Ward for stimulating discussions and professional mentoring. Research by SDS is supported by the Sedimentary Geology and Paleobiology program of the U.S. National Science Foundation and University of Washington Department Earth and Space Sciences. Research by TJA is supported by the Sedimentary Geology and Paleobiology program of the U.S. National Science Foundation, the NASA Exobiology program, the State Key Laboratory of Geological Processes and Mineral Resources at the China University of Geosciences-Wuhan (program: GPMR201301), and the Natural Science Foundation of China (NSF-C).

References:

Algeo, T.J., and Heckel, P.H., 2008. The Late Pennsylvanian Midcontinent Sea of North America: A review. Palaeogeography, Palaeoclimatology, Palaeoecology, v. 268, p. 205-221.

Algeo, T.J., and Ingall, E., 2007. Sedimentary C_{org}:P ratios, paleocean ventilation, and Phanerozoic atmospheric pO_2. Palaeogeography, Palaeoclimatology, Palaeoecology, v. 256, p. 130-155.

Algeo, T.J., Hinnov, L., Moser, J., Maynard, J.B., Elswick, E., Kuwahara, K., and Sano, H., 2010. Changes in productivity and redox conditions in the Panthalassic Ocean during the latest Permian. Geology, v. 38, p. 187-190.

Algeo, T.J., Kuwahara, K., Sano, H., Bates, S., Lyons, T., Elswick, E., Hinnov, L., Ellwood, B.B., Moser, J., and Maynard, J.B., 2011. Spatial variation in sediment fluxes, redox conditions, and productivity in the Permian-Triassic Panthalassic Ocean. Palaeogeography, Palaeoclimatology, Palaeoecology, v. 308, p. 65-83.

Algeo, T.J., Henderson, C.M., Tong, J.N., Feng, Q.L., Yin, H.F., and Tyson, R.V., 2013. Plankton and productivity during the Permian-Triassic boundary crisis: An analysis of organic carbon fluxes. Global and Planetary Change, v. 105, p. 52-67.

Amo, M., and Minagawa, M. 2003. Sedimentary record of marine and terrigenous organic matter delivery to the Shatsky Rise, western North Pacific, over the last 130 kyr. Organic Geochemistry, v. 34(9), p. 1299-1312.

Anderson, L.D., and Delaney, M.L., 2005. Use of multiproxy records on the Agulhas Ridge, Southern Ocean (Ocean Drilling Project Leg 177, Site 1090) to investigate sub-Antarctic hydrography from the Oligocene to the early Miocene. Paleoceanography, v. 20, PA3011, 16 pp.

Antia, A.N., Koeve, W., Fischer, G., Blanz, T., Schulz-Bull, D., Scholten, J., Neuer, S., Kremling, K., Kuss, J., Peinert, R., Hebbeln, D., Bathmann, U., Conte, M., Fehner, U., and Zeitzschel, B., 2001. Basin-wide particulate carbon flux in the Atlantic Ocean: regional export patterns and potential for atmospheric CO_2 sequestration. Global Biogeochemical Cycles, v. 15(4), p. 845-862.

Averyt, K.B., and Paytan, A., 2004. A comparison of multiple proxies for export production in the equatorial Pacific. Paleoceanography, v. 19, PA4003, 14 pp.

Bąk, K., 2007. Organic-rich and manganese sedimentation during the Cenomanian-Turonian boundary event in the Outer Carpathian basins; a new record from the Skole Nappe, Poland. Palaeogeography, Palaeoclimatology, Palaeoecology, v. 256, p. 21-46.

Balakrishnan Nair, T.M., Ittekkot, V., Shankar, R., and Guptha, M.V.S., 2005. Settling barium fluxes in the Arabian Sea: Critical evaluation of relationship with export production. Deep-Sea Research II, v. 52, p. 1930-1946.

Bastviken, D., Persson, L., Odham, G., and Tranvik, L., 2004. Degradation of dissolved organic matter in oxic and anoxic lake water. Limnology and Oceanography, v. 49, p. 109-116.

Behrenfeld, M.J., O'Malley, R.T., Siegel, D.A., McClain, C.R., Sarmiento, J.L., Feldman, G.C., Milligan, A.J., Falkowski, P.G., Leterlier, R.M., and Boss, E.S., 2006. Climate-driven trends in contemporary ocean productivity. Nature, v. 444(7120), p. 752-755.

Benitez-Nelson, C.R., 2000. The biogeochemical cycling of phosphorus in marine systems. Earth-Science Reviews, v. 51(1), p. 109-135.

Benner, R., Maccubbin, A.E. and Hodson, R.E., 1984. Anaerobic biodegradation of the lignin and polysaccharide components of lignocellulose and synthetic lignin by sediment microflora. Applied and Environmental Microbiology, v. 47, p. 998- 1004.

Berelson, W.M., McManus, J., Coale, K.H., Johnson, K.S., Kilgore, T., Burdige, D., and Pilskaln, C., 1996. Biogenic matter diagenesis on the sea floor: a comparison between two continental margin transects. Journal of Marine Research, v. 54, p. 731-762.

Berner, R.A., 1984. Sedimentary pyrite formation: an update. Geochimica et Cosmochimica Acta, v. 48, p. 605-615.

Berner, R.A., and Raiswell, R., 1983. Burial of organic carbon and pyrite sulfur in sediments over Phanerozoic time: a new theory. Geochimica et Cosmochimica Acta, v. 47, p. 855-862.

Bernstein, R.E., Byrne, R.H., Betzer, P.R., and Greco, A.M., 1992. Morphologies and transformations of celestite in seawater: the role of acantharians in strontium and barium geochemistry. Geochimica et Cosmochimica Acta, v. 56, p. 3273-3279.

Bernstein, R.E., Byrne, R.H., and Schijf, J., 1998. Acantharians: a missing link in the oceanic biogeochemistry of barium. Deep Sea Research Part I: Oceanographic Research Papers, v. 45(2-3), p. 491-505.

Bertram, M.A., and Cowen, J.P., 1997. Morphological and compositional evidence for biotic precipitation of marine barite. Journal of Marine Research, v. 55, p. 577-593.

Betts, J.N., and Holland, H.D., 1991. The oxygen content of ocean bottom waters, the burial efficiency of organic carbon, and the regulation of atmospheric oxygen. Palaeogeography, Palaeoclimatology, Palaeoecology, v. 97(1), p. 5-18.

Bishop, J.K.B., 1988. The barite-opal-organic carbon association in oceanic particulate matter. Nature, v. 332, p. 341-343.

Bonn, W.J., Gingele, F.X., Grobe, H., Mackensen, A., and Fütterer, D.K., 1998. Palaeoproductivity at the Antarctic continental margin: opal and barium records for the last 400 ka. Palaeogeography, Palaeoclimatology, Palaeoecology, v. 139(3), p. 195-211.

Bostrom, K., and Backman, J., 1990. Geochemistry and origin of Neogene sediments in Hole 711A. In: Duncan, R.A., Backman, J., and Peterson, L.C., et al., Proceedings of the Ocean Drilling Program, Scientific Results, v. 115, p. 699-708.

Bralower, T.J., and Thierstein, H.R., 1987. Organic carbon and metal accumulation rates in Holocene and mid-Cretaceous sediments: palaeoceanographic significance. In: Brooks, J., and Fleet, A.J. (Eds.). Marine Petroleum Source Rocks. London, Geological Society Special Publication: v. 26, pp. 345-369.

Bremner, J.M., and Rogers, J., 1990. Phosphorite deposits on the Namibian continental shelf. In: Burnett, W.C., and Riggs, S.R. (Eds.). Phosphate Deposits of the World, v. 3, Neogene to Modern Phosphorites: Cambridge University Press, Cambridge, pp. 143-152.

Broecker, W.S., 1991. The great ocean conveyor. Oceanography, v. 4(2), p. 79-89.

Brumsack, H.J., 2006. The trace metal content of recent organic carbon-rich sediments: Implications for Cretaceous black shale formation. Palaeogeography, Palaeoclimatology, Palaeoecology, v. 232(2), p. 344-361.

Calvert, S.E., and Pedersen, T.F., 2007. Elemental proxies for palaeoclimatic and palaeoceanographic variability in marine sediments: Interpretation and application. In: Hillaire-Marcel, C., and De Vernal, A. (Eds.) Proxies in Late Cenozoic Paleoceanography: Elsevier, Developments in Marine Geology 1, pp. 567-644.

Canfield, D.E., 1994. Factors influencing organic carbon preservation in marine sediments. Chemical Geology, v. 114, p. 315-329.

Canfield, D.E., 2005. The early history of atmospheric oxygen: Homage to Robert M. Garrels. Annual Review of Earth and Planetary Sciences, v. 33, p. 1-36.

Colberg, P.J., 1988. Anaerobic microbial degradation of cellulose, lignin, oliolignols, and monoaromatic lignin derivatives. In: A.J.B. Zehnder (Ed.) Biology of Anaerobic Organisms. Wiley, pp. 333-372.

Compton, J.S., Snyder, S.W., and Hodell, D.A., 1990. Phosphogenesis and weathering of shelf sediments from the southeastern United States: Implications for Miocene $\delta^{13}C$ excursions and global cooling. Geology, v. 18, p. 1227-1230.

Daly, A.R., and Edman, J.D., 1987. Loss of organic carbon from source rocks during thermal maturation: American Association of Petroleum Geologists Bulletin, v. 71(5), p. 546.

Dehairs, F., Chesselet, R., and Jedwab, J., 1980. Discrete suspended particles of barite and the barium cycle in the open ocean. Earth and Planetary Science Letters, v. 49, p. 528-550.

Dehairs, F., Lambert, C.E., Chesselet, R., and Risler, N., 1987. The biological production of marine suspended barite and the barium cycle in the Western Mediterranean Sea. Biogeochemistry, v. 4, p. 119-139.

Dehairs, F., Goeyens, L., Stroobants, N., Bernard, P., Goyet, C., Poisson, A., and Chesselet, R., 1990. On suspended barite and the oxygen minimum in the Southern Ocean. Global Biogeochemical Cycles, v. 4, p. 85-102.

Dehairs, F., Baeyens, W., and Goeyens, L., 1992. Accumulation of suspended barite at mesopelagic depths and export production in the Southern Ocean. Science, v. 258, p. 1332-1335.

Dehairs, F., Fagel, N., Antiam, A.N., Peinert, R., Elskens, M., and Goeyens, L., 2000. Export production in the Gulf of Biscay as estimated from barium-barite in settling material: A comparison with new production. Deep-Sea Research I, v. 47, p. 583-601.

Delaney, M.L., 1998. Phosphorus accumulation in marine sediments and the oceanic phosphorus cycle. Global Biogeochemical Cycles, v. 12(4), p. 563-572.

Delaney, M.L., and Filippelli, G.M., 1994. An apparent contradiction in the role of phosphorus in Cenozoic chemical mass balances for the world ocean. Paleoceanography, v. 9(4), p. 513-527.

Deuser, W.G., 1971. Organic-carbon budget of the Black Sea. Deep-Sea Research, v. 18, p. 995-1004.

Des Combes, J., Caulet, J.P., and Tribovillard, N.P., 1999. Pelagic productivity changes in the equatorial area of the northwest Indian Ocean during the last 400,000 years. Marine Geology, v. 158(1), p. 27-55.

Des Combes, J., Caulet, J.P., and Tribovillard, N., 2005. Monitoring the variations of the Socotra upwelling system during the last 250 kyr: A biogenic and geochemical approach. Palaeogeography, Palaeoclimatology, Palaeoecology, v. 223(3), p. 243-259.

Díaz, J., Ingall, E., Benitez-Nelson, C., Paterson, D., de Jonge, M.D., McNulty I., and Brandes, J.A., 2008. Marine polyphosphate: A key player in geologic phosphorus sequestration. Science, v. 320, p. 652-655.

Díaz-Ochoa, J.A., Lange, C.B., Pantoja, S., De Lange, G.J., Gutiérrez, D., Muñoz, P., and Salamanca, M., 2009. Fish scales in sediments from off Callao, central Peru. Deep-Sea Research II, v. 56(16), p. 1124-1135.

Dickens, G., Fewless, T., Thomas, E., and Bralower, T.J., 2003. Excess barite accumulation during the Paleocene-Eocene Thermal Maximum: Massive input of dissolved barium from seafloor gas hydrate reservoirs. In: Wing, S.L., Gingerich, P.D., Schmitz, B., and Thomas, E. (Ed.s). Causes and Consequences of Globally Warm Climates in the Early Paleogene: Boulder, Colorado, Geological Society of America Special Paper 369, pp. 11-23.

Diester-Haass, L., Meyers, P.A., Vidal, L., and Wefer, G., 2001. Data report: Sand fraction, carbonate and organic carbon contents of Late Miocene sediments from site 1085, middle Cape Basin. In: Berger, W.H., Wefer, G. Richter, C. (Eds.). Proceedings of the Ocean Drilling Program, Scientific Results, v. 175, p. 1-23.

Ding, H., and M.-Y. Sun, 2005, Biochemical degradation of algal fatty acids in oxic and anoxic sediment-seawater interface systems: effects of structural association and relative roles of aerobic and anaerobic bacteria. Marine Chemistry, v. 93, no. 1, p. 1–19.

Dunne, J.P., Armstrong, R.A., Gnanadesikan, A., and Sarmiento, J.L., 2005. Empirical and mechanistic models for the particle export ratio. Global Biogeochemical Cycles, v. 19, GB4026, 16 pp.

Dymond, J., Corliss, J.B., and Heath, G.R., 1977. History of metalliferous sedimentation at Deep Sea Drilling site 319 in the South Eastern Pacific. Geochimica et Cosmochimica Acta, v. 41(6), p. 741-753.

Dymond, J., 1981. Geochemistry of Nazca plate surface sediments: An evaluation of hydrothermal, biogenic, detrital, and hydrogenous sources. In: Kulm, L.D., Dymond, J., Dasch, E.J., and Hussong, D.M. (Eds.). Nazca Plate: Crustal Formation and Andean Convergence: Geological Society of America Memoir 154, pp. 133-173.

Dymond, J., and Collier, R., 1996. Particulate barium fluxes and their relationships to biological productivity. Deep-Sea Research II, v. 43, p. 1283-1308.

Dymond, J., Suess, E., and Lyle, M., 1992. Barium in deep-sea sediment: a geochemical proxy for paleoproductivity. Paleoceanography, v. **7**(2), p. 163-181.

Eagle, M., Paytan, A., Arrigo, K.R., van Dijken, G., and Murray, R.W., 2003. A comparison between excess barium and barite as indicators of carbon export. Paleoceanography, v. 18(1), 1021, 13 pp.

Emeis, K.C., Doose, H., Mix, A.C., and Schulz-Bull, D., 1995. Alkenone sea-surface temperatures and carbon burial at Site 846 (eastern equatorial Pacific Ocean): The last 1.3 My. In: Mayer, L.A., Pisias, N.G., Palmer-Julson, A., van Andel, T.H. (Eds.). Proceedings of the Ocean Drilling Program, Scientific Results, v. 138, p. 605-614.

Erwin, D.H., Bowring, S.A., and Jin, Y.G., 2002. End-Permian mass extinctions: a review. In: Koeberl, C. and McLeod, K.G. (Eds.). Catastrophic Events and Mass Extinctions: Impacts and Beyond. Boulder, Colorado. Geological Society of America Special Paper, v. 356, p. 363-384.

Fagel, N., Dehairs, F., Peinert, R., Antia, A., and André, L., 2004. Reconstructing export production at the NE Atlantic margin: potential and limits of the Ba proxy. Marine Geology, v. 204, p. 11-25.

Fahey, T.J., and Knapp, A.K. (Eds.), 2007. Principles and Standards for Measuring Primary Production. New York, New York, USA: Oxford University Press, 288 pp.

Falkner, K.K., Klinkhammer, G.P., Bowers, T.S., Todd, J.F., Lewis, B.L., Landing, W.M., and Edmond, J.M., 1993. The behavior of barium in anoxic marine waters. Geochimica et Cosmochimica Acta, v. 57, p. 537-554.

Felix, M., 2014. A comparison of equations commonly used to calculate organic carbon content and marine palaeoproductivity from sediment data. Marine Geology, v. 347, p. 1-11.

Filippelli, G.M., 2001. Carbon and phosphorus cycling in anoxic sediments of the Saanich Inlet, British Columbia. Marine Geology, v. 174, p. 307-321.

Filippelli, G.M., and Delaney, M.L., 1995. Phosphorus geochemistry and accumulation rates in the eastern equatorial Pacific. In: Mayer, L.A., Pisias, N.G., Palmer-Julson, A., van Andel, T.H. (Eds.). Proceedings of the Ocean Drilling Program, Scientific Results, v. 138, p. 757-767.

Filippelli, G.M., and Delaney, M.L., 1996. Phosphorus geochemistry of equatorial Pacific sediments. Geochimica et Cosmochimica Acta, v. 60, p. 1479-1495.

Filippelli, G.M., and Souch, C., 1999. Effects of climate and landscape development on the terrestrial phosphorus cycle. Geology, v. 27, p. 171-174.

Fisher, N.S., Guillard, R.R., and Bankston, D.C., 1991. The accumulation of barium by marine phytoplankton grown in culture. Journal of Marine Research 49(2), 339-354.

Föllmi, K.B., 1990. Condensation and phosphogenesis: example of the Helvetic mid-Cretaceous (northern Tethyan margin). In: Phosphorite Research and Development: Geological Society of London Special Publication 52; edited by: Notholt, A.J.G., and Jarvis, I., pp. 237-252.

Föllmi, K.B., 1996. The phosphorus cycle, phosphogenesis and marine phosphate-rich deposits. Earth-Science Reviews, v. 40, p. 55-124.

François, R., Honjo, S., Manganini, S.J., and Ravizza, G.E., 1995. Biogenic barium fluxes to the deep sea: implications for paleoproductivity reconstruction. Global Biogeochemical Cycles, v. 9(2), p. 289-303.

Frank, M., Gersonde, R., Loeff, M. R., Bohrmann, G., Nürnberg, C. C., Kubik, P. W., and Mangini, A. 2000. Similar glacial and interglacial export bioproductivity in the Atlantic sector of the Southern Ocean: Multiproxy evidence and implications for glacial atmospheric CO_2. Paleoceanography, v. 15(6), p. 642-658.

Freudenthal, T., Neuer, S., Meggers, H., Davenport, R., and Wefer, G., 2001. Influence of lateral particle advection and organic matter degradation on sediment accumulation and stable nitrogen isotope ratios along a productivity gradient in the Canary Islands region. Marine Geology, v. 177(1), p. 93-109.

Froelich, P.N., Klinkhammer, G.P., Bender, M.L., Luedtke, G.R., Heath, G.R., Cullen, D., Dauphin, P., Hammond, D., Hartman, B., and Maynard, V., 1979. Early oxidation of organic matter in pelagic sediments of the eastern equatorial Atlantic: suboxic diagenesis. Geochimica et Cosmochimica Acta, v. 43, p. 1075-1090.

Gächter, R., and Müller, B., 2003. Why the phosphorus retention of lakes does not necessarily depend on the oxygen supply to their sediment surface. Limnology and Oceanography, v. 48, p. 929-933.

Gallego-Torres, D., Martínez-Ruiz, F., Paytan, A., Jiménez-Espejo, F.J., and Ortega-Huertas, M., 2007. Pliocene–Holocene evolution of depositional conditions in the eastern Mediterranean: role of anoxia vs. productivity at time of sapropel deposition. Palaeogeography, Palaeoclimatology, Palaeoecology, v. 246(2), p. 424-439.

Galloway, J.N., Dentener, F.J., Capone, D.G., Boyer, E.W., Howarth, R.W., Seitzinger, S.P., Asner, G.P., and Vöosmarty, C.J., 2004. Nitrogen cycles: past, present, and future. Biogeochemistry, v. 70(2), p. 153-226.

Ganeshram, R.S., and Pedersen, T.F., 1998. Glacial-interglacial variability in upwelling and bioproductivity off NW Mexico: Implications for Quaternary paleoclimate. Paleoceanography, v. 13(6), p. 634-645.

Ganeshram, R.S., Calvert, S.E., Pedersen, T.F., and Cowie, G.L., 1999. Factors controlling the burial of organic carbon in laminated and bioturbated sediments off NW Mexico: implications for hydrocarbon preservation. Geochimica et Cosmochimica Acta, v. 63, p. 1723-1734.

Ganeshram, R.S., François, R., Commeau, J., and Brown-Leger, S.L., 2003. An experimental investigation of barite formation in seawater. Geochimica et Cosmochimica Acta, v. 67(14), p. 2599-2605.

Gardner, J.V., Dean, W.E., and Dartnell, P., 1997. Biogenic sedimentation beneath the California Current system for the past 30 kyr and its paleoceanographic significance. Paleoceanography, v. 12(2), p. 207-225.

Gingele, F., and Dahmke, A., 1994. Discrete barite particles and barium as tracers of paleoproductivity in South Atlantic sediments. Paleoceanography, v. 9(1), p. 151-168.

Giraudeau, J., Meyers, P.A., and Christensen, B.A., 2002. Accumulation of organic and inorganic carbon in Pliocene–Pleistocene sediments along the SW African margin. Marine Geology, v. 180(1), p. 49-69.

Goldhammer, T., Brüchert, V., Ferdelman, T.G., and Zabel, M., 2010. Microbial sequestration of phosphorus in anoxic upwelling sediments. Nature Geoscience, v. 3, p. 557-561.

Goñi, M.A., Ruttenberg, K.C., and Eglinton, T.I., 1997. Sources and contribution of terrigenous organic carbon to surface sediments in the Gulf of Mexico. Nature, v. 389, p. 275-278.

Gonneea, M.E., and Paytan, A., 2006. Phase associations of barium in marine sediments. Marine Chemistry, v. 100, p. 124-135.

Gonzalez-Muñoz, M.T., Martinez-Ruiz, F., Morcillo, F., Martin-Ramos, J.D., and Paytan, A., 2012. Precipitation of barite by marine bacteria: A possible mechanism for marine barite formation. Geology, v. 40(8), p. 675-678.

Gooday, A.J., and Nott, J.A., 1982. Intracellular barite crystals in two xenophyophores, *Aschemonella ramuliformis* and *Galatheammina* sp. (Protozoa: Rhizopoda) with comments on the taxonomy of *A. ramuliformis*. Journal of the Marine Biological Association of the United Kingdom, v. 62, p 595-605.

Griffith, E.M., and Paytan, A., 2012. Barite in the ocean–occurrence, geochemistry and palaeoceanographic applications. Sedimentology, v. 59(6), p. 1817-1835.

Hartnett, H.E., Keil, R.G., Hedges, J.I., and Devol, A.H., 1998. Influence of oxygen exposure time on organic carbon preservation in continental margin sediments. Nature, v. 391, p. 572-574.

Hashimoto, S., Horimoto, N., Yamaguchi, Y., Ishimaru, T., and Saino, T. 2005. Relationship between net and gross primary production in the Sagami Bay, Japan. Limnology and Oceanography, v. 50(6), p. 1830-1835.

Hedges, J.I., and Keil, R.G., 1995. Sedimentary organic matter preservation: an assessment and speculative synthesis. Marine Chemistry, v. 49, p. 81-115.

Hedges, J.I., and Parker, P.L., 1976. Land-derived organic matter in surface sediments from the Gulf of Mexico. Geochimica et Cosmochimica Acta, v. 40, p. 1019-1029.

Henrichs, S. M., 1995, Sedimentary organic matter preservation: an assessment and speculative synthesis - a comment. Marine Chemistry, v. 49, no. 2–3, p. 127–136.

Henrichs, S.M. and Reeburgh, W.S., 1987. Anaerobic mineralization of marine sediment organic matter: rates and the role of anaerobic processes in the oceanic carbon economy. Geomicrobiology Journal, v. 5, p. 191-238.

Hiatt, E.E., and Budd, D.A., 2003. Extreme paleoceanographic conditions in a Paleozoic oceanic upwelling system: organic productivity and widespread phosphogenesis in the Permian Phosphoria Sea. In: Chan, M.A., and Archer, A.W. (Eds.). Extreme Depositional Environments: Mega End Members in Geologic Time: Geological Society of America, Special Paper 370, edited by:, pp. 245-264.

Hirst, D.M., 1974. Geochemistry of sediments from eleven Black Sea cores. In: Degens, E.T., and Ross, D.A. (Eds.) The Black Sea—Geology, Chemistry, and Biology, American Association of Petroleum Geologists memoirs, Volume 20, pp. 430-455.

Hori, R., 1992. Radiolarian biostratigraphy at the Triassic/Jurassic period boundary in bedded cherts from the Inuyama Area, central Japan. Journal of Geosciences (Osaka City University), v. 35, p. 53-65.

Hotinski, R.M., Bice, K.L., Kump, L.R., Najjar, R.G., and Arthur, M.A., 2001. Ocean stagnation and end-Permian anoxia. Geology, v. 29, p. 7-10.

Hulthe, G., S. Hulth, and P. O. J. Hall, 1998, Effect of oxygen on degradation rate of refractory and labile organic matter in continental margin sediments. Geochimica et Cosmochimica Acta, v. 62, no. 8, p. 1319–1328.

Hyun, S., Ortiz, J.D., Raymo, M.E., and Taira, A., 1999. Low-frequency oscillations in Site 983 sediments: relationship between carbonate and productivity proxies. In: Raymo, M.E., Jansen, E., Blum, P. Herbert, T. (Eds.). Proceedings of the Ocean Drilling Program: Scientific Results, v.162, p. 197.

Ingall, E.D., and Jahnke, R.A., 1997. Influence of water-column anoxia on the elemental fractionation of carbon and phosphorus during sediment diagenesis. Marine Geology, v. 139, p. 219-229.

Ingall, E.D., and Van Cappellen, P., 1990. Relation between sedimentation rate and burial of organic phosphorus and organic carbon in marine sediments. Geochimica et Cosmochimica Acta, v. 54, p. 373-386.

Ingall, E.D., Bustin, R.M., and Van Cappellen, P., 1993. Influence of water column anoxia on the burial and preservation of carbon and phosphorus in marine shales. Geochimica et Cosmochimica Acta, v. 57, p. 303-316.

Ingall, E.D, Kolowith, L., Lyons, T., and Hurtgen, M., 2005. Sediment carbon, nitrogen and phosphorus cycling in an anoxic fjord, Effingham Inlet, British Columbia. American Journal of Science, v. 305, p. 240-258.

Isozaki, Y., 1997. Permo–Triassic boundary superanoxia and stratified superocean: records from lost deep-sea. Science v. 276, p. 235-238.

Iversen, M.H., and Ploug, H., 2010. Ballast minerals and the sinking carbon flux in the ocean: carbon-specific respiration rates and sinking velocity of marine snow aggregates. Biogeosciences, v. 7(9), p. 2613-2624.

Jaccard, S.L., Galbraith, E.D., Sigman, D.M., Haug, G.H., Francois, R., Pedersen, T.F., Dulski, P., and Thierstein, H.R., 2009. Subarctic Pacific evidence for a glacial deepening of the oceanic respired carbon pool. Earth and Planetary Science Letters, v. 277(1), p. 156-165.

Jaccard, S.L., Hayes, C.T., Martínez-García, A., Hodell, D.A., Anderson, R.F., Sigman, D.M., and Haug, G.H., 2013. Two modes of change in Southern Ocean productivity over the past million years. Science, v. 229, p. 1419-1422.

Jeandel, C., Tachikawa, K., Bory, A., and Dehairs, F., 2000. Biogenic barium in suspended and trapped material as a tracer of export production in the tropical N-E Atlantic (EUMELI Sites). Marine Chemistry, v. 71, p. 125-142.

Jewell, P.W., 1994. Paleoredox conditions and the origin of bedded barite along the Late Devonian North American continental margin. Journal of Geology, v. 102, p. 151-164.

Kasten, S., Haese, R.R., Zabel, M., Ruhlemann, C., and Schulz, H.D., 2001. Barium peaks at glacial terminations in sediments of the equatorial Atlantic Ocean: relicts of deglacial productivity pulses? Chemical Geology, v. 175, p. 635-651.

Kennedy, M.J., Pevear, D.R., and Hill, R.J., 2002. Mineral surface control of organic carbon in black shale. Science, v. 295, p. 657-660.

Kennedy, M.J., Löhr, S.C., Fraser, S.A., and Baruch, E.T., 2014. Direct evidence for organic carbon preservation as clay-organic nanocomposites in a Devonian black shale; from deposition to diagenesis. Earth and Planetary Science Letters, v. 388, p. 59-70.

Kennedy, M.J., and Wagner, T., 2011. Clay mineral continental amplifier for marine carbon sequestration in a greenhouse ocean. Proceedings of the National Academy of Sciences (U.S.A.), v. 108(24), p. 9776-9781.

Kinkel, H., Baumann, K.-H., and Čepek, M., 2000. Coccolithophores in the equatorial Atlantic Ocean: response to seasonal and Late Quaternary surface water variability. Marine Micropaleontology, v. 39, p. 87-112.

Klöcker, R., Ganssen, G., Jung, S.J.A., Kroon, D., and Henrich, R., 2006. Late Quaternary millennial-scale variability in pelagic aragonite preservation off Somalia. Marine Micropaleontology, v. 59, p. 171-183.

Klump, J., Hebbeln, D., and Wefer, G., 2000. The impact of sediment provenance on barium-based productivity estimates. Marine Geology, v. 169(3), p. 259-271.

Kraal, P., 2010. Redox-dependent phosphorus burial in modern and ancient marine sediments. Ph.D. dissertation, Universiteit Utrecht, Netherlands, 176 pp.

Kristensen, E., and M. Holmer, 2001, Decomposition of plant materials in marine sediment exposed to different electron acceptors (O_2, NO_3^-, and SO_4^{2-}), with emphasis on substrate origin, degradation kinetics, and the role of bioturbation. Geochimica et Cosmochimica Acta, v. 65, no. 3, p. 419–433.

Kuypers, M.M.M., Pancost, R.D., Nijenhuis, I.A., and Sinninghe Damsté, J.S., 2002. Enhanced productivity led to increased organic carbon burial in the euxinic North Atlantic basin during the late Cenomanian oceanic anoxic event. Paleoceanography, v. 17(4), 1051, 13 pp.

Latimer, J.C., and Filippelli, G.M., 2002. Eocene to Miocene terrigenous imports and export production: geochemical evidence from ODP Leg 177, Site 1090. Palaeogeography, Palaeoclimatology, Palaeoecology, v. 182, p. 151-164.

Lee, C. B., 1992, Controls on organic carbon preservation: the use of stratified water bodies to compare intrinsic rates of decomposition in oxic and anoxic systems. Geochimica et Cosmochimica Acta, v. 56, no. 8, p. 3323–3335.

Leinen, M., and Graybeal, A., 1986. Sedimentation in the vicinity of Leg-92 drill sites: studies of site survey cores. In: Bailey, M (Ed.). Initial Reports of the Deep Sea Drilling Project, v. 92, p. 237-251.

Le Moigne, F.A.C., Henson, S.A., Sanders, R.J., and Madsen, E., 2013. Global database of surface ocean particulate organic carbon export fluxes diagnosed from the ^{234}Th technique. Earth System Science Data Discussions, v. 6, p. 163-187.

Levinton, J.S., 2008. Marine Biology: Function, Biodiversity, Ecology, 3rd ed., Oxford University Press, 640 pp.

Lisecki, L.E., and Raymo, M.E., 2005. A Pliocene-Pleistocene stack of 57 globally distributed benthic $d^{18}O$ records. Paleoceanography, v. 20(1), PA1003.

Longhurst, A., Sathyendranath, S., Platt, T., and Caverhill, C., 1995. An estimate of global primary production in the ocean from satellite radiometer data. Journal of Plankton Research, v. 17(6), p. 1245-1271.

Longhurst, A.R., 2010. Ecological geography of the sea. Access Online via ScienceDirect. <http://www.sciencedirect.com/science/book/9780124555211>.

Lowenstein, T.K., Timofeeff, M.N., Brennan, S.T., Hardie, L.A., and Demicco, R.V., 2001. Oscillations in Phanerozoic seawater chemistry: Evidence from fluid inclusions. Science, v. 294(5544), p. 1086-1088.

Lückge, A., Boussafir, M., Lallier-Vergès, E., and Littke, R. 1996. Comparative study of organic matter preservation in immature sediments along the continental margins of Peru and Oman. Part I: Results of petrographical and bulk geochemical data. Organic Geochemistry, v. 24(4), p. 437-451.

Luo, G.M., Kump, L.R., Wang, Y., Tong, J., Arthur, M.A., Yang, H., Huang, J., Yin, H., and Xie, S., 2010. Isotope evidence for an anomalously low oceanic sulfate concentration following end-Permian mass extinction. Earth and Planetary Science Letters, v. 300, p. 101-111.

Lyle, A.O., and Lyle, M., 2005. Organic carbon and barium in Eocene sediments: possible controls on nutrient recycling in the Eocene equatorial Pacific Ocean. In: Wilson, P.A., Lyle, M.W., Firth, J. (Eds.) Proceedings of the Ocean Drilling Program, Scientific Results, v. 199, p. 1-33.

Lyle, M., Zahn, R., Prahl, F., Dymond, J., Collier, R., Pisias, N., and Suess, E., 1992. Paleoproductivity and carbon burial across the California Current: The Multitracers transect, 42°N. Paleoceanography, v. 7(3), p. 251-272.

Marra, J., 2008. Approaches to the measurement of plankton production. In: Williams, P.J., Le B., Thomas, D.N., and Reynolds, C.S. (Eds.) Phytoplankton Productivity: Carbon Assimilation in Marine and Freshwater Ecology, Wiley-Blackwell Publishing, pp. 78-108.

Marra, J., 2009. Net and gross productivity: Weighing in with ^{14}C. Aquatic Microbial Ecology, v. 56, p. 123-131.

Martin, R.E., 1995. Cyclic and secular variation in microfossil biomineralization: clues to the biogeochemical evolution of Phanerozoic oceans. Global and Planetary Change, v. 11(1), p. 1-23.

Martinez-Ruiz, F., Kastner, M., Paytan, A., Ortega-Huertas, M., and Bernasconi, S.M., 2000. Geochemical evidence for enhanced productivity during S1 sapropel deposition in the eastern Mediterranean. Paleoceanography, v. 15, p. 200-209.

Martinez-Ruiz, F., Paytan, A., Kastner, M., Gonzalez-Donoso, J.M., Linares, D., Bernasconi, S.M., and Jimenez-Espejo, F.J., 2003. A comparative study of the geochemical and mineralogical characteristics of the S1 sapropel in the western and eastern Mediterranean. Palaeogeography, Palaeoclimatology, Palaeoecology, v. 190, p. 23-37.

McLennan, S.M., 2001. Relationships between the trace element composition of sedimentary rocks and upper continental crust. Geochemistry, Geophysics, Geosystems, v. 2, 2000GC00109, 24 pp.

McManus, J., Berelson, W.M., Hammond, D.E., and Klinkhammer, G.P., 1999. Barium cycling in the North Pacific: Implications for the utility of Ba as a paleoproductivity and paleoalkalinity proxy. Paleoceanography, v. 14(1), p. 53-61.

McManus, J., Berelson, W.M., Klinkhammer, G.P., Johnson, K.S., Coale, K.H., Anderson, R.F., Kumar, N., Burdige, D.J., Hammond, D.E., Brumsack, H.J., McCorckle, D.C., and Rushdi, A., 1998. Geochemistry of barium in marine sediments: implications for its use as a paleoproxy. Geochimica et Cosmochimica Acta, v. 62, p. 3453-3473.

McManus, J., Berelson, W.M., Klinkhammer, G.P., Kilgore, T.M., and Hammond, D.E., 1994. Remobilization of barium in continental margin sediments. Geochimica et Cosmochimica, v. Acta 58(22), p. 4899-4907.

Meyers, P.A., 1997. Organic geochemical proxies of paleoceanographic, paleolimnologic, and paleoclimatic processes. Organic Geochemistry, v. 27, p. 213-250.

Mills, R.A., Taylor, S.L., Pälike, H., and Thomson, J., 2010. Hydrothermal sediments record changes in deep water oxygen content in the SE Pacific. Paleoceanography, v. 25, PA4226, 16 pp.

Modica, C.J., and Lapierre, S.G., 2012. Estimation of kerogen porosity in source rocks as a function of thermal transformation: example from the Mowry Shale in the Powder River Basin of Wyoming. American Association of Petroleum Geologists Bulletin, v. 96(1), p. 87-108.

Monnin, C., Jeandel, C., Cattaldo, T., and Dehairs, F., 1999. The marine barite saturation state of the world's oceans. Marine Chemistry, v. 65, p. 253-261.

Moody, J.B., Chaboudy, L.R., and Worsley, T.R., 1988. Pacific pelagic phosphorus accumulation during the last 10 my. Paleoceanography, v. 3(1), p. 113-136.

Moreno, A., Nave, S., Kuhlmann, H., Canals, M., Targarona, J., Freudenthal, T., and Abrantes, F., 2002. Productivity response in the North Canary Basin to climate changes during the last 250,000 yr: A multi-proxy approach. Earth and Planetary Science Letters, v. 196, p. 147-159.

Mort, H.P., Adatte, T., Föllmi, K.B., Keller, G., Steinmann, P., Matera, V., Berner, Z., and Stuben, D., 2007. Phosphorus and the roles of productivity and nutrient recycling during oceanic anoxic event 2. Geology, v. 35, p. 483-486.

Müller, P.J., and Suess, E., 1979. Productivity, sedimentation rate, and sedimentary organic matter in the ocean-I. Organic carbon preservation. Deep-Sea Research, v. 26, p. 1347-1362.

Muñoz, P., Dezileau, L., Cardenas, L., Sellanes, J., Lange, C.B., Inostroza, J., Muratli, J., and Salamanca, M.A., 2012. Geochemistry of trace metals in shelf sediments affected by seasonal and permanent low oxygen conditions off central Chile, SE Pacific (~36° S). Continental Shelf Research, v. 33, p. 51-68.

Murphy, A.E., Sageman, B.B., Hollander, D.J., Lyons, T.W., and Brett, C.E., 2000b. Black shale deposition in the Devonian Appalachian Basin: siliciclastic starvation, episodic water-column mixing, and efficient recycling of biolimiting nutrients. Paleoceanography, v. 15, p. 280-291.

Murray, D.W., and Prell, W.L., 1991. Pliocene to Pleistocene variations in calcium carbonate, organic carbon, and opal on the Owen Ridge, northern Arabian Sea. In: Emeis, K.C., Meyers, P.A., Niitsuma, N., Prell, W.L. (Eds.). Proceedings of the Ocean Drilling Program, Scientific Results, v. 117, p. 343-363.

Murray, R.W., Knowlton, C.W., Leinen, M., Mix, A.C., and Polsky, C.H., 2000. Export production and carbonate dissolution in the central equatorial Pacific Ocean over the past 1 Myr. Paleoceanography, v. 15(6), p. 570-592.

Murray, R.W., Christensen, B.A., Kalbas, J.L., and Kryc, K.A., 2002. Pliocene export production and terrigenous provenance of the Southern Cape Basin, southwest African margin. Marine Geology, v. 180(1), p. 133-150.

Murray, R.W., Leinen, M., and Knowlton, C.W., 2012. Links between iron input and opal deposition in the Pleistocene equatorial Pacific Ocean. Nature Geoscience, v. 5(4), p. 270-274.

Nijenhuis, I.A., Bosch, H.-J., Sinninghe Damsté, J.S., Brumsack, H.J., and De Lange, G.J., 1999. Organic matter and trace element rich sapropels and black shales: a geochemical comparison. Earth and Planetary Science Letters, v. 169, p. 277-290.

Nürnberg, C.C., Bohrmann, G., Schlüter, M., and Frank, M., 1997. Barium accumulation in the Atlantic sector of the Southern Ocean: Results from 190,000-year records. Paleoceanography, v. 12(4), p. 594-603.

Opsahl, S., and Benner, R., 1997. Distribution and cycling of terrigenous dissolved organic matter in the ocean. Nature, v. 386, p. 480-482.

Owen, R.M., and Zimmerman, A.R.B., 1991. Geochemistry of the Cretaceous/Tertiary boundary at Hole 752B, Broken Ridge. In: Weissel, J., Alt, J. Peirce, J., Taylor, E. (Eds.) Proceedings of the Ocean Drilling Program, Scientific Results, v. 121, p. 423-433.

Pace, M.L., Knauer, G.A., Karl, D.M., and Martin, J.H., 1987. Primary production, new production and vertical flux in the eastern Pacific Ocean. Nature, v. 325, p. 803-804.

Paytan, A., and Griffith, E.M., 2007. Marine barite: recorder of variations in ocean export productivity. Deep-Sea Research II, v. 54, p. 687-705.

Paytan, A., and Kastner, M., 1996. Benthic Ba fluxes in the central Equatorial Pacific, implications for the oceanic Ba cycle. Earth and Planetary Science Letters, v. 142, p. 439-459.

Paytan, A., and McLaughlin, K., 2007. The oceanic phosphorus cycle. Chemical Reviews, v. 107, p. 563-576.

Paytan, A., Kastner, M., and Chavez, F.P., 1996. Glacial to interglacial fluctuations in productivity in the Equatorial Pacific as indicated by marine barite. Science, v. 274, p. 1355-1357.

Paytan, A., Averyt, K., Faul, K., Gray, E., and Thomas, E., 2007. Barite accumulation, ocean productivity, and Sr/Ba in barite across the Paleocene-Eocene Thermal Maximum. Geology, v. 35, p. 1139-1142.

Pedersen, T.F., and Calvert, S.E., 1990. Anoxia vs. productivity: what controls the formation of organic-rich sediments and sedimentary rocks? American Association of Petroleum Geologists Bulletin, v. 74, p. 454-466.

Peters, K.E., Magoon, L.B., Bird, K.J., Valin, Z.C., and Keller, M.A., 2006. North Slope, Alaska: source rock distribution, richness, thermal maturity, and petroleum charge. American Association of Petroleum Geologists Bulletin, v. 90(2), p. 261-292.

Pfeifer, K., Kasten, S., Hensen, C., and Schulz, H.D., 2001. Reconstruction of primary productivity from the barium contents in surface sediments of the South Atlantic Ocean. Marine Geology, v. 177(1), p. 13-24.

Pirrung, M., Illner, P., and Matthießen, J., 2008. Biogenic barium in surface sediments of the European Nordic Seas. Marine Geology, v. 250(1), p. 89-103.

Prakash Babu, C., Brumsack, H.-J., Schnetger, B., and Böttcher, M.E., 2002. Barium as a productivity proxy in continental margin sediments: A study from the eastern Arabian Sea. Marine Geology, v. 184, p. 189-206.

Rageneau, O., Tréguer, P., Leynaert, A., Anderson, R.F., Brzezinski, M.A., DeMaster, D.J., Dugdale, R.C., Dymond, J., Fischer, G., François, R., Heinze, C., Maier-Reimer, E., Martin-Jézéquel, V., Nelson, D.M., and Quéguiner, B., 2000. A review of the Si cycle in the modern ocean: recent progress and missing gaps in the application of biogenic opal as a paleoproductivity proxy. Global and Planetary Change, v. 26, p. 317-365.

Raiswell, R., and Berner, R.A., 1987. Organic carbon losses during burial and thermal maturation of normal marine shales. Geology, v. 15(9), p. 853-856.

Rao, V.P., and Lamboy, M., 1995. Phosphorites from the Oman Margin, ODP Leg 117. Oceanologica Acta, v. 18(3), p. 289-307.

Raymo, M.E., Hodell, D., and Jansen, E., 1992. Response of deep ocean circulation to initiation of Northern Hemisphere glaciation (3–2 Ma). Paleoceanography, v. 7(5), p. 645-672.

Rea, D.K., Pisias, N.G., and Newberry, T., 1991. Late Pleistocene paleoclimatology of the central equatorial Pacific: Flux patterns of biogenic sediments. Paleoceanography, v. 6(2), p. 227-244.

Redfield, A.C., 1958. The biological control of chemical factors in the environment. American Scientist, v. 46(3), p. 205-221.

Reichart, G.J., den Dulk, M., Visser, H.J., van der Weijden, C.H., and Zachariasse, W.J., 1997. A 225 kyr record of dust supply, paleoproductivity and the oxygen minimum zone from the Murray Ridge (northern Arabian Sea). Palaeogeography, Palaeoclimatology, Palaeoecology, v. 134(1), p. 149-169.

Reitz, A., Pfeifer, K., de Lange, G.J., and Klump, J., 2004. Biogenic barium and the detrital Ba/Al ratio: a comparison of their direct and indirect determination. Marine Geology, v. 204, p. 289-300.

Ridgwell, A., 2005. A Mid Mesozoic Revolution in the regulation of ocean chemistry. Marine Geology, v. 217(3), p. 339-357.

Rieder, N., Ott, H.A., Pfundstein, P., and Schoch, R., 1982. X-ray micro-analysis of the mineral contents of some protozoa. Journal of Protozoology, v. 29, p. 15-18.

Robinson, R.S., Meyers, P.A., and Murray, R.W., 2002. Geochemical evidence for variations in delivery and deposition of sediment in Pleistocene light–dark color cycles under the Benguela Current Upwelling System. Marine Geology, v. 180(1), p. 249-270.

Rostek, F., Bard, E., Beaufort, L., Sonzogni, C., and Ganssen, G., 1997. Sea surface temperature and productivity records for the past 240 kyr in the Arabian Sea. Deep Sea Research II, v. 44, p. 1461-1480.

Ruhlin, D.E., and Owen, R.M., 1986. The rare earth element geochemistry of hydrothermal sediments from the East Pacific Rise: Examination of a seawater scavenging mechanism. Geochimica et Cosmochimica Acta, v. 50(3), p. 393-400.

Russell, A.D., and Morford, J.L., 2001. The behavior of redox-sensitive metals across a laminated–massive–laminated transition in Saanich Inlet, British Columbia. Marine Geology, v. 174(1), p. 341-354.

Rutsch, H.-J., Mangini, A., Bonani, G., Dittrich-Hannen, B., Kubik, P.W., Suter, M., and Segl, M., 1995. ^{10}Be and Ba concentrations in West African sediments trace productivity in the past. Earth and Planetary Science Letters, v. 133, p. 129-143.

Ruttenberg, K.C., and Goñi, M.A., 1997. Phosphorus distribution, C:N:P ratios, and $\delta^{13}C_{oc}$ in arctic, temperature, and tropical coastal sediments: tools for characterizing bulk sedimentary organic matter. Marine Geology, v. 139, p. 123-145.

Sadler, P.M., 1981. Sediment accumulation rates and the completeness of stratigraphic sections. Journal of Geology, v. 89, p. 569-584.

Sarnthein, M., Winn, K., Duplessy, J.C., and Fontugne, M.R., 1988. Global variations of surface ocean productivity in low and mid latitudes: influence on CO_2 reservoirs of the deep ocean and atmosphere during the last 21,000 years. Paleoceanography v. 3, p. 361-399.

Schenau, S.J., and De Lange, G.J., 2001. Phosphorus regeneration vs. burial in sediments of the Arabian Sea. Marine Geology, v. 75, p. 201-217.

Schenau, S.J., Prins, M.A., De Lange, G.J., and Monnin, C., 2001. Barium accumulation in the Arabian Sea: controls on barite preservation in marine sediments. Geochimica et Cosmochimica Acta, v. 65(10), p. 1545-1556.

Schenau, S.J., Reichart, G.J., and De Lange, G.J., 2005. Phosphorus burial as a function of paleoproductivity and redox conditions in Arabian Sea sediments. Geochimica et Cosmochimica Acta, v. 69(4), p. 919-931.

Schink, B., 1988. Principles and limits of anaerobic degradation: environmental and technological aspects. In: A.J.B. Zehnder (Ed.), Biology of Anaerobic Organisms. Wiley, pp. 771-846.

Schultz, H., von Rad, U., and Erlenkeuser, H., 1998. Correlation between Arabian Sea and Greenland climate oscillations of the past 110,000 years. Nature, v. 393, p. 54-57.

Scopelliti, G., Bellanca, A., Coccioni, R., Luciani, V., Neri, R., Baudin, F., Chiari, M., and Marcucci, M., 2004. High-resolution geochemical and biotic records of the Tethyan 'Bonarelli Level' (OAE2, latest Cenomanian) from the Calabianca-Guidaloca composite section, northwestern Sicily, Italy. Palaeogeography, Palaeoclimatology, Palaeoecology, v. 208, p. 293-317.

Shimmield, G.B., 1992. Can sediment geochemistry record changes in coastal upwelling palaeoproductivity? Evidence from northwest Africa and the Arabian Sea. In: Summerhayes, C.P., Prell, W.L., and Emeis, K.C., (Eds.) Upwelling Systems: Evolution since the Miocene: Geological Society of London, Special Publications 64, pp. 29-46.

Shimmield, G.B., and Mowbray, S.R., 1991. The inorganic geochemical record of the northwest Arabian Sea: A history of productivity variation over the last 400 ky from Sites 722 and 724. In: Emeis, K.C., Meyers, P.A., Niitsuma, N., Prell, W.L. (Eds.). Proceedings of the Ocean Drilling Program, Scientific Results, v. 117,, p. 409-429.

Shimmield, G., Derrick, S., Mackensen, A., Grobe, H., and Pudsey, C., 1994. The history of barium, biogenic silica and organic carbon accumulation in the Weddell Sea and Antarctic Ocean over the last 150,000 years. In: Zahn, R., Kaminski, M., Labeyrie, L., and Pedersen, T. (Eds.). Carbon Cycling in the Glacial Ocean: Constraints on the Ocean's Role in Global Change, NATO ASI Series, Springer, Berlin, pp. 555-574.

Showers, W.J., and Angle, D.G., 1986. Stable isotopic characterization of organic carbon accumulation on the Amazon continental shelf. Continental Shelf Research, v. 6, p. 227-244.

Simon, A., Poulicek, M., Velimirov, B., and MacKenzie, F.T., 1994. Comparison of anaerobic and aerobic biodegradation of mineralized skeletal structures in marine and estuarine conditions. Biogeochemistry, v. 25, p. 167-195.

Skjervoy, A., and Sylta, Ø., 1993. Modeling of expulsion and secondary migration along the southwestern margin of the Horda platform. In: Doré, A.G., Augustson, J.H., Stewart, D.J., Sylta, Ø. (Eds.). Basin Modeling: Advances and Applications. Proceedings of the Norwegian Petroleum Society Conference, Stavanger, Norway, 13-15 March 1991, NPF Special Publication No. 3, Elsevier, pp. 499-538.

Song, H., Tong, J., Algeo, T.J., Song, H., Qiu, H., Zhu, Y., Tian, L., Bates, S., Lyons, T.W., Luo, G., and Kump, L., 2014. Early Triassic seawater sulfate drawdown. Geochimica et Cosmochimica Acta, v. 128, p. 95-113.

Sternberg, E., Tang, D., Ho, T.Y., Jeandel, C., and Morel, F.M.M., 2005. Barium uptake and adsorption in diatoms. Geochimica et Cosmochimica Acta, v. 69(11), p. 2745-2752.

Sternberg, E., Jeandel, C., Miquel, J.C., Gasser, B., Souhaut, M., Arraes-Mescoff, R., and Francois, R., 2007. Particulate barium fluxes and export production in the northwestern Mediterranean. Marine Chemistry, v. 105(3), p. 281-295.

Suess, E., 1980. Particulate organic carbon flux in the oceans — surface productivity and oxygen utilization. Nature, v. 288, p. 260-263.

Taylor, G.H., Teichmüller, M., and Davis, C. (Eds.), 1998. Organic Petrology, 16th ed., Gebrüder Borntraeger, Berlin, 704 pp.

Taylor, S.R. and McLennan, S.M., 1985. The Continental Crust: Its Composition and Evolution. Blackwell, Oxford, 312 pp.

Thevenon, F., Bard, E., Williamson, D., and Beaufort, L. 2004. A biomass burning record from the West Equatorial Pacific over the last 360 ky: methodological, climatic and anthropic implications. Palaeogeography, Palaeoclimatology, Palaeoecology, v. 213(1), p. 83-99.

Thomson, J., Higgs, N.C., Wilson, T.R.S., Croudace, I.W., De Lange, G.J., and Santvoort, P.J.M., 1995. Redistribution and geochemical behavior of redox-sensitive elements around S1, the most recent eastern Mediterranean sapropel. Geochimica et Cosmochimica Acta, v. 59, p. 3487-3501.

Timothy, D.A., and Soon, M., 2001. Primary production and deep-water oxygen content of two British Columbian fjords. Marine Chemistry, v. 73(1), p. 37-51.

Tomas, C.R. (Ed.), 1997. Identifying Marine Phytoplankton. Academic Press, Elsevier, Amsterdam, 858 pp.

Torres, M.E., Brumsack, H.J., Bohrman, G., and Emeis, K.C., 1996. Barite front in continental margin sediments: a new look at barium remobilization in the zone of sulfate reduction and formation of heavy barites in diagenetic fronts. Chemical Geology, v. 127, p. 125-139.

Trask, P.D., 1953, Chemical studies of sediments of the western Gulf of Mexico. Papers in Physical Oceanography and Meteorology, v. 12(4), p. 49-120.

Tribovillard, N., Algeo, T.J., Lyons, T.W., and Riboulleau, A., 2006. Trace metals as paleoredox and paleoproductivity proxies: an update. Chemical Geology, v. 232, p. 12-32.

Tribovillard, N., Riboulleau, A., Lyons, T., and Baudin, F., 2004. Enhanced trapping of molybdenum by sulfurized marine organic matter of marine origin in Mesozoic limestones and shales. Chemical Geology, v. 213, p. 385-401.

Tromp, T.K., Van Cappellen, P., and Key, R.M., 1995. A global model for the early diagenesis of organic carbon and organic phosphorus in marine sediments. Geochimica et Cosmochimica Acta, v. 59, p. 1259-1284.

Tyson, R.V., 1995. Sedimentary Organic Matter: Organic Facies and Palynofacies. Chapman and Hall, London, 615 pp.

Tyson, R.V., 2001. Sedimentation rate, dilution, preservation, and total organic carbon: some results of a modeling study. Organic Geochemistry, v. 32, p. 333-339.

Tyson, R.V., 2005. The "productivity versus preservation" controversy; cause, flaws, and resolution. In: Harris, N.B. (Ed.). Deposition of Organic-Carbon-Rich Sediments: Models, Mechanisms, and Consequences: Society for Sedimentary Geology (SEPM-SSG) Special Publication 82, pp. 17-33.

Van Beek, P., François, R., Conte, M., Reyss, J.L., Souhaut, M., and Charette, M., 2007. $^{228}Ra/^{226}Ra$ and $^{226}Ra/Ba$ ratios to track barite formation and transport in the water column. Geochimica et Cosmochimica Acta, v. 71(1), p. 71-86.

Van Cappellen, P., and Ingall, E.D., 1994. Benthic phosphorus regeneration, net primary production, and ocean anoxia: a model of the coupled marine biogeochemical cycles of carbon and phosphorus. Paleoceanography, v. 9, p. 677-692.

Van Os, B.J.H., Middelburg, J.J., and De Lange, G.J., 1991. Possible diagenetic mobilization of barium in sapropelic sediment from the eastern Mediterranean. Marine Geology, v. 100, p. 125-136.

Van Santvoort, P.J.M., De Lange, G.J., Thomson, J., Cussen, H., Wilson, T.R.S., Krom, M.D., and Ströhle, K., 1996. Active post-depositional oxidation of the recent sapropel (S1) in sediments of the eastern Mediterranean Sea. Geochimica et Cosmochimica Acta, v. 60, p. 4007-4024.

Vink, S., Chambers, R.M., and Smith, S.V., 1997. Distribution of phosphorus in sediments from Tomales Bay, California. Marine Geology, v. 139, p. 157-179.

Von Breymann, M., Emeis, K.-C., and Suess, E., 1992. Water depth and diagenetic constraints on the use of the barium as a paleoproductivity indicator. In: Summerhayes, C.P., Prell, W.L., and Emeis, K.C. (Eds.). Upwelling Systems: Evolution since the Early Miocene. Geological Society of London Special Publication 64, pp. 273-284.

Weijers, J.W., Schouten, S., Schefuß, E., Schneider, R.R., and Sinninghe Damsté, J.S., 2009. Disentangling marine, soil and plant organic carbon contributions to continental margin sediments: A multi-proxy approach in a 20,000 year sediment record from the Congo deep-sea fan. Geochimica et Cosmochimica Acta, v. 73(1), p. 119-132.

Weldeab, S., Emeis, K.-C., Hemleben, C., Schmiedl, G., and Schulz, H., 2003. Spatial productivity variations during formation of sapropels S5 and S6 in the Mediterranean Sea: evidence from Ba contents. Palaeogeography, Palaeoclimatology, Palaeoecology, v. 191, p. 169-190.

Westrich, J. T., and Berner, R. A. 1984. The role of sedimentary organic matter in bacterial sulfate reduction: The G model tested. Limnology and Oceanography, v. 29(2), p. 236-249.

Wheatcroft, R.A., 1990, Preservation potential of sedimentary event layers. Geology, v. 18, p. 843-845.

Wignall, P.B., and Newton, R., 2003. Contrasting deep-water records from the Upper Permian and Lower Triassic of South Tibet and British Columbia: evidence for a diachronous mass extinction. Palaios, v. 18, p. 153-167.

Winckler, G., Anderson, R.F., and Schlosser, P., 2005. Equatorial Pacific productivity and dust flux during the mid-Pleistocene climate transition. Paleoceanography, v. 20(4), 10 pp.

Winguth, A.M.E., and Winguth, C., 2012. Simulating Permian-Triassic oceanic anoxia distribution: Implications for species extinction and recovery. Geology, v. 40, p. 127-130.

Wortmann, U.G., and Paytan, A., 2012. Rapid variability of seawater chemistry over the past 130 million years. Science, v. 337, p. 334-336.

Yarincik, K.M., Murray, R.W., Lyons, T.W., Peterson, L.C., and Haug, G.H., 2000. Oxygenation history of bottom waters in the Cariaco Basin, Venezuela, over the past 578,000 years: results from redox-sensitive metals (Mo, V, Mn, and Fe). Paleoceanography, v. 15(6), p. 593-604.

Zachos, J.C., Arthur, M.A., and Dean, W.E., 1989. Geochemical evidence for suppression of pelagic marine productivity at the Cretaceous/Tertiary boundary. Nature, v. 337, p. 61-64.

Zarriess, M., and Mackensen, A. 2010. The tropical rainbelt and productivity changes off northwest Africa: A 31,000-year high-resolution record. Marine Micropaleontology, v. 76(3), p. 76-91.

Zonneveld, K.A.F., Versteegh, G.J.M., Kasten, S., Eglinton, T.I., Emeis, K.C., Huguet, C., Koch, B.P., de Lange, G.J., Middelburg, J.J., Mollenhauer, G., Prahl, F.G., Rethemeyer, J., and Wakeham, S.G., 2010. Selective preservation of organic matter in marine environments; processes and impact on the sedimentary record. Biogeosciences, v. 7, p. 483-511.

Conclusions and potential for future work

The studies at Opal Creek have helped to constrain the nature of oceanographic conditions and processes on the western Pangaean margin during the Late Permian, and to address the biogeochemical changes that occurred during the Permian-Triassic crisis. Nitrogen fixers appear to have become increasingly important in the Early Triassic, although not to the extent seen elsewhere (e.g. Luo et al. 2011). The high productivity that characterized this system in the Permian appears to have reached a peak coincident with the onset of euxinic conditions and then eventually fallen off in the Early Triassic, although subsequent studies using the equations derived in Chapter III may expand on and complicate this picture. The geochemical data are in good agreement with independent paleontological evaluations of the Middle Permian environment, with the demosponge-dominated benthos having been associated with cold, upwelling waters (Beauchamp and Baud 2002), and the abundant but homogenous conodont fauna suggesting eutrophic conditions (Brasier 1995). These results are also in good agreement with the predictions of recent modeling studies for this region (Winguth and Winguth 2012).

While it should be stressed that the northeastern Panthalassic Ocean was only a small region of the Permian world and not a sufficient area for drawing global conclusions, these results provide field-based, geochemical ground truth to the increased ocean stratification that has been hypothesized (Kump et al. 2005) and predicted by global circulation models (Hotinski 2001, Kiehl and Shields 2005, Winguth and Winguth 2012). Along with geochemical contributions from the Tethyan region (Song et al. 2013), we can now begin to say confidently that stagnation of the ocean did in fact occur in

response to the (increasingly well constrained) warming in the latest Permian (Sun et al. 2012; Romano et al., 2013).

Work in the northeastern Panthalassic region is continuing, and datasets comparable to that from Opal Creek are being generated for two additional sections in northern British Columbia. The first is the condensed Ursula Creek section on Williston Lake, which has been the subject of a carbon isotope study (Wang et al. 1994) and more comprehensive petrographic study (Wignall and Newton 2003) to which I hope to add nitrogen isotopes and trace elements. The other section, Peck Creek (Henderson 2011) has been measured, but never been the subject of geochemical study. While the sequence of facies is comparable to Opal Creek, these sections were likely deposited in deeper water, and while conodont analysis is still in progress, the sections appear to be conformable, without the complicating effects of the early Lopingian erosional surface and condensed Changhsingian sedimentation at Opal Creek.

These studies are also being extended far offshore into the open Panthalassic Ocean. The open ocean, despite covering the majority of the Earth's surface area, is poorly represented in the Paleozoic rock record. The Mino-Tamba Terrane of central Japan, representing deposition in the equatorial Panthalassic Ocean at abyssal depths (Algeo et al. 2010a,b), provides a unique glimpse at the Permian Triassic extinction as it occurred far from any land. As a result, the effects of changing terrestrial sediment runoff and sea level are minimized, and geochemical proxies may represent a well-integrated global signal. Like northeastern Panthalassa, these sections are characterized by cherts in the Permian (here formed by radiolarian tests), transitioning to black shales in the early Triassic (Algeo et al. 2010a,b). Despite low organic content, carbon and nitrogen isotopes

have been measured from two Mino-Tamba Terrane sections: Gujo Hachiman, and Ubara (Appendix C), showing that the well known negative carbon isotope excursion at the end Permian is small but present in the equatorial ocean, and that isotopes of N are persistently near atmospheric values throughout the time interval surveyed, suggesting an important role for N-fixers in the primary producer community.

The review of paleoproductivity proxies described in Chapter III found sedimentation rate to be an extremely important control on the preservation rate of productivity proxies, and one that can work in two directions by enhancing preservation and diluting the flux of organic components. The relationship between sediment accumulation and organic carbon preservation was strong, an encouraging result in light of the independent origin of the productivity measurements, which formed the basis of the preservation calculations. Phosphorus accumulation also appeared to have a significant relationship with productivity despite redox effects on preservation. Barium was found to have little discernible relationship to productivity, and its use may best be limited to the fully pelagic marine environments in which the proxy was developed. The equations derived in this chapter will hopefully serve as the beginning of a geochemical toolkit for translating geochemical proxies into paleoproductivity estimates..

Working with collaborators here and in China, the toolkit developed in Chapter III is now being applied to a number of Permian-Triassic sections worldwide, including Opal Creek. Revisiting this and other sections with new ideas applied to existing data will allow for a better understanding of the extent and duration of the pulse of terrigenous sediment and high productivity that has been inferred at Opal Creek, especially in light of the strong relationship between these processes (sedimentation rate and apparent

productivity) investigated in Chapter III. Going forward, estimates of paleoproductivity using these tools and new ones can be compared side by side with proxy records of nitrogen availability, including in sections in which pervasive N limitation is evident (as in the Japanese PTB sections discussed above). In the coming years, this will allow us to expand our understanding of the disturbed nutrient cycles that may have undercut the base of the marine food chain during the catastrophic warming that accompanied the Permian-Triassic mass extinction (Joachimski et al. 2012, Sun et al. 2012).

References:

Algeo, T.J., Hinnov, L., Moser, J., Maynard, J.B., Elswick, E., Kuwahara, K., Sano, H., 2010a. Changes in productivity and redox conditions in the Panthalassic Ocean during the latest Permian. Geology 38, 187-190; doi:10.1130/G30483.1.

Algeo, T.J., Kuwahara, K., Sano, H., Bates, S., Lyons, T., Elswick, E., Hinnov, L., Ellwood, B., Moser, J., Maynard, J.B., 2010b. Spatial variation in sediment fluxes, redox conditions, and productivity in the Permian-Triassic Panthalassic Ocean, Palaeogeography, doi: 10.1016/j.palaeo.2010.07.007.

Beauchamp, B., Baud, A., 2002. Growth and demise of Permian biogenic chert along northwest Pangea: evidence for end-Permian collapse of thermohaline circulation. Palaeogeography, Palaeoclimatology, Palaeoecology 184, 37-63.

Brasier, M.D., 1995. Fossil indicators of nutrient levels, 1. Eutrophication and climate change. Geological Society of London Special Publications 83, pp. 113–132.

Henderson, C.M. 2011. Biostratigraphic correlation and shale fabric of Lower Triassic strata, east-central British Columbia (NTS 093I, O, P); in Geoscience BC Summary of Activities 2010, Geoscience BC, Report 2011-1, p. 223–228.

Hotinski, R.M., Bice, K.L., Kump, L.R., Najjar, R.G., Arthur, M.A., 2001. Ocean stagnation and end-Permian anoxia. Geology 29, 7-10.

Joachimski, M. M., Lai, X., Shen, S., Jiang, H., Luo, G., Chen, B., Chen, J., Sun, Y. 2012. Climate warming in the latest Permian and the Permian–Triassic mass extinction. Geology, v. 40(3), p. 195-198.

Kiehl, J.T., and Shields, C.A., 2005. Climate simulation of the latest Permian: implications for mass extinction. Geology 33, 757–760.

Kump, L.R., Pavlov, A., Arthur, M.A., 2005. Massive release of hydrogen sulfide to the surface ocean and atmosphere during interval of oceanic anoxia. Geology 33, 397–400.

Luo, G., Wang, Y., Algeo, T. J., Kump, L. R., Bai, X., Yang, H., Yao L., and Xie, S. 2011. Enhanced nitrogen fixation in the immediate aftermath of the latest Permian marine mass extinction. Geology, v. 39(7), p, 647-650.

Romano, C., Goudemand, N., Vennemann, T. W., Ware, D., Schneebeli-Hermann, E., Hochuli, P. A., Brühwiler, T., Brinkmann, W. & Bucher, H. 2013. Climatic and biotic upheavals following the end-Permian mass extinction. Nature Geoscience, v. 6(1), p. 57-60.

Song, H., Tong, J., Algeo, T. J., Horacek, M., Qiu, H., Song, H., & Chen, Z. Q. 2013. Large vertical $\delta^{13}C_{DIC}$ gradients in Early Triassic seas of the South China craton: Implications for oceanographic changes related to Siberian Traps volcanism. Global and Planetary Change, v.105, p. 7-20.

Sun, Y., Joachimski, M. M., Wignall, P. B., Yan, C., Chen, Y., Jiang, H., Wang, L., Lai, X. 2012. Lethally hot temperatures during the Early Triassic greenhouse.Science, v. 338(6105), p. 366-370.

Wang, K., Geldsetzer, H.H.J., Krouse, H.R. 1994. Permian-Triassic extinction: Organic $\delta^{13}C$ evidence from British Columbia, Canada. Geology, v. 22(7), p. 580-584.

Wignall, P.B. and Newton, R. 2003. Contrasting deep-water records from the Upper Permian and Lower Triassic of South Tibet and British Columbia: evidence for a diachronous mass extinction. Palaios, 18, 153–167.

Winguth, C., and A.M.E. Winguth, 2012b. Simulating Permian-Triassic oceanic anoxia distribution: Implications for species extinction and recovery. Geology, 40, p. 127-130.

Acknowledgments:

I would like to extend my gratitude to the many people who helped me complete this dissertation, including my advisor, Peter Ward, and my committee members Bruce Nelson, Eric Steig, Roger Buick, Thomas Algeo and Loveday Conquest, for their invaluable scientific and professional advice. My research collaborators Charles Henderson and Shuzhong Shen have also gone above and beyond in helping me to get involved in international research projects that I hope to continue working on in the future. None of this work would have been possible without Andy Schauer, Kyle Samek, and the staff of the UW IsoLab helping with measurements and technique development, or without the many coauthors who contributed to the studies published here.

I would also like to thank the National Science Foundation for financial support, through the GK-12 Oceans and Coasts Interdisciplinary Science program and other grants to the Ward Lab. The Earth and Space Science Department and its donors provided crucial support through department grants that allowed me to pursue fieldwork and independent research projects. The department also gave me plenty of opportunities to TA courses, which in addition to supporting my research were a fantastic opportunity to learn about teaching and solidify my own knowledge. The University of Washington Astrobiology was another generous source of exciting learning opportunities.

Lastly, I would like to thank my labmates (and companions on many adventures), Tom Tobin, Kelly Hillbun, Ricky Dooley, David Smith, and Loren Ballanti, for many useful and fascinating conversations over the past few years. To all of my family and friends in Seattle and elsewhere, I couldn't have done this without you. Thanks again.